1-1-2007

The dynamics of satellite and dark matter halo interactions on galaxy formation and evolution.

Jun-Hwan, Choi
University of Massachusetts Amherst

THE DYNAMICS OF SATELLITE AND DARK MATTER HALO INTERACTIONS ON GALAXY FORMATION AND EVOLUTION

A Dissertation Presented

by

JUN-HWAN CHOI

Submitted to the Graduate School of the
University of Massachusetts Amherst in partial fulfillment
of the requirements for the degree of

DOCTOR OF PHILOSOPHY

September 2007

Astronomy Department

UMI Number: 3289249

ProQuest Information and Learning Company
300 North Zeeb Road
P.O. Box 1346
Ann Arbor, MI 48106-1346

THE DYNAMICS OF SATELLITE AND DARK MATTER HALO INTERACTIONS ON GALAXY FORMATION AND EVOLUTION

A Dissertation Presented

by

JUN-HWAN CHOI

Approved as to style and content by:

Martin D. Weinberg, Co-chair

Neal Katz, Co-chair

Houjun Mo, Member

Jennie Traschen, Member

Ronald L. Snell, Department Chair
Astronomy Department

THE DYNAMICS OF SATELLITE AND DARK MATTER HALO INTERACTIONS ON GALAXY FORMATION AND EVOLUTION

A Dissertation Presented

by

JUN-HWAN CHOI

Approved as to style and content by:

Martin D. Weinberg, Co-chair

Neal Katz, Co-chair

Houjun Mo, Member

Jennie Traschen, Member

Ronald L. Snell, Department Chair
Astronomy Department

Deo gratias

ACKNOWLEDGMENTS

I am greatly indebted to my co-adviser and mentor Martin Weinberg for his guidance throughout my thesis work. Without his advice and encouragement, it is impossible to complete my dissertation. He has alos provided both his N-body code and his perturbation theory calculation which are widely used in this thesis. During my thesis work, I have learned from him not only science itself but also the attitude toward science. I am also indebted Neal Katz, my co-adviser, for priceless advice. His keen advice many times enlightened me how to solve astronomical problems. Many thanks also go to Houjun Mo who helped me publish my first journal paper and provided helpful comments as thesis committee member.

During my graduate school, it has been very lucky to meet many wonderful astronomers in our department. Dusan who was my long term officemate has often stimulated my passion for astronomy. Many discussions with the members in theoretical astrophysics group, especially Mark Fardal, Kelly Holley-Bockelmann, Dan McIntosh, Yu Lu, and Yun Li have enlarged my view of the astronomy. I would like to thank to the Korean crowd in the department, Aeree, Ilsang, and Sungroung and other friends in astronomy department, especially Daisuke, Nicolas, Chung, Dan, and Li. The life would be boring without them.

All other members in Astronomy department, including three GPDs (Mike Skrutskie, John Kwan, and William Irvine) and one department chair (Ronald Snell), help me a lot to smoothly proceed my degree. Prof. Min Yun often gave me kind advice about overall graduate life. I thank to Jim Luippold for his careful reading this manuscript. Shashi Kanbur, Craig West, and Daniel Popowich make my computers run smoothly.

I have been indebted to all my family members: My father has been supporting and encouraging me constantly; my mother gives me endless love and prayers; my brother and sister have cheered me during my graduate school; and, Heekyoung has been my side with love, support and understanding.

ABSTRACT

THE DYNAMICS OF SATELLITE AND DARK MATTER HALO INTERACTIONS ON GALAXY FORMATION AND EVOLUTION

SEPTEMBER 2007

JUN-HWAN CHOI

B.S., YONSEI UNIVERSITY

M.S., YONSEI UNIVERSITY

Ph.D., UNIVERSITY OF MASSACHUSETTS AMHERST

Directed by: Professor Martin D. Weinberg and Professor Neal Katz

In my thesis, I research four consequences of satellite and dark matter halo interaction on galaxy formation.

First, I investigate detailed physical processes in interaction between satellites and dark matter halos using analytic perturbation theory calculations and N-body simulations. The results suggest that resonant dynamics is a responsible physical mechanism for satellite-halo interaction. Comparison of different resolution simulations demonstrates that some resonances requires a larger number of halo particle to be reproduce and a low resolution simulation fails to do so. My results show two interesting physical processes in the satellite-dark matter halo interaction: significant dark matter halo central cusp excursion and effects of dark matter halo responses influence on a satellite decay rate.

Second, I investigate detailed physical processes of satellite disruption in cold dark matter host halos using idealized N-body simulations. The simulation results show that the satellite heating by resonant interactions with its host halo is important. This resonant effect appears in two distinct types: resonant shock and resonant torque. Simulation results also show that the pattern of satellite stripping is outside-in process in energy space. Based on our simulation results, I suggest a new crude analytic estimation of satellite mass loss.

Third, I study the evolution of satellite dark matter halos due to the interaction with cold dark matter subhalos by comparing simulations of the satellite evolution in halos with and without subhalos. According to my results, the satellites in the halo with subhalo lose more mass than the satellites in the smooth halo. The results also suggest that close encounter with subhalos is a more efficient way to satellite destruction. Satellite dark matter halo responses due to the interaction with the host halo and the subhalos produce a symmetric distortion.

Fourth, I investigate the dynamical mechanisms responsible for producing tidal tails from dwarf satellites using N-body simulations. Using N-body simulations I identify two important dynamical co-conspirators: (1) the satellite deformation shows asymmetric distortion; (2) the satellite tail is continuously affected by satellite gravity. These two dynamical mechanisms significantly influence expected tidal tail morphology.

TABLE OF CONTENTS

LIST OF TABLES

LIST OF FIGURES

Figure **Page**

CHAPTER 1

DYNAMICAL EFFECTS OF THE SATELLITE ON DARK MATTER HALO STRUCTURE EVOLUTION

1.1 Introduction

According to cold dark matter (CDM) cosmology, smaller galaxies merge to build larger galaxies. In this scenario, interactions between galaxies are ubiquitous (e.g. Davis et al., 1985). The interactions significant influence galaxy formation and evolution. In high redshift, most galaxy interactions are strong interactions such as a galaxy merger. The strong interactions dramatically change galaxy morphology. As the universe expands, the cumulative effect of weak interactions between galaxies become important. Unlike strong interactions weak and long term interactions do not destroy a galaxy structure but drive a quiescent galaxy evolution such as secular galaxy evolution. Observations show a large population of thin disk galaxies which have experienced only few minor mergers. Their existence suggests that there are a population of galaxies which has not been experienced a strong interaction. Weak interactions play a major role in their evolution (e.g. Kormendy & Kennicutt, 2004).

CDM cosmology claims that all galaxies are located in their host dark matter halo. Dark matter halo formation and evolution eventually governs galaxy formation and evolution. Moreover, recent CDM cosmological simulation reveals large populations of dark matter halo subhalos (Ghigna et al., 1998; Klypin et al., 1999). This situation suggests that an interaction between dark matter halo and its subhalos is a key ingredient of the dark matter halo evolution. Most previous studies about dark matter halo evolution focused on halo mass accretion history which is consequence of

strong interactions. However, there has been little investigation of dynamical evolution of dark matter halo due to interaction with its subhalos because detailed physical processes of these interactions are more complicated than simple mass accretion. In this study, we investigate detailed physical processes of satellite and dark matter halo interaction as a simple experiment of dynamical evolution of dark matter.

For example, a decaying satellite loses its energy and angular momentum due to dynamical friction and transfers its energy and angular momentum to the host halo. The amount of the energy and angular momentum transfer determines orbital decay rate. The dark matter host halo structure responds to this energy and angular momentum transfer. The dynamical friction between the satellite and the host halo governs the satellite-halo interaction and understanding this mechanism is a key to dark matter halo evolution.

Chandrasekhar dynamical friction has been widely used in many circumstances (e.g. Tremaine, 1981; Quinn & Goodman, 1986; Governato et al., 1994). Although the standard dynamical friction which is based on a local scattering process provides a fair estimation of a satellite decay rate, it does not produce correct halo response. In a dark matter halo system, dark matter particles and a satellite complete several orbits during the course of satellite evolution. In this situation, an energy and angular momentum transfer between satellite and halo orbits is cancelled out after several orbits due to repeated interactions. However, the energy and angular momentum transfer to orbits whose frequency is commensurable with satellite frequency is not cancelled. These orbits are called resonance orbits, and play a key role in dynamical friction in an orbiting system. An important characteristic of resonant dynamics is that an energy and angular momentum transfer is a global process. Unlike a local scattering process, any orbit in the halo can be resonant and exchange energy and angular momentum with the satellite if its frequency is commensurable with the satellite frequency. Therefore, the entire dark matter halo responds to the decaying

satellite. Compared the dark matter halo response estimated from the standard Chandrasekhar dynamical friction, this response results in different consequences in satellite-halo interaction. The global response driven by resonant dynamics is the dominant physical process in the satellite-halo interaction (Weinberg, 1986, 1989; Vesperini & Weinberg, 2000; Colpi et al., 1999).

Recently, this global response has gained attention as one of the possible solutions for the CDM central cusp problem. CDM simulations predict that a dark matter halo has universal density profile which has a central cusp (Navarro et al., 1996, 1997, hereafter NFW) [1]. More recently other researchers have debated the real value of γ, but most estimates are in the range of $1 < \gamma < 1.5$ (Moore et al., 1998a; Jing & Suto, 2000). In contrast with what CDM simulation predicts, many observed disk rotation curves suggest that dark matter halos have a core. Since these controversies have arisen, many solutions to the CDM discrepancies have been proposed. Some authors advocate alternative dark matter models and others suggest that the discrepancies result from the complexity of astrophysical processes. Weinberg & Katz (2002) suggested that angular momentum transfer from a galactic bar to its dark matter halo can soften a halo cusp. This phenomenon is driven by resonant dynamics. In particular, the inner Lindblad resonance couples bar and halo orbits in the central cusp. The energy and angular momentum of this bar is transferred to the halo orbits and it heats these orbits (Holley-Bockelmann et al., 2005; Weinberg & Katz, 2007a,b).

In order to properly reproduce the resonant dynamics in N-body simulation very high resolution simulations are required because intrinsic non-astronomical noise in a low resolution N-body simulation can obscure the resonant dynamics effects. The resolution of many large cosmological simulations are too poor to reproduce accurate resonant dynamics. Therefore, high resolution idealized simulations with cosmologi-

---

[1] $\rho \propto r^{-\gamma}(1 + r/r_s)^{\gamma-3}$ where $\gamma = 1$. r_s is a scale length characterized by the concentration parameter $c = R_{vir}/r_s$ and R_{vir} is a virial radius of the halo

cally motivated initial condition are better way to investigate resonant dynamics. In addition, a perturbation theory provides a clear insight because this dynamics based on weak and long-term interaction.

In this study, we use perturbation theory calculations and N-body simulations to investigate detailed physical process in a satellite-halo interaction. In Section 1.2, we describe initial conditions and numerical algorithm for our N-body simulations. In Section 1.3, we briefly describe the resonant dynamics which is responsible for satellite-halo interaction. In Section 1.4, we investigate roles of the resonances in this interaction and provide the required particle number criteria to reproduce effects of these resonances. In Section 1.5, we present the satellite decay history using an N-body simulation. In Section 1.6, we present the dark matter halo response due to the decaying satellite. In both Section 1.5 and Section 1.6, we focus on the investigation of roles of the resonant dynamics. In Section 1.7, we present the satellite decaying rate and the dark matter halo response of an eccentric orbit simulation. In Section 1.8, the astronomical implications of our findings are discussed. And the summary of this study is presented in Section 1.9.

1.2 Numerical technique

For N-body simulations, we use a 3-dimensional self-consistent field code (SCF, also known as an expansion code) (Clutton-Brock, 1972, 1973; Hernquist & Ostriker, 1992; Weinberg, 1999). The expansion algorithm determines a bi-orthogonal basis set of density-potential pair whose lowest-order basis function matches the unperturbed system. From these basis sets, the expansion algorithm computes the gravitational potential of an N-body system. An expansion algorithm is an attractive Poisson equation solver for the study of satellite-halo interaction for two reasons. First, the expansions can be chosen to filter the structure over an interesting range of scales and simultaneously suppress small-scale noise. As we will describe below, the force

in the expansion algorithm, which is applied to individual particles, is computed from the system's gravitational potential field. We do not have to be concerned about a particle-particle scattering. Therefore, the resolution of the simulation only depends on the number of particles in the interesting region. Second, the expansion algorithm is computationally efficient: The computational time increases linearly with the number of particles. Hence, the expansion algorithm permits the use of a much larger number of particles and a smaller timestep than most of the other algorithms with the same computational cost. The required timestep in simulation has not been seriously considered as a source of numerical noise. However, if one needs to resolve the galaxy evolution on a very small scale, the timestep should be an order of magnitude smaller than the dynamical time of that scale. In our simulation, we will use a single timestep which is a few times smaller than a dynamical time of an interesting scale.

The brief description for how our potential solver works is as follow: Many important physical systems in quantum and standard dynamics reduce to the Sturm-Liouville form,

$$\frac{d}{dx}\Big[p(x)\frac{d\Phi(x)}{dx}\Big] - q(x)\Phi(x) = \lambda\omega(x)\Phi(x), \tag{1.1}$$

where λ is a constant and $\omega(x)$ is a known function called either the density or weight function. If $\Phi(x)$ and $\omega(x)$ are positive in an interval $a < x < b$ then the Sturm-Liouville equation is satisfied only for a discrete set of eigenvalues λ_j with corresponding eigenfunctions $\phi_j(x)$ where $j = 0, 1, \ldots$. The eigenfunctions form a complete basis set (Courant & Hilbert 1953) and can be chosen to be orthogonal with the following additional properties: 1) the eigenvalues λ_n are countable infinite and can be ordered: $\lambda_n < \lambda_{n+1}$; 2) there is a smallest non-negative eigenvalue, $\lambda_1 > 0$, but there is no greatest eigenvalue; and 3) the eigenfunctions, ϕ_n, possess nodes

between a and b, and the number of nodes increases with increasing n, for example the eigenfunction $\phi_1(x)$ has no nodes, $\phi_2(x)$ has one node, etc.

In the special case of Poisson's equation, we use the eigenfunctions to construct biorthogonal density and potential pairs, d_k and u_j given by:

$$-\frac{1}{4\pi G}\int dr r^2 d_k^{lm*}(r) u_j^{lm}(r) = \delta_{jk}. \tag{1.2}$$

The lowest order potential-density pair ($n = 1$, $l = m = 0$) is defined to be the equilibrium profile, and the higher order terms represent deviations from this profile.

Traditionally a basis functional pair is represented by known special functions such as the Bessel function. Nevertheless, shapes of galaxies usually differ from generally known special functions. To accurately represent galaxies using those functions, simulations need to include high order terms. Including high order terms require more computational cost and cause small scale diffusion. This problem has been dramatically improved by Weinberg (1999) using numerical solutions of the Sturm-Liouville equation provided by Pruess & Fulton (1993). With this improvement, one can choose the lowest order potential-density pair as the equilibrium profile instead of a known special function. Hence, one needs to use fewer terms to achieve similar accuracy of force calculation than with previous schemes.

Despite this improvement, due to the algorithm's sensitivity to the model's geometry, the accuracy of force calculation deteriorates when the system's geometry is deformed. This is a crucial issue in the study of a satellite-halo interaction because this interaction results in an m=1 offset of the host halo. An accurate potential solver for a cuspy halo demands a precise determination of the expansion center, $\mathbf{C}$, therefore we developed and tested the following algorithm for cuspy dark matter halos:

1. At time step n, we compute $\mathbf{C}_n$ from the center of mass of the N_{min} most bound particles;

2. To evaluate the expansion center at time step $n+1$, a predicted center $\mathbf{C}_{pred,n+1}$ is estimated from a linear least squares solution using the previous N_{keep} centers: $\{\mathbf{C}_j | n - N_{keep} < j \leq n\}$;

3. For $n < 2$, we set $\mathbf{C}_{pred,n+1} = \mathbf{C}_n$.

4. To reduce truncation error, we separately track the motion relative to the halo's center and the motion of the center itself.

Since the expansion center is computed by the finite number of sampled most bound particles, this centering can suffer from Poisson noise. The linear least squares estimation using current and previous centers reduces a sudden jump of the expansion center due to this noise. In addition, we develop a two center expansion technique. In this technique, one expansion of the basis function is centered on the center of mass (COM) of the entire dark matter halo and the other one is the new center $\mathbf{C}$ which is introduced above. At an every timestep, the simulation computes the energy of each particles and sorts out the N_{min} lowest energy particles from all halo particles. These N_{min} lowest energy particles are considered the N_{min} most bound particles. Hereafter we will call the new center as the EJ center[2]. The expansion from the COM represents an entire system and the expansion from the EJ center represents a central cusp in the halo. In Figure 1.1, we check how well the EJ center traces the central cusp. It shows the trajectory of the EJ center and the density maximum as function of time for a fiducial simulation which will be studied below. The density maximum is computed as the center of the 128 densest particles in the halo. The density of each dark matter halo particles is computed using *smooth* algorithm [3]. Figure 1.1 shows that the EJ center and the density maximum show very good agreement ($|r_{EJ} - r_{SMT}| \sim 0.0004$).

---

[2]This "EJ" term comes from generalized approach to compute the center of system. The "E" refers to the N_{min} most bound particles and the "J" refers to the mean angular momentum for defining the cylindrical axis. Here, we use this approach to select N_{min} most bound particles

[3]http://www-hpcc.astro.washington.edu/tool/smooth.html

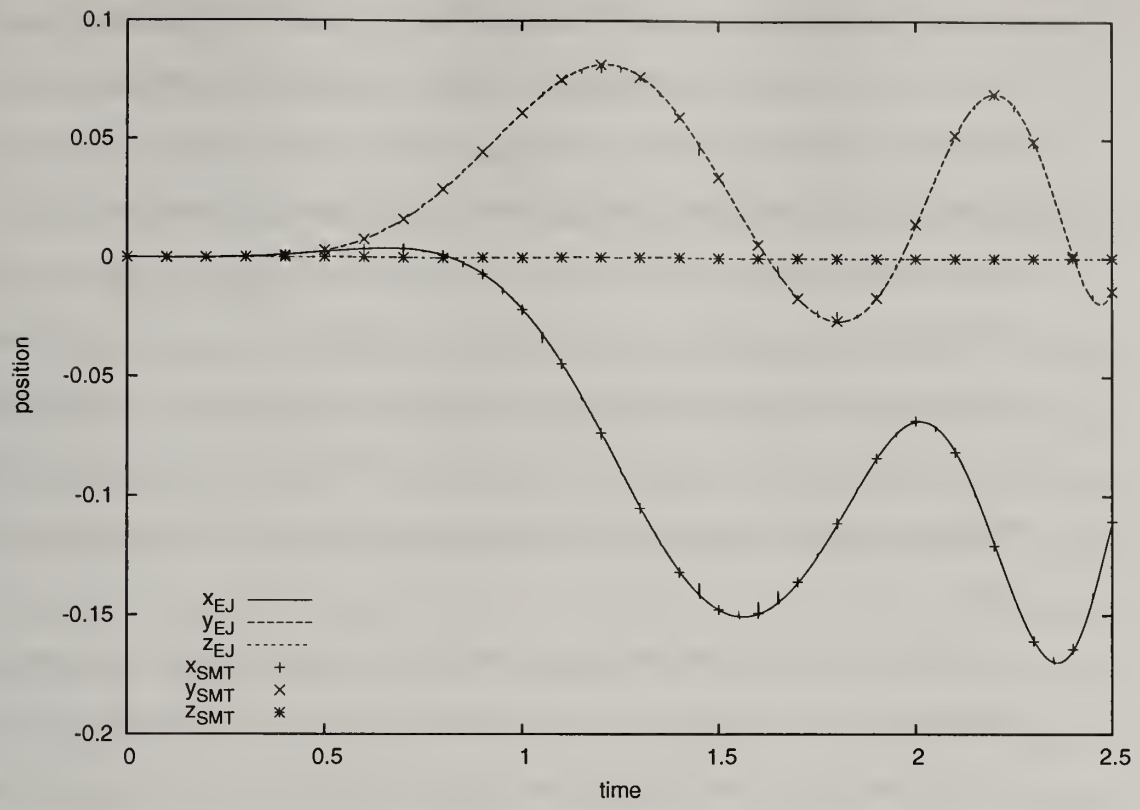

Figure 1.1 The motion of the EJ center (lines) and the density maximum in the fiducial simulation (symbols). The lines represent the EJ center x, y and z distance from the origin as function of time and the cross symbols represent the density maximum location as some given time. Two centers agree very well almost all the time of the satellite evolution.

It confirms that the EJ center accurately follows the dark matter halo cusp and that the computed force in the central cusp is accurate.

An important ingredient of this study is cosmologically motivated initial conditions. Our dark matter halo is a concentration $c = 15$ NFW dark matter halo. The spatial distribution of dark matter halo particles is computed by a Monte Carlo technique based on the given NFW density profile. The velocity of particles is computed from the dark matter halo distribution using an acceptance-rejection method.

The objective of this study is an understanding the role of resonant dynamics in a satellite-halo interaction. According to the perturbation theory calculation (Weinberg & Katz, 2007b), the inner halo needs a higher resolution than the outer halo to

accurately reproduce resonant dynamics effects. In order to populate a large number of dark matter particles inside of the halo we generate multi-mass particle initial conditions (Weinberg & Katz, 2007b). In these initial conditions the mass density follows an NFW profile while the particle number density follows a $n(r) \propto r^{-2.5}$ profile which is steeper than an NFW profile. The assigned mass is the mean particle mass multiplied by $f_{mass}(E)/f_{number}(E)$ where $f_{mass}(E)$ and $f_{number}(E)$ are phase space distribution function of the mass density profile and the number density profile, and E is particle's energy. Using this technique we achieve the equivalent of about a 10^9 single mass particle halo resolution inside $\frac{1}{10}r_s$ using only 4×10^7 particles (see Figure 1.4).

Unlike a live dark matter halo, a satellite in the simulation is represented by a rigid point mass particle with a 0.01 softening length. The satellite interacts with the dark matter halo and decays due to dynamical friction. Throughout this study, we investigate two different orbits. The first orbit is initially circular and defines the fiducial simulation. In the fiducial simulation, a starting radius is $0.4R_{vir}$ and let the satellite decay due to dynamical friction. The retained halo basis terms for the fiducial simulation are up to $n_{max} = 20$ and $l_{max} = 8$ (see Equation 1.2). The second orbit is an initially eccentric orbit $e = 0.5$ [4]. In the eccentric orbit simulation, the starting radius is $1.0R_{vir}$ and we let the satellite decay due to the dynamical friction. Since the satellite starts from the halo virial radius, higher force resolution is required to compute accurate force to the satellite. Therefore, the retained halo basis terms for the eccentric orbit simulation have $n_{max} = 20$ and $l_{max} = 10$. In both orbits, the satellite mass is $0.08M_{vir}$. In addition, to avoid a transient due to sudden introduction of the satellite, the satellite mass is slowly turned on to its full mass as $M = \frac{M_0}{2}\{1 + erf[(t - t_0)/\delta]\}$, where M_0 is the original satellite mass and M is the

[4] $e \equiv (r_a - r_p)/(r_a + r_p)$ where r_a and r_p are the apocenter and the pericenter of a satellite.

satellite perturbation at a given time t [5]. In the simulation, we set the total halo mass, and the gravitational constant as equal to one.

1.3 Physical principles of resonant dynamics in satellite-halo interaction

As mentioned in Section 1.1, long term galaxy evolution is governed by resonant dynamics. In this Section we describe physical principles of resonant dynamics in satellite-halo interaction. We also present a numerical perturbation calculation for computing the effects of resonant dynamics of satellite-halo interaction. In order to accurately reproduce resonance effects in a simulation, certain criteria introduced by Weinberg & Katz (2007a) should be satisfied. A brief description of these criteria is presented later in this section. Detailed explanation of resonant dynamics can be found in other references including Lynden-Bell & Kalnajs (1972), Tremaine & Weinberg (1984), Weinberg (2004), and Weinberg & Katz (2007a).

1.3.1 Principle of Hamiltonian perturbation theory for a dynamical friction

Chandrasekhar (1943) showed that a satellite moving through an infinite homogeneous sea of stars experiences a drag force, namely dynamical friction, due to interaction with the stars. The amount of the drag force is easily computed using the following formula:

$$M\frac{dv}{dt} = -\frac{4\pi G^2 M^2}{v^2}\ln\Lambda\rho(<v) \tag{1.3}$$

where M is the satellite mass, v is the satellite speed, $\rho(<v)$ is the density of stars with speed less than v, and $\ln\Lambda$ is the Coulomb logarithm. Dynamical friction makes

[5] In the simulation, we set $t_0 = 0.5$ and $\delta = 0.25$.

the satellite slow down and enhances density wake of the background stars. This mechanism plays an important role in many astronomical phenomena such as the evolution of central cluster galaxies, the formation of galactic nuclei, and the evolution of galaxy bars. Dynamical friction is also a fundamental physical process in satellite-halo interaction. The standard Chandrasekhar dynamical friction formula (Equation 1.3) has often been used to compute satellite decay rates.

In deriving the standard Chandrasekhar dynamical friction formula, the background stellar sea is assumed isotropic, homogeneous, and infinite. This assumption is inappropriate to real astronomical systems. Most astronomical systems such as galaxies and dark matter halos are bounded inhomogeneous systems. In these systems, the background stars or dark matter particles orbit in a galaxy or a dark matter halo, so that a satellite and the background particles have experienced multiple interactions. These multiple interactions result in significantly different consequences than the standard Chandrasekhar dynamical friction formula estimate.

The effect of multiple interactions are briefly described as follows: Assume that a satellite orbits in a spherical dark matter halo. Since the satellite and dark matter particles orbit in the halo, they interact repeatedly. How this repeated interaction proceeds depends on the dark matter particles orbits. In the satellite rotating frame arbitrary dark matter particles precess either forward or backward depending on energy and angular momentum of dark matter particle in the rotating frame. Over a short period, the dark matter torques the satellite and the later the satellite torques the dark matter. After a time interval longer than both orbit and precession period, most dark matter orbits fill an axisymmetric ring in the satellite rotating frame. Such orbits do not change their energy and angular momentum with respect to the satellite. However, there are always some orbits whose precession in a satellite rotation frame appears to stop or precess very slowly. These are called commensurate or resonance orbits. The interactions between the satellite and resonance orbits do

not vanish, and this interaction causes satellite orbital decay and consequent halo evolution. According to this physical description, the resonant dynamics is a key mechanism in satellite-halo interaction.

Hamiltonian perturbation theory has been used to study resonant dynamics. Lynden-Bell & Kalnajs (1972) provided a formula to compute the torque due to resonant interactions between spiral arms and a disk. Thereafter, it has been extended to many other interactions which occur in the bounded system and has been widely used to compute the torque by resonant interactions. Recently, Weinberg (2004) has improved this formulation to be appropriate for realistic astronomical time scales and has provided a theory of time-dependent secular evolution. This formulation can be applied to compute the resonant dynamics in satellite-halo interaction. Here, we briefly review the theory.

The total torque on a halo by a satellite perturbation is the sum of the torque on every halo orbit:

$$\langle \frac{dL_z}{dt} \rangle = \int_\Gamma d^3x d^3v f(\vec{x}, \vec{v}, t) \frac{dL_z}{dt}(\vec{x}, \vec{v}) \tag{1.4}$$

where Γ is the phase-space domain, $f(\vec{x}, \vec{v}, t)$ is the phase-space distribution function, $\dot{L} \equiv dL_z/dt$ is the torque per halo orbit, and $\langle \cdot \rangle$ denotes the phase-space average. The angular momentum L_z is a conserved quantity in an equilibrium axisymmetric system and therefore dL_z/dt is a first-order in the perturbation amplitude. The distribution $f(\vec{x}, \vec{v}, t)$ can be expanded to $f_0(\vec{x}, \vec{v}) + f_1(\vec{x}, \vec{v}, t)$. Over a long period of time, the first-order contribution of dL_z/dt averages to zero: $\int_\Gamma d^3x d^3v f_0(\vec{x}, \vec{v}) \frac{dL_z}{dt}(\vec{x}, \vec{v}) = 0$. At the next order, the oscillating components from the first-order term in dL_z/dt and the first-order expansion of the distribution function, $f_1(\vec{x}, \vec{v}, t)$, coherently reinforce each other, leading to a non-vanishing contribution as $t \to \infty$. However, a closed-form solution does not need a time-asymptotic limit ($t \to \infty$ limit) because most of interested astrophysical have a time limit such as Hubble time. The detailed

treatment and the applicability in astrophysical problems of the time-asymptotic limit can be found in Weinberg (2004) and Weinberg & Katz (2007a).

To achieve the closed-form solution we need dL_z/dt and $f_1(\vec{x}, \vec{v}, t)$. We calculate dL_z/dt through Liouville theorem.

$$\begin{aligned} \frac{dL_z}{dt} &= \frac{\partial L_z}{\partial t} + [H, L_z] \\ &= \frac{\partial H_1}{\partial \vec{w}} \cdot \frac{\partial L_z}{\partial \vec{I}} + O(A^2) \\ &= -\sum_{\vec{l}} i l_3 H_{1\vec{l}}(\vec{I}, t) e^{-i\vec{l}\cdot\vec{w}} + O(A^2) \end{aligned} \tag{1.5}$$

where $\vec{I}$ and $\vec{w}$ are angle-action variables, H_1 is the first-order perturbation Hamiltonian, and A is the perturbation amplitude. In perturbation calculation, the subscripts '0' and '1' indicate zeroth- and first-order quantities. Since the orbits in an axisymmetric equilibrium galaxy are quasi-periodic in the angles and the actions are invariant, the phase-space quantity such as H_1 can be expanded in a Fourier series in angles. In Equation 1.5, we expand H_1 to the an action-angle expansion $(\sum_{\vec{l}} H_{1\vec{l}}(\vec{I}, t) e^{i\vec{l}\cdot\vec{w}}$. $\vec{l} = (l_1, l_2, l_3)$ is a vector integer for the action-angle expansion of the H_1 in a series of angle variables $(\vec{w})$.

In order to evaluation the second order torque (Equation 1.4), we need a first-order distribution function. It is driven from the linearized collisionless Boltzmann equation (LCBE):

$$\frac{\partial f_1}{\partial t} + \frac{\partial H_0}{\partial \vec{I}} \cdot \frac{\partial f_1}{\partial \vec{w}} - \frac{\partial H_1}{\partial \vec{w}} \cdot \frac{\partial f_0}{\partial \vec{I}} = 0 \tag{1.6}$$

We will solve Equation 1.6 for phase-space dependence by angle-action expansion and the time dependence by Laplace transform. The angle-action expansion is Fourier transform as a series of angle variables. After Fourier-Laplace transform of Equation 1.6, we get

$$\tilde{f}_{\vec{l}}(\vec{I},s) = \frac{i\vec{l}\cdot\frac{\partial f_0}{\partial \vec{I}}}{s+i\vec{l}\cdot\vec{\Omega}} e^{i\vec{l}\cdot\vec{w}} \tilde{H}_{1\vec{l}}(\vec{I},s) \tag{1.7}$$

where $\vec{\Omega} \equiv \partial H_0/\partial \vec{I}$. Here we denote the Laplace transformed variable by a tilde and an angle-action transformed variable by subscript $\vec{l}$. To get the closed-form of the $f_1(\vec{I},\vec{w},t)$, we need to perform inverse Fourier-Laplace transform of Equation 1.7. The final closed-form of the $f_1(\vec{I},\vec{w},t)$ is

$$f_1(\vec{I},\vec{w},t) = \sum_{l_1,l_2,l_3=-\infty}^{\infty} i\vec{l}\cdot\frac{\partial f_0}{\partial \vec{I}} e^{i\vec{l}\cdot\vec{w}} \{\int_0^t dt' H_{1\vec{l}}(\vec{I},t') e^{i\vec{l}\cdot\vec{\Omega}(t'-t)}\} \tag{1.8}$$

To get the total torque, we put Equations 1.5 and 1.8 into Equation 1.4. The final closed-form of the total torque on a halo orbit by satellite interaction is

$$\begin{aligned}\langle\frac{dL_z}{dt}\rangle = -(2\pi)^3 \sum_{l_1,l_2,l_3=-\infty}^{\infty} \quad & l_3 \int_E \int_J \int_{\beta=-\pi/2}^{\beta=\pi/2} \frac{dEdLLd(\cos\beta)}{\Omega_1(E,L)} \vec{l}\cdot\frac{\partial f_0}{\partial \vec{I}} \times \\ & \{\int_0^t dt' H_{1\vec{l}}(\vec{I},t') e^{i\vec{l}\cdot\vec{\Omega}(t'-t)}\} H^*_{1\vec{l}}(\vec{I},t)\end{aligned} \tag{1.9}$$

where E and L are energy and angular momentum respectively, and $\beta \equiv \arccos(L_z/L)$. Equation 1.9 is a generalization of Lynden-Bell & Kalnajs (1972). In the limit $t \to \infty$, we recover the time-asymptotic formula presented by Lynden-Bell & Kalnajs (1972).

$$\{\int_0^t dt' H_{1\vec{l}}(\vec{I},t') e^{i\vec{l}\cdot\vec{\Omega}(t'-t)}\} H^*_{1\vec{l}}(\vec{I},t) \quad \to \quad H_{1\vec{l}}(\vec{I},0) H^*_{1\vec{l}}(\vec{I},0) \pi\delta(\vec{l}\cdot\vec{\Omega} - m\Omega_s) \tag{1.10}$$

Here we simply assume a constant circular orbit with the orbital frequency Ω_s, and the perturbed Hamiltonian becomes $H_{1\vec{l}}(\vec{I},0)\exp(im\Omega_s t)$ which means that $\exp(im\Omega_s t)$ is an only time-depend term in the perturbed Hamiltonian.

Equation 1.9 emphasizes the importance of resonance orbits in satellite-halo interaction. The resonance orbits for an orbiting satellite with Ω_s is characterized by

$$l_1\Omega_1 + l_2\Omega_2 + l_3\Omega_3 = m\Omega_s \tag{1.11}$$

where Ω_1 and Ω_2 are the radial and azimuthal orbital frequencies of a dark matter particle, and Ω_3 is the frequency of the azimuth of the ascending node [6]. Three integers l_1, l_2, and l_3 are the same as the vector integer for Fourier expansion in a series of angle variables ($\vec{l}$ in Equation 1.5). m is the azimuthal multipole index of the satellite defined by spherical harmonics (Y_{lm}). In a non-rotating spherical halo, $\Omega_3 = 0$, and it allows us to set $l_3 = m$ when we project the orbital plane to the equatorial plane (Tremaine & Weinberg, 1984; Weinberg, 1985, 1986).

Through this derivation, we show that satellite-halo interaction is governed by resonant dynamics and that a second-order perturbation is a leading contributor. However, some resonances need a longer time period than the galaxy lifetime to converge into the time-asymptotic limit. For these resonances, a transient effect to which the first-order change is still important plays a major role in galaxy evolution. One remarkable feature in Equation 1.9 is that dark matter orbits which torque the satellite are not localized around the satellite. According to the standard Chandrasekhar dynamical friction, the interaction between the satellite and dark matter orbits only happens around the satellite because it is a local scattering process. In contrast, according to resonant dynamics, any orbits in the halo can be coupled with the satellite orbit as long as their orbit is commensurate with the satellite orbit frequency. Therefore, halo response of the decaying satellite is global: that is, the response includes orbits from a large measure of phase space. The important improvement in time-dependent secular evolution theory is that the history of galaxy evolution should be taken into account. In other words although the galaxy evolution is governed by resonant dynamics, transient effects of the formation history of the galaxy play an important role in the galaxy evolution. Equation 1.9 also shows that there should be a gradient in phase space density in order to make resonances drive galaxy evolution.

---

[6] an ascending node is the point where the orbit crosses the reference plane moving from below to above the plane.

If there is no phase space density gradient near of the resonance, the same resonance with opposite directions cancel out the resonance evolution over long periods of time. The gradient in phase space makes the incomplete cancellation of the resonance effect on the orbit due to unbalance of the same resonance with opposite directions. There is a misconception of the resonant dynamics in the galaxy evolution that the width of the resonance is very narrow and it dose not result in significant evolution. But the narrowness of the resonance appears in frequency space not in phase space and only in the time-asymptotic limit! Single resonance can occupy significant volume in phase space and can affect a large population of background orbits. Moreover, spectrum of the resonance becomes broader due to the finite time scale of galaxy evolution. According to above description, the main physical process for galaxy evolution due to satellite-halo interaction is resonant dynamics and it is necessary to accurately reproduce resonant dynamics in order to properly investigate this galaxy evolution.

1.3.2 The numerical perturbation calculation

Although the perturbation theory presented in Equation 1.9 provides a deep insight into the resonant dynamics in satellite-halo interaction, there is one crucial limitation in this theory. Tremaine & Weinberg (1984) defined the ratio of the evolution of a perturber's orbiting speed to the square of the natural width in frequency space as *speed* (s) and claims that the scale of the action change depends on s. In slow limit ($s \ll 1$), an orbit lingers near the resonance for many periods and the action change is scaled as the square root of the perturbation strength. In fast limit ($s \gg 1$), an orbit quickly moves through the resonance and the action change is scaled as the square of the perturbation strength. These two regimes complicate the quantitative estimation of the perturbation theory but do not result in qualitative change in the evolution. The standard perturbation theory assumes the fast limit (e.g. Lynden-Bell & Kalnajs, 1972; Weinberg, 2004). However, some important resonances can be in

the slow limit. Weinberg & Katz (2007a) claims that most of the low order resonances in bar-halo interaction shows that s is between slow and fast limits. It is necessary to have a tool to compute perturbation theory which is adaptive from slow to fast limits.

Unfortunately, solving LCBE for arbitrary speed using standard perturbation theory is difficult. In order to get around this difficulty, Weinberg & Katz (2007a) describes a direct approach to compute secular evolution using Monte Carlo realizations of orbit ensembles. The direct approach transfers particle phase space variables to slow and fast canonical variables. After a period, the fast oscillation term from fast variable vanishes according to averaging theorem (Arnol'd, 1995). In this case only the resonance term that is related to slow variable survives. And the problem for each resonance is reduced to a one dimensional pendulum equation in slow angle. This direct approach which we call the numerical perturbation calculation does not require a different treatment for fast and slow limits. In the following Section we will briefly describe the numerical perturbation calculation and the detailed description presented in Weinberg & Katz (2007a).

1.3.2.1 Slow and fast variables and average theorem in Canonical perturbation theory

Solutions of Equation 1.5 and Equation 1.8 is a Fourier series and each angle in this series corresponds to an angle variable. Each term in those solutions is oscillatory, which is proportional to $\exp(i\vec{l} \cdot \vec{w})$.

For a fixed perturbing frequency Ω_p, the solution couples each term to the perturbing frequency and yields oscillations of the form $\exp[i(\vec{l} \cdot \vec{w} - m\Omega_p t)]$. Orbits with $(\vec{l} \cdot \vec{\Omega} - m\Omega_p) \rightarrow 0$ are defined as the closed resonance orbits. For the part of phase space very near a resonance, the argument of the exponential will change very slowly for one term and rapidly vary for most other terms.

The separation of these characteristic motions is easily performed by making a canonical transformation to two new degrees of freedom where one of the new coordinates corresponds to the angle of the commensurability $w_s = \vec{l} \cdot \vec{w} - m\phi_p(t)$ where $\phi_p(t) = \int^t dt' \Omega_p(t')$ which is the position angle of the perturbation (Goldstein, 1950). This can be done with the canonical transformation generating function : $F = w_f I_F + [\vec{l} \cdot \vec{w} - m\phi_p(t)] I_s$.

$$\begin{aligned} w_f &= w_1 \\ w_s &= \vec{l} \cdot \vec{w} - m\phi_p(t) \\ I_s &= \frac{1}{l_2} I_2 \\ I_f &= I_1 - \frac{1}{l_2} I_2 \end{aligned} \tag{1.12}$$

with $H_{new} = H_{old} - m\Omega_p I_s$ and with w_3 and I_3 have not been changed in this transformation. The angle w_s is often called the "slow" angle because its conjugate frequency vanishes at the resonance. There is some arbitrariness in the choice of the "fast" angle, w_f. For example, the choice $w_f = w_2$ yields the conjugate action $I_s = I_1/l_1$ and $I_f = I_2 - l_2 I_2/l_1$. This choice might be useful when $l_2 = 0$. In both cases, the slow angle varies very slowly and the fast angle varies rapidly relative to the slow angle near the resonance. We average the action change over some interval T that is long enough so that all the terms except for the resonant one vanish owing to the rapid oscillation in w_f and is small enough so that the argument of exponent is nearly unchanged. In this way the problem is reduced to a collection of one dimensional pendulum equations in w_s. The motion near a typical resonance is like that of a pendulum. This is a generic characteristics of Hamiltonian systems near resonance and forms the basis for the treatment of chaotic motion near the separatrix associated with these resonances (Lichtenberg & Lieberman, 1983).

The averaged new Hamiltonian in these new coordinates is

$$H(I_s) = H_0(I_{s,r}) + \frac{1}{2}\frac{\partial^2 H_0(I_s)}{\partial I_s^2}|_{I_{s,r}}(I_s - I_{s,r})^2 + H_{1\vec{l}}\cos(w_s) \tag{1.13}$$

where $I_{s,r}$ is the slow action at resonance and H_0 is the averaged unperturbed Hamiltonian with constant Ω_p, up to some arbitrary constant. Equation 1.13 is a pendulum equation with arm length $M \equiv (\partial^2 H_0(I_s)/\partial I_s^2)^{-1/2}$ and periodic forcing acceleration $H_{1\vec{l}}$.

Individual resonances can overlap in phase space and lead to chaotic motion due to diffusion. However, in galaxy dynamics on large scales, a few low order resonances dominate, and the resonance overlap for these rarely happens. Beside that, if a dark matter halo is strongly triaxial or rotating, the orbital motion can have more than two degree of freedom. In this case, Arnold diffusion, which results from intersection of two resonance surfaces in an action space, may occur (Arnol'd, 1995). Consequences of the Arnold diffusion are not considered here.

1.3.2.2 Directly computing the perturbing potential

The averaging theorem with canonical transformation to slow and fast variables reduces the orbit around resonance to a one dimensional problem. In this situation, the evolution due to the satellite perturbation results from the evolution of slow variables:

$$\begin{aligned} \frac{w_s}{dt} &= \vec{l}\cdot\vec{\Omega} - m\Omega_{sat} + \frac{\partial H_{1l}(\vec{I})}{\partial I_s}e^{iw_s} \\ \frac{I_s}{dt} &= -iH_{1l}(\vec{I})e^{iw_s} \end{aligned} \tag{1.14}$$

where $H_{1l}(\vec{I})$ is the transform of the perturbation which is shown in Equation 1.5.

Since our interest is in the evolution of quasi-periodic orbits caused by a satellite perturbation, this evolution is computed as a combination of the simple orbit motion of the particle in the halo. The direct computation of the orbit evolution due to Equation 1.14 is as follows:

1. Uses a Monte Carlo realization for the phase space of the perturbed system.

2. Compute perturbation potential at a given time.

3. Compute angle and action of each dark matter particle in the ensemble.

4. Perform the canonical transformation to slow and fast variables based on Equation 1.12.

5. Advance the particle's slow angle and corresponding action according to Equation 1.14 for a given perturbation.

6. Perform the canonical transformation back to the original phase space ($\vec{x}$ and $\vec{v}$).

This numerical perturbation calculation uses a symplectic Runge-Kutta method for advancing slow angle and action. This numerical perturbation calculation does not include the self-gravitation of the perturbed system.

One advantage of using the numerical perturbation calculation is that it does not require a separate treatment for slow and fast limits and allows us to investigate individual resonances so that we can gain a clear understanding of the role of each resonance. Since Monte Carlo realizations use the same initial conditions as N-body simulations, the comparison between perturbation calculation results and simulation results is straightforward.

1.3.3 Criteria for reproducing the resonant dynamics in N-body simulation

As mentioned in Section 1.1, in order to accurately reproduce the resonant interaction effects, N-body simulations need to satisfy consistency criteria. Weinberg & Katz (2007a) proposed following three criteria: First, a sufficient number of particles are required to cover the phase space near resonance (hereafter coverage criterion).

Second, a sufficient number of particles are required to reduce artificial diffusions. Artificial non-astronomical diffusion comes from both the gravitational force of individual particles (hereafter small-scale noise criterion) and potential fluctuation from Poisson noise (hereafter large-scale noise criterion). Besides particle number criteria, the potential solver must be able to resolve the scale of the resonance potential scale and the realized phase space distribution must cover this region. Weinberg & Katz (2007a) provide a estimator of these particle number requirements using perturbation theory calculation. We will examine our simulation using these estimators.

1.4 Investigation of resonances due to a circular orbiting satellite

N-body simulations should satisfy particle number criteria which are presented in Section 1.3.3 in order to properly study resonant dynamics in satellite-halo interaction. In this section, we test whether or not the halo resolution really affects the reproducibility of the resonance effects. In addition, we investigate the characteristics of resonances using the perturbation theory calculation presented in Section 1.3.

Throughout this section, we assume that a satellite is on a circular orbit motivated by the fiducial simulation. The first step in investigating the role of resonances is to figure out which resonances are important. Since the power of a resonance is proportional to $(1/r)^l$, where r is the distance from the perturber and l is the order of a resonance, low order resonances generally drive halo evolution. Here, we focus on both dipole (l=m=1) and quadrapole (l=m=2) resonances.

In order to determine which resonances exist in dark matter halo phase space, it is necessary to know the satellite frequency. Equation 1.11 shows that the satellite frequency determines the location of the resonance in dark matter halo. A satellite frequency generally consists of a radial frequency and an azimuthal frequency. Unfortunately, computing the resonance effects from the combination of the two frequencies

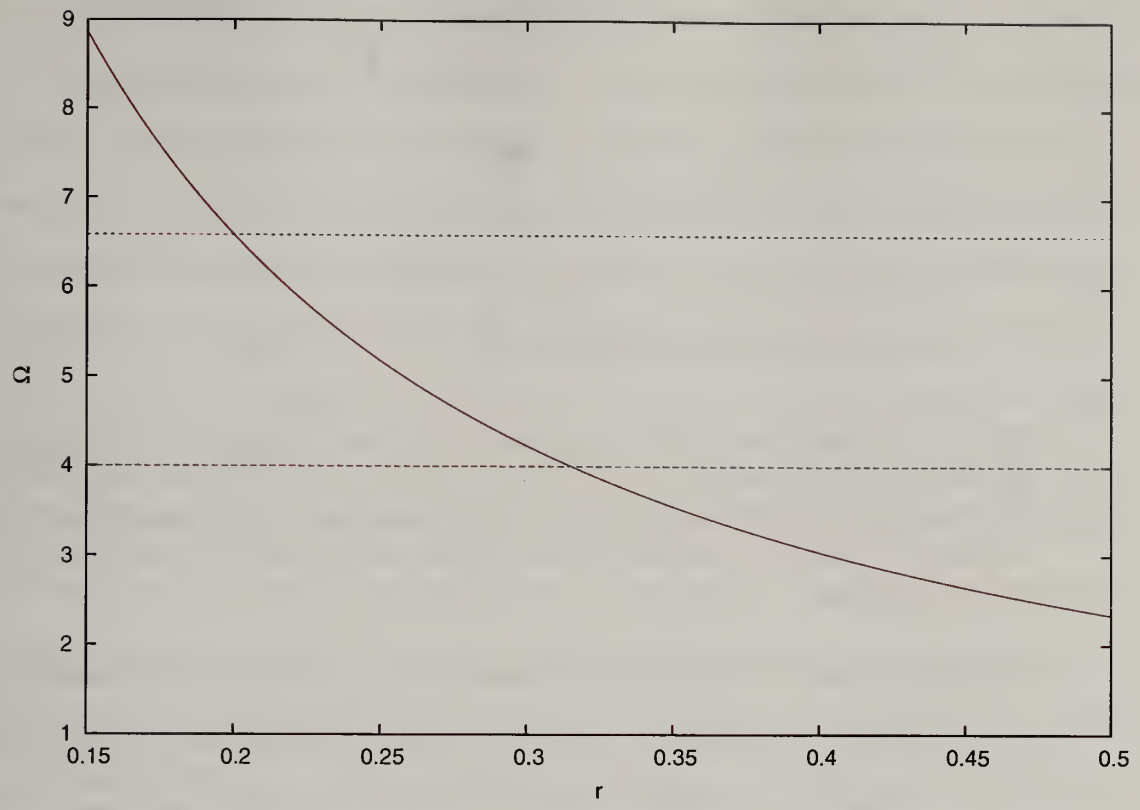

Figure 1.2 Azimuthal frequency in the dark matter halo as function of the halo radius. The x-axis is the halo radius and the y-axis is the azimuthal frequency at a given radius. Two horizontal lines represent two sampled frequencies which are used in the perturbation calculation. The lower horizontal line shows a $\Omega_{sat} = 0.4$ case and the upper horizontal line shows a $R_{vir} = 0.2$ case.

requires very complicated calculations and significant computational costs. In order to avoid these difficulties, we assume a circular orbit satellite for our perturbation calculation. Although this assumption simplifies the situation, there are two advantages. First, understanding of physical processes for a circular orbit is straightforward due to the simple perturbation condition. Second, since our fiducial simulation is the decaying satellite initially on a circular orbit at $0.4R_{vir}$, the perturbation calculation can be clearly compared with the simulation results.

In the fiducial simulation, the satellite starts a circular orbit at $0.4R_{vir}$ and gradually decays due to dynamical friction. The evolution of the satellite trajectory will be investigated in Section 1.5. As the satellite decays, the satellite frequency is con-

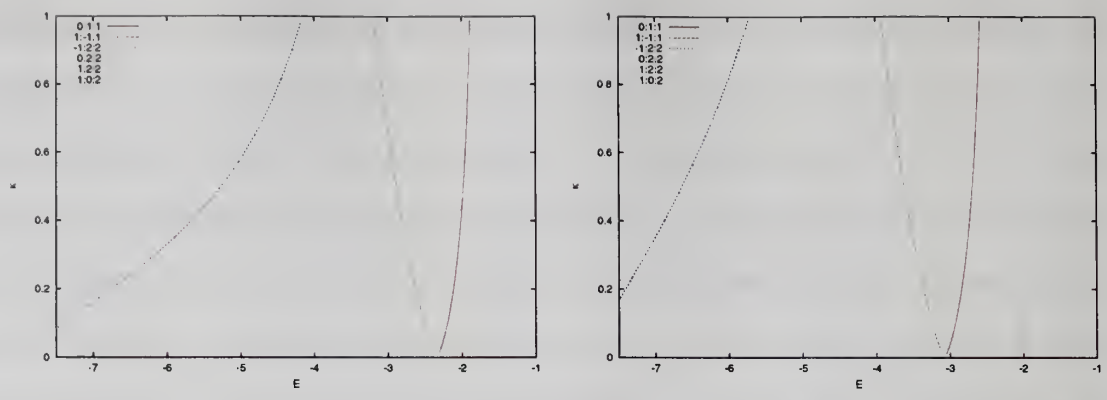

Figure 1.3 Chosen low order resonances in the dark matter halo phase space. The figures show the location of 0:1:1, 1:-1:1, -1:2:2, 0:2:2, 1:2:2, and 1:0:2 resonances in the phase space. The locations of 0:1:1 resonance and 0:2:2 resonance are identically overlapped. The left panel is for the w4 calculation and the right panel is for the R0.2 calculation.

tinuously increased. The satellite frequency of the perturbation calculation is chosen in the range of the satellite frequency. Figure 1.2 shows two sampled frequencies: $\Omega_{sat} = 4.0$ and $\Omega_{sat} = 6.5835$. The perturbation calculation with $\Omega_{sat} = 4.0$, which we call the w4 calculation, represents early evolution. The perturbation calculation with $\Omega_{sat} = 6.5835$, which we call the R0.2 calculation because it is the azimuthal frequency at $0.2R_{vir}$, represents late evolution. The comparison study of the perturbation calculation presents the results of two different frequencies also provides an insight how different frequencies result in different resonance effects because all the setups for these two perturbation calculations are identical except the perturbation frequencies.

We examine which resonances are in our dark matter halo phase space for each of the two frequencies. As discussed above, we focus on $m = 1$ and $m = 2$ resonances. The range of resonances examined has in $-10 \leq l_1 \leq 10$ and $l = m = 1, 2$. Due to symmetry in the spherical expansion, $|l_2|$ must be equal to or less m. Many resonances in this range are found in dark matter halo phase space but most of them are high l_1 resonances. In this study, we choose two low l_1 resonances for $m = 1$ resonances which are 0:1:1 and 1:-1:1 resonances and four low l_2 resonances for $m = 2$ resonances which

are -1:2:2, 0:2:2, 1:2:2, and 1:0:2 resonances. These are the two lowest order $m = 1$ resonances and the four lowest order $m = 2$ resonances which are located at inside of the satellite phase space. In fact, 0:1:1 and 0:2:2 resonances are both corotation resonances and located at the same place in the halo phase space. Since a corotation is a strong resonance in both the $m = 1$ and the $m = 2$ resonances, both corotation resonances are investigated here. Comparing two corotation resonances provides an insight how two resonance with the same location in the phase space but with a different m are different. Figure 1.3 shows the location of the associated periodic orbits in the halo phase space. Since the dark matter halo is assumed to be a non-rotating spherical system, the phase space is described by energy (E) and normalized angular momentum [7] (κ). We find several interesting features in Figure 1.3. The figures confirm that the locations of the 0:1:1 resonance and the 0:2:2 resonance are identically overlapped. The -1:2:2 resonance extends in considerable range of energy space; resonant coupling is a global mechanism. Therefore, some dark matter orbits which are located at a considerable distance from the satellite can strongly couple with a perturbation. Moreover, the -1:2:2 resonance extends to the lowest energy. Due to this resonance, the decaying satellite affects a dark matter halo center. One of the main objectives in this study is this satellite and halo center interaction. We find an interesting pattern of the resonance location by comparing the resonance location of the w4 calculation and the R0.2 calculation. The relative location of each resonance in the phase space is almost the same in both cases. The difference is that the resonances in the R0.2 calculation are shifted to lower energy. This pattern gives us an important insight into resonant dynamics. The resonance location moves to lower energy as the perturbation frequency increases because the lower energy orbits generally have a higher frequency and can couple with higher frequency perturbation. The relative

[7] $\kappa = L/L_{max}(E)$ where L is the particles angular momentum and $L_{max}(E)$ is the maximum angular momentum at given energy

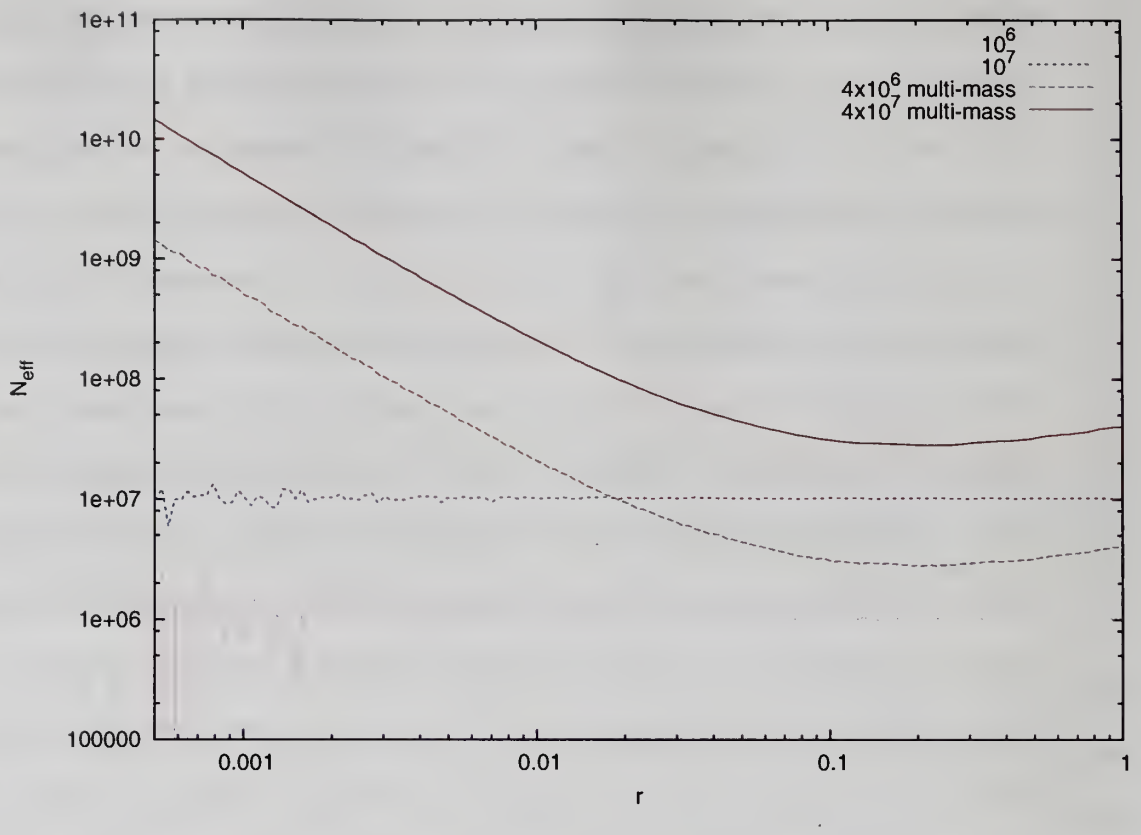

Figure 1.4 The effective particle number for the 10^6 single mass particle halo, the 10^7 single mass particle halo, the 4×10^6 multi-mass particle halo, and the 4×10^7 multi-mass particle halo. Noise which is shown at very small radii for single mass particle halos results from a small number fluctuation.

location of each resonance is preserved although the perturbation frequency changes due to the self-similarity of the halo profile. Therefore, change of the perturbation frequency does not affect the relative importance of the resonances as long as the dark matter halo structure remains constant.

Before testing the particle number requirement criteria for the chosen resonances, we compare an effective particle number for four dark matter halos which are used in numerical perturbation calculation. All four dark matter halos, which are a 10^6 single mass particle halo, a 10^7 single mass particle halo, a 4×10^6 multi-mass particle halo, and a 4×10^7 multi-mass particle halo, have a c=15 NFW mass profile. These are the same as our fiducial simulation and only differ in particle number and mass assignment per particle. The multi-mass particle halos adapt a steeper particle

number distribution to achieve a higher effective number at small radii. In particular, the number density profile is $n(r) \propto r^{-2.5}$ while the mass density profile follows the c=15 NFW model. Figure 1.4 shows an effective particle number distribution for these four halo realizations. At any given radius, we define the effective particle number, $N_{eff}(r) = M_{total}/ < m >_r$ where $< m >_r$ is the mean particle mass inside of $0.01R_{vir}$. For example, the 4×10^7 multi-mass particle halo achieves $\sim 2 \times 10^8$ single mass particle halo resolution.

Among these four halos, the 4×10^7 multi-mass particle halo has the highest resolution and the 10^6 single mass particle halo has the lowest resolution. Noise which is shown at very small radii for single mass particle halos results from a small number fluctuation. We use these four halo realizations during studies of the numerical perturbation calculation and the studies of the particle number effects for resonant interaction.

Figures 1.5 and 1.6 show the results of the particle number criteria test, which is presented in Weinberg & Katz (2007a), for the w4 calculation and the R0.2 calculation. In general, a -1:2:2 resonance requires the highest resolution to be correctly reproduced. By comparing Figures 1.5 and 1.6, we find that the particle number requirements for both the w4 calculation and the R0.2 calculation are very similar. The coverage criteria and the small scale criteria requirements are comparable to each other and are higher than the large scale noise criteria requirement. Since the expansion algorithm is not affected by small scale noise, our simulations have to satisfy only coverage criteria and large scale criteria. The bottom plot in Figure 1.5 shows the effective particle number for the 4×10^7 multi-mass particle halo top of the particle number test results. This shows that this halo satisfies all criteria for all examined resonances. In fact, the small scale noise of 1:2:2 resonance and -1:2:2 resonance requires a higher resolution than the 4×10^7 multi-mass particle halo, but fortunately our N-body code is not affected by this criteria. Figure 1.5 shows that if

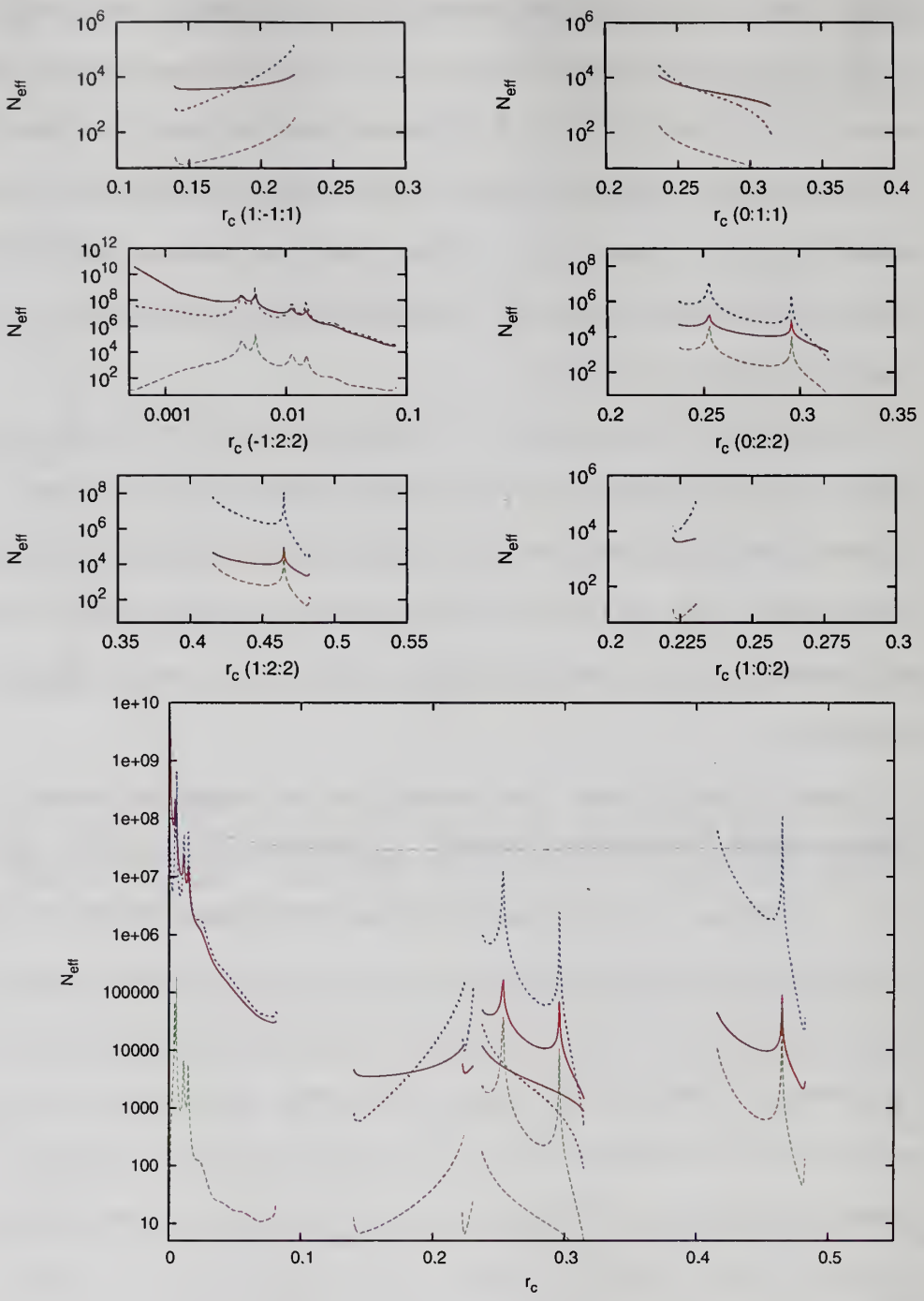

Figure 1.5 The particle number requirements for each resonance for the w4 calculation. For each panel, the red line represents the coverage criteria, the blue line represents the small scale noise criteria, and the green line represents the large scale noise criteria. The x-axis is the circular radius for given energy and the y-axis is the required particle number at that radius. The top six panels show the results for each resonance. In order to sketch the relative spatial location, the bottom panel plots all resonances in one panel. The cyan line shows an effective particle number profile for the 4×10^7 multi-mass particle halo.

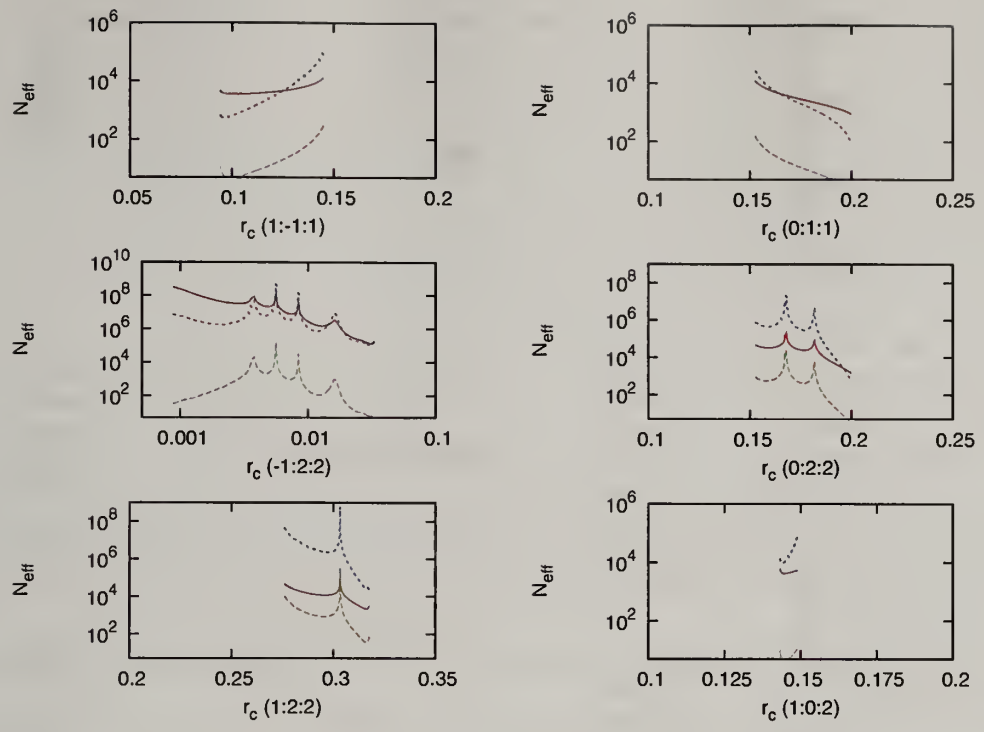

Figure 1.6 The same as top six panels in Figure 1.5 but for the R0.2 calculation.

an N-body code is not affected by the small scale noise, all halos satisfy the criteria for all examined resonance except for the -1:2:2 resonance for the w4 calculation. The 4×10^6 multi-mass particle halo and the 10^7 single mass particle halo can not satisfy the coverage criteria of the -1:2:2 resonance $r \leq 0.01 R_{vir}$. The resolution limit of these two halos is $0.01 R_{vir}$. The 10^6 single mass particle halo can not satisfy the coverage criteria of the -1:2:2 resonance. We also find that even the 4×10^7 multi-mass particle halo can not satisfy the coverage criteria of the -1:2:2 resonance $r \leq 0.0005 R_{vir}$. The resolution limit of the 4×10^7 multi-mass particle halo is $0.0005 R_{vir}$. We investigate how these different resolution halos produce different results using the numerical perturbation calculation.

Using the numerical perturbation calculation which is introduced in Section 1.3.2, we investigate the characteristics of the resonances of both the w4 calculation and the R0.2 calculation. In the numerical perturbation calculation, in order to avoid non-linear effect due to sudden introduction of the perturbation the satellite perturbation

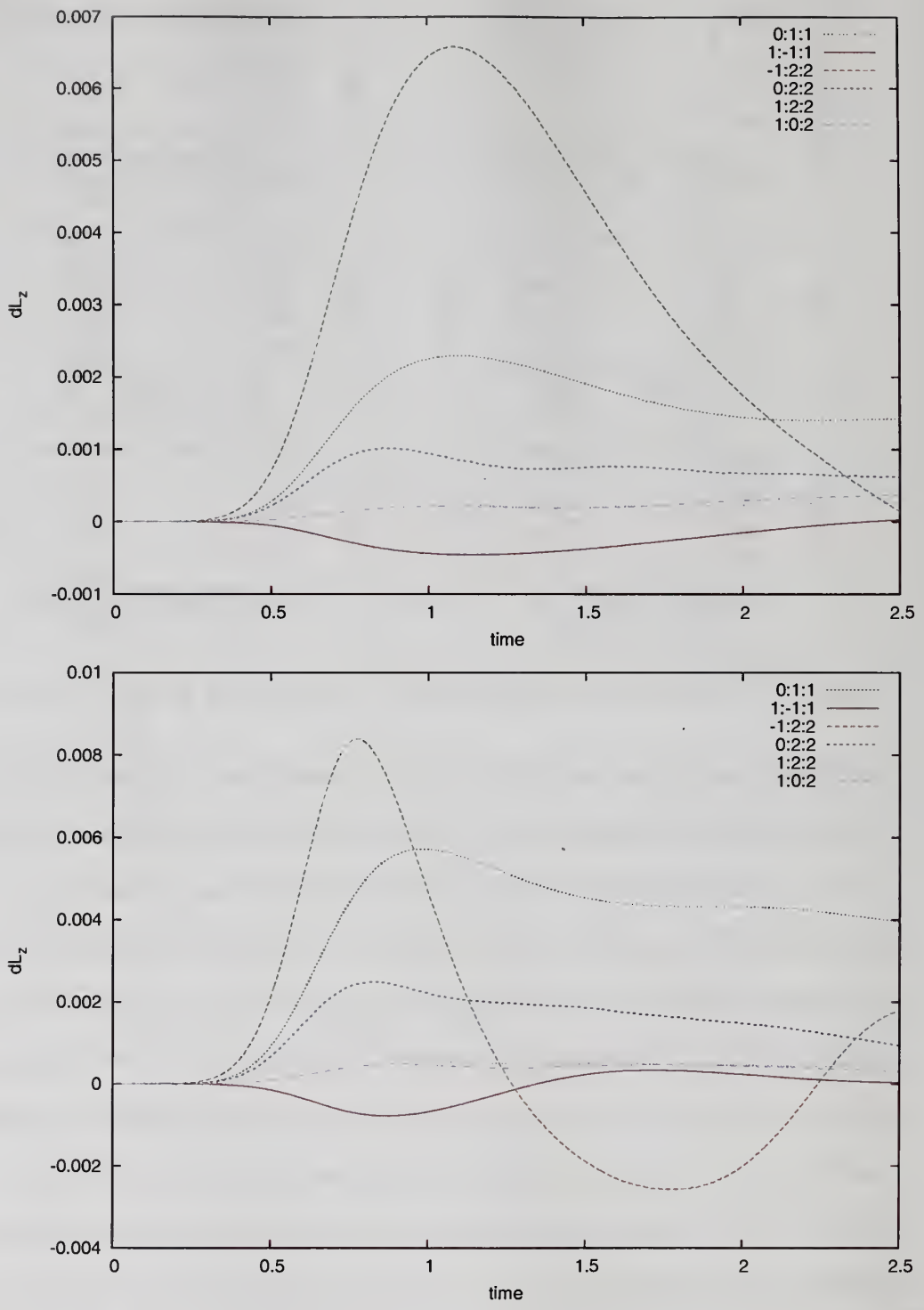

Figure 1.7 Amount of angular momentum transfer from the perturber to the satellite as function of time for six chosen resonances using the numerical perturbation calculation. The 4×10^7 multi-mass particle halo is used as the halo realization in these plots. The top plot shows the results from the w4 calculation and the bottom plot shows the results from the R0.2 calculation. In both cases the -1:2:2 resonance is the strongest resonance.

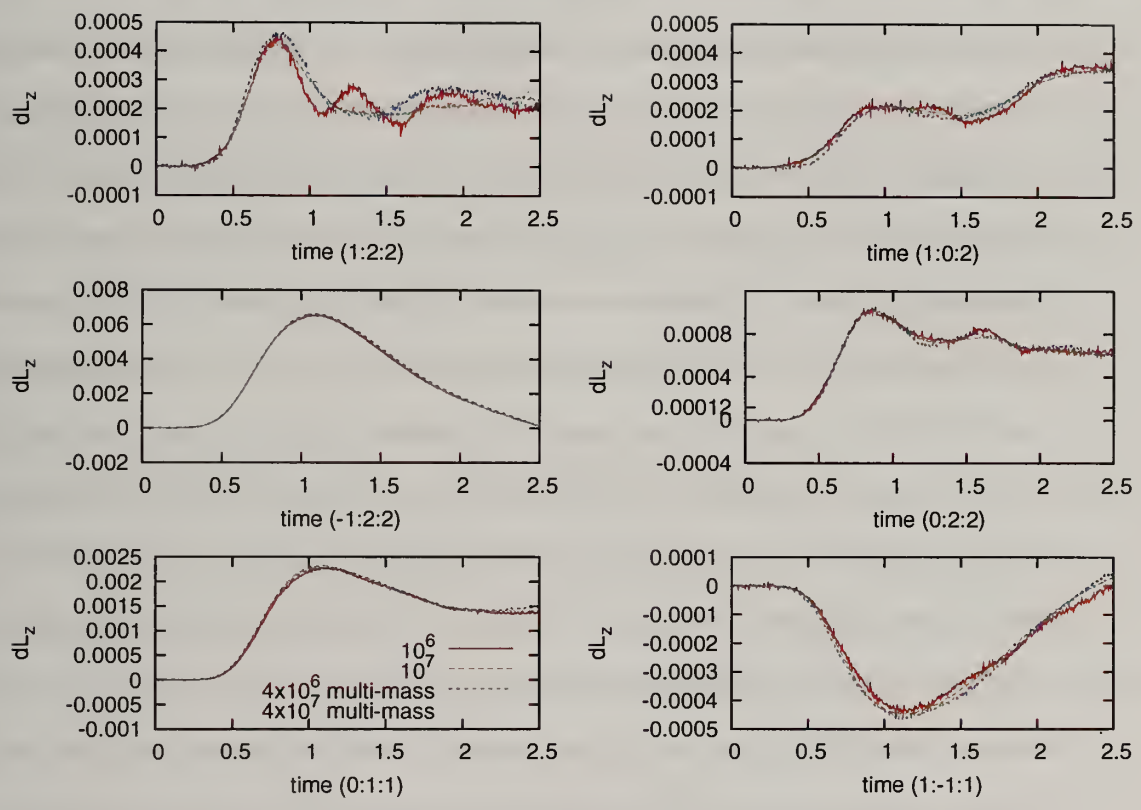

Figure 1.8 Difference of the amount of angular momentum transfer depending on halo particle numbers. Each panel shows the amount of angular momentum transfer for each a given resonance. The results from four dark matter halos, which are 10^6 single mass particle halo, 10^7 single mass particle halo, 4×10^6 multi-mass particle halo, and 4×10^7 multi-mass particle halo, are compared in each resonances.

is slowly turned on as introduced in Section 1.2. Using the numerical perturbation calculation, we investigate the power of each resonance as function of time, the location and power of each resonance in the halo phase space, and the resonance effect depending on the halo resolution.

Figure 1.7 shows the amount of angular momentum transfer due to each resonance for the w4 calculation and the R0.2 calculation. The 4×10^7 multi-mass particle halo is used as the halo realization in these numerical perturbation theory calculations. In both calculations the -1:2:2 resonance is the strongest resonance among six chosen resonances. Both corotation resonances (0:1:1 and 0:2:2) are the second strongest resonances. The 1:2:2 resonance and the 1:0:2 resonance are comparably weak resonances. Interestingly, the 1:-1:1 resonance transfer angular momentum from dark matter halo to the satellite but the amount is smaller than angular momentum transferred by the -1:2:2, 0:1:1, and 0:2:2 resonances. Comparison study of the w4 calculation and the R0.2 calculation shows several interesting differences. Since the orbiting radius of the perturber of the R0.2 calculation is smaller than that of the w4 calculation, the amount of angular momentum transfer in the R0.2 calculation is larger than that in the w4 calculation. Some resonances such as the -1:2:2 and the 1:-1:1 resonances show a sinusoidal feature and their frequency increases as the perturber's frequency increases. This sinusoidal feature suggests that these resonances are still in a transient limit. Investigating the detailed characteristics of the transient effect will be an interesting future task. The comparison study claims that although there are some differences, the relative strength of the resonances is the same for both cases.

Figure 1.8 shows the amount of angular momentum transfer by each resonance for four different resolution halos. The time evolution of the amount of angular momentum transfer for each resonance is similar in all four halos. Although the overall evolutions for all halos are similar, the low resolution halo (10^6 single mass particle halo) shows some fluctuations, which are clearly shown in the 1:2:2 and

the 1:0:2 resonances and is not shown in the -1:2:2 and the 0:1:1 resonances. It is not consistent with the results from the particle number requirement test; the -1:2:2 and the 0:1:1 resonances requires higher resolution than the 1:2:2 and the 1:0:2 resonances. Interestingly, two resonances which show an evident noisy feature are two weak resonances. Therefore, we can conclude that this noisy feature in Figure 1.8 does not result from poor resolution for resonance effect but results from Poisson noise in averaging the amount of angular momentum transfer. This result does not mean that the particle number criteria are invalid. The reason why Figure 1.8 does not reflect the difference is that resonances extend in a wide range in the phase space. And even in one resonance, the particle number requirement varies with phase space location. For example, the -1:2:2 resonance in the w4 calculation ranges from the halo center to $\sim 0.1R_{vir}$ which is equivalent with -7.7 to -4 in the energy space (see Figures 1.3 and 1.5). According to Figure 1.5, even the 10^6 single mass particle halo can resolve the -1:2:2 resonance outside of $\sim 0.01R_{vir}$. If most of the angular momentum transfer due to -1:2:2 resonance occurs at $r > 0.01R_{vir}$, total amounts of the angular momentum transfer from the high resolution halo simulation and the low resolution halo simulation can show a similar result. If this is the case, we need to study the resonance effect as an extended feature in the phase space not as a total sum in order to discriminate the resonance effects in different resolution halo simulation. It should be pointed out that although the difference is not great, the amount of angular momentum transfer through -1:2:2 and 0:1:1 resonances in the high resolution halo is in fact a few percentages larger than that in the low resolution halo.

The resonance effects in the phase space are clearly visualized as the distribution of relative change in L_z in the phase space. Relative ΔL_z is ΔL_z respected to the total angular momentum for a given energy bin. Due to the normalized angular momentum (κ) is used as the phase space coordinate, the absolute value of L for different energy

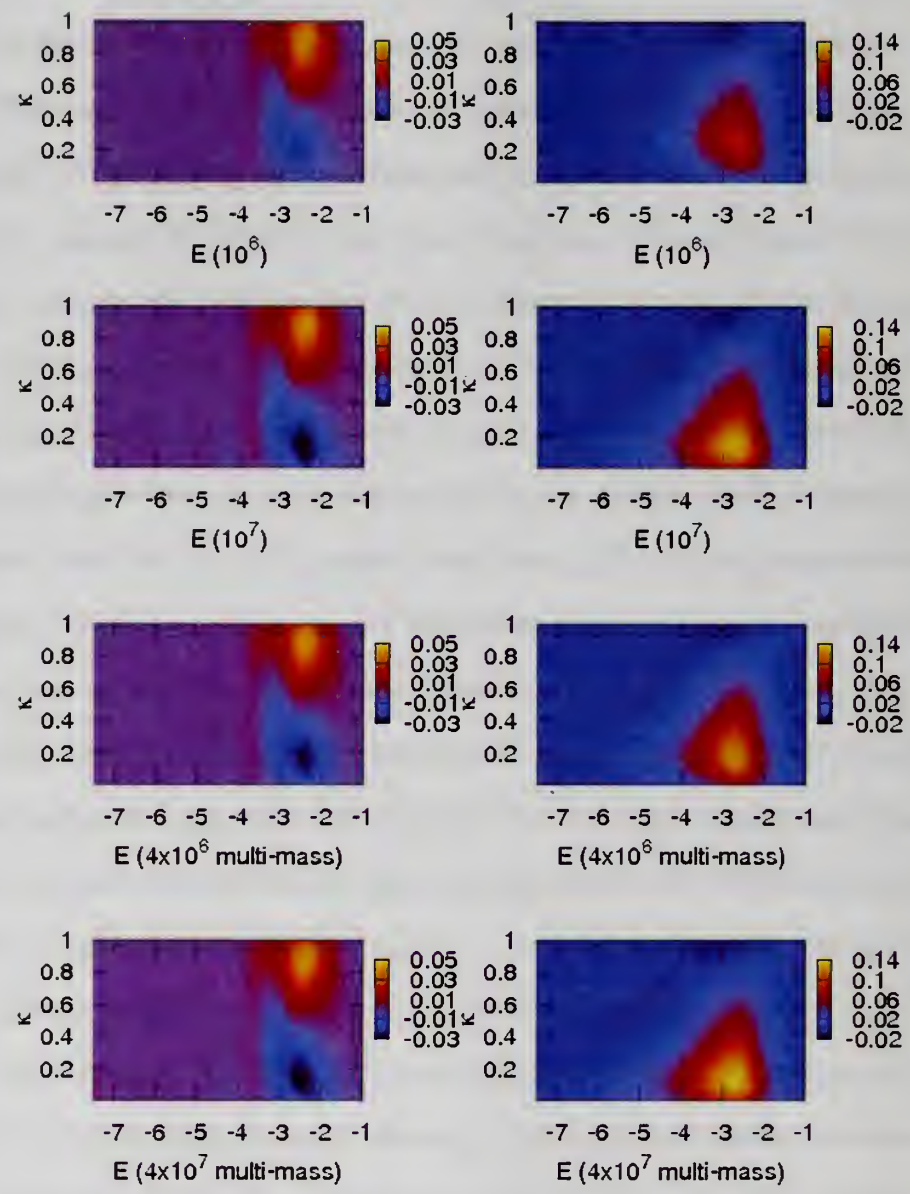

Figure 1.9 Difference of the amount of angular momentum transfer due to given resonances depending on halo particle numbers computed using the numerical perturbation theory calculation. Left panels show the relative ΔL_z distribution due to m=1 resonances effects (0:1:1 and 1:-1:1 resonances) and right panels show that due to m=2 resonances (-1:2:2, 0:2:2, 1:2:2, and 1:0:2 resonances). Each row shows the results from four different resolution halos.

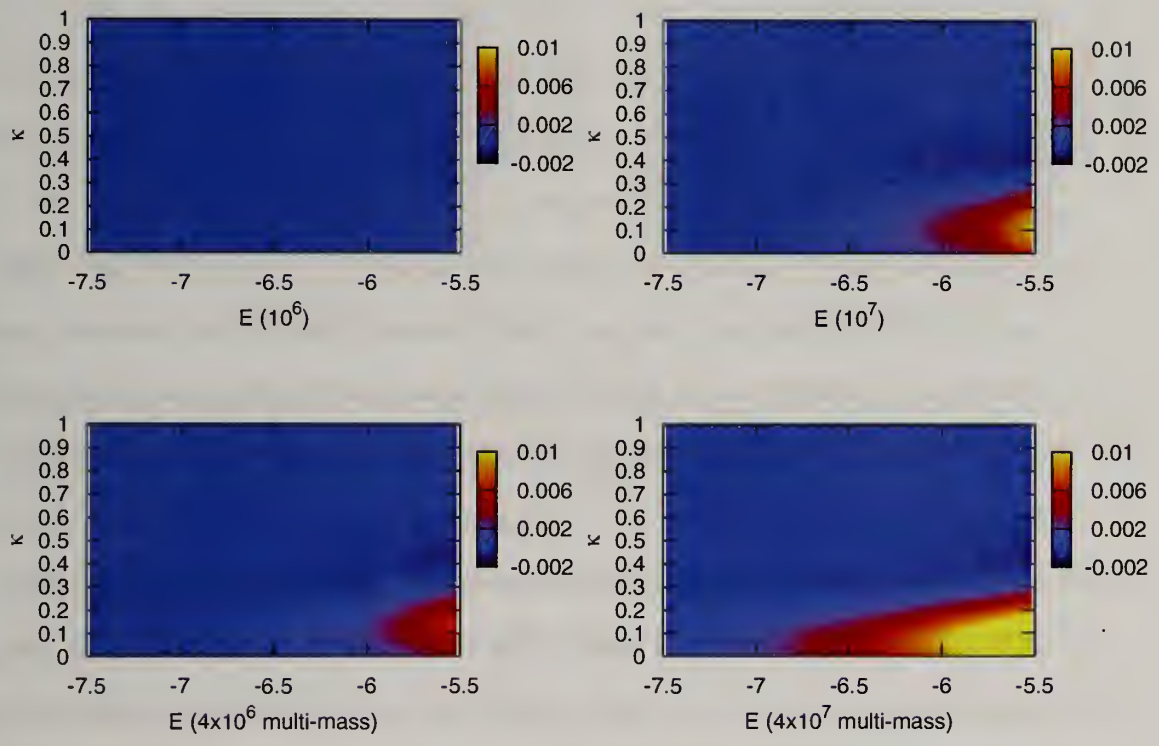

Figure 1.10 The same as the ΔL_z distribution by $m = 2$ resonances in Figure 1.9 but blown-up the low energy regime ($E = -7.5$ to $E = -5.5$)

bin is different; $L_{max}(E)$ increases with energy. As a result, total angular momentum itself is small in low energy so that a simple demonstration of the absolute ΔL_z distribution possibly smears out ΔL_z features in low energy. By normalizing the total angular momentum at a given energy bin, the relative ΔL_z distribution enhances ΔL_z features at low energy. Figure 1.9 shows the distribution of relative ΔL_z for four different resolution halos from the numerical perturbation theory calculation. In Figure 1.9, the results from $m = 1$ resonances (0:1:1 and 1:-1:1) and the results from $m = 2$ resonances (-1:2:2, 0:2:2, 1:2:2, and 1:0:2) are shown. In order to examine a resolution effect on reproducibility of resonant dynamics, we present results from four different resolution halos. After comparing these different resolution results, we find that there is almost no difference in the relative ΔL_z distribution due to $m = 1$ resonances. However, there is a noticeable difference in the relative ΔL_z distribution due to $m = 2$ resonances. Compared with the other three higher resolution results, the relative ΔL_z distribution in the 10^6 single mass particle halo result shows a different distribution. In particular, the region for gaining angular momentum distribution in the other results extends to a low energy and low angular momentum area but this region in the 10^6 single mass particle halo result dose not extend to such a low energy and low angular momentum area. This difference is clearly shown in Figure 1.10 which zooms in on the low energy region. In order to roughly quantify the angular momentum transfer for four different resolution halos we sum up the relative ΔL_z for $E < -5.5$ in Figure 1.10 and obtain relative $\Delta L_z(E < -5.5) \simeq 0.0$, 6.9, 4.9, and 19.5 for the 10^6 single mass particle halo result, the 10^7 single mass particle halo result, the 4×10^6 multi-mass particle halo result, and the 4×10^7 multi-mass particle halo result respectively. In addition, the overall strength of the relative ΔL_z in the 10^6 single mass particle halo result is weaker than that of other cases. Compared with Figure 1.3, this region coincides with the location of -1:2:2 resonance. It is exactly what the particle number criteria address. Moreover, although the 10^7 single mass particle

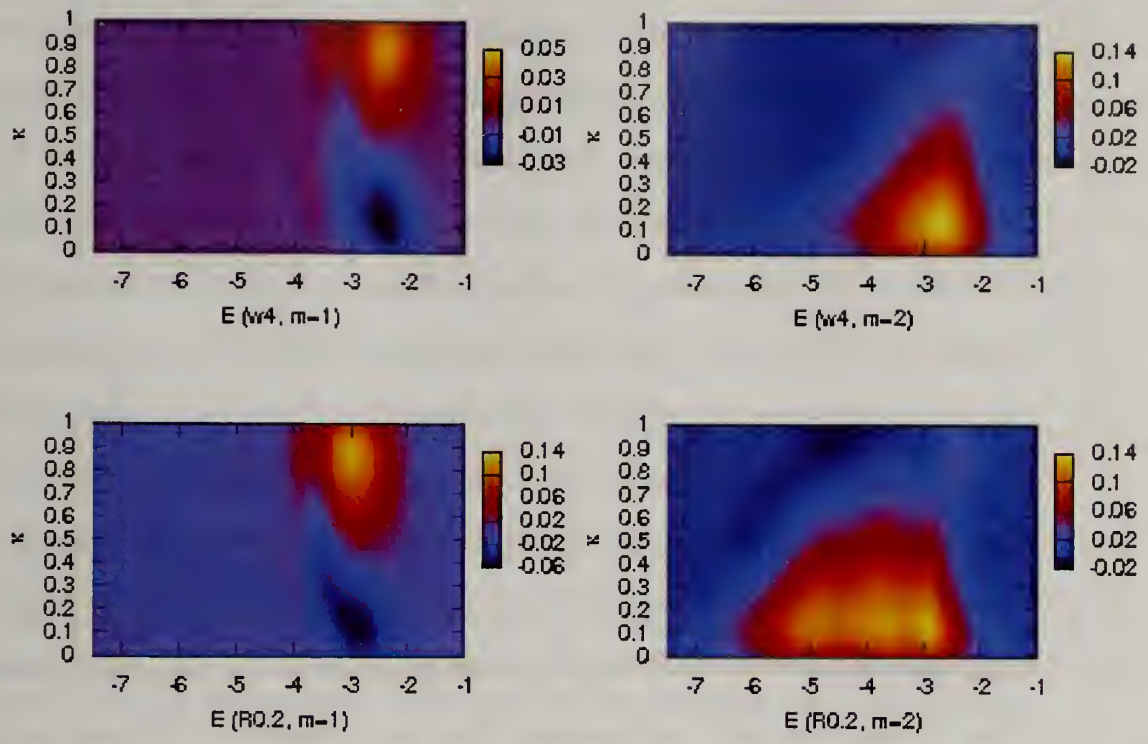

Figure 1.11 Difference of the amount of angular momentum transfer due to given resonances for the w4 calculation and the R0.2 calculation. The 4×10^7 multi-mass particle halo results are shown for both calculations.

halo result and the 4×10^6 multi-mass particle halo result show an extended gaining angular momentum feature into low energy and low angular momentum area, it is not as clear and strong as the feature shown in the 4×10^7 multi-mass particle halo case. This comparison study concludes that the -1:2:2 resonance is clearly reproduced in the 4×10^7 multi-mass particle halo and partially reproduced in the 10^7 single mass particle halo and the 4×10^6 multi-mass particle halo but is not reproduced in the 10^6 single mass particle halo. The overall weakness of the relative ΔL_z in the low resolution halo also comes from poor reproducibility of the resonance effects. In the next sections, we compare the results from the 10^6 single mass particle halo as the low resolution halo and 4×10^7 multi-mass particle halo as the high resolution halo to emphasize the reproducibility of the resonance effects.

Figure 1.11 shows the relative ΔL_z distribution for the w4 calculation and R0.2 calculation from the high resolution halo calculation. This figure shows several interesting characteristics of the resonant interaction. The area of the gaining and losing angular momentum is similar with the resonance location predicted by Figure 1.3. The relative ΔL_z distribution due to $m = 1$ resonances shows the contribution from 0:1:1 and 1:-1:1 resonances. According to Figure 1.7, the 0:1:1 resonance transfers angular momentum from the satellite to the halo while the 1:-1:1 resonance transfer angular momentum from the halo to the satellite and the 1:-1:1 resonance is located in lower energy region than the 0:1:1 resonance (see Figure 1.3). The relative ΔL_z distribution due to $m = 1$ resonances in Figure 1.11 also shows a gaining angular momentum region and a losing angular momentum region. And the losing angular momentum region tend to be located lower energy area than the gaining angular momentum region as prediction resonance location in Figure 1.3. In contrast, there is a different feature between the relative ΔL_z distribution and predicted resonance location in Figure 1.7; the relative ΔL_z distribution shows broad distribution. This broad distribution is already expected in Weinberg (2004) and Weinberg & Katz (2007a) as a result of finite time-dependent perturbation. Comparison analysis of the w4 calculation and the R0.2 calculation shows how different perturbations result in different resonance effects. The resonance location moves to lower energy with increasing frequency as shown in Figure 1.3. The strength of the relative ΔL_z distribution in the R0.2 calculation is stronger than that in the w4 calculation. It should be point out that although resonant interactions are a global process, many important resonances couple with particles near the satellite. Since the satellite in the R0.2 calculation is located in a denser region than the satellite in the w4 calculation, the satellite in R0.2 calculation transfers more angular momentum than that of the w4 calculation.

In this section, we have investigated the resonance effects in satellite-halo interaction using the perturbation theory. The perturbation theory provides a keen insight

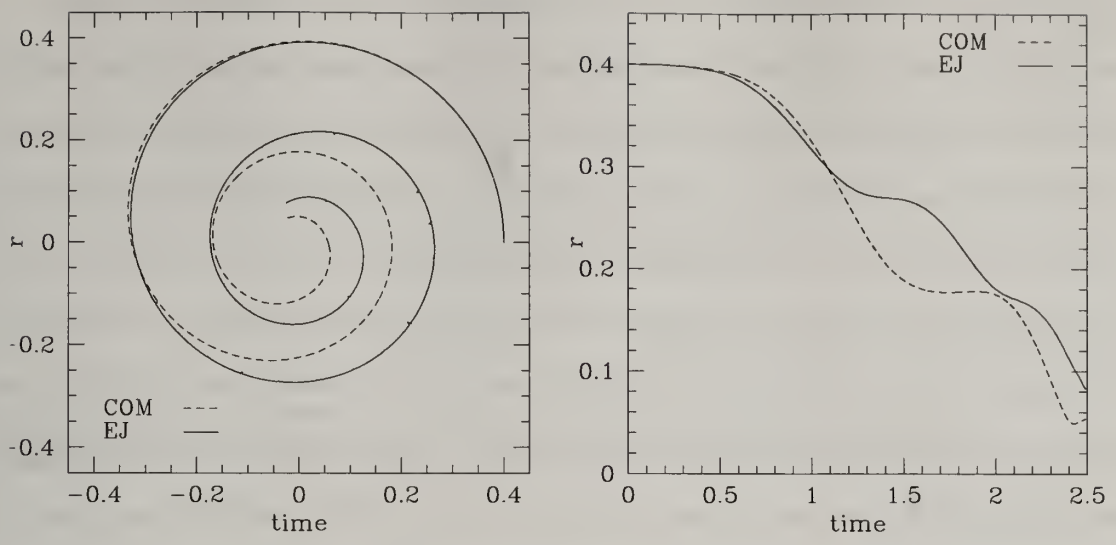

Figure 1.12 The trajectory of the satellite in the fiducial simulation. The dark matter halo is made up 4×10^7 multi-mass particles. The left panel shows the satellite trajectory on the orbital plane. The right panel shows the decay history of the satellite. In the both panels, the solid line is the trajectory whose center is the EJ center and the dashed line is the trajectory whose center is the halo COM.

into the characteristic of resonant dynamics. Unfortunately, our perturbation calculation can not reproduce effects of dark matter halo structure evolution and satellite decaying. It is indeed a doable calculation, but a computational cost for a perturbation theory calculation which includes these effects is similar to or more than that for N-body simulations. Moreover, there is a non-linear effect in the satellite-halo interaction which is hardly reproduced in the perturbation theory calculation. In following sections, we investigate resonant dynamics effects using N-body simulations with bearing in mind a physical insight from a perturbation theory calculation.

1.5 Satellite decaying

A satellite decays due to dynamical friction in the dark matter halo. During decay, a satellite loses its energy and angular momentum by dynamical friction, and its energy and angular momentum are transferred to the host halo. The amount of the energy and angular momentum loss determines a satellite decaying rate.

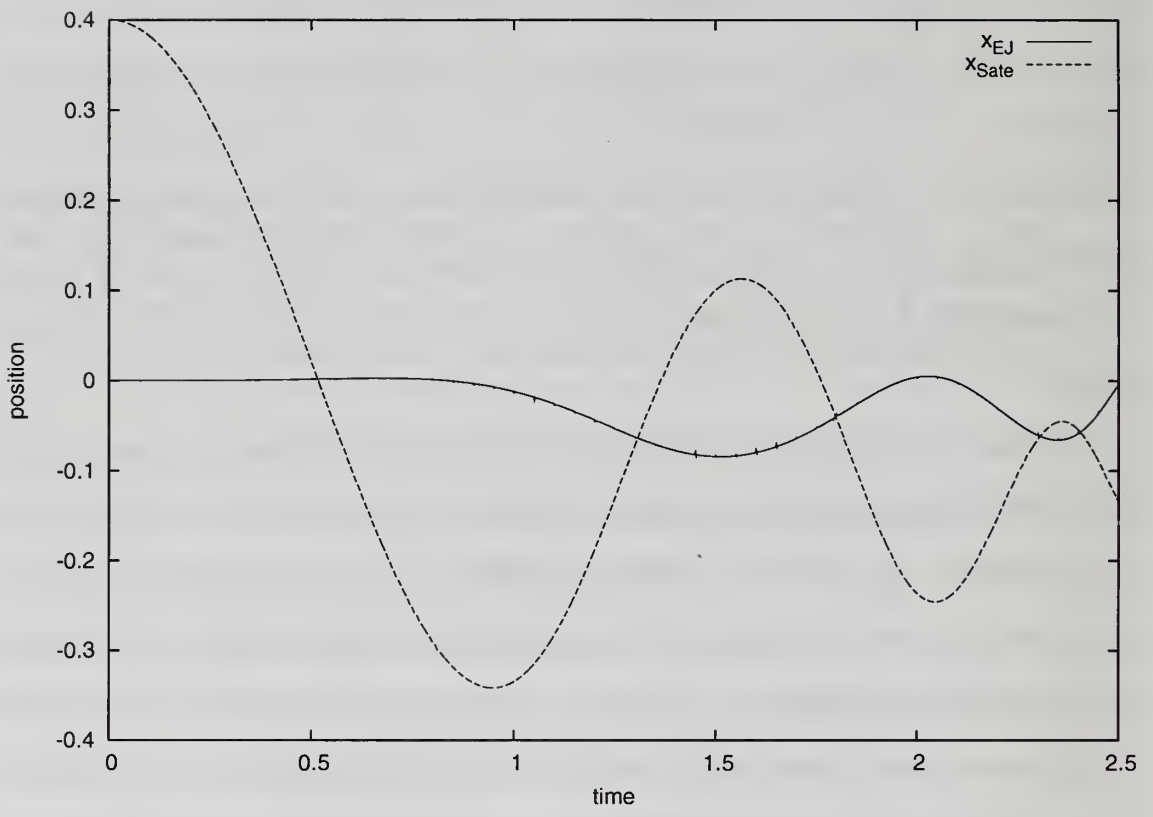

Figure 1.13 The phase of the satellite orbit and the halo cusp. The plot shows x positions of the satellite and the EJ center of the fiducial simulation.

Figure 1.12 shows a satellite trajectory on orbital plane and a satellite decay history of the fiducial simulation for the high resolution halo. The two different trajectories result from two different centers: the EJ center and the halo COM. Both trajectories show similar pattern, but they are offset. The relative motion of the EJ center and the halo COM causes this offset.. It implies that the halo cusp which is represented by the EJ center and the center of entire halo which is represented by the halo COM do not coincide. Due to the orbiting satellite, the halo cusp couples with satellite and shows a binary motion. This motion produces the separation between the EJ center and the halo COM. Figure 1.13 show the x-axis positions of the satellite and the halo cusp. The phases of the satellite and the cusp are synchronized and indicates that the cusp excursion comes from the interaction with the satellite. Recall that the satellite mass is slowly turned on, so that the satellite hardly affects cusp until $t \sim 1.0$. One surprising point of the cusp excursion is that the separation distance between the halo cusp and the halo COM is strikingly large. Assuming that the scale of our fiducial simulation is Milky Way system scale, the host halo virial radius becomes about 250 kpc (Klypin et al., 2002) and the maximum cusp excision can be larger than 20 kpc! It implies that the scale of the cusp excursion is significant in the real Universe due to the prevalence of host halo and subhalo interaction.

Recently, van den Bosch et al. (2005) claimed that the brightest galaxy in a dark matter halo does not reside at the center of its host halo. They suggested two possible origins of this phenomenon. First, central galaxies reside at the minimum of the dark matter halo potential, but the halo itself is not fully relaxed. Second, the dark matter halo is relaxed, but the central galaxy oscillates in the halo potential well. Figure 1.14 shows the equidensity contours of dark matter halo of the fiducial simulation. Due to the interaction of the orbiting satellite, the inner equidensity contours are skewed and the density peak does not coincide with the halo COM while outer contours are centered on the halo COM. According to our results, the halo cusp

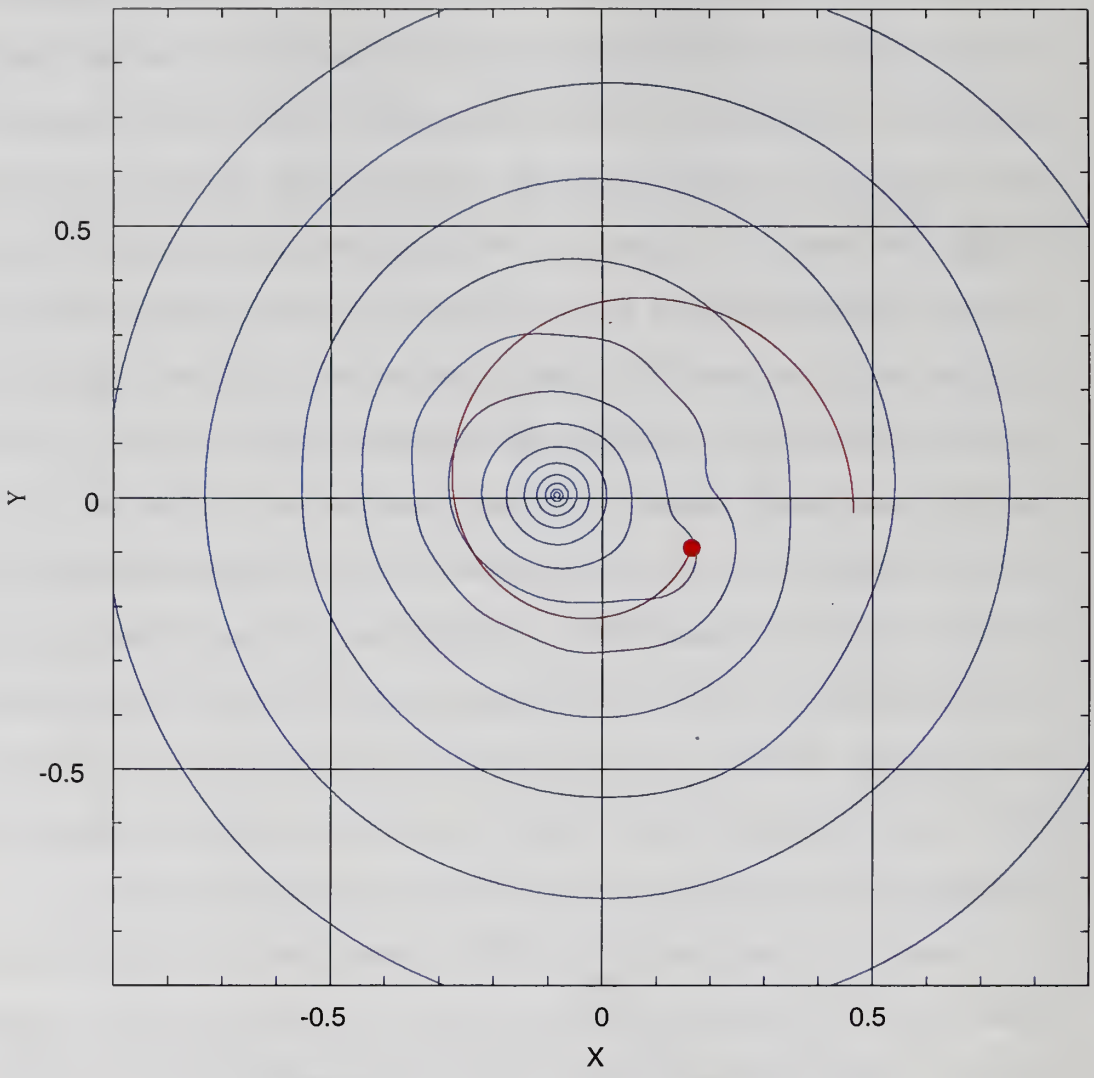

Figure 1.14 The equidensity contour plot of the dark matter halo from the fiducial simulation. Due to the satellite orbiting (red trajectory), the originally spherical dark matter halo shows a skewed density structure. In this plot, the origin coincides with the halo COM. The density peak, which is equivalent of the halo cusp, is offset about $0.1R_{vir}$ from the halo COM.

excurses the significant distance from the halo COM due to the decaying satellite. Orbiting satellite can even induce dark matter halo center movement whose host halo is already relaxed. According to our tests, the magnitude of the cusp movement is linearly correlated with satellite mass. Therefore, any mass satellite can drive the halo center movement. Under the hierarchical structure formation paradigm, subhalos will always be interacting with the host halo and therefore a dark matter halo can never be relaxed.

As mentioned above, the dynamical friction in the satellite-halo interaction which is responsible for satellite decay is governed by resonant dynamics. The resonance effects only appear when simulations satisfy particle number criteria (Weinberg & Katz, 2007a). Section 1.4 shows that the high resolution simulation (the 4×10^7 multi-mass particle halo) satisfies the particle number criteria of all chosen low order resonances while the low resolution simulation (the 10^6 single mass particle halo) does not satisfy the particle number criteria of the -1:2:2 resonance. Figure 1.15 shows a satellite decaying of the fiducial simulations with two different resolution halos. Interestingly, the satellite in the high resolution halo decays faster than in the low resolution halo. This result is consistent with the particle number test results in Section 1.4. The low resolution halo simulation fails to correctly reproduce the -1:2:2 resonance effect, so that its angular momentum transfer is underestimated. However, the satellite in this halo can still decay as similar pattern with that in the high resolution halo because even the low resolution halo simulation can resolve most of other resonances in Section 1.4. This results point out that simulations need to accurately reproduce most of important resonances in order to accurately estimate a satellite decaying rate.

One strange feature is observed in the satellite decaying (see Figure 1.15). The satellite decaying stalls a moment. This phenomenon seems like to suggest that the satellite-halo interaction has lost a resonance coupling (Sellwood & Debattista, 2006).

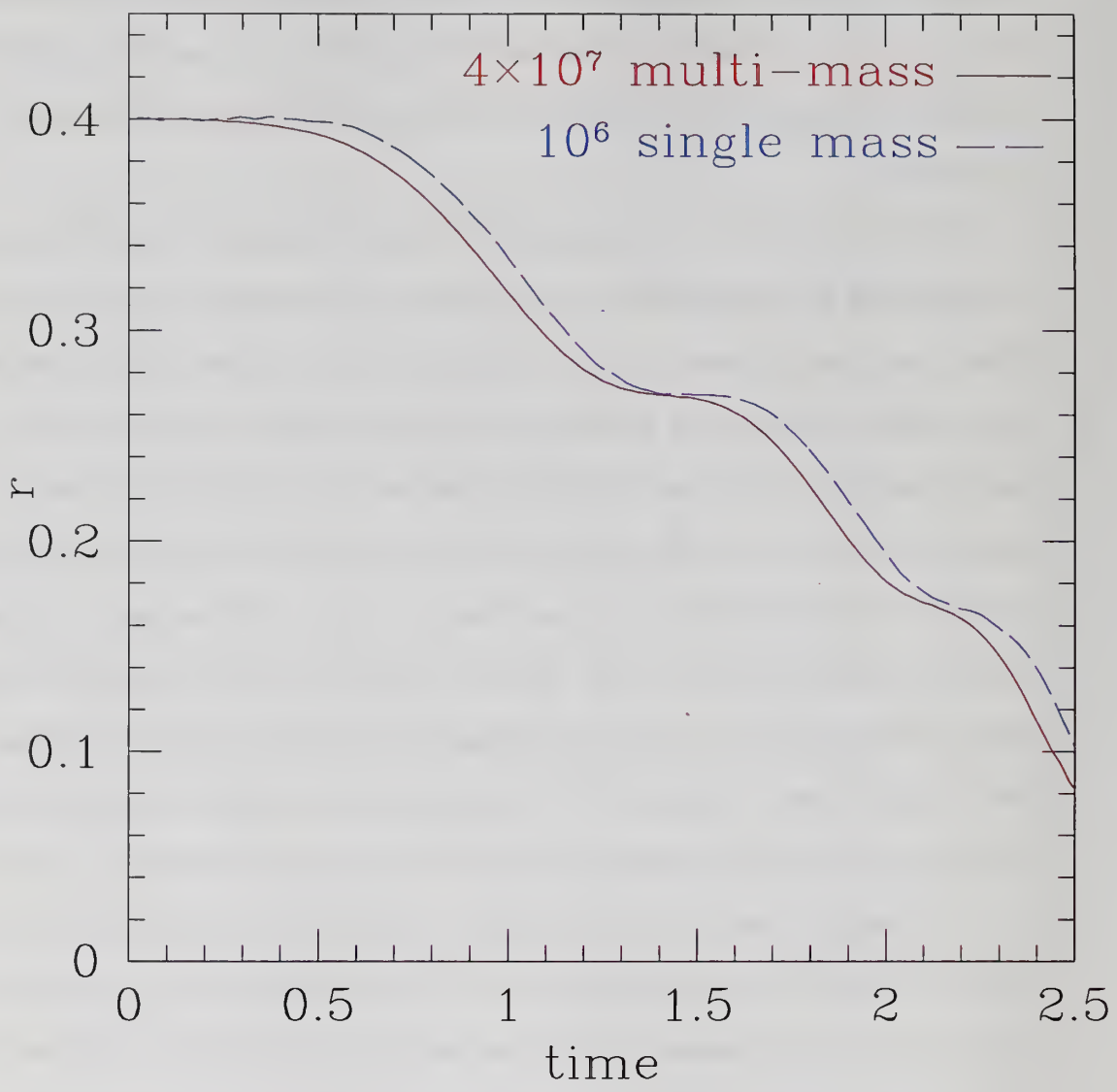

Figure 1.15 Satellite decaying in the dark matter halo due to dynamical friction. Both simulations are a fiducial simulation with different resolutions of the dark matter halo: the 10^6 single mass particle halo and the 4×10^7 multi-mass particle halo. The EJ center is the center of halo. The satellite in the high resolution halo decays faster than that in the low resolution halo.

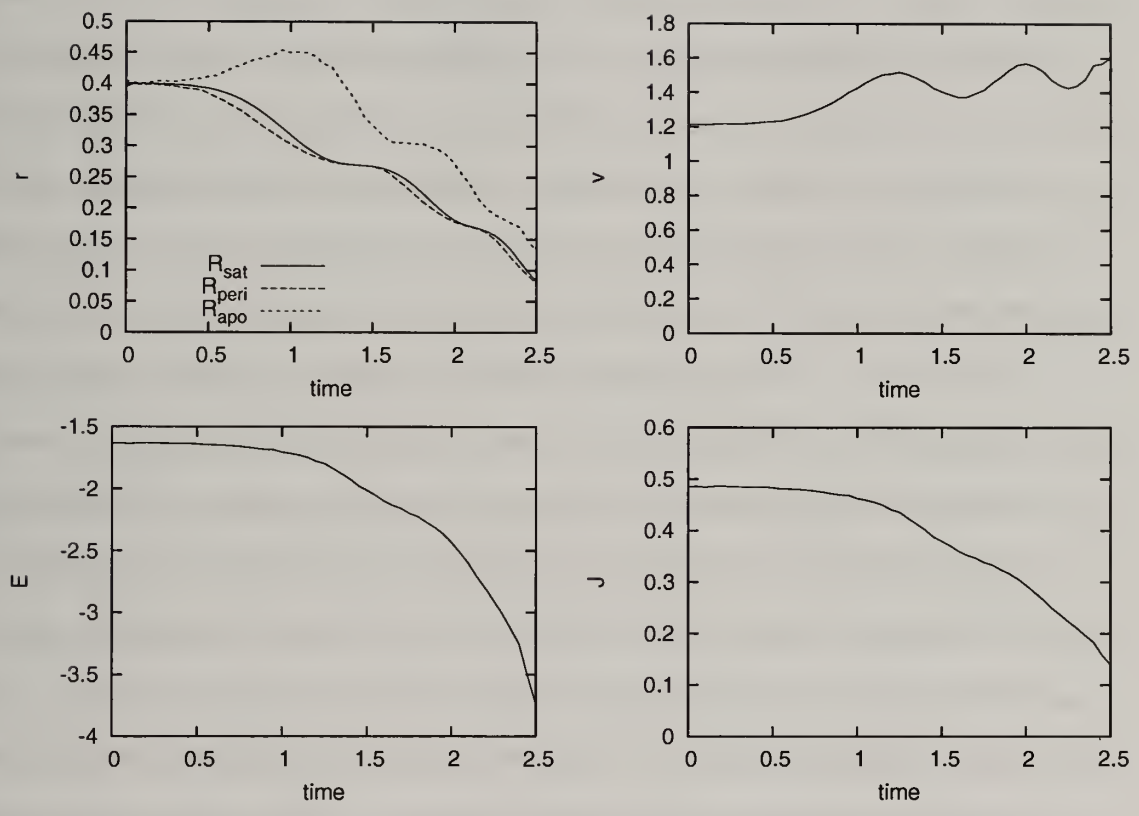

Figure 1.16 Evolution of characteristics of satellite orbit for the fiducial simulation. *Top left:* Evolution of the pericenter and the apocenter of the satellite in fiducial simulation. They are determined by the energy of the satellite orbit at a given time. *Top right:* Evolution of the satellite speed relative to the EJ center. *Bottom left:* Evolution of the satellite energy. *Bottom Right:* Evolution of the angular momentum.

Some previous studies suggested that during resonant interaction, energy and angular momentum transfer can be halt if the phase space density at which the resonance is located becomes zero. However, Figure 1.16 shows that this is not the reason in this case. The stalling satellite decay results from the halo response. If the dark matter halo is static, satellite decay only depends on a satellite energy loss. In reality, the dark matter halo response affects the satellite decay rate. Early in this section, we found that the halo cusp excurses a significant distance from the halo COM. This motion can reduce the distance between the halo center and the satellite without decreasing the satellite orbital energy. This results in the additional decay of the satellite. Due to this additional decay effect, the satellite happens to be located at its pericenter and produces a stalling the decay. This argument is clearly demonstrated in Figure 1.16. The top left panel shows the decaying of satellite's orbit, pericenter, and apocenter. This panel shows that the plateau at the satellite decaying plot results from the pericenter. In absence of the halo response, the satellite would be located between its pericenter and apocenter as determined by the satellite energy and angular momentum. If satellite is at its pericenter, the satellite can not move inwards until it loses additional energy to reduce the pericenter radius. In contrast with the stalling satellite decay, the satellite energy and angular momentum loss does not show any signature of slow-down (the bottom panels)! The rates of energy and angular momentum transfer does not decrease even while the satellite decay stalls. The energy loss during stalling satellite comes from the kinetic energy loss. The top right panel show that the satellite speed decreases when the satellite is located around the pericenter. It implies that the satellite loses the kinetic energy at that period. According to this argument, we can conclude that the stalling satellite decay results from halo responses not from losing resonant couplings. In addition, the satellite energy and angular momentum loss continuous. This investigation also suggests that

the apparent satellite decaying is affected by the dark matter halo response as well as the loss of energy and angular momentum.

1.6 Dark matter halo response of a decaying satellite

During satellite decay, its energy and angular momentum transfer to its dark matter halo. The input energy and angular momentum stimulate the dark matter halo structure evolution. Standard dynamical friction and resonant dynamics clearly predict distinct dark matter halo responses due to the decaying satellite. Investigating this response illustrates the characteristic of resonant dynamics. In addition, the dark matter halo response due to the decaying satellite influences many astronomical phenomena such as a non-axisymmetric mode of galaxies. In this Section, we investigate the dark matter halo response of the fiducial simulations.

The most basic characteristic of a dark matter halo structure is its density profile. Figure 1.17 shows the density profile evolution of the low resolution fiducial simulation (10^6 single mass particle halo) and the high resolution fiducial simulation (4×10^7 multi-mass particle halo). The center of the halo of density profiles is the center of mass of densest 128 particles and it almost coincides with the EJ center. The satellite decay in these simulations is shown in Figure 1.15. Almost no density profile evolution is observed in this figure during the course of the satellite decaying. The influence of satellite decay to the mass structure of a dark matter halo is negligible. However, the density profile shows an mild increase in density at the radial range from $r = 0.2R_{vir}$ to $r = 1.0R_{vir}$ This location coincides to the region at which the largest amount of angular momentum is deposited in the satellite phase space (see Figure 1.19). Since the halo cusp is separated from the halo COM, it is possible that this increase in density potentially results from the definition of the halo center instead of the real density change. We inspected density profiles with the halo COM center and still see this feature. As a result, there is energy angular momentum transfer from the

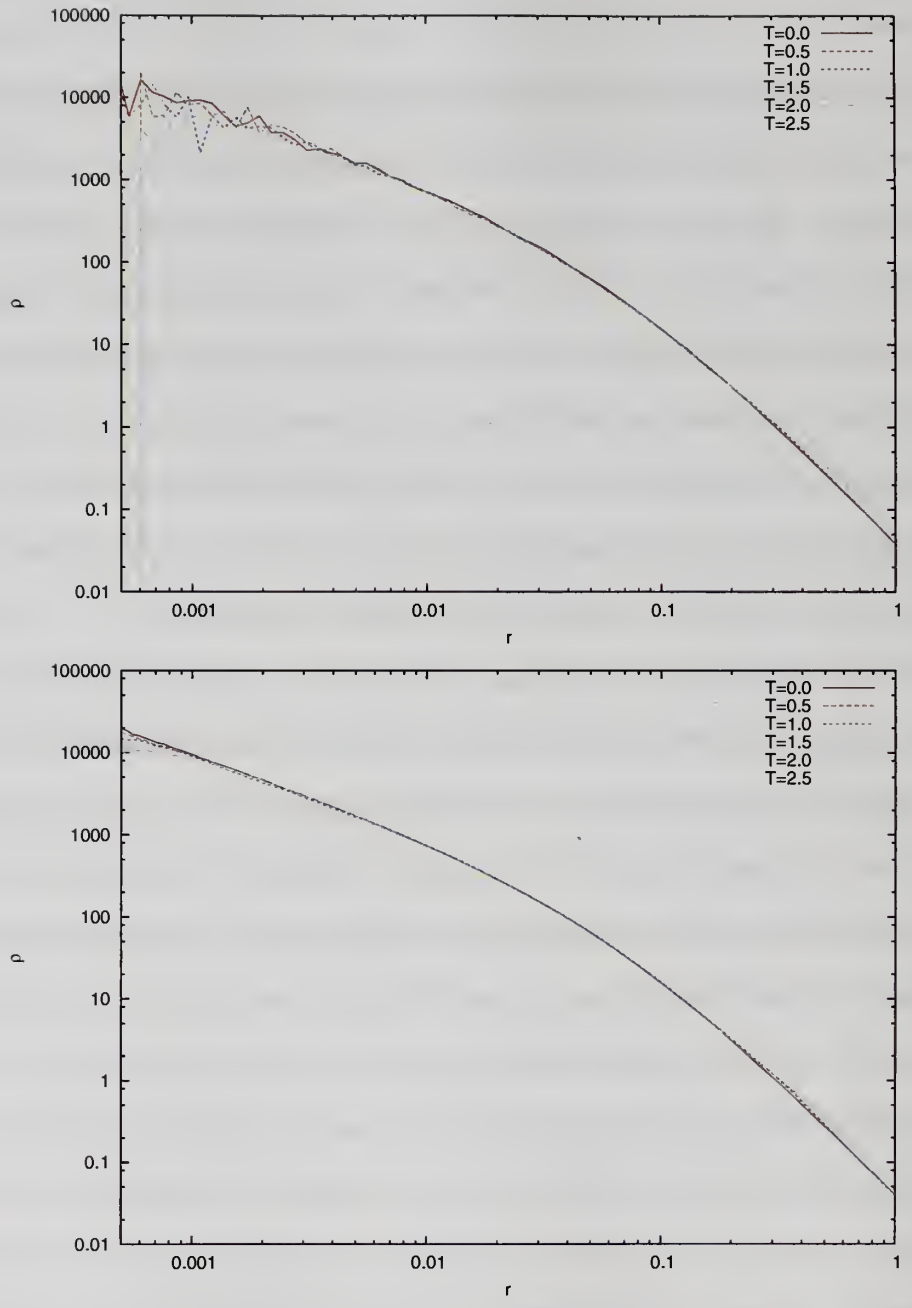

Figure 1.17 The density profiles of the dark matter halo for the fiducial simulations with different resolution halos. The top panel is the density profiles from the 10^6 single mass particle halo and the bottom panel is the density profiles from the 4×10^7 multi-mass particle halo. Both density profiles do not show significant evolution.

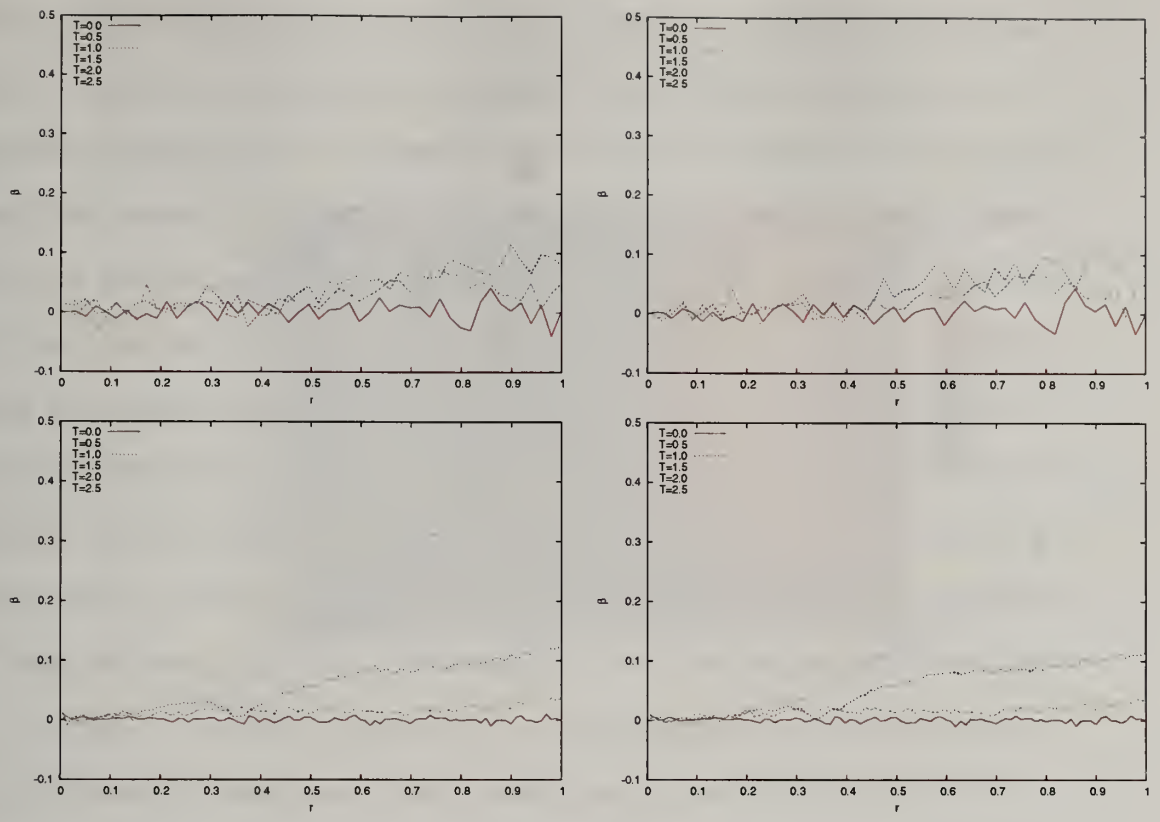

Figure 1.18 The velocity anisotropy (β) profiles of the dark matter halos for the fiducial simulation. The top panels are the velocity anisotropy profiles from the low resolution halo simulation and the bottom panels are those from the high resolution halo simulation. The halo center for the left panels is the halo COM and the halo center for the right panels is the EJ center.

decaying satellite to the dark matter halo but its amount is not large enough to drive the significant dark matter halo evolution.

Although the halo density profile does not show significant evolution, the decaying satellite changes the velocity distribution of the dark matter halo. Figure 1.18 shows velocity anisotropy profiles of the dark matter halo. A velocity anisotropy is defined as $\beta = 1 - \frac{\sigma_t^2}{2\sigma_r^2}$, where σ_t is a tangential velocity dispersion and σ_r is a radial velocity dispersion. A pure radial orbit halo implies $\beta = 1$, while an isotropic velocity distribution halo implies $\beta = 0$. Defining the location and velocity of the halo center is critical in computing the velocity dispersion. In Figure 1.18, both the halo COM and the EJ center are used as a halo center. The figure also shows the velocity anisotropy

profile from two different resolution halos. Due to interaction with the satellite, the velocity anisotropy profile shows gradually increasing features. For a given halo, β is increased as the radius is increased. At a given radius, β is increased as the satellite decays. Interestingly, the region in which the radial bias is observed in Figure 1.18 is almost overlapped with the region in which the increase in density is observed in Figure 1.17. This suggests that both phenomena result from the energy and angular momentum transfer from the decaying satellite. The velocity anisotropy profiles of the two different resolution halos in Figure 1.18 appear to be almost the same. This is consistent with comparison studies of the density profile evolution with different resolution halos. Both simulations can satisfy this requirement and the overall halo response is similar because most resonances which result in most dominant energy and angular momentum transfer do not require high resolution.

Section 1.4 claims that although most strong resonances are reproduced in both the high resolution halo and the low resolution halo, the inner part of the -1:2:2 resonance can be reproduced only in the high resolution halo. This difference does not affect the overall structure, but it can still make a different halo response where that resonance is located. In order to understand this different halo response, we need to study the resonance effect in the phase space. Figure 1.19 is the distribution of relative change of L_z in the phase space for two different resolution halos. Carefully defining the position and velocity of the halo center is a crucial issue in order to properly compute angular momentum. In Figure 1.19, the position and velocity of the halo center are assumed the position and velocity of the EJ center. Due to the interaction with a satellite, the halo cusp (the EJ center) is separated from the dark matter halo COM. Therefore, pinning the halo center onto halo cusp may result in incorrect estimations of the amount of angular momentum transfer for the outer halo particles. However, the angular momentum of the outer halo particles is less sensitive

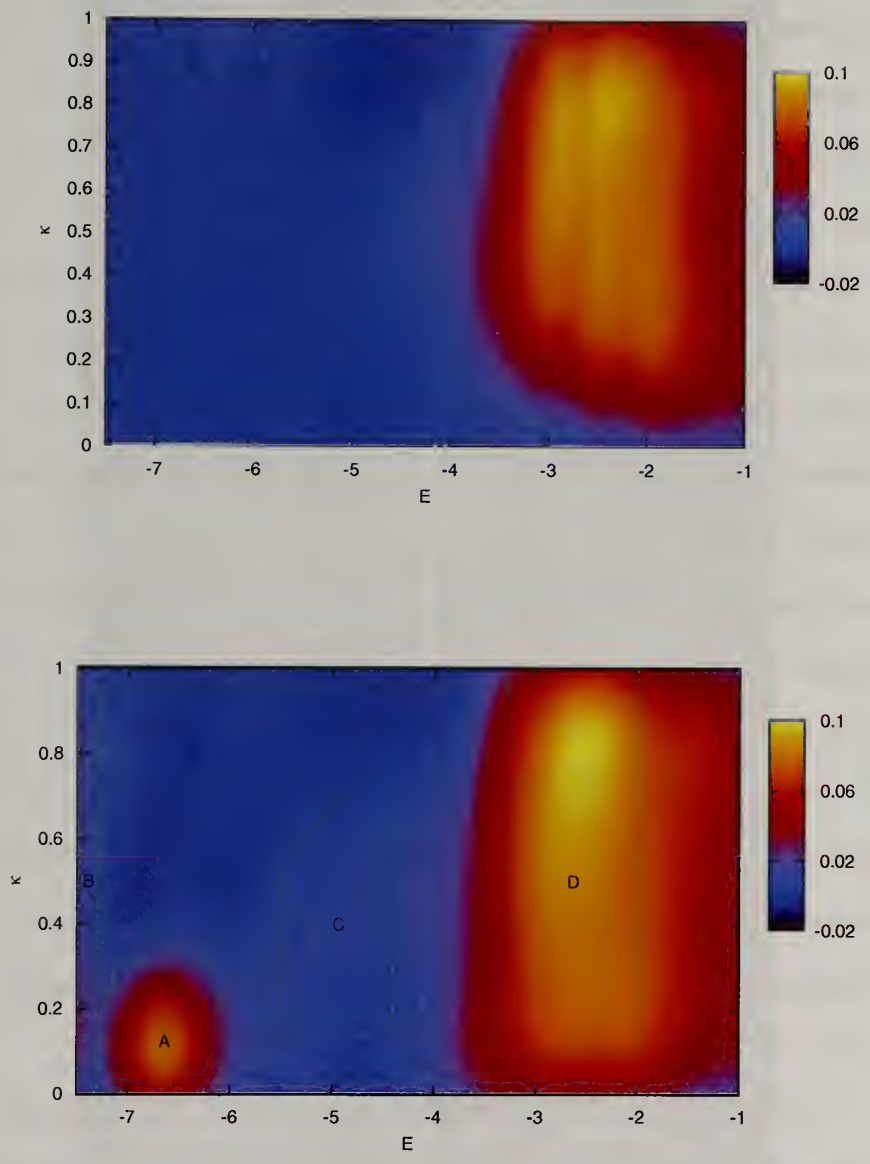

Figure 1.19 Distribution of relative change of L_z in phase space for the fiducial simulation. ΔL_z is the difference between $T = 1.5$ and $T = 0.0$. The top panel is the relative ΔL_z distribution from the low resolution halo simulation and the bottom panel is the relative ΔL_z distribution from the high resolution halo simulation. The bottom panle also shows the phase space locations of four regions.

to the halo center than the angular momentum of the inner halo particles so that using the halo cusp as the halo center is an acceptable choice.

The bottom panel in Figure 1.19 shows the relative ΔL_z distribution for the high resolution halo simulation. In this distribution, there are four gaining angular momentum regions in the phase space: Region A ($-7.15 < E < -6.1$ and $\kappa < 0.3$), Region B ($E < -7.3$), Region C ($-5.5 < E < -4.4$ and $0.14 < \kappa < 0.7$), and Region D ($-3.3 < E < -2.0$ and $\kappa > 0.1$) (see the bottom figure in Figure 1.19 for the accurate phase space location of these four regions). Most of these regions are related with the low order resonances studied in Section 1.4. Region A is related to the low energy tip of the -1:2:2 resonance. Region B is probably to with the inner edge of the resolved halo cusp not related to any resonance feature. Region C is approximately located in the -1:2:2 resonance line shown in Figure 1.3. This region shows very small angular momentum gain and it looks like a diagonal strip in the phase space. Region D shows the strongest angular momentum gain and it is located where the most resonances lines in Figure 1.3 are populated except the -1:2:2 resonance line. The numerical perturbation calculation claims that the phase space location in which most of angular momentum transfers due to the -1:2:2 resonance happens to be the high energy side of the resonance line. This location also coincides with Region D. Therefore, Region D is the location where almost all the resonant interactions occur. Below, we investigate the evolution in these four regions.

In Figure 1.19, we find a few difference features in the relative ΔL_z distributions for two different resolution halos. The most noticeable difference is the absence of Region A for the low resolution halo simulation. In addition, the strength of the low energy part of Region C is weaker in the low resolution halo than the high resolution halo. These two differences result from the poor resolution of the low resolution halo for the low energy part of the -1:2:2 resonance as discussed in Section 1.4.

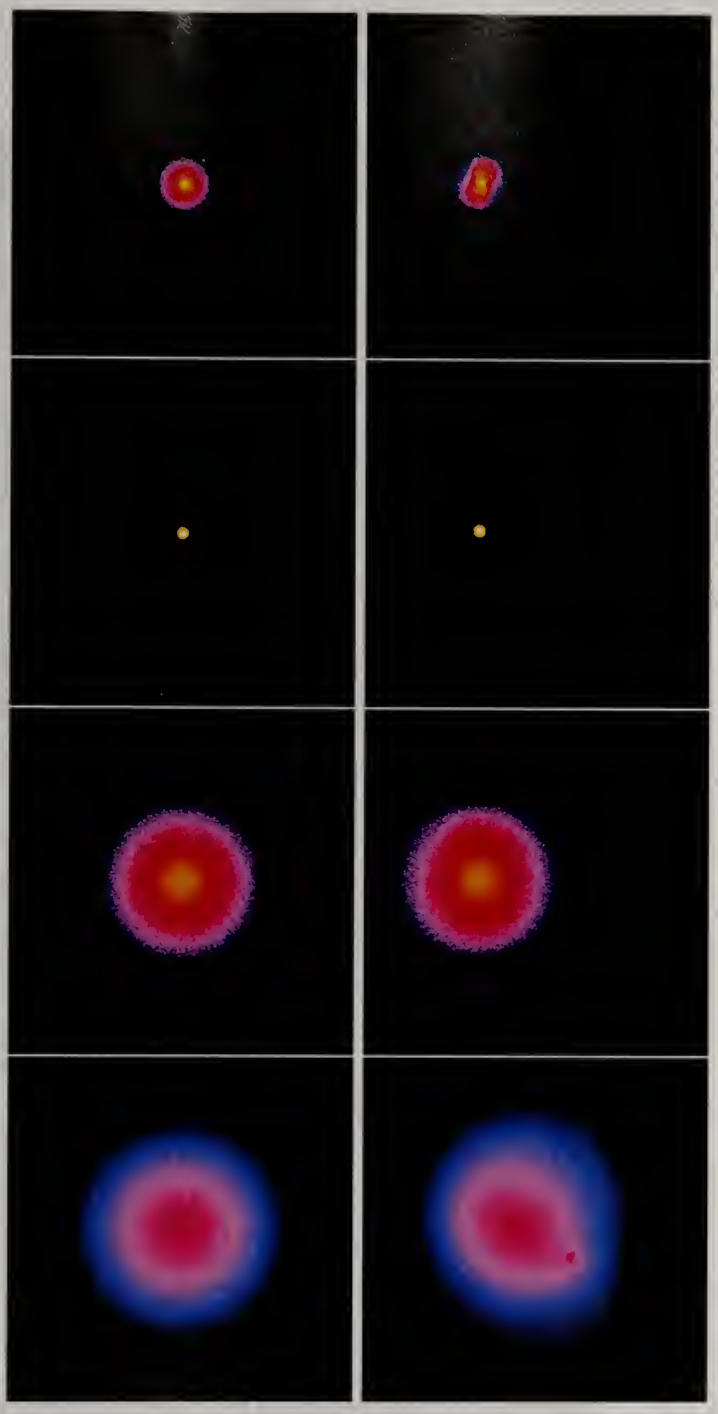

Figure 1.20 The spatial distribution of particles in four regions in Figure 1.19 for 4×10^7 multi mass particle halo simulation. Panels shows the particle distribution for Region A, Region B, Region C and Region D from top row to bottom row. This distribution is projected onto the satellite orbital plane. The left column is the snapshots at $T = 0.0$ and the right column is the snapshots at $T = 1.5$. The axis size of the snapshots for Regions A, B, and C is $0.5R_{vir}$. The axis size of the snapshots for Region D is $1.5R_{vir}$. The center of each panel is the halo COM.

Figure 1.21 The same as Figure 1.20, but for 10^6 single mass particle halo simulation.

Figures 1.20 and 1.21 show the spatial distribution of the four regions for the high and the low resolution halos. The definition of the four regions for both results follows the definition which is set in the high resolution results. Since the center of the snapshots is fixed at the halo COM, the spatial distribution of Regions A, B, and C are skewed from the halo center at $T = 1.5$. This skewed distribution results from the barycentric motion of the halo cusp due to interaction with the decaying satellite. In contrast, the distribution of Region D is not skewed from the halo center. This difference suggests that the only inner halo shows a barycentric motion. The distributions of Regions B and C are not changed during the simulation, but the distribution of Region A shows a interesting change. This distribution is initially a spherical shape but it becomes an elongated shape at $T = 1.5$. This elongation resembles the $m = 2$ bar-like mode. It possibly results from the -1:2:2 resonance since Region A is located at the tip of predicted location of the -1:2:2 resonance in the phase space. In contrast with the distribution of the high resolution halo, the elongated feature does not clearly appear in the distribution of the low resolution halo. This is consistent with the absence of Region A in the relative ΔL_z distribution for the low resolution halo and the predicted resolution limit for the -1:2:2 resonance discussed in Section 1.4. This elongated feature evidently results from the -1:2:2 resonance coupling and a simulation has to satisfy the particle number requirements to reproduce this feature.

The spatial distribution of Region D shows a few unique features compared with the distributions of the other regions. First, Region D extends to such a large volume that it is unaffected by the barycentric motion. Second, some particles appear to be scattered at $T = 1.5$. The outskirts of Region D is close to the satellite at $T = 1.5$. The predicted location of the angular momentum transfer in Figure 1.11 coincides with Region D. It suggests that most of the energy and angular momentum transfer

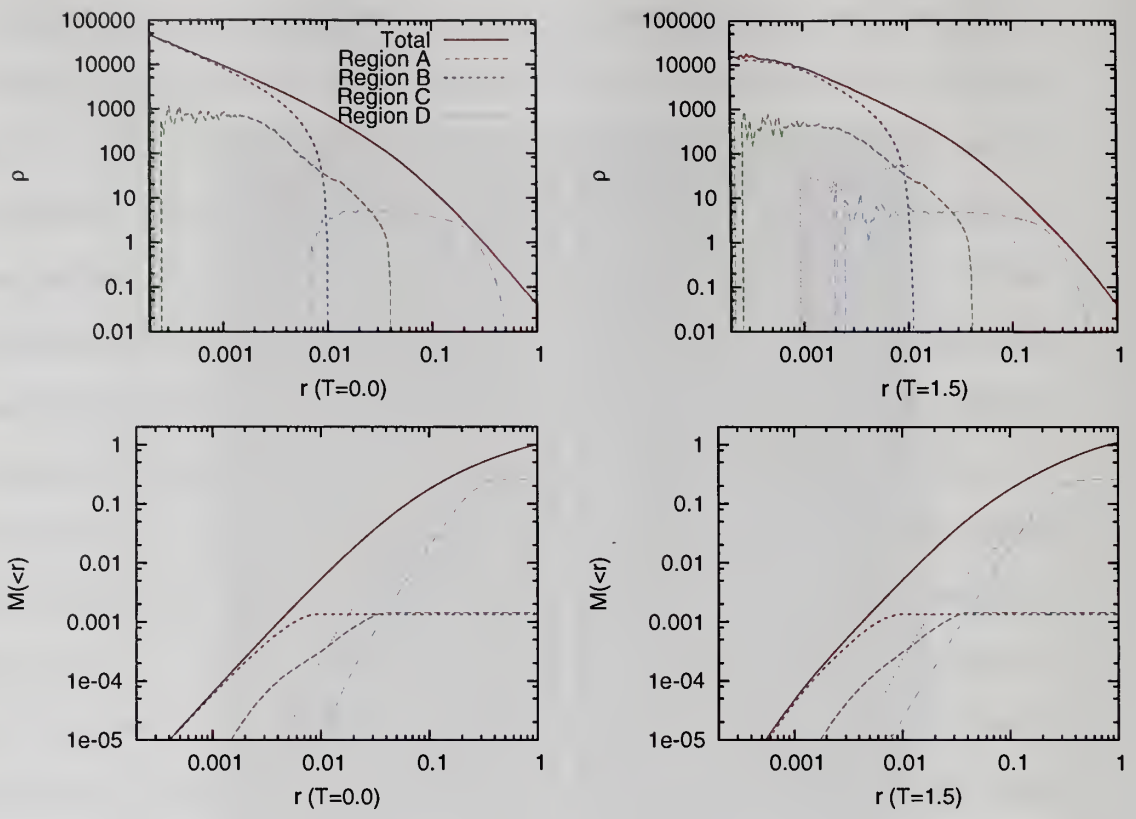

Figure 1.22 Density profiles (top panels) and mass profiles (bottom panels) for total halo and the four regions in the 4×10^7 multi-mass particle halo simulation. The left panels are both profiles at $T = 0.0$ and the right panels are at $T = 1.5$. The center of the profiles for the total halo is center of mass of densest 128 particles and the center of four regions is the center of mass of particles for each region.

occurs at Region D and the scattered distribution is consequence of this input energy and angular momentum.

Figures 1.22 and 1.23 show the density and mass profiles for the four regions along with the total halo. These figures show the mass contribution for these four regions. Region B constitutes most of the inner halo $r < 0.0025$ with minor contribution from Region A. The mass contribution of Region C is only about 10% of the material at their radius range. The figures show that Regions A and C can not contribute the profile evolution because of their small mass contribution. In addition, the elongated distribution of Region A is smeared out with a spherical average of the profiles. The

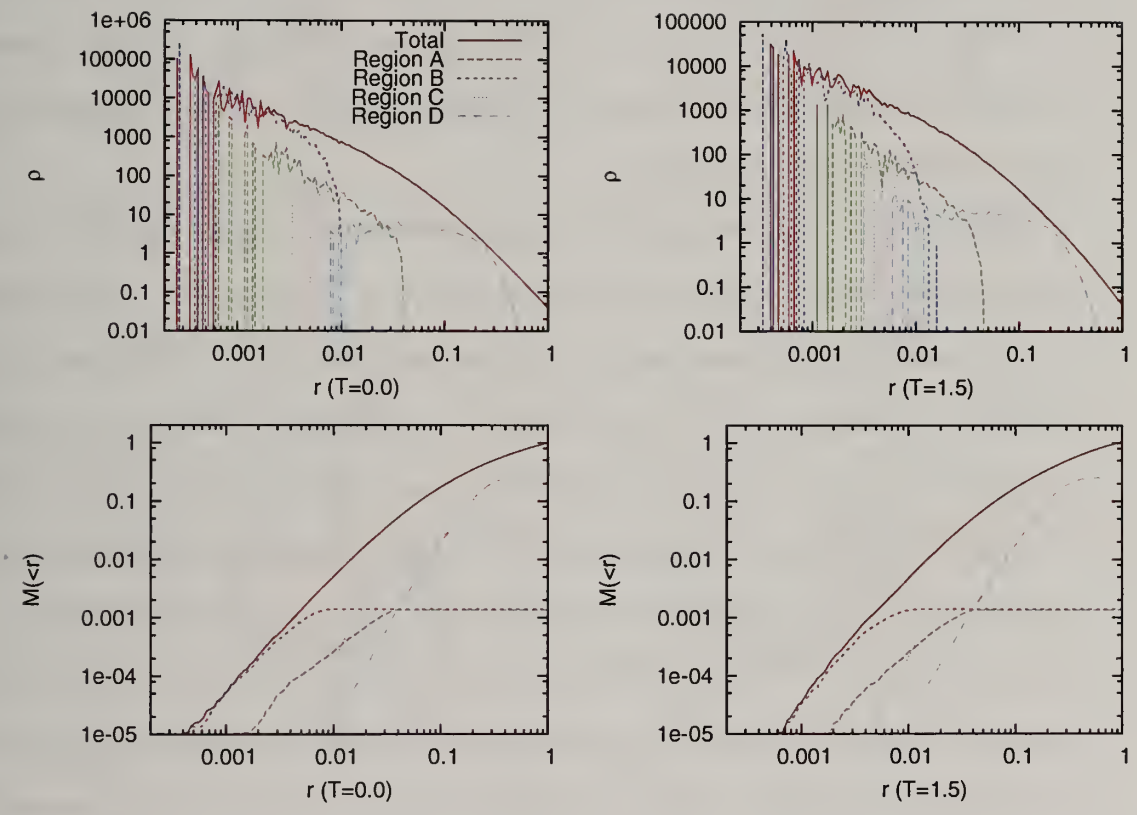

Figure 1.23 The same as Figure 1.22, but for 10^6 single mass particle halo simulation.

figures also show that the density and mass profile evolution of the two different resolution simulations are insignificant.

This negligible density profile evolution has been already pointed out in discussion of Figure 1.17. However, Region D causes a mild density profile evolution. The density profile of Region D develops a outer tail. This extended distribution results from the scattered feature shown in the spatial distribution in Figures 1.20 and 1.21 because radial ranges of both the density profile evolution region and Region D are almost overlapped. It is also consistent with the increase in density shown in Figure 1.17. This mild profile evolution results from the energy and angular momentum transfer due to the resonant interaction.

Dark matter halo response due to a decaying satellite are obvious in the dark matter halo density wakes and potential responses. Figures 1.24 – 1.29 present the dark matter halo responses of the fiducial simulations. Figure 1.24 shows the density wake for the high resolution halo simulation. In this figure, note that the overdensity wake develops just behind the satellite and keeps trailing the satellite during the course of the decay. This overdensity wake plays a major role in satellite decay. We also find that the center of the density peak, which coincides to the halo cusp, is offset from the center of the halo mass. This is caused by the barycentric motion of the halo center. In addition to the wake which trails the satellite (hereafter outer wake), there is another density wake is shown around the halo cusp which is located around (-0.75, 0.01) in $T = 1.5$ snapshot for example. This wake (hereafter inner wake) is located in well inside of the satellite position and its phase is about 90^o lagged behind both the satellite phase and the outer wake phase. The location of the inner wake coincides to Region A in Figure 1.19. The shape of the wake resembles the elongated distribution which is observed in Region A in Figure 1.20. It suggests that the -1:2:2 resonance develops the inner wake which excites a bar-like mode well inside of the satellite location. This inner wake feature is clearly shown in a potential response (Figures

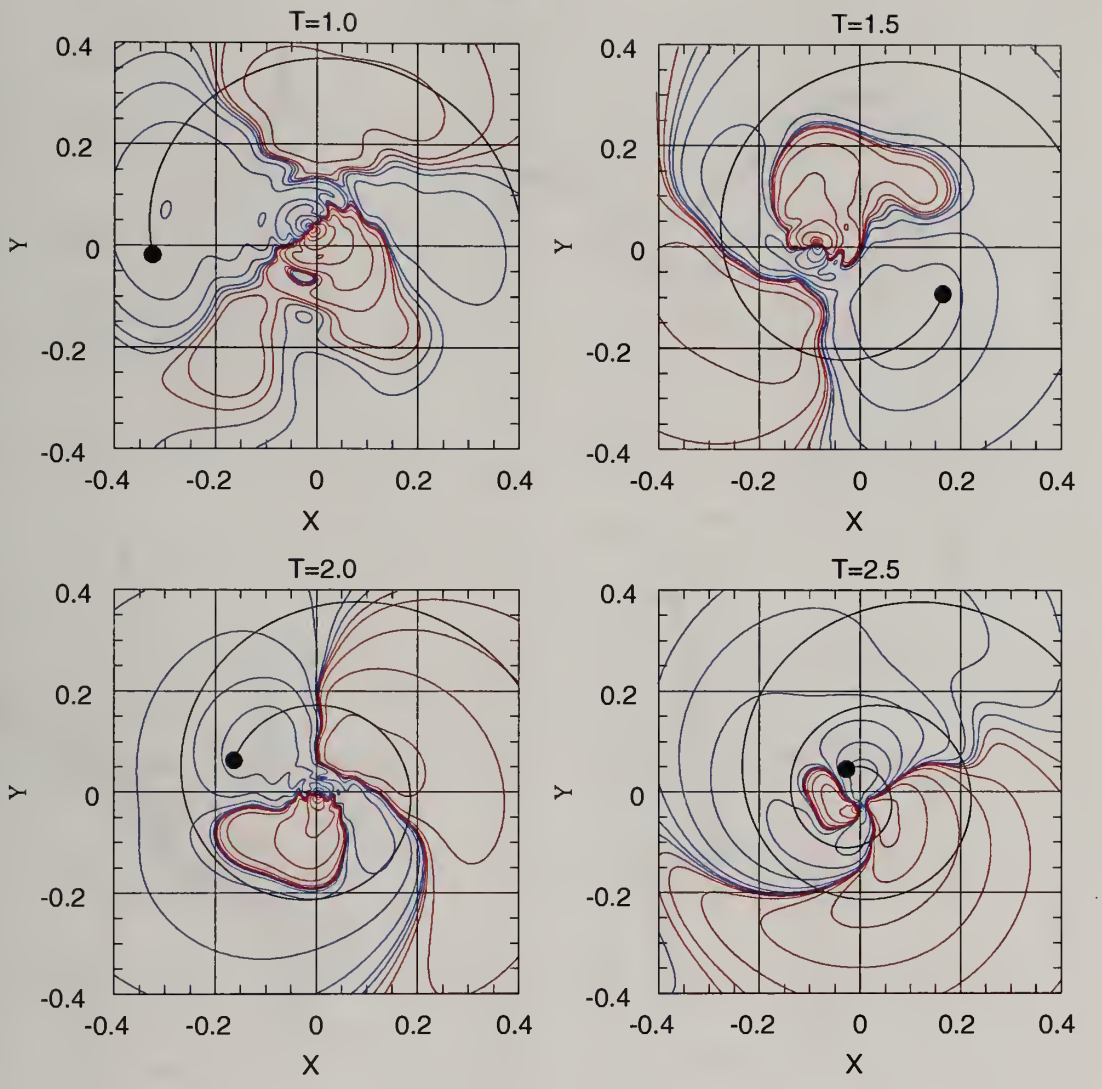

Figure 1.24 Density wakes due to the decaying satellite of the 4×10^7 multi-mass particle halo. The each panel shows a snapshot of a density wake at a given time. The origin of the plot is the center of dark matter halo mass. The blue contours represent overdensity wake and the red contours represent underdensity wake. The black line represents the satellite trajectory from $T = 0$ to the given time and the black dot represents the current location of the satellite.

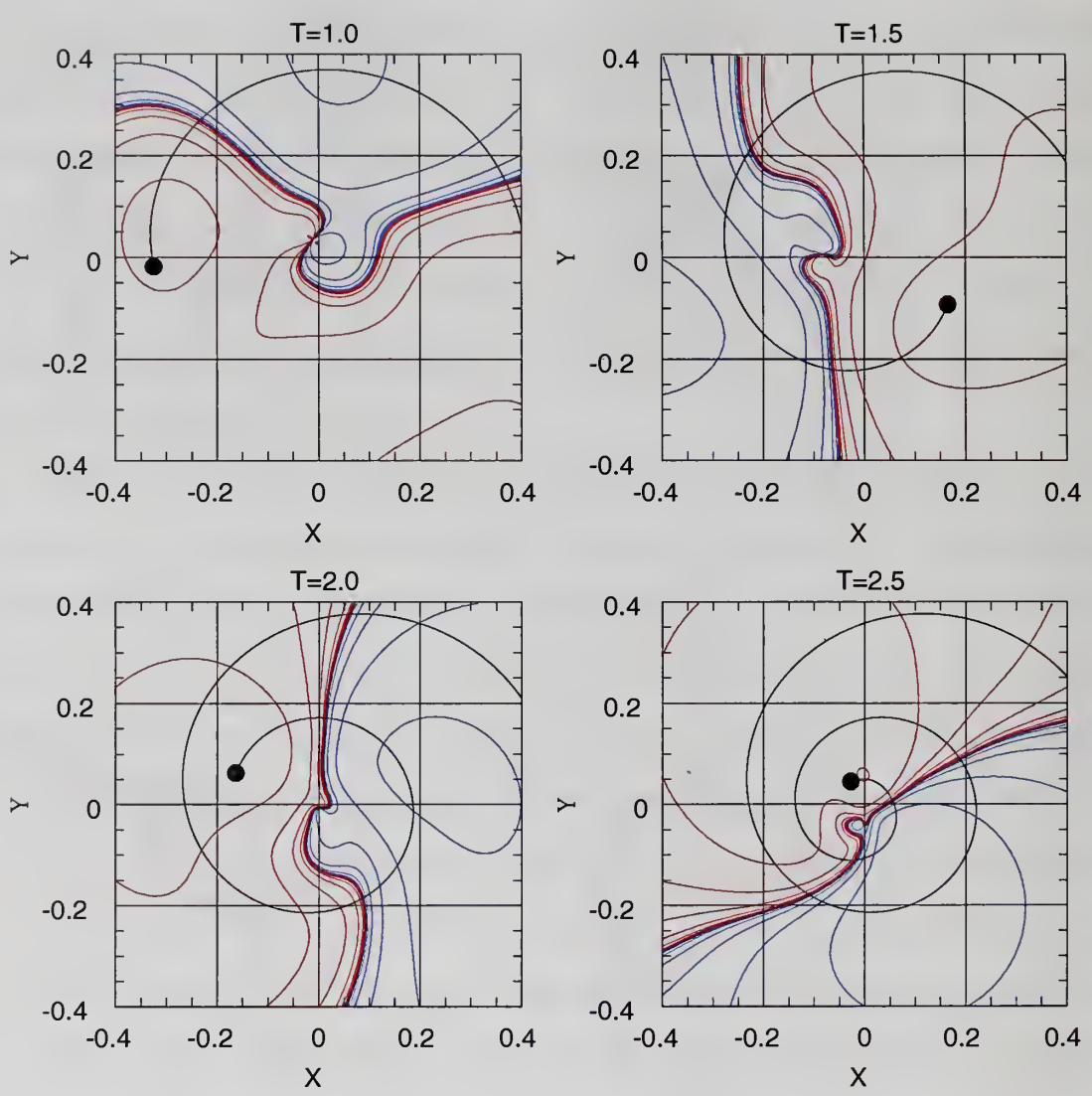

Figure 1.25 Potential response due to the decaying satellite of the 4×10^7 multi-mass particle halo. The each panel shows a snapshot of a potential response at a given time. The origin of the plot is the center of dark matter halo mass. The blue contours represent a positive potential response and the red contours represent a negative potential response. The black line represents the satellite trajectory from $T = 0$ to the given time and black dot represents the current location of the satellite.

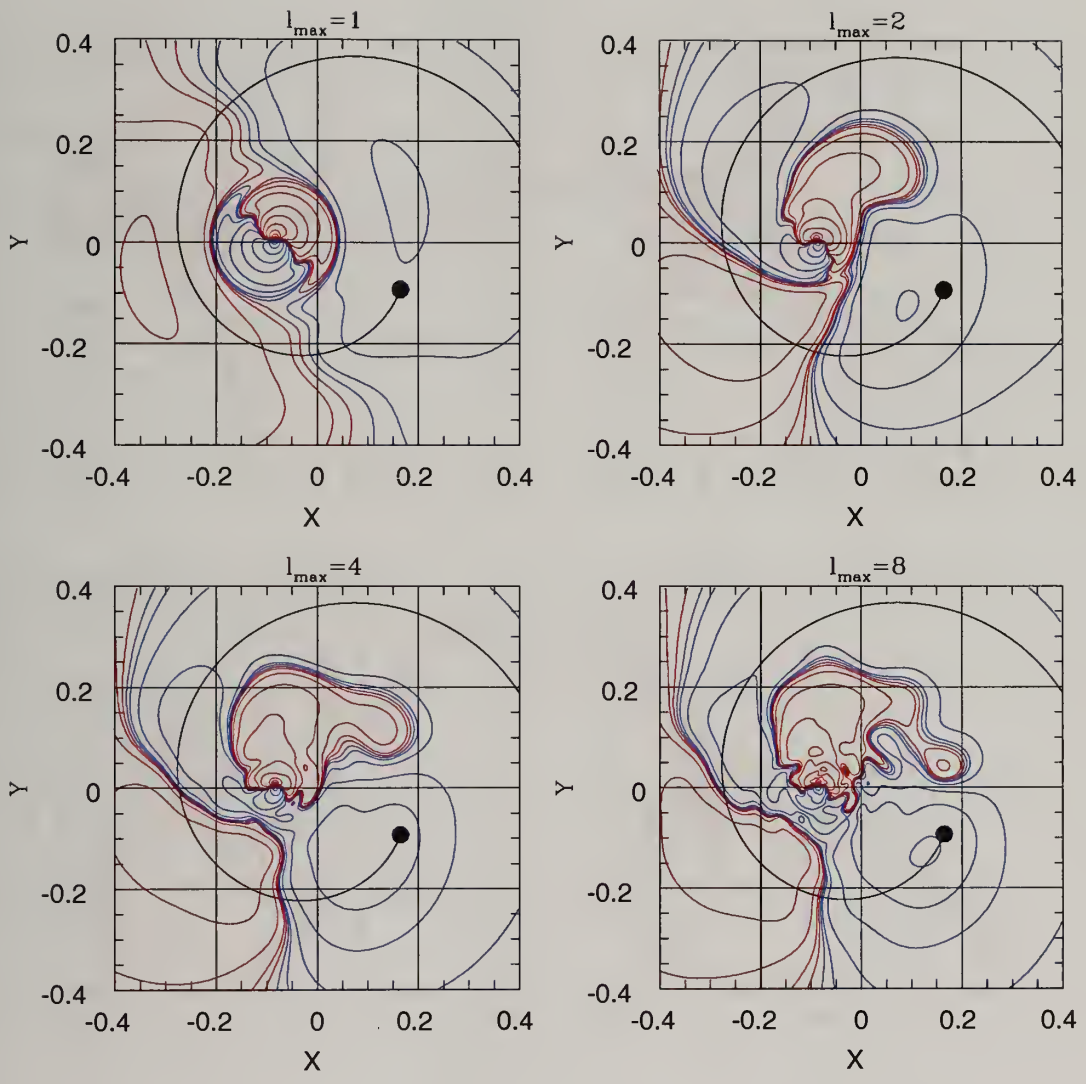

Figure 1.26 The density wake of the high resolution halo at $T = 1.5$ with different l_{max} for the fiducial simulation.

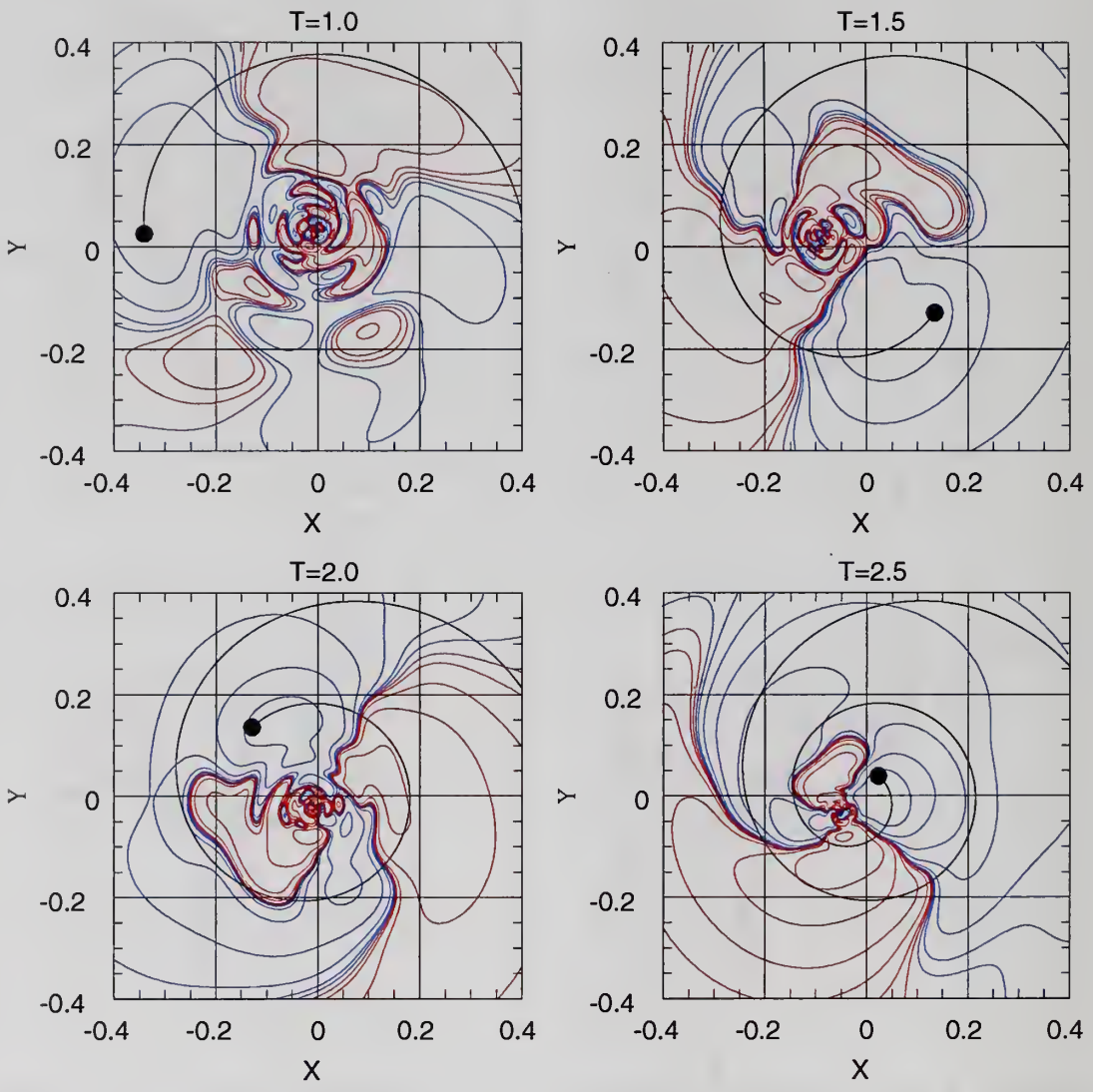

Figure 1.27 The same as Figure 1.24 but the 10^6 single mass particle halo simulation results.

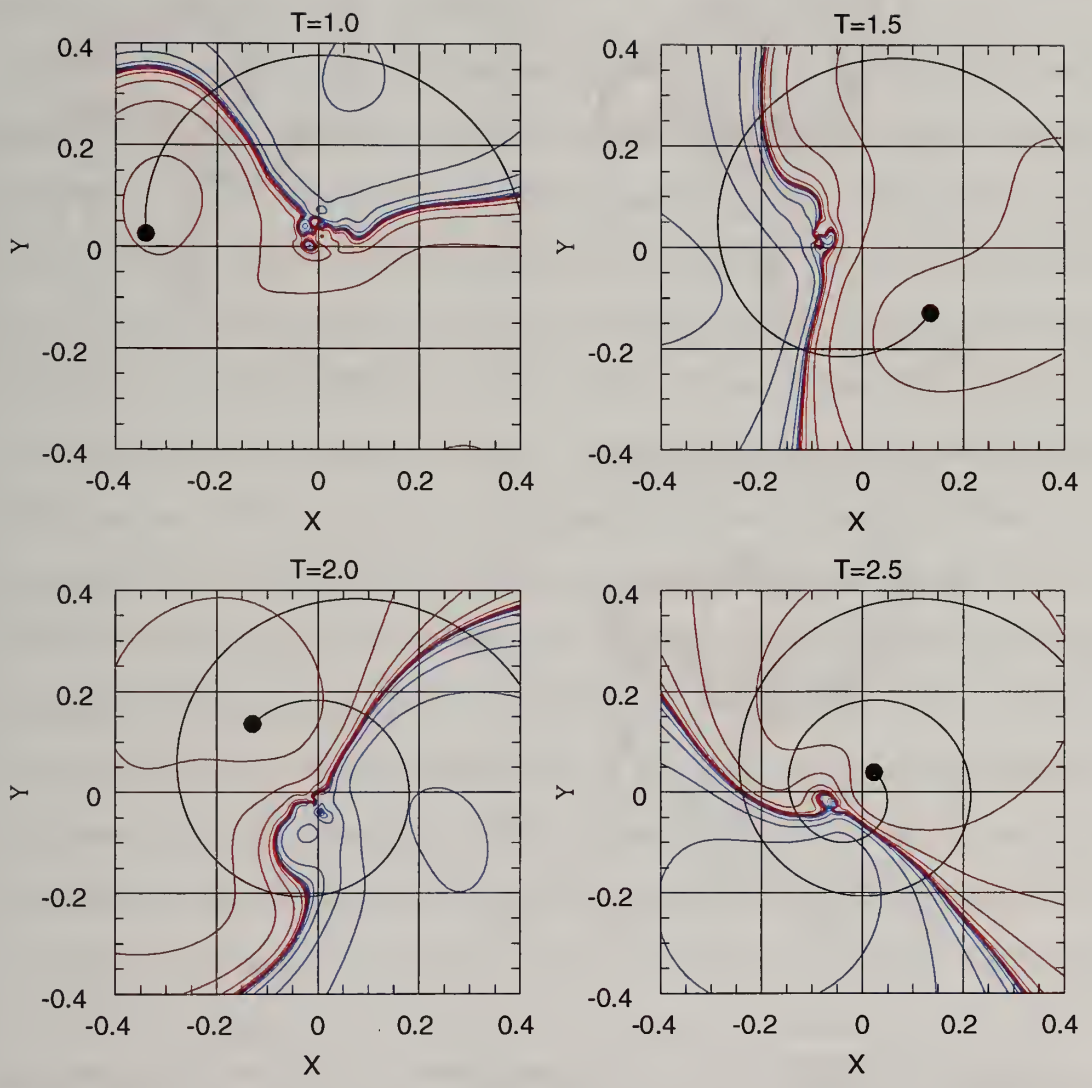

Figure 1.28 The same as Figure 1.25 but the 10^6 single mass particle halo simulation results.

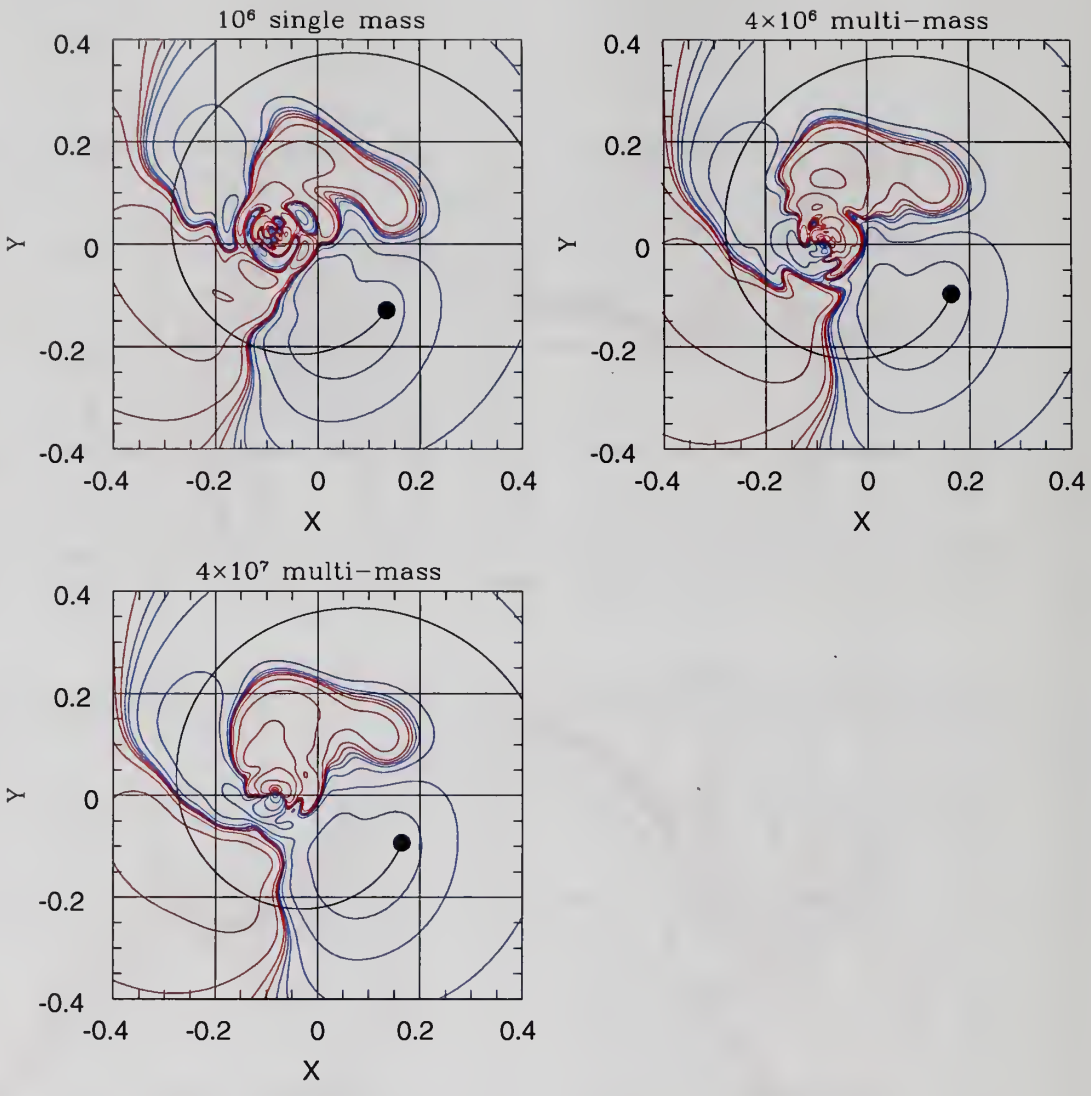

Figure 1.29 Density wakes of the dark matter halo stimulated by decaying satellite for three different resolution halos: 10^6 single mass particle halo, 4×10^6 multi-mass particle halo, and 4×10^7 multi-mass particle halo. The time of a snapshot for all three halos is $T = 1.5$ and the density wakes for all three halos consist with l =1, 2, 3, and 4 contributions. The outer wake is similar in all three halos. But the inner wake is not clearly developed in the 10^6 single mass particle halo while it is shown in both 4×10^6 multi-mass particle halo, and 4×10^7 multi-mass particle halo

1.25). In this figure, we can observe an inner 's'-shaped feature in the contours. This contour structure is equivalent to the inner density wake. In contrast with the outer wake, the amplitude of inner wake increases and then diminishes as the satellite decays. This suggests that there is an optimized distance from the halo center to the satellite to develop the inner wake.

In order to compute the dark matter halo response from the simulation, we calculate density and potential of the halo using the expansion algorithm. In this calculation, we need to determine the maximum harmonic order of the expansion, l_{max}. Since the lowest order basis function is based on the global structure of the dark matter halo, only a small number of terms are necessary. Figure 1.26 shows the same halo response constructed with different l_{max}. Large scale structures of the wakes for different l_{max} are almost similar. As higher l contribution is introduced, the small-scale detail improves without significantly changing large scale structures. However, the decreasing l_{max} to 1 presents different features than other density wakes. First, the outer wake does not appear to trailing the satellite. This suggests that the trailing the satellite feature results from $l = 2$ contribution. Second, although the inner wake is shown, the wake structure is different than other l_{max} results. In particular, the wake presents a strong inner dipole. This suggests that both l =1 and 2 contributions are required to properly reproduce the inner wake structure and $l = 2$ contribution is responsible for developing an elongated shape as one might anticipate. The sequence in Figure 1.26 confirms that the low order resonances dominate the response. Although the density wake with $l_{max} = 1$ fails to correctly reproduce the density wake, it indicates one important characteristic of the dark matter halo response: the inner wake and the outer wake are clearly separated. This suggests that these two wakes have different origins. Note that both Figures 1.24 and 1.25 includes l =1, 2, 3,and 4 contributions, $l_{max} = 4$.

Figures 1.27 shows the density wakes for the low resolution halo and Figures 1.28 shows the wake in the gravitational potential. Both the density and and potential responses reproduce the outer wake feature and the barycentric motion. But the inner wake is not well developed in these results. The low resolution halo satisfies particle number criteria for the resonances responsible for developing the outer wake but not for the resonance responsible for the inner wake. This result agrees with the result from particle number requirement test in Section 1.4. It is also easily envisaged that the presence and absence of the inner wake causes the different satellite decay rate shown in Figure 1.15.

Figure 1.29 shows the density wake at $T = 1.5$ for three resolution halos: the low resolution halo, the medium resolution halo, and the high resolution halo. These density wakes suggest a resolution limit for the inner wake. In this figure, we find that the density wake in the medium resolution halo marginally reproduces the inner density wake while the low resolution halo can not reproduce it at all. This is consistent with the result from the particle number requirements in Section 1.4: the medium resolution halo can marginally reproduce the inner -1:2:2 resonance effects. We also find that the satellite decay rate in the medium resolution halo simulation is closer to the decay rate of the high resolution halo simulation than that of the low resolution halo simulation. This suggests that the resolution of this simulation is acceptable to reproduce -1:2:2 resonance effects.

Overall these results confirm the role of the resonant dynamics and the particle number requirement necessary to observe resonance effects. Due to the -1:2:2 resonance, the inner halo is excited with elongated bar-like mode and this excitation does not appear in the low resolution halo simulation. We conclude that the energy and angular momentum transfer through resonant interaction truly occurs and sufficient resolution simulation is required to reproduce these effects.

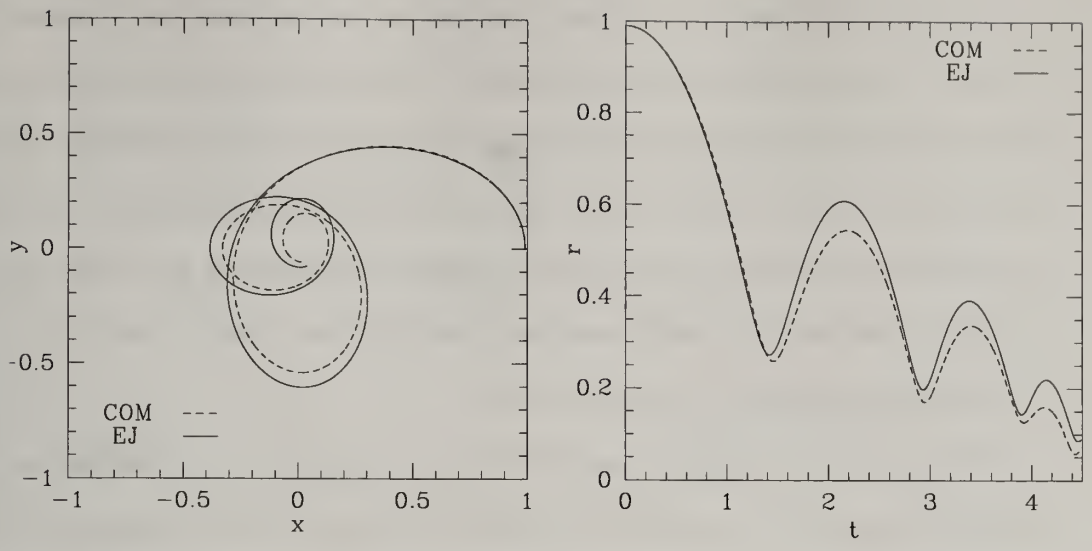

Figure 1.30 The trajectories of the satellite in the eccentric orbit simulation. The left panel shows the satellite trajectory on the orbital plane. The right panel shows the decay history of the satellite. On both panels, the solid line is the trajectory whose center is the EJ center and the dashed line is the trajectory whose center is the halo COM.

1.7 Eccentric orbit

The initially circular orbit simulation, the fiducial simulation, has been investigated in previous sections in detail. Although it provides clear and detailed insight to the physical processes in satellite-halo interaction, most real satellite galaxies are on an eccentric orbit. Hence, it is important to apply this insight to more realistic situations. In general, the physical processes responsible for the satellite-halo interaction in an eccentric orbit satellite are not different with those for the fiducial simulation. The differences involve perturbation frequencies and the evolution of these frequencies. In this section, we present results from an eccentric orbit simulation. The configuration and initial conditions for this satellite orbit are introduced in Section 1.2. The dark matter halo is made of 4×10^6 multi-mass particles, the medium resolution halo. Although its resolution is not as high as the high resolution halo in the fiducial simulation, reproducibility of the low order resonances of the 4×10^6 multi-mass particle is still acceptable.

Figure 1.30 shows the satellite trajectory on orbital plane and the satellite decay history of the eccentric orbit simulation. The satellite trajectories centered on the EJ center and the halo COM show an obvious offset. This offset results from the halo cusp excursion which is also shown in the fiducial simulation. As claimed in the fiducial simulation, the separation distance between the halo cusp and the halo COM is significant. It advocates that the significant cusp excursion is a common phenomenon regardless a satellite orbit.

Figure 1.31 compares the satellite decaying history from our simulation with that from the standard Chandrasekhar dynamical friction with three different $\ln \Lambda$ values: 3.00, 3.25, and 3.5. The figure shows that the standard estimation with $\ln \Lambda = 3.25$ shows the most similar decaying history to the simulation results. However, none of three estimations clearly reproduces the time of the first pericenter. This discrepancy results from the halo cusp excursion which is not included in the standard estimation. Due to the halo cusp movement, the decay time is shortened. In addition, due to the halo cusp excursion, the pericenter distance in the simulation is smaller than that in the standard Chandrasekhar estimation. This suggests that the halo response is necessary to estimate satellite decay properly.

Section 1.5 indicated that satellite decay is constrained by not only energy and angular momentum loss but also dark matter halo responses. Figure 1.32 shows the evolution of the orbit parameters of the eccentric orbit simulation. One interesting feature is that the satellite gains energy and angular momentum near pericenter. In contrast, since the dark matter halo is a nonrotating sphere, the satellite hardly gains energy and angular momentum. We find that the halo cusp movement leads this contradictive feature. The gaining energy and angular momentum does not result from the resonant interaction result from the halo cusp movement. The halo cusp movement accelerates the satellite at its pericenter. This increases the satellite velocity and produces gaining energy and angular momentum feature. Figure 1.33

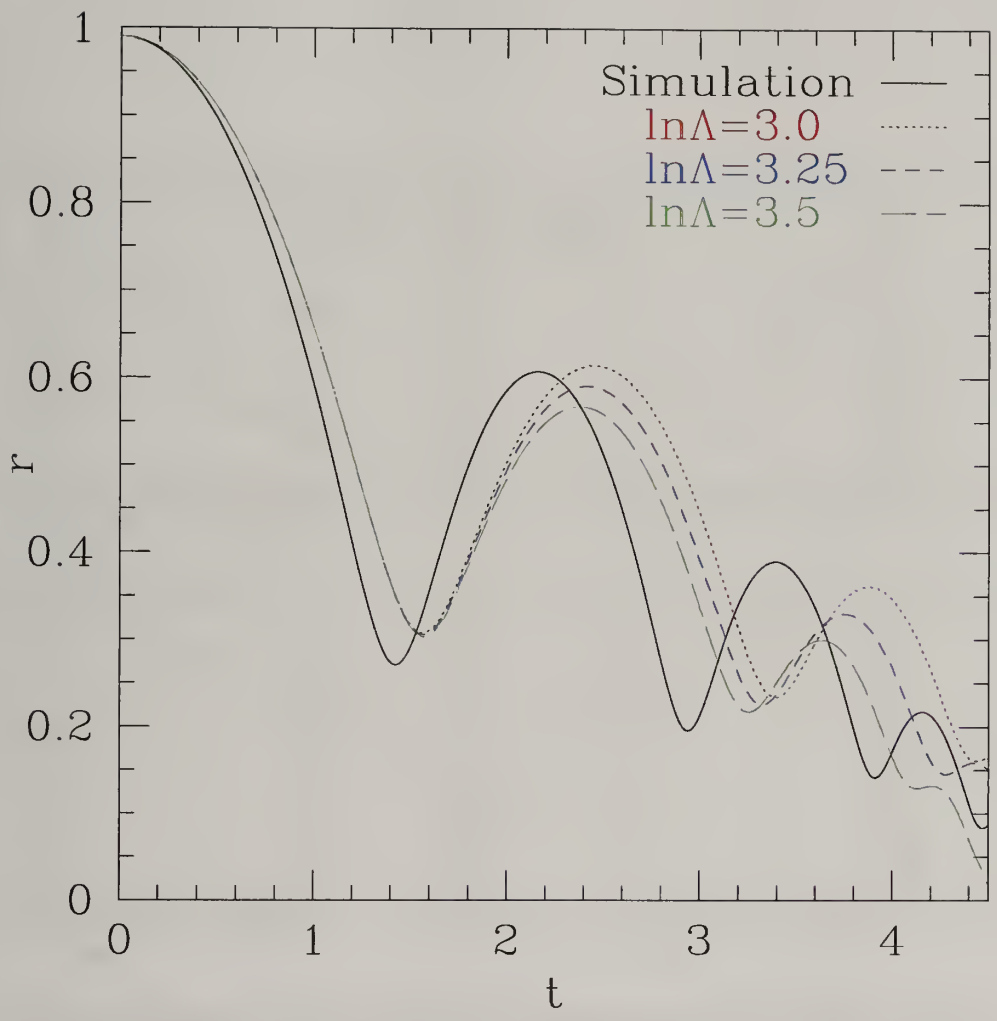

Figure 1.31 The satellite decaying history for the eccentric orbit simulation comparing with that for the standard Chandrasekhar dynamical friction. The simulation results is the same as the right panel in Figure 1.30. The EJ center is assumed the halo center. The estimations from the standard Chandrasekhar dynamical friction with three different $\ln \Lambda$ (3.0, 3.25, and 3.5) are compared.

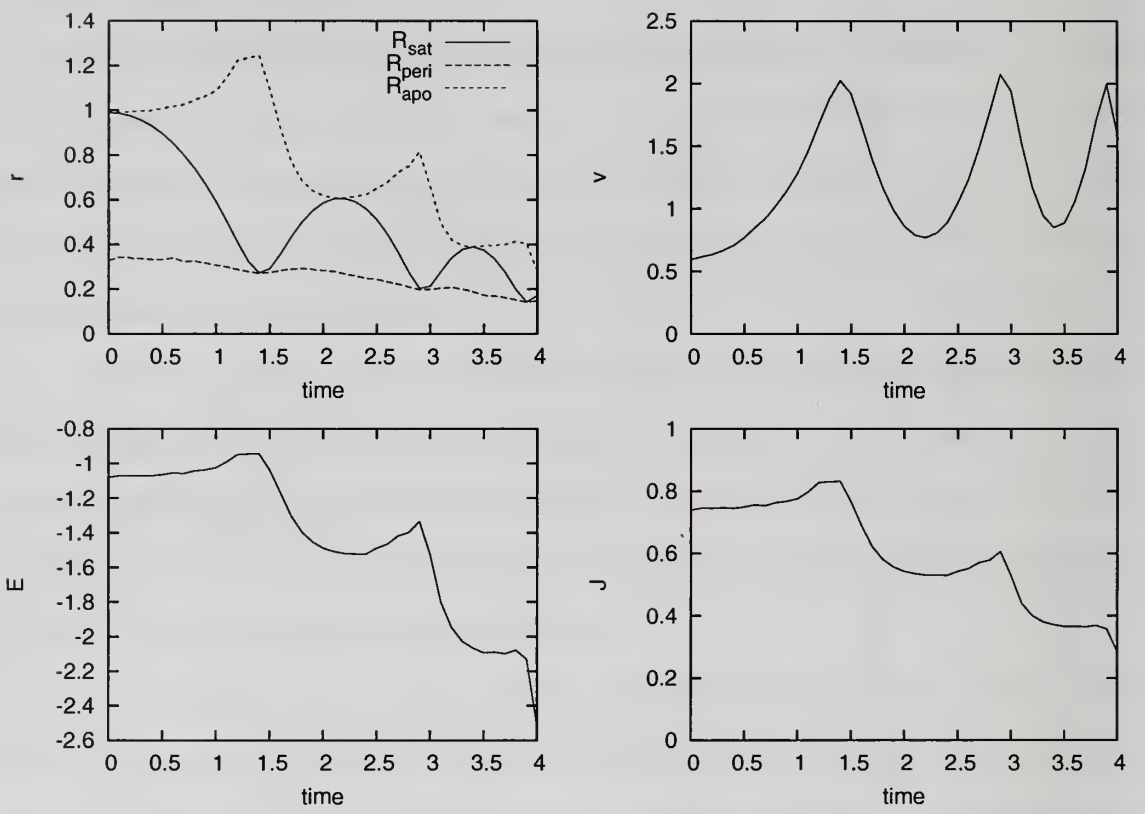

Figure 1.32 Same as Figure 1.16, but eccentric orbit simulation results

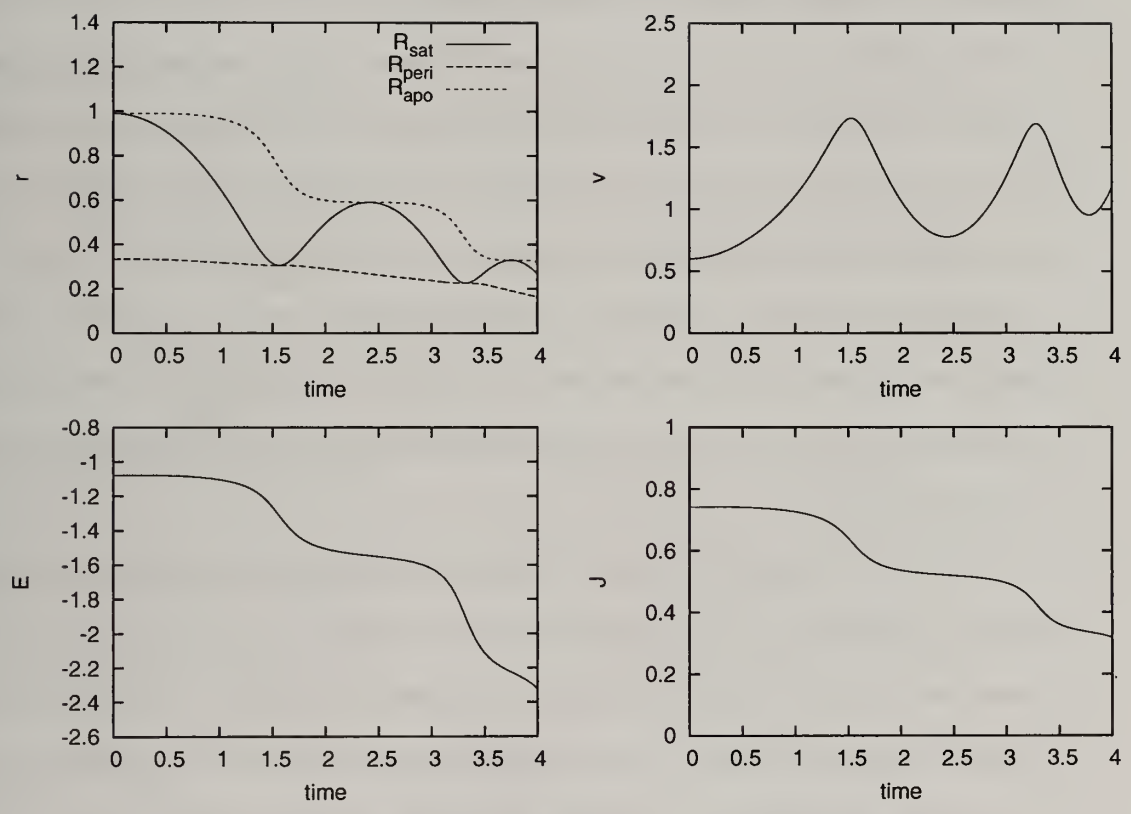

Figure 1.33 Same as Figure 1.32, but decaying is computed by standard Chandrasekhar dynamical friction with $\ln \Lambda = 3.25$.

helps to clarify the situation. This figure is similar to Figure 1.32 but the satellite decay is computed by the standard Chandrasekhar dynamical friction with the $\ln \Lambda = 3.25$. In this case, the structure of host halo is fixed. In Figure 1.33, the satellite does not gain energy and angular momentum. The pericenter velocity in the static halo case is lower than that in the live halo case. The absence of the acceleration from the halo cusp movement produces lower pericenter velocity. Therefore, the gain in energy and angular momentum results from the halo response. In addition, Figures 1.32 and 1.33 show that the satellite loses most of its energy during approach to the pericenter and hardly loses any energy from pericenter to apocenter. We speculate that this results from the phase space density gradient difference around the satellite in the satellite frame. Figures 1.32 and 1.33 show that both the energy and angular momentum transfer by satellite-halo interaction and the halo structure evolution influence the satellite decay. In order to estimate the accurate satellite decaying trajectory one need to know the information about the halo structure change at a given time.

Due to the decaying satellite, a dark matter halo gains energy and angular momentum. This energy and angular momentum transfer leads to the dark matter halo response. The top panel in Figure 1.34 shows the density profile evolution of the eccentric orbit simulation. The density profiles do not show any significant evolution. Similar to Figure 1.17, this density profiles show the mild increase in density at $r > 0.2R_{vir}$. The bottom panel in Figure 1.34 shows velocity anisotropy profiles of the dark matter halo. β of the outer halo is increased due to the satellite interaction. Both results are similar to the fiducial simulation in that the energy and angular momentum transfer from the eccentric orbit satellite is not sufficient to drive significant dark matter halo structure evolution.

Figure 1.35 shows the distribution of the relative ΔL_z for the eccentric orbit simulation. Each panel shows the relative of ΔL_z distribution in the E and κ space for

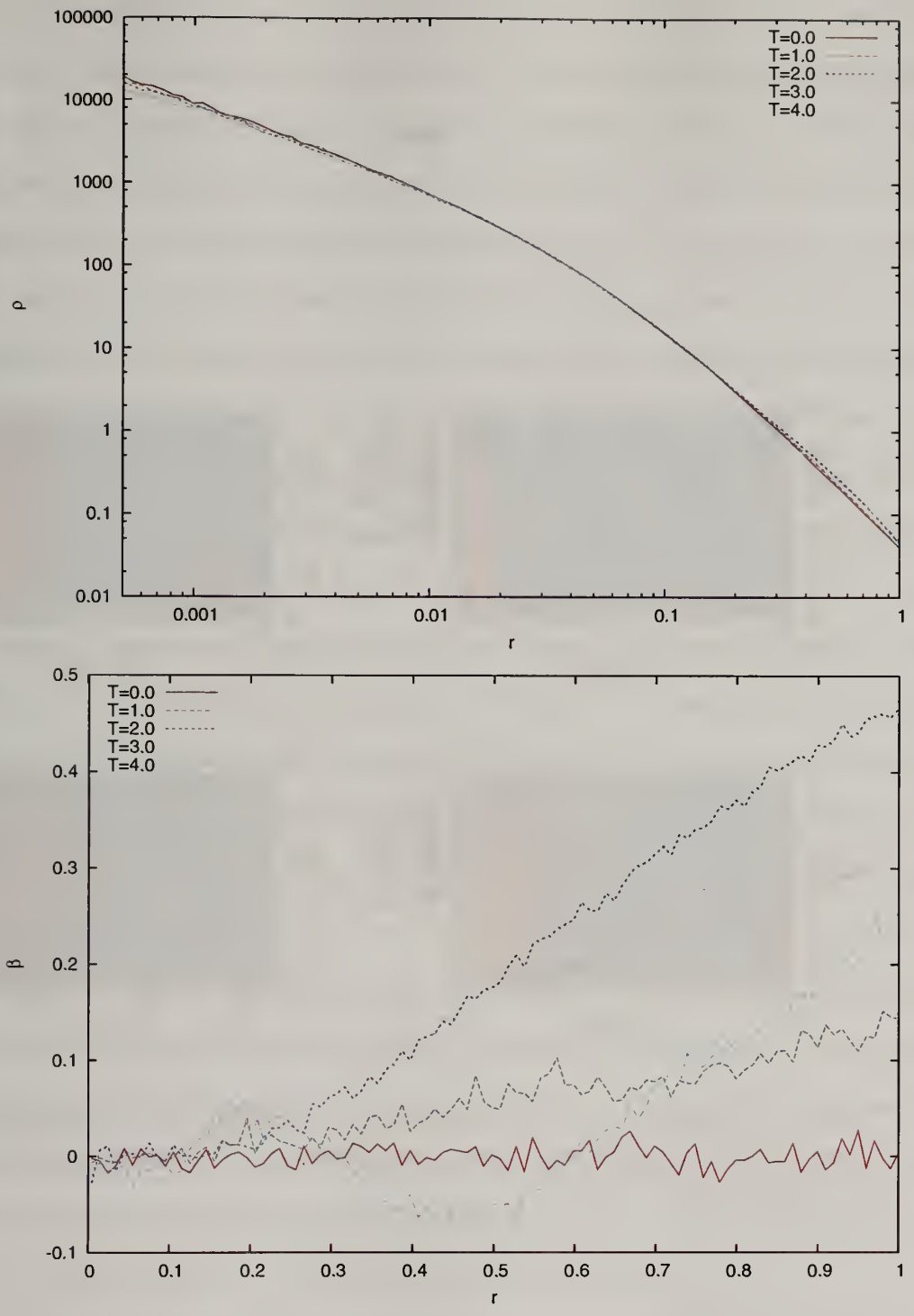

Figure 1.34 Density and velocity anisotropy profiles of the dark matter halo for the eccentric orbit simulation. *Top panel:* Density profiles of the dark matter halo for the eccentric orbit simulation. The density profiles do not show noticeable profile evolution. The center of the halo is the center of mass of 128 densest particles. *Bottom panel:* Velocity anisotropy profiles of the dark matter halo for the eccentric orbit simulation. Position and velocity of the halo center are those of the EJ center.

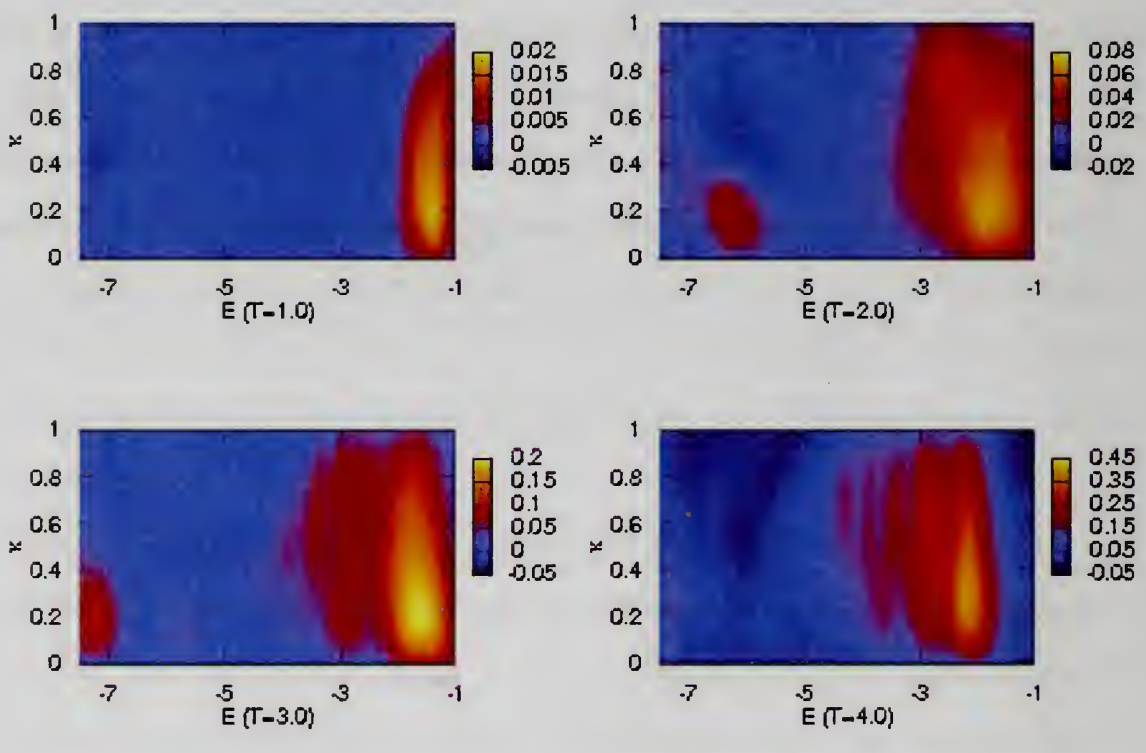

Figure 1.35 Distribution of the relative ΔL_z in phase space for the eccentric orbit simulation for four different times. The difference of L_z is measured value between a given time T and $T = 0.0$.

between $T = 0.0$ and given times. In general, similar features are found in the high resolution fiducial simulation in Figure 1.19. For example, the four gaining angular momentum regions is observed in Figure 1.19. However, there are a few interesting features which result from characteristics of an eccentric orbit. The distribution of Region D shows a multiple discrete resonances feature. In the eccentric orbit simulation, the satellite orbits between its pericenter and its apocenter a few times. From pericenter to apocenter, the satellite hardly loses its energy and angular momentum. As a result, the time evolution of the energy and angular momentum loss becomes discrete. In addition, the satellite frequency is increased with satellite decaying. This causes the resonance location moves to lower energy and leads to discrete location for energy and angular momentum deposition in Figure 1.19. Due to this discrete energy and angular momentum deposition, Region D shows a wrinkled feature at $T = 3.0$ and $T = 4.0$. We also find that the location of Region C moves up between apocenter and pericenter and temporally disappears between pericenter and apocenter. This phenomenon results from the same reason which causes the multiple discrete resonances feature in Region D: discrete energy and angular momentum deposition and increasing satellite frequency.

Figure 1.36 shows the density wakes for the eccentric orbit simulation. This density wake clearly shows the outer wake which trails the satellite. The inner wake is observed in the density wake at $T = 2.0$ and $T = 3.0$ but is rather unclear. This unclear inner wake may results from poor resolution. Although the satellite orbit is different with the fiducial simulation in Figure 1.36, the overall characteristic of its density wake is similar to that from the fiducial simulation.

The eccentric orbit simulation study shows that the main characteristics of the satellite decay and the dark matter halo response are similar to these from the fiducial simulation.

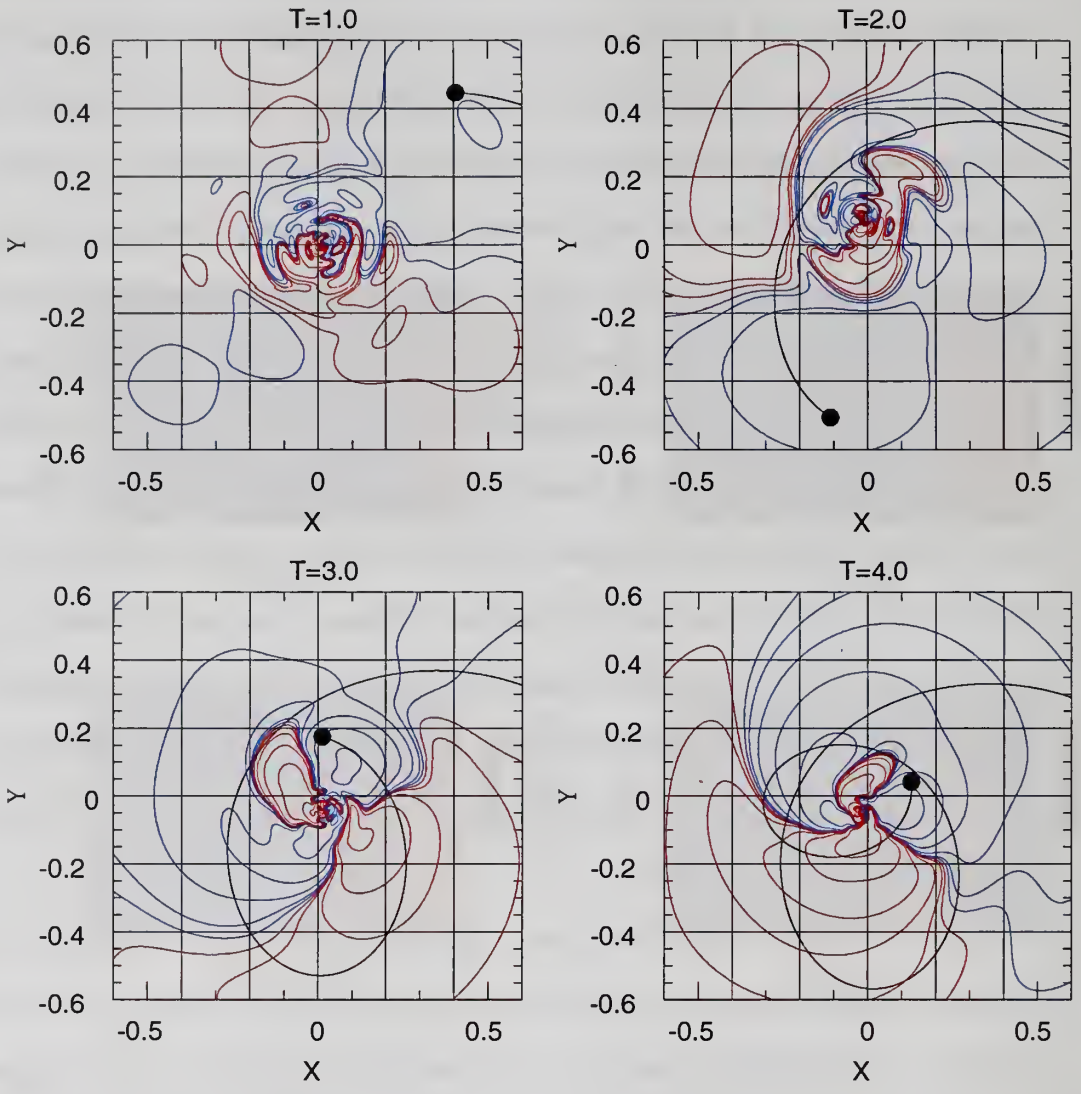

Figure 1.36 Density wakes due to the decaying satellite for the eccentric orbit simulation. The each panel shows a snapshot of a density wake at a given time. The origin of the plot is the center of dark matter halo mass. The blue contours represents overdensity wake and the red contours represents underdensity wake. The black line represents the satellite trajectory from $T = 0$ to the given time and black dot represents the current location of the satellite. The density wake includes l =1, 2, 3, and 4 contribution.

1.8 Discussion

The most important finding in this study is that resonant dynamics is responsible for satellite-halo interaction. Some resonance effects such as an accurate satellite decay rate and an inner wake only appear when a simulation satisfies particle number criteria. According to the particle number criteria, a huge number of halo particles is required to accurately reproduce these resonance effects. In particular, more than 10^8 single mass particles are required to resolve the -1:2:2 resonance in the satellite-halo interaction. We use a multi-mass particle scheme to fulfill these requirement with only 4×10^7 particles. However, this requirement excludes the small-scale noise criterion because our expansion algorithm is insensitive to does this noise. For an N-body algorithm with small-scale noise such as tree algorithm and direct summation algorithm, the required particle number dramatically increases. For our satellite-halo interaction case, more than 10^9 particles is required to resolve the -1:2:2 resonance and more than 10^8 particles is required to resolve the 1:2:2 resonance. Our multi-mass particle scheme can not be used in this situation because the 1:2:2 resonance is located in rather outer halo. Therefore, at least 10^8 single mass particles are required for halo to properly resolve the resonance effects. The highest resolution simulation today (Diemand et al., 2007) is about to reach this resolution for the Milky Way size halo, but true reproducibility of the resonance effects for this simulation has not been confirmed.

N-body simulations with a poor resolution fail to provide some important consequences from satellite-halo interaction. Section 1.5 shows that the orbital decay is weaker in the low resolution halo than the high resolution halo although the difference is not huge. This difference results from the resolution issue in resonant dynamics. In the satellite-halo interaction, a resonance coupling transfers the energy and angular momentum from a satellite to a halo. If some important resonances are not reproduced in a low resolution halo, the transfer is reduced and the orbital decay is lower.

Therefore, N-body simulations need to satisfy most of important resonance effects to correctly estimate a satellite decay rate.

A poorly resolved halo simulation fails to correctly reproduce dark matter halo response. Section 1.6 shows that the low resolution halos simulation can not reproduce the inner wake feature. This inner wake has an interesting astrophysical implication. The phase of the inner wake is about 90^o lagged behind both the satellite phase and the outer wake phase, and the location of the inner wake is well inside of the satellite position. The inner wake may excite inner galaxy evolution such as inner bar formation. The consequent galaxy evolution by this inner wake excitation will be a challenging task for future studies.

Although the low resolution halo simulation can not correctly reproduce some resonance effects, the satellite decay and the dark matter halo response are not significantly different than those of the high resolution simulation. Since many important resonances do not require high resolution (see Section 1.4), even the low resolution halo simulation can reproduce the dominant resonance effects. This explains why many published low resolution simulation provide acceptable results from intrinsical resonant interactions such as satellite decay (e.g. Binney & Tremaine, 1987, Chapter 7) and bar slow-down (Valenzuela & Klypin, 2003; Sellwood, 2006).

Our simulation results show that the evolution of dark matter halo density profiles is negligible. The amount of energy and angular momentum transfer is not large enough to drive significant density profile evolution. This weak evolution might be enhanced in a realistic situation by multiple sequential interactions. However current cold dark matter simulations suggest that there is large population of substructures (Ghigna et al., 1998; Klypin et al., 1999; Ghigna et al., 2000; De Lucia et al., 2004; Diemand et al., 2004; Gao et al., 2004). The large population of substructure can enhance the amount of energy and angular momentum transfer and may drive dark matter halo density evolution. Weinberg & Katz (2007a) claims that coherent sub-

structure noise does not destroy the resonance for a sufficiently small number of interactions. Therefore, the energy input from substructures can be additive. Unfortunately, analytical estimation of the resonance effects from multiple satellites is difficult so that an estimate of the resonant dynamics effects is difficult in this case. The speculation is that most predicted substructures are smaller than the satellite in our fiducial simulation, so that the amplitude of the resonance effects from single substructure may be weak and the required resolution may be excessive.

Beside the resonant dynamics effects in satellite-halo interaction, our study suggests other interesting physical processes: significant excursion of a halo center and stalling of satellite decay. These effects have not been considered in theoretical modeling and interpretations in galaxy formation and evolution. Since the magnitude of the cusp excursion is strikingly large, it is worth to try with other N-body algorithm such as tree code. If this phenomenon is also observed in different N-body simulations, these effects should be included in order to model accurate galaxy formation and evolution.

We find that the dark matter halo cusp excursion is up to 10% of a halo virial radius. The halo cusp motion shakes the central galaxy and can excite strong m=1 mode. These effects may also generate non-axisymmetry features of galaxies such as a disk warp (e.g. Briggs, 1990; Binney, 1992) and a lopsidedness (e.g. Baldwin et al., 1980; Haynes et al., 1998). These non-axisymmetry features are ubiquitously observed and there are many suggestions about their origin. The effects of the halo cusp motion should be considered one of the possible sources.

This halo cusp motion not only affects already cooled gas but also affects cooling gas. Galaxy formation models assume that gas in the dark matter halo cools and condenses in the center of halo (White & Rees, 1978). If the center of dark matter halo moves while the gas cools, the cooling time can be different than for a static halo.

Hence the simple cooling time calculation in the simple galaxy formation modeling may not precisely estimate the amount of cooled gas and star formation rate.

Section 1.5 shows that satellite decay stalls temporarily near the pericenter. The dark matter response as well as the energy and angular momentum transfer affects satellite decay and this stalling results from the effect of the halo response not from the losing resonance coupling. The satellite energy loss never stalls during the satellite decay stalls.

First, recent observation and theoretical studies claim that the lifetime of five globular clusters in the Fornax dwarf spheroidal is longer than expected decaying time if the Fornax has a cuspy dark matter halo (Mackey & Gilmore, 2003; Coleman et al., 2005; Goerdt et al., 2006). In order to solve this puzzle, Goerdt et al. (2006) and Read et al. (2006) suggested that the Fornax dwarf spheroidal has a core dark matter halo and this halo core reduces the decay rate of their globular clusters. According to our finding, the dark matter halo structure evolution influence on an orbital decay can be another suggestion. If the Fornax dark matter halo is not relaxed so that its center moves large distance, the cluster's decay rate can be significantly different from the simple estimation using the standard Chandrasekhar dynamical friction. In order to verify this scenario, we need implement a high resolution simulation which also needs to well reproduce the structure of the Fornax dark matter halo.

Second, galactic bar evolution simulations sometimes show that bar slow-down stalls. Some authors (e.g. Sellwood & Debattista, 2006) suggests that this stalling may result from losing resonance coupling. However, since the responsible physical process for bar slow-down is the same as that for satellite decay and the halo center is not fixed in both cases, stalling the bar slow-down may result from the effect of dark matter halo structure evolution. Moreover, a cuspy halo consists with particles from large frequency range so that losing the resonance coupling hardly happens.

Therefore, detailed investigation, which includes the effects of the dark matter halo structure evolution, is required for this problem.

1.9 Summary

In this study, we investigate detailed physical processes responsible for satellite-dark matter halo interaction using perturbation theory calculations and high resolution N-body simulations. We find following interesting consequences of this interaction:

- resonant dynamics dominates the satellite-halo interaction. A large number of halo particles are often required to correctly reproduce important low order resonance. In order to verify the reproducibility of resonance effects, we compare results from different resolution simulations. The comparison study demonstrates that a low resolution simulation fails to reproduce some resonance effects while a high resolution simulation can reproduce these effects.

- The satellite decay rate in simulations requires the resolution of the resonance effects. If a simulation can not reproduce resonance effects correctly, it can underestimate the satellite decay rate due to missing resonance contribution to energy and angular momentum transfer.

- During the satellite decay, a dark matter halo cusp excurses a considerable distance from a halo COM. The separation between the halo cusp and the halo COM is so significant that it can not be ignored in mass modeling of the galaxies. This significant halo cusp excursion can affect galaxy formation and evolution.

- Satellite decay rate is affected by not only its energy and angular momentum loss but also the dark matter halo response. As a result, we sometimes observe that satellite decay stalls although the satellite still loses its energy and angular momentum.

- A satellite decay hardly drives dark matter halo density profile evolution because the amount of energy and angular momentum transfer from a satellite to a halo is not large enough to drive the halo evolution.

- A dark matter halo response is subject to the resolution of the resonance effects. According to a high resolution simulation, we can observe both an inner density wake and an outer density wake. An inner density wake is excited around halo cusp which is located way inside from the current satellite location. This inner density wake only appears in a high resolution simulation. An outer density wake almost trails the satellite position but it is a little lagging behind and this wake is responsible for satellite decay.

- Although there are different as in the response at small scales between the high resolution simulation and the low resolution simulation, most of strong resonances do not require very high resolution, so that the overall torque is reproduce in both simulations.

- We investigate the satellite decay and the dark matter halo response of the eccentric orbit satellite simulation and find that the overall results are similar with the circular orbit simulation results.

CHAPTER 2

THE DYNAMICS OF SATELLITE DISRUPTIONS IN COLD DARK MATTER HALOS

2.1 Introduction

Physical processes affect satellite galaxy evolution in their host halo is an important component of galaxy formation in the cold dark matter (CDM) cosmology. According to the CDM cosmogony, galaxies are built up from the assembly of small structures. This assembly always incorporates the process of a satellite galaxy merging into its host galaxy. Moreover, recent CDM cosmological simulations advocate the existence of a large number of *subhalos* (Ghigna et al., 1998; Klypin et al., 1999). Under these circumstances, how these subhalos interact with their host halo and other subhalos, and what subsequent subhalo evolution owes to these interactions are important questions in understanding dark matter halo evolution. Consequently, understanding the detailed physical processes of satellite evolution in its host halo are key ingredients to understanding galaxy formation in the CDM cosmology.

There are several basic questions about satellite halo evolution. First, what parts in the satellite are already stripped, and what parts remain? Second, what is the rate of satellite halo disruption? Third, how does a satellite's internal structure evolve? These are all important issues for understanding galaxy formation and evolution. In the process of a satellite galaxy merger, the stars and gas of the satellite galaxy are stripped and become halo stars and halo gas (Quilis et al., 2000; Bullock et al., 2001, e.g.). The interaction between the satellite galaxy and external components during the course of the merger results in satellite galaxy evolution (Moore et al., 1996a,

e.g.). The remaining components of the satellite galaxy merge with the host galaxy and this merging helps governs the growth of the host galaxy (Murali et al., 2002, e.g.).

Unfortunately, current cosmological simulations can only provide statistical properties of subhalos since even in the highest resolution cosmological simulations (Ghigna et al., 2000; De Lucia et al., 2004; Diemand et al., 2004; Gao et al., 2004; Oguri & Lee, 2004). Owing to limited resolution, the detailed physical processes of individual subhalo evolution have not been properly studied. To investigate the physical processes in detail, we perform high resolution idealized simulations with cosmologically motivated initial conditions instead using cosmological simulations. In these idealized simulations, a live satellite orbits in a static host halo. This setup may be too simplified to reproduce the real satellite evolution history, but it makes it possible to investigate the detailed physical processes of satellite evolution in the host halo correctly.

When a time-dependent force acts on a bounded system such as a galaxy and a dark matter halo, resonance interactions play an important role in the system evolution. Resonant interactions between a satellite galaxy and its host halo should be carefully investigated to understand the physical processes responsible for satellite evolution. Recent studies of resonant dynamics in galaxy evolution claim that high resolution simulations are required to accurately reproduce resonance effects (Weinberg & Katz, 2007a,b) and Weinberg & Katz (2007a) provide particle number guidelines. Our idealized high resolution simulations, which are designed to satisfy these particle number guideline, allow us to investigate the role of resonant dynamics in satellite disruptions.

Resonant interactions occur through the resonant coupling of a time-dependent perturbing force with orbits in the system. The frequency of the time-dependent perturbing force characterizes the resonant interaction. For a satellite orbiting in its

host halo, the satellite's orbital frequency is the frequency of the time-dependent force. A satellite orbit in general is an eccentric orbit, which can be decomposed a radial orbit and a circular orbit. The physics of eccentric orbit resonant dynamics is a very complicated process. Fortunately, we can arbitrarily characterize the total eccentric orbit resonant effects by separating it into two distinct resonant effects: a resonant shock and resonant torque. A resonant shock represents coupling with the radial orbital frequency and resonant torque represents coupling with the azimuthal orbital frequency. Hereafter, we investigate the resonant effects with this characterization.

In satellite evolution, the two resonant effects mostly appear in two different situations. The resonant shock effect is related to the gravitational shock. During the gravitational shock, some orbits in the satellite gain energy through resonant coupling even though the dynamical time of the orbit is much shorter than the time scale of the gravitational shock. The resonant torque relates to the azimuthal orbit. During the satellite's orbit with azimuthal angle, some orbits in the satellite get torqued through resonant coupling with the rotating external potential. For resonant torque, the magnitude of the external potential does not have to change; only a change in the direction of the external potential can produce an effect. The resonant shock has been considered and is included in the impulsive approximation as an adiabatic correction. In contrast, the resonant torque has not been seriously considered in satellite evolution studies. The resonant torque, however, has been extensively investigated in the dynamics of barred galaxies. In this study, we will carefully investigate the resonant effects on satellite evolution using this separation.

Globular cluster evolution in a host galaxy is a well established field in astrophysics (e.g. Spitzer, 1987; Chernoff & Weinberg, 1990). During the life of a globular cluster, it has experienced both tidal truncation and heating by both compressive gravitational shocks and tidal shocks. Globular cluster evolution studies provide simple analytic formulas such as the impulse approximation, which can estimate the effect

of each individual process. Because satellite halo evolution in a host halo is analogous to globular cluster evolution in a host galaxy, many galaxy formation studies employ simple analytic formulas taken from globular cluster evolution studies to estimate satellite galaxy evolution. However, there are several distinctions between two phenomena. First, satellite galaxy evolution is governed by collisionless dynamics, while globular cluster evolution is governed by collisional dynamics. Second, the assumed the external potential for satellite galaxy evolution is a host dark matter halo, while that for globular cluster evolution is either a disk galaxy or a spherical galaxy. Third, models of satellite galaxy halos are different than globular cluster models in general. Therefore, it is necessary to examine how the consequent evolution of satellite galaxies is different from that of globular clusters owing to theese distinct properties of satellite galaxies. Our high resolution, idealized simulations are able to handle these differences.

In this study, we present numerical simulation results of satellite galaxy disruption. In Section 2.2, we present an overview of the numerical techniques used in this study: the N-body simulation code, our way of generating initial conditions, and a relevant perturbation theory. In Section 2.3, we present the results of a circular orbit simulation. We show that the resonant torque effect results in significant satellite mass loss. In Section 2.4, we present the results of eccentric orbit simulations. We show that satellite heating by compressive gravitational shocks at pericenter, which also includes internal structure evolution, is the dominant process responsible for disrupting the satellite. In Section 2.5, we show that the process of satellite stripping is tan outside-in process in satellite energy space. Using this finding, we suggest an explanation for the missing LMC stellar stream. In Section 2.6, we provide an improved analytic estimation for satellite mass loss, and in Section 2.7 we summarize our study.

2.2 Numerical methods

The objective of our study is to understand the physical processes of satellite evolution in detail. To this aim, we use high resolution idealized simulations with cosmologically motivated initial conditions.

To evolve our N-body simulations, we use the 3-dimensional self-consistent field code (SCF, also known as an expansion code; Clutton-Brock, 1972, 1973; Hernquist & Ostriker, 1992; Weinberg, 1999). The expansion code determines bi-orthogonal basis sets of density-potential pairs and computes the gravitational potential of the system from these basis sets. The expansion code is an attractive gravitational potential solver for two reasons: First, the expansions can be chosen to follow the structure over an interesting range of scales and simultaneously suppresses small-scale noise. In contrast, the noise from two-body scattering can arise at all scales in direct-summation, tree, and mesh based codes. Small-scale noise can give rise to diffusion in conserved quantities, which can then lead to unphysical outcomes particularly for studies of long-term galaxy evolution (Weinberg & Katz, 2007a,b). Second, the expansion code is computationally efficient; the computational time only increases linearly with particle number. Hence, the expansion code permits the use of a much larger number of particles than most other codes for the same computational cost.

Unfortunately, the expansion code is not adaptive. The basis function pair should resemble a galaxy as much as possible. Otherwise, the expansion code requires a large number of basis function sets, which introduces small-scale noise and results in a greater computational overhead. This restriction has been alleviated by recent improvements (Weinberg, 1999; Choi et al., 2007). First, employing a numerical solution of the Sturm-Liouville equation, the initial galaxy model can be used as the zero-order basis function for the expansion code. Using this scheme, the expansion code requires only a few basis function sets to accurately compute the potential. Second, the center of expansion, which we assume to be the energy minimum, can be

traced during the course of a simulation. This centering scheme provides an accurate center for the expansion that is a critical issue in the potential calculation of the expansion code. Third, to reduce truncation error, the simulation separately tracks the motion relative to the satellite's center and the motion of the satellite center itself. With these improvements, the expansion simulations are now able to achieve a high enough resolution and low enough noise to properly investigate the detailed physical processes important for satellite disruption.

An important ingredient of our study is that we use cosmologically motivated initial conditions. All the halo models used in our simulations are based on the universal CDM halo (Navarro et al., 1997, hereafter NFW), $\rho(r) \propto r^{-1}(r + r_s)^{-2}$, where r_s is a scale length characterized by the concentration parameter $c = R_{vir}/r_s$ and R_{vir} is the virial radius of the halo. We represent the host halo potential by a concentration c=15, static NFW halo. Hence, our simulations ignore the effects of dynamical friction and the subsequent reaction of the host halo. Obviously, this is not realistic but since the satellite masses of interest are often much smaller than that of the host halo, the consequences are minor. Moreover, the prime motivation of our study is to understand the physical processes of satellite disruption and not the evolutionary history of the satellite.

Initially, we represent a satellite halo is by a c=15, live NFW halo. The NFW profile extends out to infinity but a real satellite has a finite size, which is determined by the host halo tidal field. The host halo tidal field will affect a satellite halo even before the satellite halo passes within the host halo's virial radius. As a result, it is computationally expensive to simulate the entire evolution of a satellite. Since the objective of our study is only to understand the physical processes responsible for satellite disruption, having a simulation of the entire satellite evolution is not necessary. To get around this difficulty, we place the satellite in the host halo on

the desired orbit to start and include the host halo tidal field when we generate a satellite's initial conditions.

The details of the procedure that we use to generate a satellite's initial conditions are as follows (see Figure 2.1). We start from an initial NFW satellite halo model. We characterize the satellite's size by the rotation velocity $V = \sqrt{M_{vir}/R_{vir}}$, since maximum rotation velocity is a better measure of a satellite's size than mass owing to the continuous mass loss that makes satellite mass an inexact measure. We set the initial satellite halo model such that the density of a satellite model $\rho(R_{sat,vir}) = \rho(R_{host,vir})$ and the rotation velocity of the satellite $V_{sat} = \frac{1}{12}V_{host}$. We then determine the truncation radius at a given satellite location in the host halo (see Figure 2.1a). We assume the satellites in our simulations are on circular orbits with $R = 0.4R_{host,vir}$ when determining the truncation radius. We call this fixed distance the tidal distance. As shown in Figure 2.1a, the truncated model is identical to the initial NFW model but is chopped at the truncation radius. After truncating the initial satellite model at this radius, we perform an Eddington inversion to compute the distribution function (Binney & Tremaine, 1987, Chapter 4, see Figure 2.1b). We calculate the final satellite density profile by integrating the distribution function over velocity. In contrast with the truncated model, the final satellite model does not show a sudden drop at the outer edge of the profile. Owing to this smooth outer profile, the final satellite model is closer to equilibrium than the truncated model. We use this satellite model as our initial satellite halo model. Figure 2.1d shows the circular velocity profiles of the initial and final satellite model. Even though the final satellite model is considerably truncated compared to the initial model, the maximum circular velocities of both models are more less the same. It confirms that the maximum circular velocity is a good choice to characterize satellite size. We generate the satellite halo realization using acceptance-rejection method. Our procedure allows us to generate equilibrium

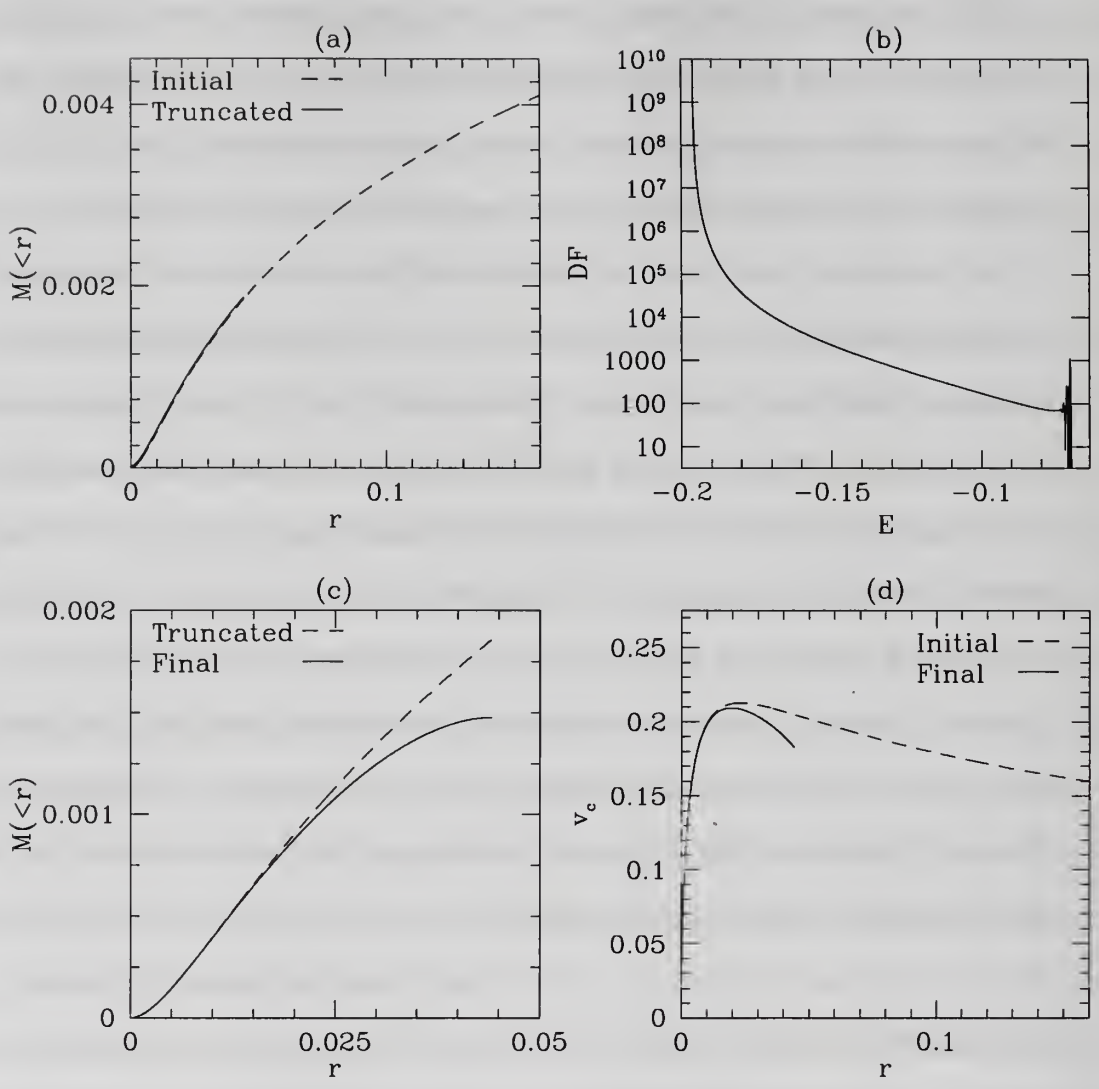

Figure 2.1 The effect of our truncation procedure on a satellite's initial NFW profile. (a) The enclosed mass profiles of the initial NFW model and the truncated model. (b) The distribution function versus energy, computed the Eddington inversion. (c) The enclosed mass profiles of the truncated model and the final satellite model. (d) The circular velocity profiles of the initial NFW model and the final satellite model. The truncation radius in this figure is x_e when a satellite is on a circular orbit at $R = 0.4R_{vir}$ We use *system* units unless otherwise specified: $G = 1$, $M_{vir,host} = 1$, and $R_{vir,host} = 1$.

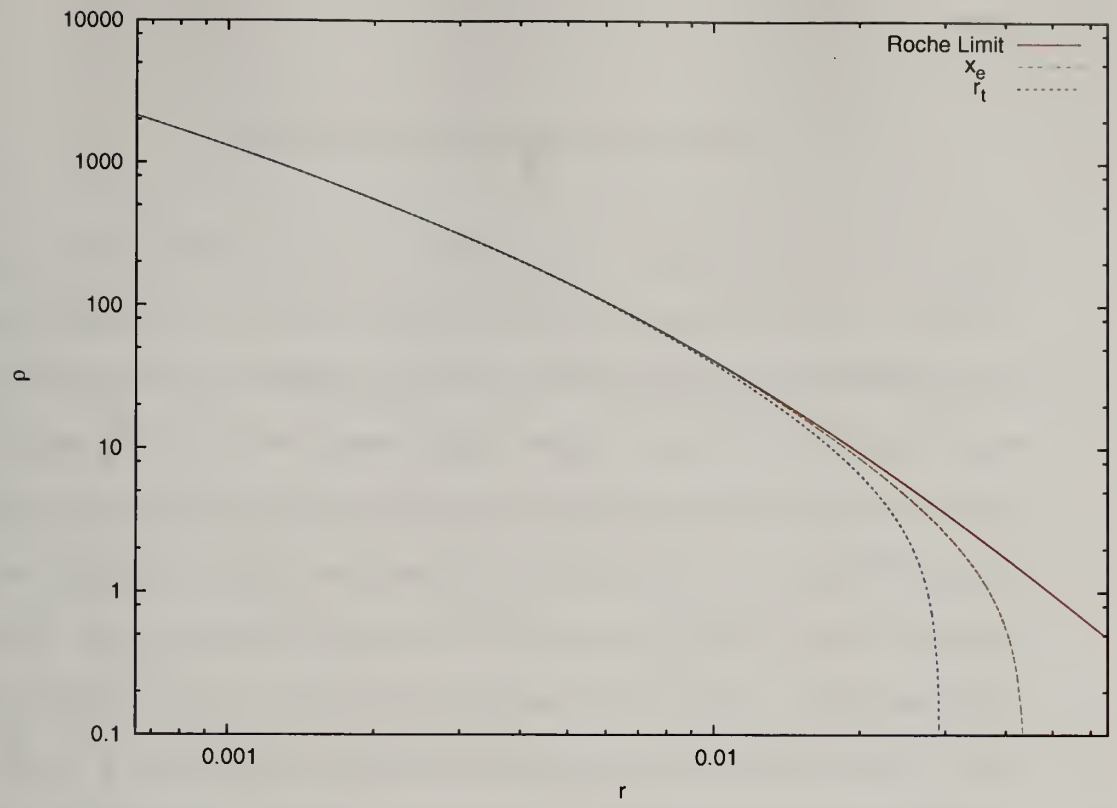

Figure 2.2 Density profiles for three satellite initial conditions, truncated at three different radii. The red line is for Roche limit truncation, the green line for x_e truncation, and the blue line for r_t truncation.

and stable satellite halos. In our simulations, all the satellites are assumed to have an isotropic velocity distribution and are made of 10^6 equal-mass particles.

One can think of three different truncation radii: the Roche limit, x_e, and the tidal cut-off radius (r_t) (Spitzer, 1987, Chapter 5). The Roche limit is the radius where the satellite density and the host halo density are the same. [1] x_e is the radius of the critical potential, where the derivative of the total potential $d\Phi_{total} = d\Phi_{sat} + d\Phi_{host} = 0$. $d\Phi_{sat}$ is easily computed from the initial satellite model. We assume that the satellite is much smaller than host halo and $d\Phi_{host}$ can be approximated as function of satellite

[1]This naming possibly misleads readers because the Roche limit and x_e are based on the same physical principle. However, some researchers have defined the Roche limit to be the radius where the satellite density and the host halo density are same. Here, we adopt the equal density radius as a working definition of the Roche limit.

radius:

$$d\Phi_{host}(r) = (4\pi\rho_{host}(R) - 3\Omega^2(R))r \tag{2.1}$$

where R is the tidal distance, r is the distance from the satellite's center, $\rho_{host}(R)$ is the density of the host halo at the tidal distance, and $\Omega^2(R)$ is the angular frequency of the satellite at the tidal distance, where we assumed that the satellite is on a circular orbit. The tidal cut-off is the radius where $r_t = 2/3x_e$. The satellite radius of the critical potential perpendicular to the direction toward the host halo center is $2/3$ of x_e. Therefore, $r_t = 2/3x_e$ implies the maximum spherical satellite halo radius, so that the satellite halo does not exceed the critical potential in any direction. As we discuss below, x_e is the most appropriate choice for satellite truncation. The density profiles of the truncated satellite halo models are presented in Figure 2.2. We apply Eddington inversion to the satellite halo models truncated at x_e and r_t, but do not apply it to the satellite halo model truncated at the Roche limit. Because Eddington inversion severely reduces the outer density of the halo, the Roche limit would no longer be an equal density spot between the satellite and the host halo if the Eddington inversion were applied. Figure 2.2 shows that at a given tidal distance $(0.4R_{host,vir})$, the satellite truncated at the Roche limit is the largest and the satellite truncated at the r_t is the smallest.

Before moving to our investigation of the physical processes affecting satellite disruption, we had better choose the most appropriate truncation radius. Figure 2.3 shows the mass loss from circular orbit simulations of all three satellites (see Section 2.3 for a detailed discussion); all three satellites show continuous mass loss. The amount of mass loss correlates with the satellite size: the satellite truncated at the Roche limit loses the largest mass fraction and the satellite truncated at r_t loses the least. All three satellite models lose mass so that the degree of adjustment to the host halo cannot help determine the most appropriate model. Therefore, we make

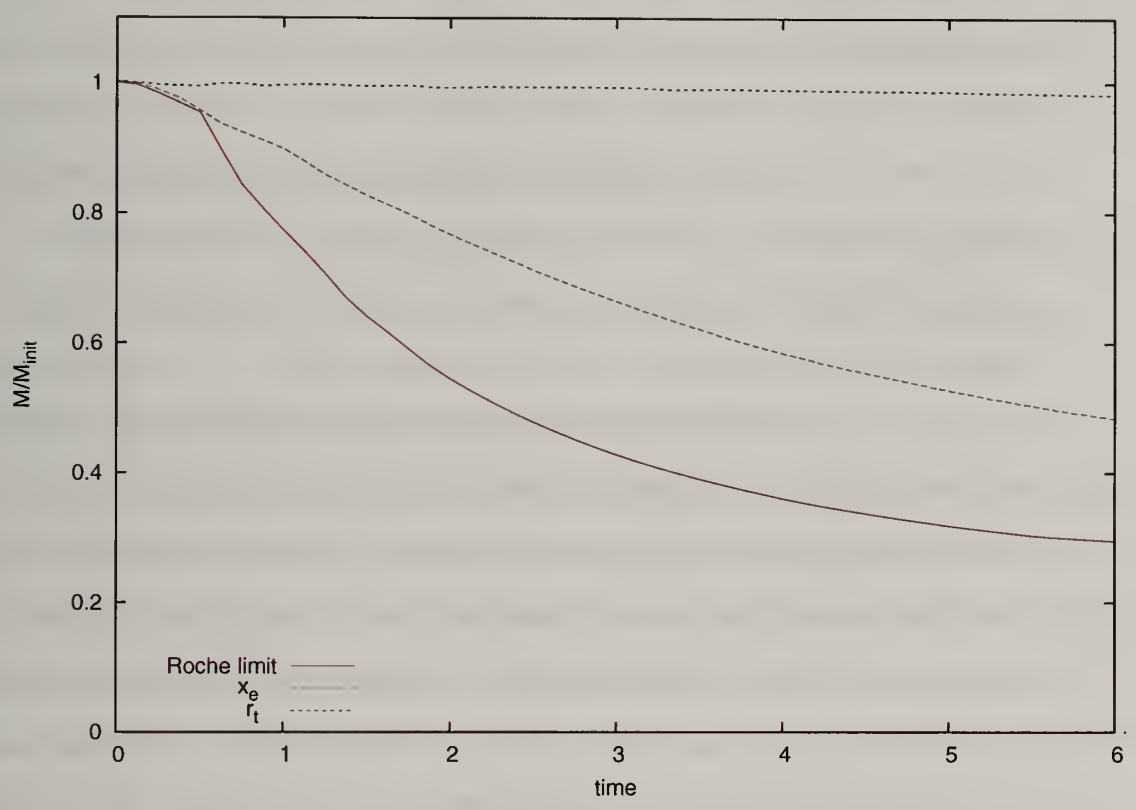

Figure 2.3 The fraction of remaining satellite mass as function of time for satellites on a circular orbit. Red, green, and blue lines are the remaining mass fractions of the satellites which are truncated at the Roche limit, x_e, and r_t. The figure shows that the satellite truncated at Roche limit loses the most mass and the satellite truncated at r_t loses the least mass but all three simulations show continuous mass loss.

the determination by considering which truncation radius makes the most sense on physical grounds. We choose x_e because it is the transition point where satellite particles on a circular orbit become unbound, and hence this radius represents that of a bound system. The Roche limit for an NFW halo overestimates the satellite size. Where the satellite density matches the host halo density, the host halo potential already dominates the potential for a particle at radius. In contrast, the r_t truncation underestimates the satellite size. This truncation radius is a sensible choice for globular clusters, which have already orbited many times around a galaxy and are already severely truncated. However, satellite halos only make a few complete orbits. Hereafter, we restrict our study to satellite halos that are truncated at x_e.

As mentioned in Section 2.1, resonant interactions are expected to be one of the dominant physical processes to heat and disrupt satellites. To accurately reproduce the resonant interaction, N-body simulations need to satisfy several numerical criteria. Weinberg & Katz (2007a) suggested concrete requirements for these criteria. First, a sufficient number of particles are required to cover the phase space near resonance (hereafter call the coverage criterion). Second, a sufficient number of particles are required to reduce artificial diffusion. Artificial diffusion can come from both gravitational forces of individual particles (hereafter call the small-scale noise criterion) and potential fluctuation caused by Poisson noise (hereafter call the large-scale noise criterion). Besides these particle number criteria, the potential solver must also be able to resolve the scale of the resonant potential and the realized phase space distribution must cover this region. In our study, we will verify that our simulations satisfy all these criteria.

Although a simulation can produce resonant interactions, it is hard to provide detailed accounting of the physical properties of individual resonances. However, the resonant interaction effects can be investigated using perturbation theory calculations. In this study, we use a numerical perturbation theory calculation as in Weinberg &

Katz (2007a) to investigate the resonant interaction effects. The numerical perturbation calculation performs a direct integration of the perturbed Hamiltonian and evolves the halo realization. Since this perturbation calculation uses the same satellite halo realization, comparison with the N-body simulation result is straightforward. A comparison between the results of the N-body simulation and those of the numerical perturbation theory calculation provides us with concrete evidence for the existence of resonant dynamics and a definite understanding of its role in satellite evolution.

2.3 Satellite disruption on circular orbit

To investigate the resonant torque effect, we simulate a satellite on a circular orbit, which isolated this since the satellite does not experience a gravitational shock.

2.3.1 Investigation of the resonance torque effect

Figure 2.3 shows the mass loss history of satellites on a circular orbit. An important fact demonstrated in Figure 2.3 is that satellites continuously lose mass. Continuous mass loss from truncated satellite halos suggests that it results from satellite heating and not from a transient initial adjustment of the satellite halo to its host halo potential. If a transient adjustment were the cause of the mass loss, the mass loss should lessen and eventually stop altogether as the satellite adjusts to the halo potential. But in fact the truncated satellites lose their mass continuously and have lost a significant fraction of their original mass. In a circular orbit simulation, the magnitude of the external potential does not vary, and therefore, there is no gravitational shock. The only mechanism that can disrupt a satellite under these circumstances is the resonant torque.

The dynamics of the resonant torque is similar to the dynamics of the bar-halo interaction. Owing to the coupling with the time-dependent perturbation, particular

orbits whose frequency is nearly commensurate with the perturber's frequency get torque:

$$l_1\Omega_1 + l_2\Omega_2 = l_3\Omega_{pert} \tag{2.2}$$

where Ω_1 and Ω_2 are the radial frequency and azimuthal frequency of a satellite orbit, Ω_{pert} is the perturber's frequency, and l_1, l_2, and l_3 are integers. The orbits which satisfy Equation 2.2 are called resonant orbits and are located in a particular place in phase space. The angular momentum transfer by the resonant interactions follow a second-order, time-dependent perturbation calculation (Weinberg, 2004; Weinberg & Katz, 2007a,b). Although we characterize the coupled orbit using a rather simple relationship, the situation becomes complicated for a real astronomical system. Owing to the finite age of the galaxy and the time-dependence of the perturbation, the frequency spectrum becomes broader. In addition, some resonances need a longer time period than the galaxy lifetime to convegee into the time-asymptotic limit and show a transient effect in which the first-order change plays an important role. More detailed discussion of the resonant dynamics is presented in Section 1.3.

The resonant torque heats the satellite, reduces the satellite binding energy, and enhances the satellite mass loss. Although particular resonance orbits get torque, the pattern of satellite mass loss is not confined to the resonance orbits. Since a satellite is a self-gravitational system, the torque reduces the entire satellite binding energy. In short, the consequences of torque by resonance interactions enhance satellite mass loss. The pattern of satellite mass loss in general will be discussed in Section 2.5.

Perturbation theory calculations can provide a clear understanding of resonant dynamics. Here we use numerical perturbation theory calculation to investigate the detailed mechanism resemble for the resonant torque effect. To do this calculation, we invert the problem. In the simulation, the satellite is on a circular orbit in its host halo, but in the perturbation calculation, the host halo potential is represented by

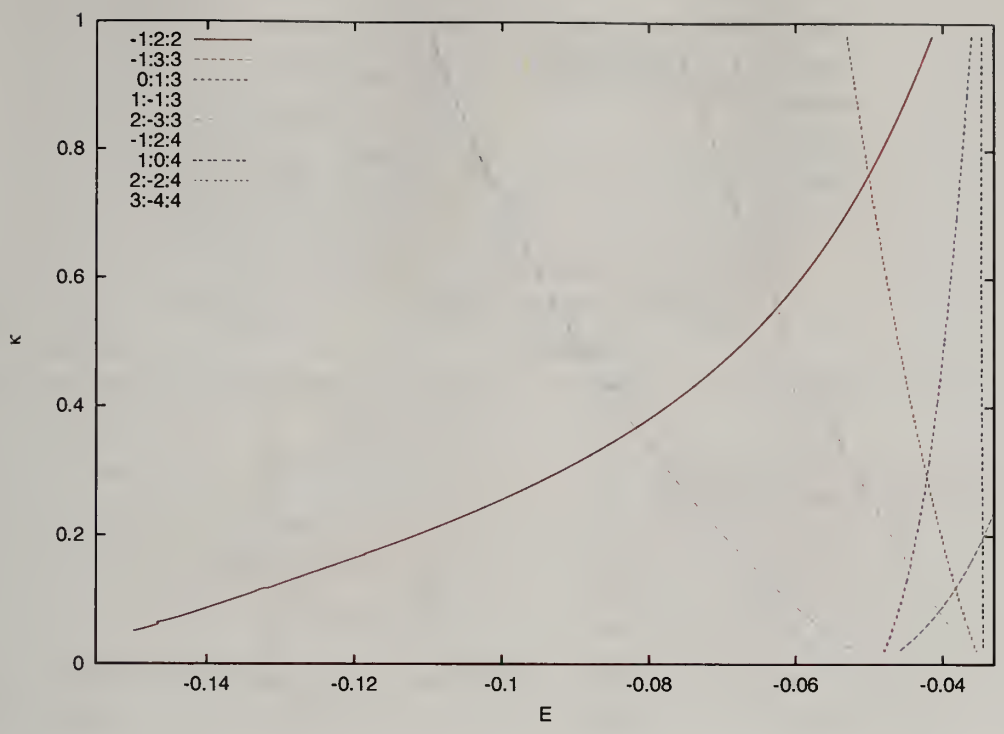

Figure 2.4 Resonances in the satellite owing to its orbit in the host halo. The locations of resonances are shown in energy-angular momentum space for the satellite. We examine low-order resonances: $-10 \leq l_1 \leq 10$ and $l = 1, 2, 3, 4$ (see text for details).

an orbiting perturber around a stationary satellite with the distance of the perturber from the satellite the same as the distance between the satellite and the host halo center in the simulation. The mass of the perturber is the enclosed mass of the host halo inside the satellite orbit in the simulation, and the perturber's frequency is the same as the satellite's frequency in the simulation. Using this procedure, we can make the force, which acts on the particles in the satellite, the same for both the simulation and the perturbation calculation.

Using this perturbation theory calculation, we investigate the resonant torque with the following three steps: (1) we find the resonances that are located within the satellite, (2) we estimate the particle number requirements for a given resonance using the criteria from Weinberg & Katz (2007a), and (3) we compute the individual resonant effects using the numerical perturbation theory calculation and compare them to the simulations.

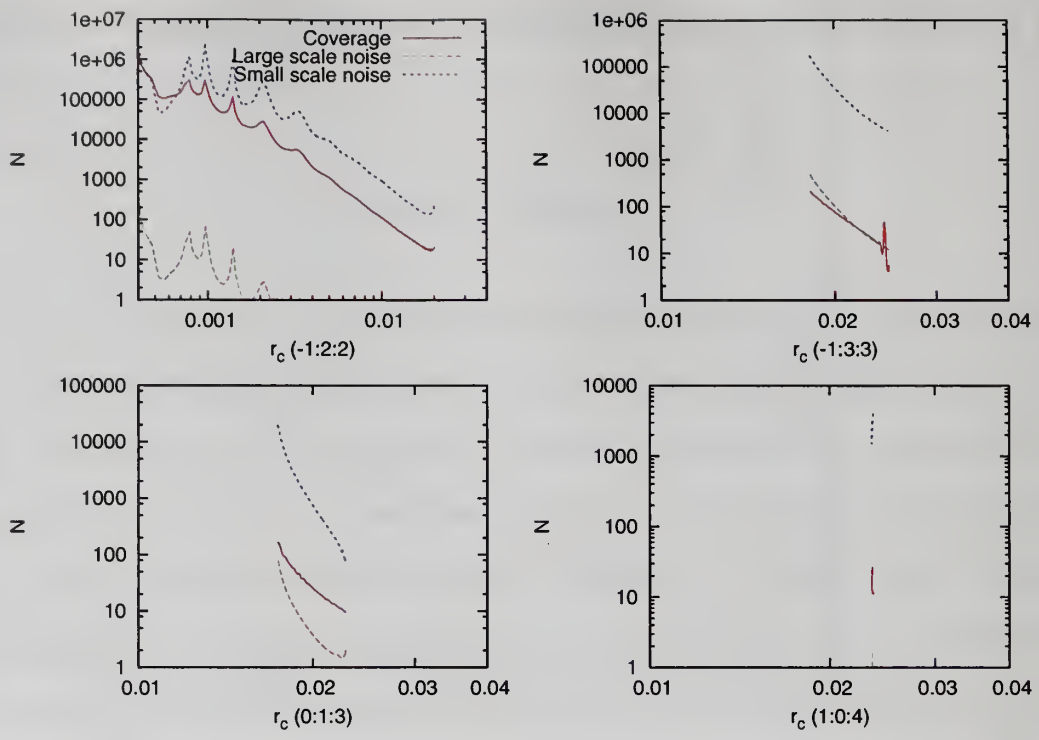

Figure 2.5 Particle number requirements within the virial radius for the -1:2:2, -1:3:3, 0:1:3, and 1:0:4 resonances. These four resonances are the most dominant resonances for the circular orbit satellite. Each panel shows three particle number requirements in Weinberg & Katz (2007a). The figures show that our 10^6 particle halo simulation is sufficient studying for these resonances.

Figure 2.4 shows the locations of the resonances in the satellite phase space. The phase space location is represented by energy (E) and normalized angular momentum[2] (κ). The range of resonances we examine is $-10 \leq l_1 \leq 10$ and $l = 1, 2, 3, 4$. Owing to symmetry, l_2 and l_3 should be equal or less than l [3]. Since l_2 and l_3 are indices of the azimuthal expansion in spherical harmonics for the halo and perturber respectively, l_2 and l_3 should have the same parity as l (Tremaine & Weinberg, 1984). According to Figure 2.4, nine resonances are located within the satellite.

[2] $\kappa = J/J_{max}(E)$ where J is a particle's angular momentum and $J_{max}(E)$ is the maximum angular momentum at given energy

[3] l is the number of orders in the expansion of spherical harmonics.

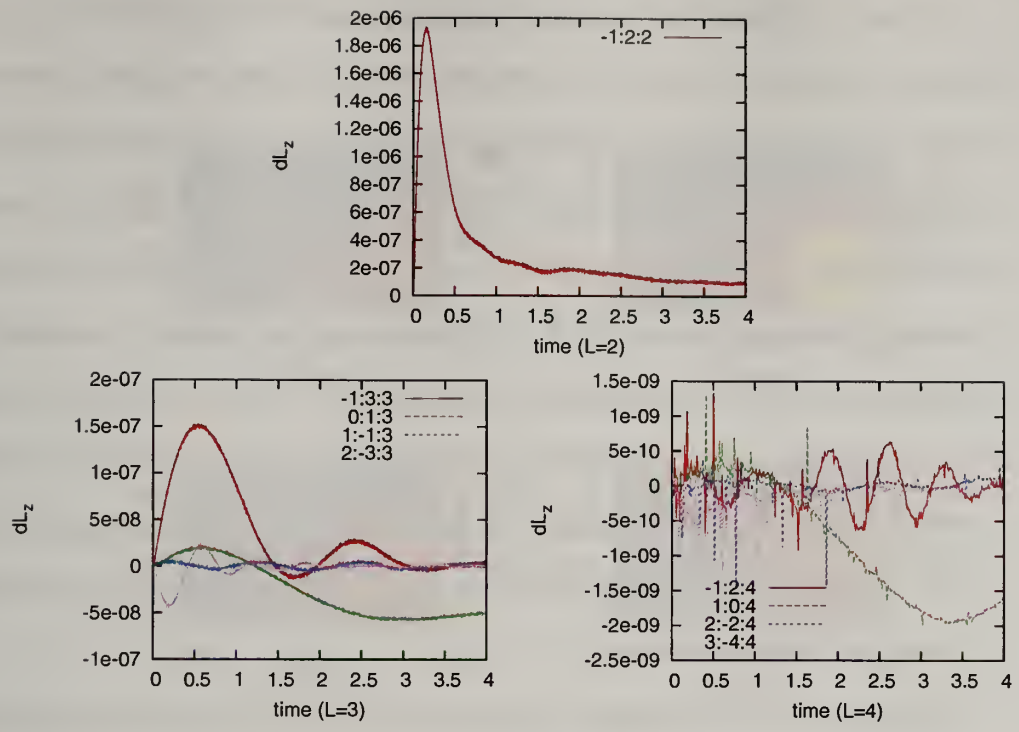

Figure 2.6 The amount of angular momentum transferred from the perturber to the satellite as function of time. The figures show that the amount of angular momentum transferred by the -1:2:2 resonance is the largest.

The required particle number for four resonances are presented in Figure 2.5. There are three particle number criteria for each resonance: coverage, small-scale noise, and large-scale noise (Weinberg & Katz, 2007a). Because we use an expansion code, the small-scale noise criterion is not applicable to our simulations. According to this estimation, more than 10^5 halo particles within the virial radius are required to correctly reproduce the -1:2:2 resonance, which requires highest resolution. Hence, our 10^6 equal-mass particle halo simulation satisfies all the criteria (see Figure 2.5) for all the important resonances. If the N-body simulations were to suffer from small-scale noise, an order of magnitude larger particle number would be required for these resonances. N-body simulations which use direct-summation, tree, or mesh based codes are compromised by small-scale noise and would require this lager particle number. Note that these four resonances are the four strongest resonances, as we will show next.

Figure 2.6 shows the amount of angular momentum deposited by an orbiting perturber. The angular momentum deposition is calculated using the numerical perturbation theory calculation. According to this calculation, the most significant angular momentum deposit is by the -1:2:2 resonance. The -1:3:3 and 0:1:3 resonances are the strongest resonances among the $l_3 = 3$ resonances, and the 1:0:4 resonance is the strongest resonance among the $l_3 = 4$ resonances. The amount of angular momentum deposited by the -1:2:2 resonance is more than an order of magnitude larger than the amount of angular momentum deposited by any of the $l_3 = 3$ resonances and three orders of magnitude larger than the amount of angular momentum deposited by any of the $l_3 = 4$ resonances. Hence, the -1:2:2 resonance plays the dominant role in resonant satellite torque.

The location of the angular momentum transfer owing to resonant interactions in phase space is easily shown. Figure 2.7 plots the distribution of the relative change of L_z in phase space of different time from both the N-body simulation and the numerical perturbation theory calculation. Relative ΔL_z is ΔL_z respected to the total angular momentum for a given energy bin. Due to the normalized angular momentum (κ) is used as the phase space coordinate, the absolute value of L for different energy bin is different; $L_{max}(E)$ increases with energy. As a result, total angular momentum itself is small in low energy so that a simple demonstration of the absolute ΔL_z distribution possibly smears out ΔL_z features in low energy. By normalizing the total angular momentum at a given energy bin, the relative ΔL_z distribution enhances ΔL_z features at low energy. Each panel shows relative the ΔL_z over a given time span. Both the phase space location and magnitude of the angular momentum change from the simulation agrees well with the numerical perturbation calculation. In addition, the time evolution of the angular momentum exchange is also similar in both cases. Together this provides strong evidence that torque by resonant interactions is a major mechanism responsible for circular orbit satellite

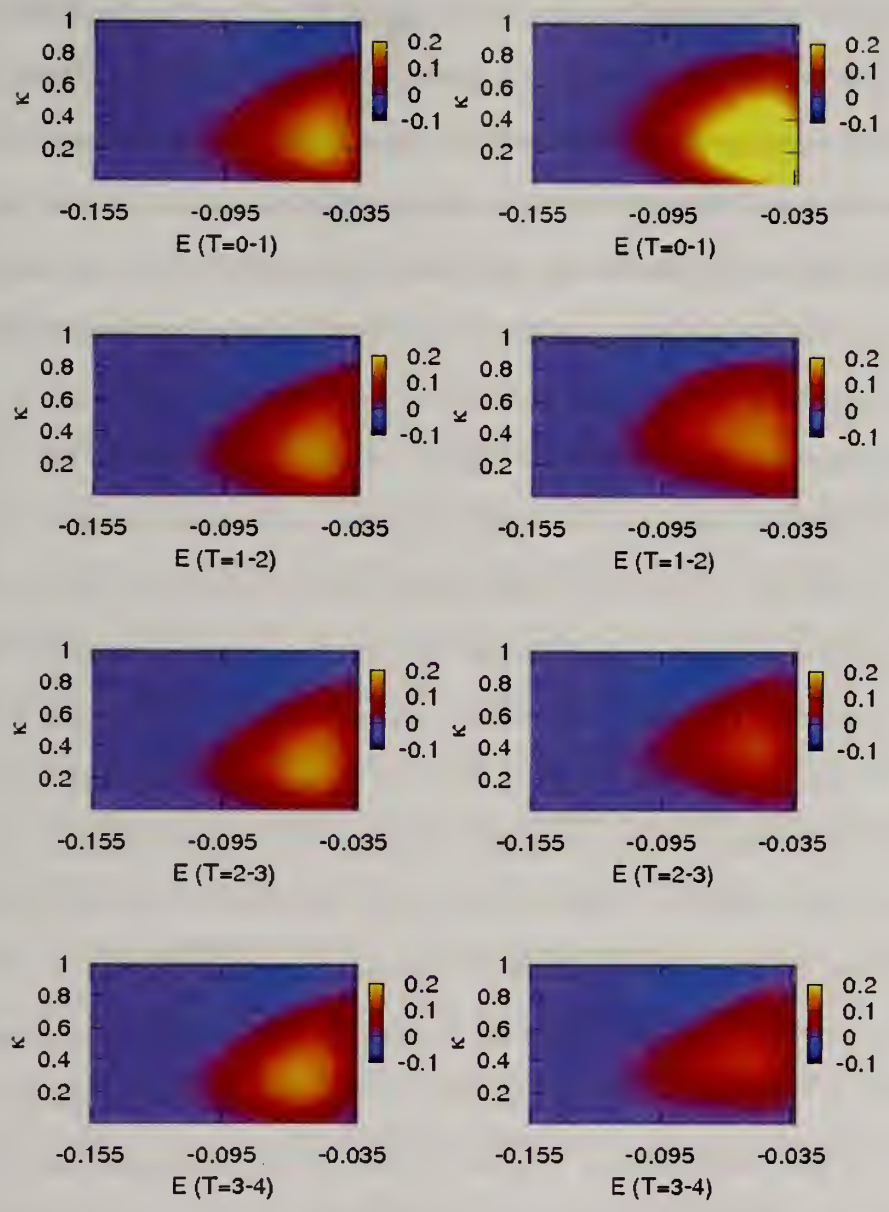

Figure 2.7 The distribution of the relative change in L_z in phase space for the N-body simulation (left panels) and the numerical perturbation theory calculation (right panels) The perturbation theory calculation only includes the -1:2:2 resonance, but as shown in Figure 2.6, the -1:2:2 resonance is the dominant resonance. Except for $T = 0.0 - 1.0$, both results show good general agreement. This agreement provides robust evidence for resonant effects in the circular orbit simulation.

evolution. Although the simulation and the perturbation calculation are similar in general, there are minor discrepancies. First, the amplitude of the relative ΔL_z from the perturbation calculation is larger than that from the simulation at $T = 0.0 - 1.0$. This results from the abrupt introduction of the perturber. This abrupt introduction leads to a non-linear feature, which may not be properly treated in the perturbation calculation. Second, the shape of the region of angular momentum change is a little different in the simulation compared to the perturbation calculation. In particular, the simulation shows a relative ΔL_z distribution in the lower right region of phase space, while the perturbation calculation does not. There are two reasons for this discrepancy. The first is the absence of other resonances in the perturbation theory calculation except for the -1:2:2 resonance, while the simulation includes all possible resonances. Currently, our perturbation theory calculation cannot compute the effects of the resonances with different l at once because of a computational cost problem. Under this limitation the relative ΔL_z distribution from the perturbation theory calculation only can show the effects from the most dominant resonance. Even if the -1:2:2 resonance is the dominant resonance, there are several minor resonances, which also contribute the resonant torque. In particular, the lower right region is location of the -1:3:3 resonance, which is the second strongest resonance. The second reason is the satellite mass loss during the simulation. The satellite loses mass in the simulation but in the perturbation calculation. In fact, the simulation results in Figure 2.7 only show the distribution of the relative ΔL_z for the remaining particles. Hence the few minor disagreements between the simulation and the perturbation theory calculation does not invalidate our assertion that the evidence that the resonant torque is a major mechanism responsible for satellite disruption.

It is surprising that there is no $l = 1$ resonance contribution. Absence of a $l = 1$ resonance contribution results from the satellite truncation. Roughly, the tidal radius of the satellite coincide with the corotation radius of the satellite. In other words,

$\Omega_{pert} \sim \Omega_2$, and the satellite halo is isotropic so $|\frac{\Omega_{pert}}{\Omega_2}| < 1$. Using Equation 2.2, this relationship means that $|l_1\frac{\Omega_1}{\Omega_2} + l_2| < 1$ to make the resonance occur within the satellite. Calculatig the orbital frequencies for the all orbits in the satellite, Ω_1/Ω_2 is always larger than 1. In this case, $|l_1\frac{\Omega_1}{\Omega_2} + l_2|$ has its lowest value when $l_1 = 1$ and $l_2 = -1$. We examine the location of the 1:-1:1 resonance in phase space and find that it is located just outside the satellite. Hence, interestingly, if the satellite is tidally truncated there is no $l = 1$ resonance contribution to satellite disruption because the tidal radius approximately coincides with the corotation radius.

2.3.2 Verifying mass loss by the resonant torque

The simulation results and the perturbation theory calculation prediction are roughly in accord on to the amplitude and phase space location of the angular momentum exchange, which confirms the importance of the resonant torque. However, it does not directly show that the mass loss results from this mechanism. Moreover, there is another process that causes mass loss. If some satellite particles are tidally stripped by the host halo potential, the satellite system readjusts after this mass loss. This readjustment forces some particles to move outside the tidal radius and these particles then become tidally stripped. This process results in a continuous mass loss. The mass loss observed in the circular orbit simulation potentially results from this process. In our simulation, the satellite initial conditions are designed to reduce the mass lost through this process by truncating satellites at the tidal radius but, owing to the Eddington inversion, a small amount of mass loss is inevitable. To clarify the resonant torque affect on satellite mass loss, we conduct both an input resonance experiment and a rotating satellite experiment.

For the input resonance experiment, we compare the mass loss from three different simulations: a circular orbit simulation, a control simulation, and an input resonance simulation. The circular orbit simulation is the simulation we investigated in Section

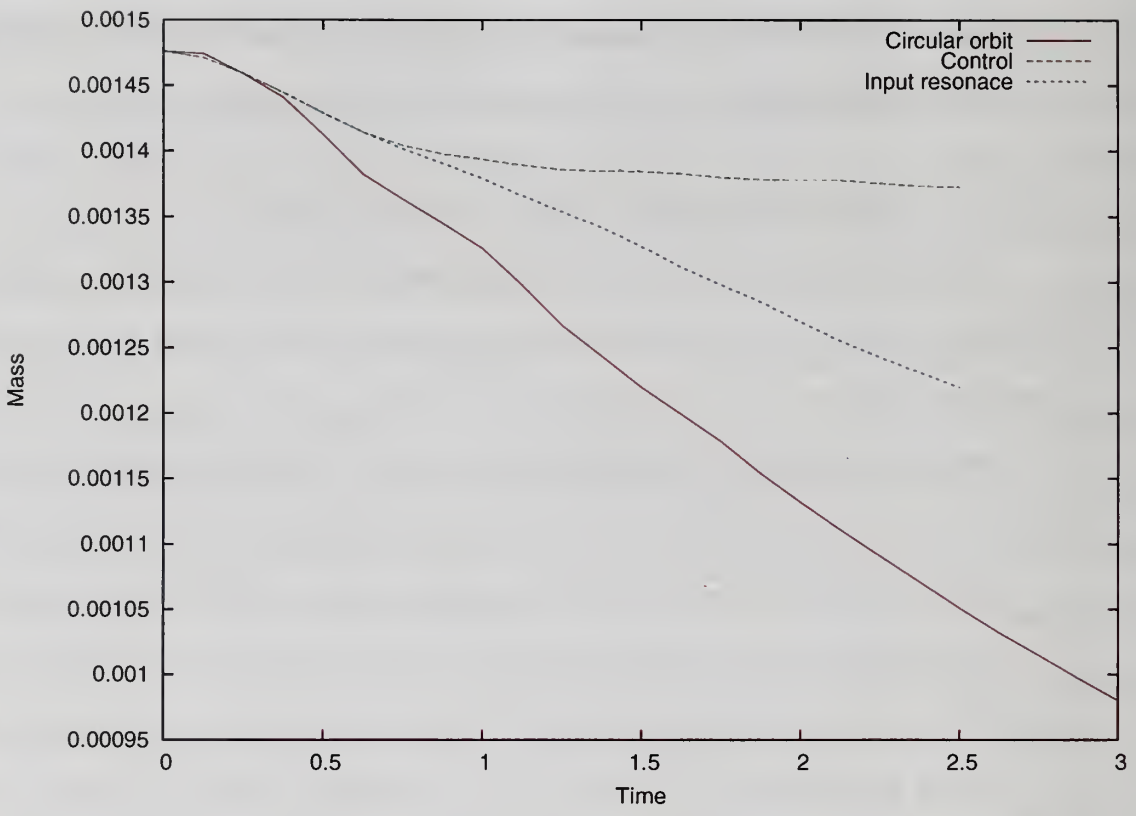

Figure 2.8 The mass loss history of the circular orbit simulation, the control simulation, and the input resonance simulation (see text). The satellite in the input resonance simulation loses more mass than the satellite in the control simulation demonstrating that the heating by resonant interactions provoke mass loss.

2.3.1. The control simulation and the input resonance simulation are the same N-body simulation as the circular orbit simulation but without a host halo potential. The control simulation simply evolves the satellite in isolation, but is designed to reproduce the mass loss and readjustment process. To reproduce this process, we artificially setup the initial condition such that dark matter particles outside a certain radius do not feel the satellite's self-gravity. That radius is set to be halfway in mass between x_e in the circular orbit simulation and the satellite's maximum radius. The input resonance simulation is designed to incorporate the resonant effects on satellite mass loss in the control simulation. We incorporate the resonant effects as follows: Figure 2.7 provides the phase space information of the angular momentum change owing to the resonant interaction computed using numerical perturbation theory. We apply this to the simulation: Each particle's energy and angular momentum are computed during the course of the simulation to determine its phase space location and for a given phase space location, the change in angular momentum is estimated from perturbation theory. This estimated torque is then applied to each particle. Hence, the input resonance simulation can incorporate the effects of the resonant torque on the control simulation. We use the angular momentum change between $T = 1.0$ and $T = 2.0$ (second row, left column in Figure 2.7). Since the input resonance simulation incorporates the resonant effect in the control simulation, any differences between the two simulations shows mass loss by the resonant effect.

Figure 2.8 shows the mass loss history from these three simulations. The control simulation loses mass initially but the mass loss rate decreases after $T = 1.0$. The input resonance simulation loses mass of about the same rate as the control simulation before $T = 1.0$ but the rate does not decrease after $T = 1.0$. The circular orbit simulation shows the most significant mass loss among the three simulations. The control simulation suggests that although there is a mass loss and readjustment process the amount of mass loss owing to this process is minor, and the mass loss

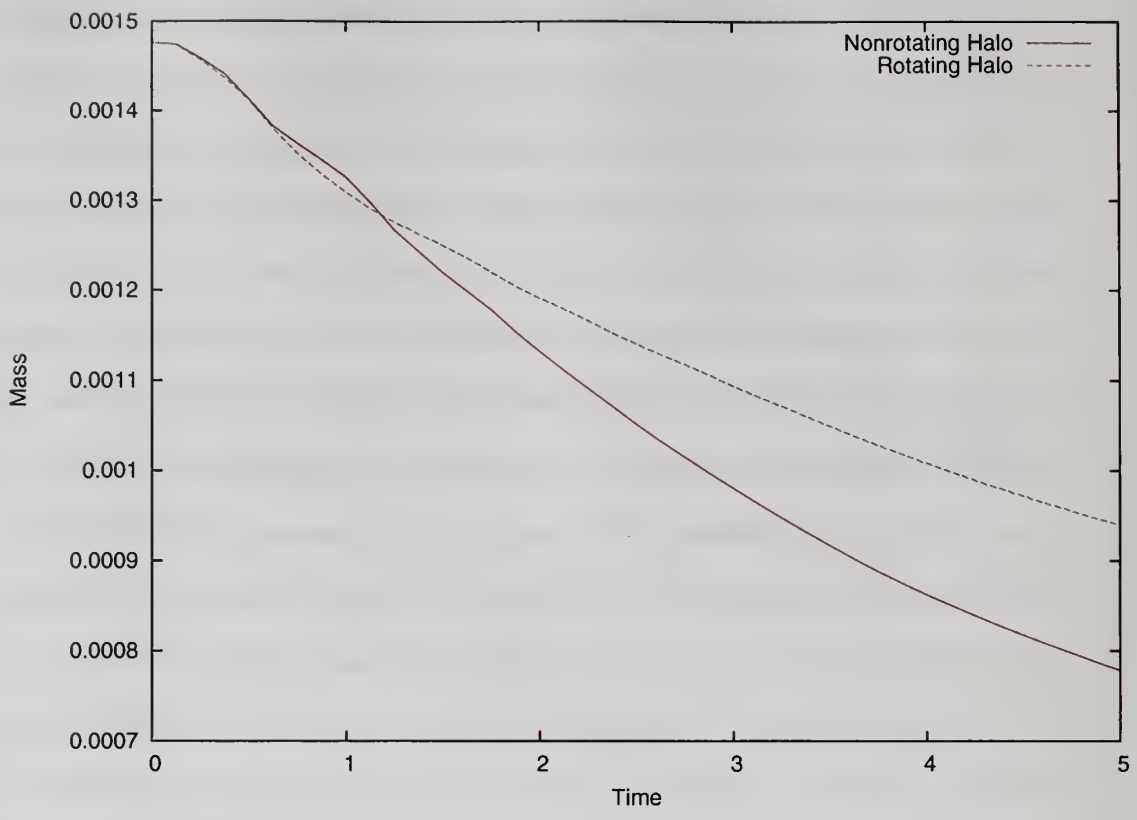

Figure 2.9 The mass loss history of the circular orbit simulation for both a non-rotating and rotating satellite. At $T = 5.0$, the rotating satellite simulation loses about 25% less mass than the non-rotating satellite simulation.

rate decrease and eventually stops. The comparison between the control simulation and the input resonance simulation confirms that the mass loss is driven by torques from the resonant interaction. The circular orbit simulation loses more mass than the input resonance simulation not because there are other mass loss mechanisms but because the real resonance interaction is time dependent. According to Figure 2.7, the angular momentum exchange rate varies with time. In addition, the circular orbit simulation includes more resonances than the input resonance simulation, which only includes the strongest -1:2:2 resonance. This results in the difference in mass loss rate between the circular orbit simulation and the input resonance simulation.

To further investigate the resonance torque mechanism, we compare the mass loss from a non-rotating satellite simulation to a rotating satellite simulation. The non-

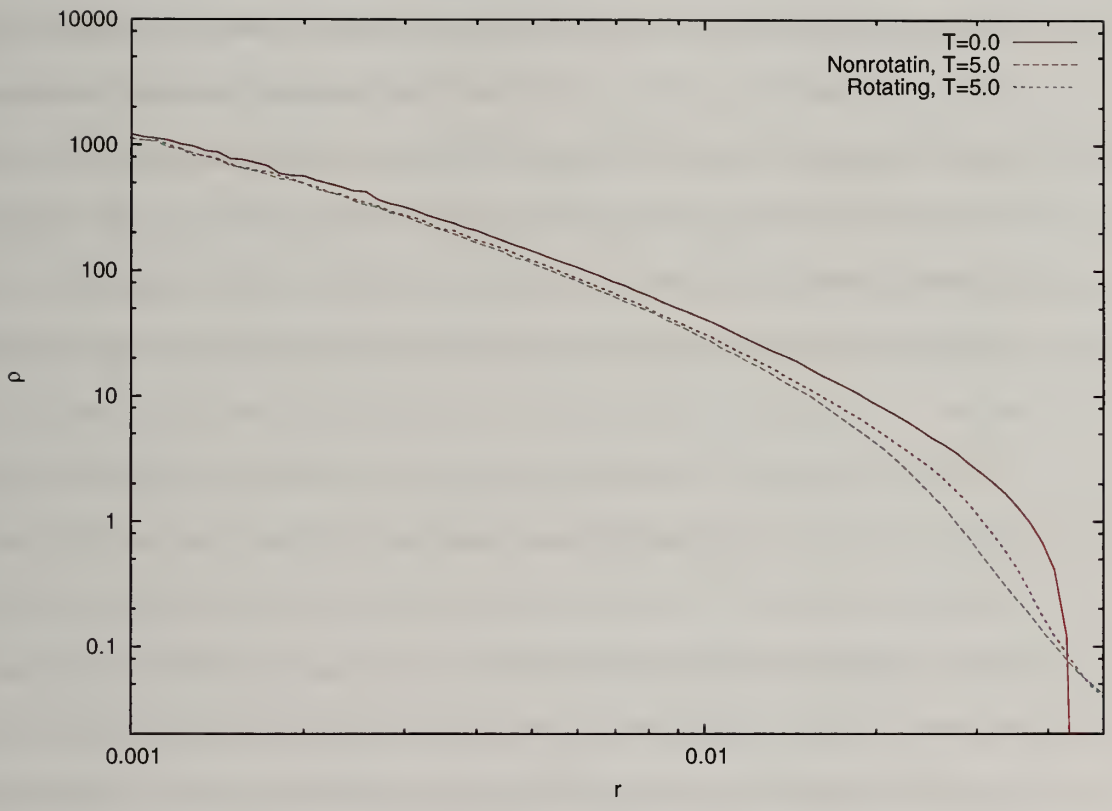

Figure 2.10 Density profiles of both the non-rotating satellite simulation and rotating satellite simulation. The initial density profiles for both satellites are identical. At $T = 5.0$, the non-rating satellite profile shows more mass loss than the rotating satellite.

rotating satellite simulation is the same as the previous input resonance experiment. The rotating satellite simulation is also except that the satellite halo is rotating. In this experiment, the rotation is added in an artificial manner. The initial condition for the rotating satellite experiment is non-rotating. During the course of the simulation, a particle's motion in the non-rotating satellite consists of two parts: the satellite's orbital motion in the host halo and the particle's orbital motion in the satellite. The rotating satellite simulation adds one additional rotating motion to the satellite particles; the satellite particles are rotated every timestep around the z-axis, which passes through the satellite EJ center [4], with a rotation frequency that is the same as the circular orbit frequency of the satellite orbit in the host halo. Therefore, the direction of the host halo center is fixed in the satellite frame. Owing to this rotation, the halo does not feel the time-dependent external potential that causes the resonant torque.

Figure 2.9 presents the mass loss history from these two simulations and shows that the rotating satellite simulation loses about 25% less mass than the non-rotating satellite simulation at $T = 5.0$, which supports the idea that the resonant torque causes the satellite's mass loss. This becomes even more convincing when one investigates the location of the additional mass loss in the non-rotating satellite simulation. Figure 2.10 shows the density profiles from both simulations. Since the initial satellite halos are the same for both simulations, the initial density profiles are identical. However, at $T = 5.0$ the density profiles from two simulations become different. Besides the non-rotating satellite profile showing more mass loss than the rotating satellite, there is a large difference in the shape of the two profiles. The rotating satellite density profile shows a noticeable increase in density between $r = 0.015$ and $r = 0.035$ compared to the non-rotating satellite density profile. This radial range coincides

[4]The EJ center is the center of mass of the $N_{min} = 512$ most bound particles at a given time.

with the region where most of the angular momentum transfer occurs in Figure 2.7. Although Figure 2.7 is shown in the phase space coordinates, a given phase space location has a corresponding location in halo radius. This feature suggests an absence of the resonant torque effect. Since the rotating satellite is not affected by the resonant torque effect, this satellite can contain more material at the resonance location than the satellite affected by the resonance torque. This comparison study of the non-rotating and rotating satellite simulations demonstrates that the resonance torque causes satellite mass loss.

One surprising feature shown in Figure 2.9 is that the rotating satellite still loses significant mass. The amount of mass loss in the rotating satellite is about 75% of the non-rotating satellite's mass loss. This can result from an additional Coriolis force, which is introduced by our artificial scheme. Owing to this scheme, the simulation artificially adds two additional terms to the equation of motion

$$\vec{\Omega} \times \vec{q} \quad and \quad \vec{\Omega} \times \vec{p} \tag{2.3}$$

where $\vec{q} = \vec{r} - \vec{R}$ is the distance from the satellite center to satellite particles, $\vec{p} = \vec{v} - \vec{\Omega}$ is the velocity of a satellite particle in the satellite frame, $\vec{r}$ is the distance from the host halo center to a satellite particle, $\vec{R}$ is the distance from the host halo center to the satellite center, and $\vec{v}$ and $\vec{\Omega}$ are their respective velocities. When we evaluate the force on a satellite particle, the first term in Equation 2.3 becomes

$$\begin{aligned} &\rightarrow \quad \vec{\Omega} \times (\vec{v} - \vec{\Omega}) + \vec{\Omega} \times (\vec{\Omega} \times (\vec{r} - \vec{R})) \\ &\sim \quad \vec{\Omega} \times \vec{v}. \end{aligned} \tag{2.4}$$

In this equation, we assume that $\vec{\Omega} \times (\vec{\Omega} \times (\vec{r} - \vec{R})) = 0$ because the satellite is very small compared to the host halo size ($\vec{r} \sim \vec{R}$). The combined contribution from the

second term in Equation 2.3 and the result in Equation 2.4 is equivalent to a Coriolis force. Hence, the rotating satellite experiment introduces an additional Coriolis force, while reducing the time-dependent external potential that causes the resonant torque. In addition to an additional Coriolis force, mass loss in the rotating satellite experiment also results from satellite deformation. According to Choi et al. (2007), a spherical satellite halo gets stretched during its disruption. The host halo tidal field is responsible for this deformation. For the non-rotating satellite experiment, the direction of the tidal force is rotating in the satellite frame. However, this direction is fixed in the rotating satellite experiment. This fixed direction of the tidal force enhances the satellite deformation. In Figure 2.9, we notice that the rotating satellite temporally loses more mass than the non-rotating satellite around $T = 1.0$. Note that the definition of the satellite mass for this figure is the enclosed mass inside the satellite's initial radius (see Section 2.4 for a discussion of this definition). As a result, the initial deformation from the spherical halo is counted as mass loss. Excess mass loss of the rotating satellite around $T = 1.0$ results from this enhanced deformation. It suggests that the 25% difference in the mass loss is a lower limit to the resonance torque contribution. Although the exact amount of the contribution and the role of other processes are still uncertain, these two tests clearly show the important role that resonant torque plays in satellite mass loss and confirms that the resonance torque contribution to the mass loss is larger than 25% of the total mass lost.

2.4 Satellite disruption on an eccentric orbit

Most satellites have an eccentric orbit. Several physical processes such as resonant torquing, gravitational shocking with resonant shock effects, and continuous tidal truncation simultaneously play a role in an eccentric orbit satellite. To study this complicated situation and understand the characteristics of the individual physical processes, we compare the satellite evolution of three different orbit simulations: a

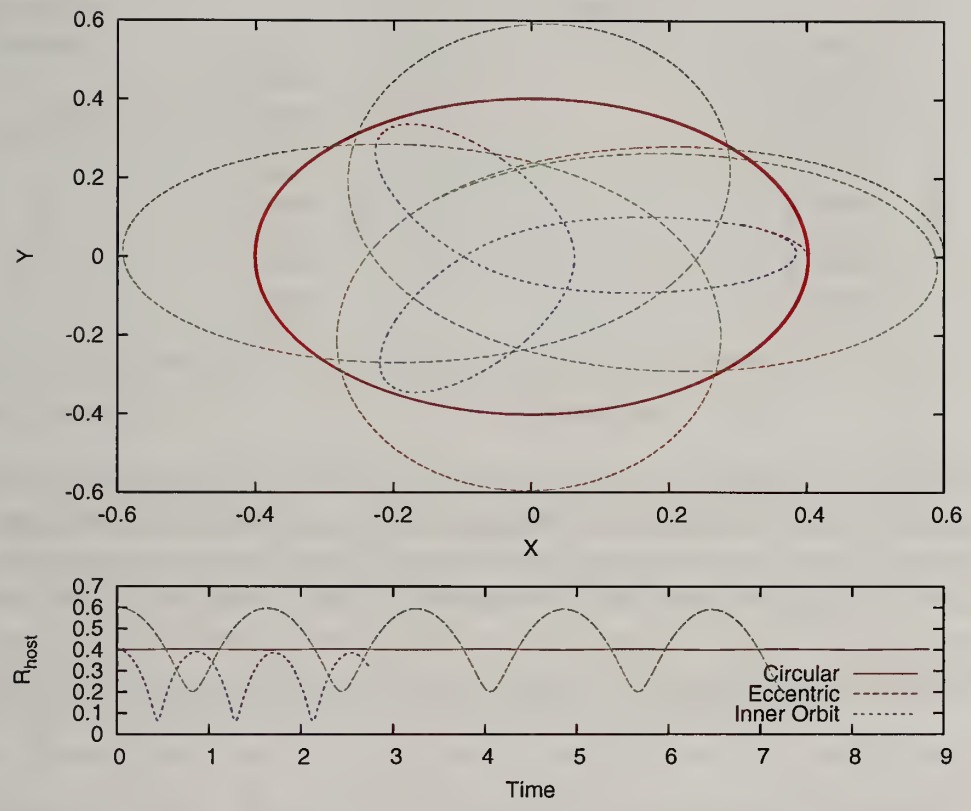

Figure 2.11 The orbits of three simulations: the circular orbit, the eccentric orbit, and the inner orbit. *Top panel:* the orbit trajectory of the three simulations in the orbital plane. *Bottom panel:* shows the time evolution of the distance between the satellite and the host halo center.

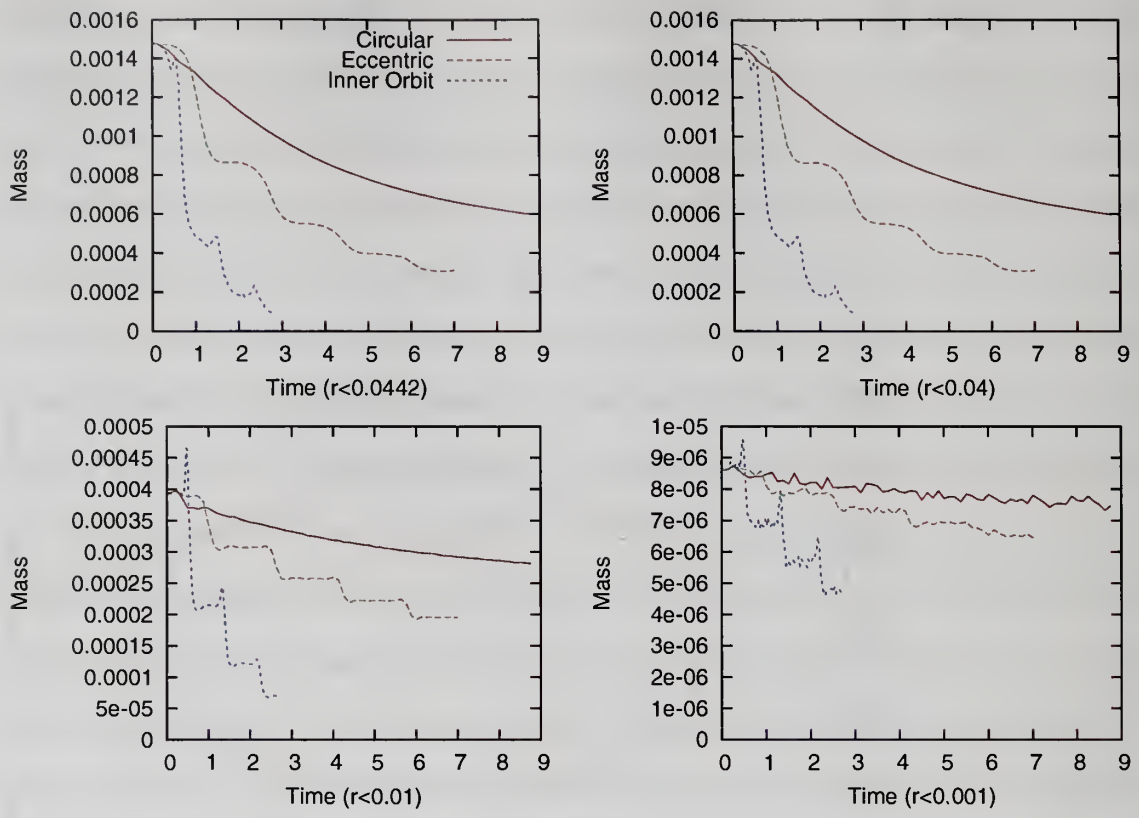

Figure 2.12 The figures show the enclosed mass evolution for three simulations: the circular orbit simulation, the eccentric orbit simulation, and the inner orbit simulation. The enclosed radii are 0.045, 0.04, 0.01, and 0.001 for top left, top right, bottom left, and bottom right panels, respectively. 0.045 is the initial satellite radius.

circular orbit simulation, an eccentric orbit simulation, and an inner orbit simulation (see Figure 2.11 for the three orbits). The circular orbit simulation is the same simulation we investigated in Section 2.3. The eccentric orbit simulation is an $e = 0.5$ orbit whose apocenter $r_{apo} = 0.6$ and pericenter $r_{peri} = 0.2$ [5]. The circular orbit and the eccentric orbit have the same orbital energy. The inner orbit simulation is an $e = 0.72$ orbit whose apocenter $r_{apo} = 0.4$ and pericenter $r_{peri} = 0.064$. The normalized angular momentum (κ) of the inner orbit is 0.55, which is about the median κ of subhalos in a sample taken from recent cosmological simulations (Ghigna et al., 1998; Zentner et al., 2005).

[5]The eccentricity of an orbit is defined as $e \equiv (r_{apo} - r_{peri})/(r_{apo} + r_{peri})$

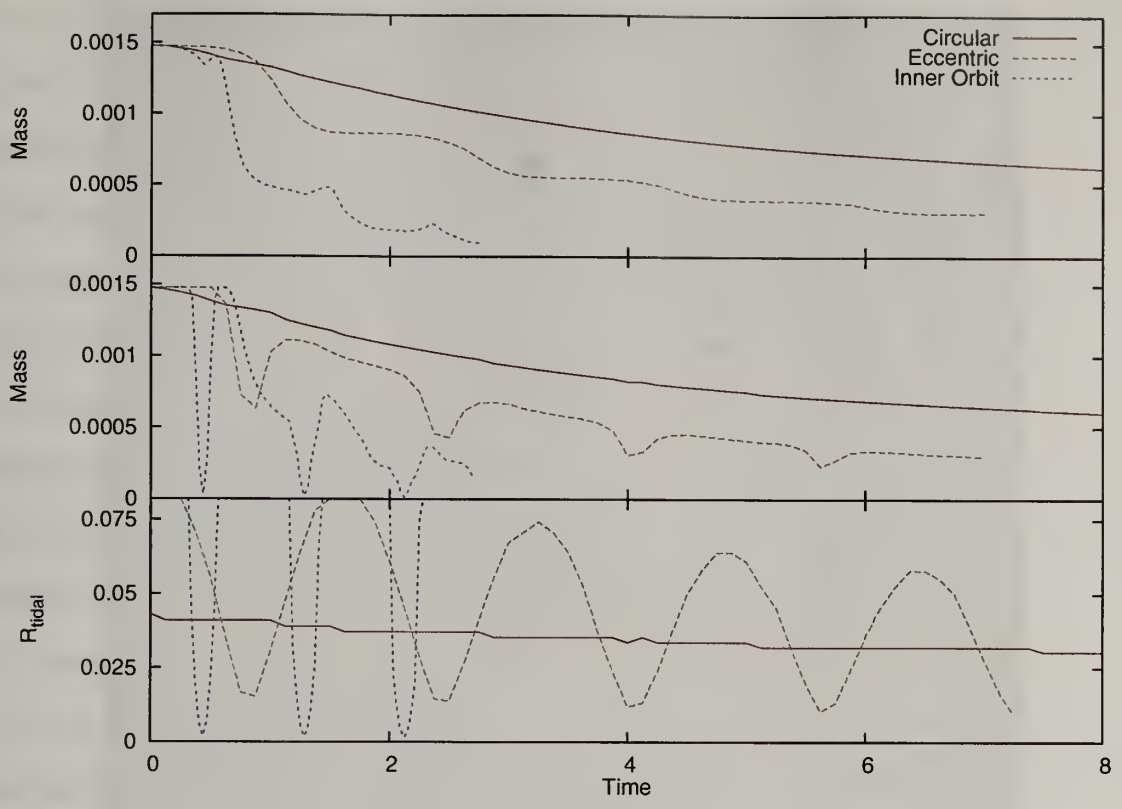

Figure 2.13 The top and middle panels show the mass loss histories of three different orbit simulations: the circular orbit simulation, the eccentric orbit simulation, and the inner orbit simulation. The top panel shows the mass loss history using the initial satellite radius. The middle panel shows the mass loss history using the instantaneous tidal radius. The bottom panel shows the time evolution of the tidal radius. Since the tidal radius at apocenter can become bigger than the entire satellite system, we set the maximum tidal radius to be twice the initial satellite radius.

Figure 2.12 shows the mass loss histories of the three satellite simulations. It also shows the evolution of the enclosed mass within 90%, 22%, and 2.2% of the original satellite radius. The two eccentric orbit satellites lose their mass mostly at pericenter. The pattern of their mass loss as a function of time resembles a staircase while the pattern of satellite mass loss for a circular orbit resembles a steady slope. The two satellites on an eccentric orbit lose significantly more mass than a satellite on a circular orbit. Investigating the heating mechanisms that are important for eccentric orbits is the major objective of this section.

Before investigating the physical processes responsible for eccentric orbit satellite disruptions, we had better discuss the definition of satellite mass. The definition of satellite mass is usually the mass bound to the satellite. However, in practical usage this definition is often vague. Figure 2.13 shows the mass loss history for the three simulations using two different definitions of the bounded satellite mass. The first definition is total mass inside the initial maximum radius. The second definition is total mass inside the instantaneous tidal radius. We find that the satellite mass rapidly decreases and then increases again around the time of pericenter passage if we use the tidal radius definition for mass. This mass evolution results from the evolution of the tidal radius (see the bottom plot in Figure 2.13). When the satellite moves deep inside of the host halo the tidal radius decreases. It takes a time the satellite material outside of the tidal radius to be stripped. If the time scale of the change in tidal radius is faster than the stripping time scale the mass outside of the tidal radius is not stripped and returns to the satellite when the tidal radius increases. Owing to this issue in the tidal radius definition of mass, we generally use the initial maximum radius definition as our working definition of the satellite mass.

2.4.1 Heating by the compressive gravitational shock at pericenter

According to Figure 2.12, satellites on eccentric orbits lose mass mostly at pericenter. This suggests that satellite heating by the compressive gravitational shock at pericenter is the most dominant mechanism for satellite disruption. In addition, we can discriminate two distinct effects of this gravitational shock: evolution of the satellite structure and the host halo potential effect.

The inner orbit simulation results in Figure 2.12 show that the enclosed mass of the satellite increases temporarily at the pericenter. This increase in enclosed mass results from a squeezing of the satellite by the external potential. Since the satellite is embedded in the host halo potential, compression by the host halo is not from one

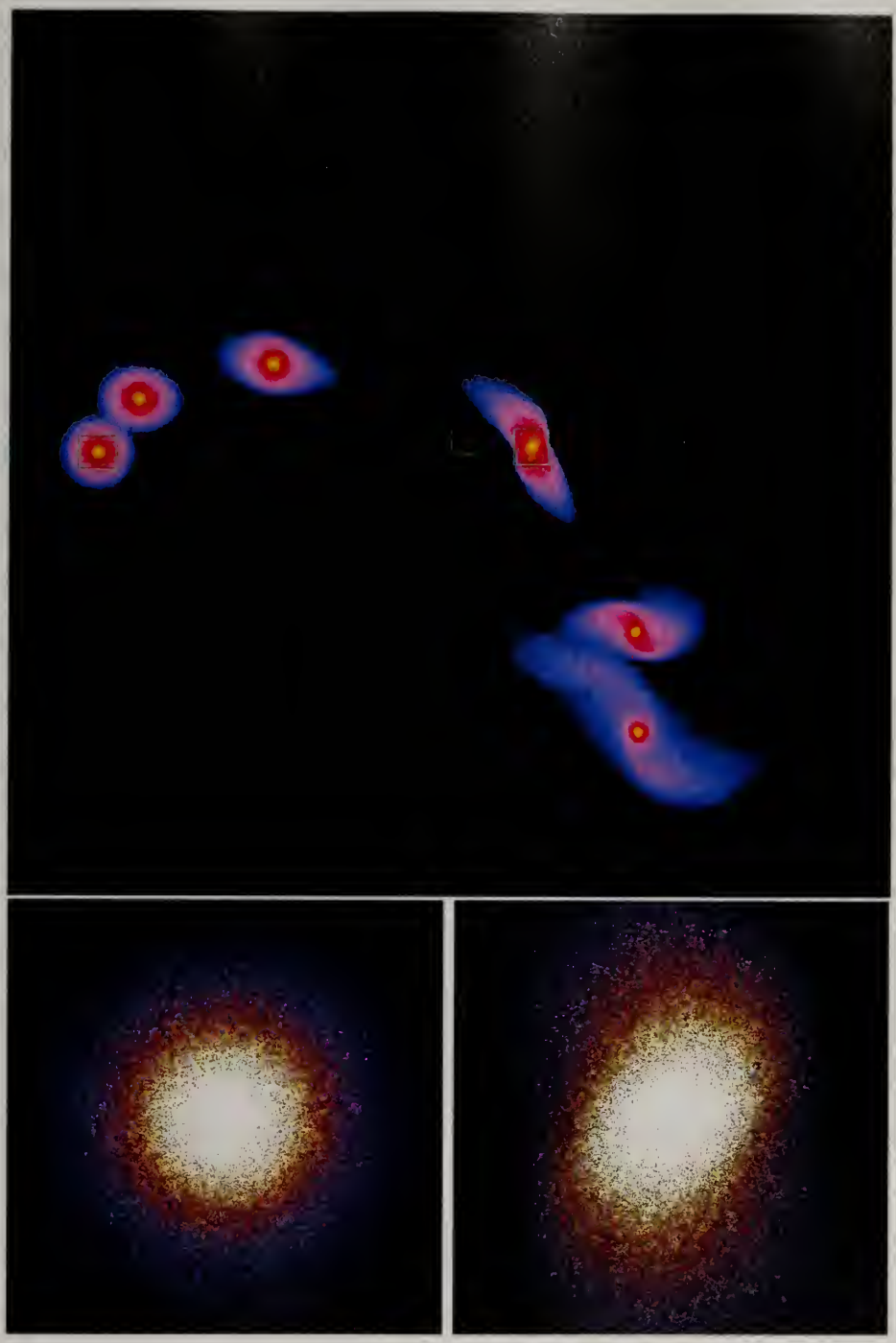

Figure 2.14 Snapshots of the inner orbit simulation from one apocenter to the next apocenter. *Top panel:* Overlapping snapshots of the satellite, shown at T =0.0, 0.15625, 0.3125, 0.46875, 0.625, and 0.78125. The inner small axis shows the center of the host halo. The color code represents a logarithmic scale in dark matter density and the scale is same for all satellites. *Bottom panels:* Zoom in view for the satellites at $T = 0.0$ and $T = 0.3125$. The box size is the same as the green box in the top panel. To emphasize the dark matter density differences, the color code represents a linear scale in density. The bottom snapshots show the increase in high density regions at $T = 0.3125$ compared with the satellite at $T = 0.0$; the inner density of the satellite is increased at pericenter.

direction but from all three orthogonal directions. In addition, the strength of the compression is strong enough to drive internal evolution. In Figure 2.12 the enclosed masses within 90%, 22%, and 2.2% of the original satellite radius also increases at pericenter. In particular, the enclosed mass within 22% of original satellite radius clearly shows a rapid increase in enclosed mass. Figure 2.14 shows pictures of the inner satellite orbit simulation. The top panel in Figure 2.14 shows overlapping snapshots of the inner orbit simulation from one apocenter to the next. The color scale represents a logarithmic scale in satellite density. The two bottom panels show blown-up of the two boxed areas in the top panel. To highlight the density difference, the color code now represents a linear scale in satellite density from $\rho = 1$ to $\rho = 100$, and white represents $\rho > 100$. The panels clearly show that the area in the white region of the right panel is larger than that of the left panel because the satellite gets squeezed at pericenter. That internal structure evolution violates the impulse assumption in the impulse approximation (Spitzer, 1987), which is broadly used to estimate satellite heating by a gravitational shock. Under the impulse assumption, there is no potential energy change but particles gain kinetic energy owing to the interaction with the external potential. However, our satellite evolution shows that both the kinetic and potential energy evolve during the interaction. Therefore, the impulse approximation cannot accurately estimate the heating at the pericenter.

Since a satellite is always embedded in the host halo potential, the tidal radius constantly restricts the satellite size. Owing to satellite heating by the gravitational compressive shock at pericenter, the satellite particles gain energy. This energy input reduces the satellite's binding energy and expands the satellite. When this expansion occurs, some satellite particles move outside the tidal radius and are stripped from the satellite. This truncation enhances the satellite mass loss. In contrast, if the host halo potential did not exist, some expanded orbits could again contract. In addition to enhancing the mass loss, the tidal truncation causes the satellite halos to be out

of equilibrium. Figure 2.13 shows that when the satellite moves deep inside the host halo, the tidal radius decreases. At this time, the satellite material outside of the tidal radius is not completely stripped and a considerable fraction of this material comes back into the satellite when it moves toward the outer halo and the tidal radius again increases. This rapidly changing tidal radius makes the satellite halos stay out of equilibrium.

Both the internal structure evolution and the tidal truncation lead to nonlinear satellite evolution. The nonlinear physical processes are essential ingredients to accurately predict satellite disruption, and it makes an simple formalism for describing satellite mass loss inaccurate.

2.4.2 The resonant torque effect in an eccentric orbit satellite

As we mentioned above, the resonant dynamics of satellite evolution can be easily understood by separating it into two kinds of resonant effects: the resonant shock and the resonant torque, but this distinction is arbitrary. When a satellite is on an eccentric orbit, both resonant effects contribute to the satellite evolution simultaneously. An eccentric orbit satellite is intrinsically coupled to both the radial and azimuthal frequencies. To investigate the complete resonant effect that results from an eccentric orbit, performing a perturbation theory calculation for an eccentric orbit perturber is necessary. This results in a perturber with a radial frequency as well as an azimuthal frequency that shows a continuous spectrum. It is hard to track the continuous perturbation spectrum and to compute the coupled resonances in the halo. The perturbation theory calculation for the eccentric orbit perturber is exceedingly complicated calculation and requires an extreme computational expense. To get around this difficulty we choose one important frequency and compute the resonant dynamics of it instead of computing the entire resonant dynamics. It is obvious that the resonance coupled with the frequency at the pericenter produces the strongest

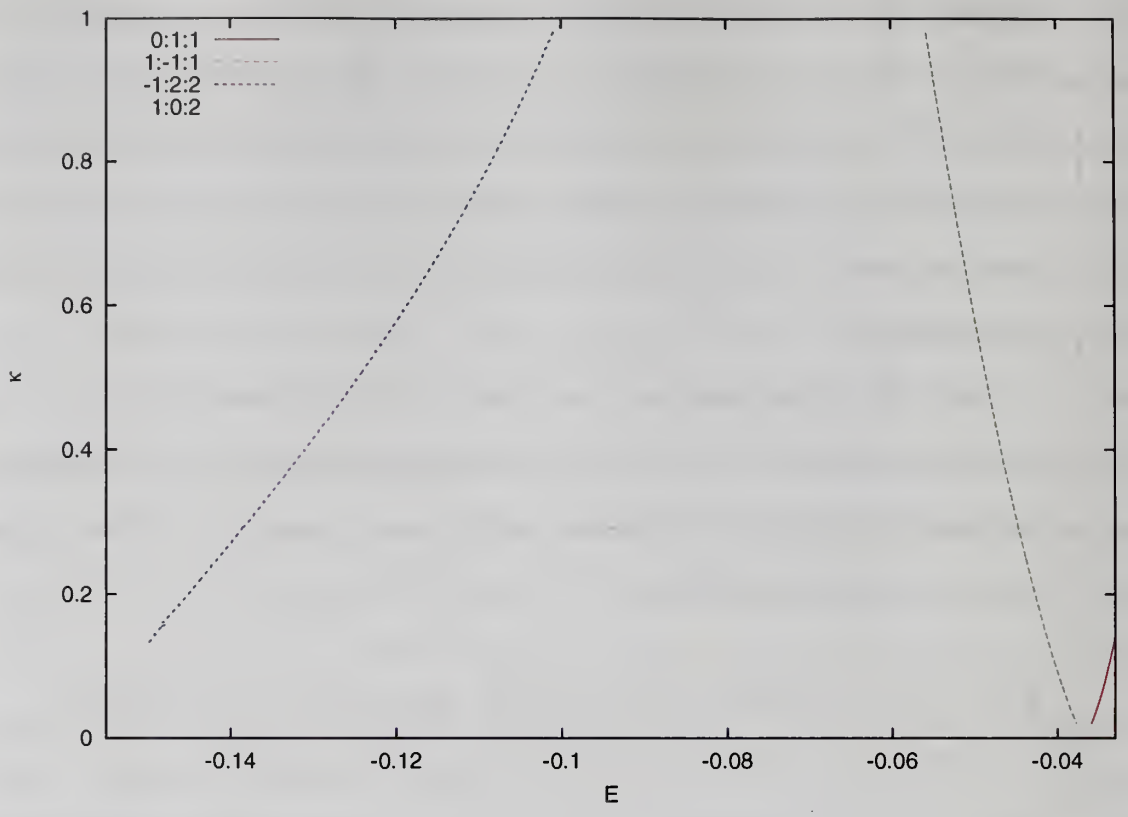

Figure 2.15 The same as Figure 2.4 but assuming $\Omega_{sat} = 6.56$. This satellite frequency corresponds with the frequency of the circular orbit at r_{peri} of the eccentric run. It only shows l=1 and 2 resonances. Unlike Figure 2.4, 1:-1:1, 0:1:1, and 1:0:2 resonances are located inside the satellite.

resonance. In fact, this strongest resonance coupling is related to the resonant effects of the compressive gravitational shock at pericenter. Here we assume that the satellite is on a circular orbit at pericenter and proceed as in Section 2.3.1.

Under this simplified assumption, we examine what low order resonances are located within the satellite. Figure 2.15 shows the locations of the resonances in satellite phase space. All resonances, which are in the $-10 \leq l_1 \leq 10$ and $l = 1, 2, 3, 4$ range, are examined. In addition to the -1:2:2 resonance, the 0:1:1, 1:-1:1, and 1:0:2 resonances occur within the satellite phase space. Comparing to the results from Section 2.3.1, the number of resonances within the satellite increases because the orbital frequency increases as a satellite moves toward the center of the host halo. This causes a few resonances that were outside the satellite to move into the satellite. According

to the numerical perturbation theory calculation, the strength of the 1:-1:1 and 1:0:2 resonances are comparable to the strength of the -1:2:2 resonance, which is much stronger than the -1:2:2 resonance in Section 2.3.1. The decrease in the distances between the perturber and the coupled orbits results in an increase in the strength of a particular resonance. Consequently, heating by resonant interactions is enhanced, when the orbital radius of the satellite decreases, both because the number of resonances increases and because the strength of each resonance also increases.

This experiment provides insight to help understand resonant effects for an eccentric orbit satellite. This calculation is related to resonant effect of the compressive gravitational shock at pericenter. However, it does not give us a full understanding about the resonant shock process and does not estimate the heating by the resonant shock. To accurately estimate the total heating, full perturbation calculations that include the effects of a continuous perturbation spectrum as well as the effects of time-dependent perturbations are required but are beyond the scope of the work presented here.

2.5 The pattern of satellite stripping

Owing to satellite heating, particles in a satellite gain energy (and angular momentum). This injected energy reduces the satellite's binding energy and enhances the satellite mass loss. There are several mechanisms that heat a satellite, but the consequent mass loss only depends on the amount of added energy because evolution under self-gravity relaxes and spreads out any localized energy input. For example, when a particular resonant orbits gain angular momentum through the resonant interaction, this additional angular momentum eventually heats the entire satellite system and drives mass loss. Therefore, knowing the pattern of satellite mass stripping provides useful insight into investigating the observational signatures of the disrupted satellites.

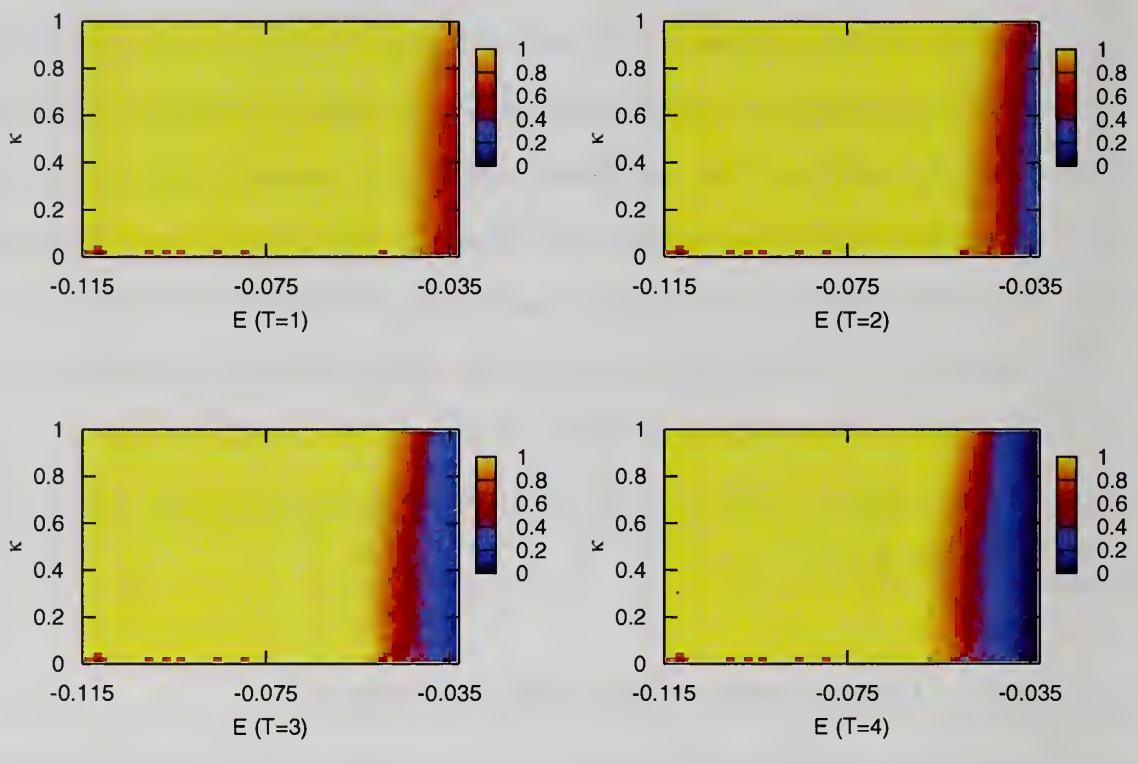

Figure 2.16 The fractions of particles remaining during the satellite orbit in the host halo in phase space. The color code is linear in fraction with 1 meaning that all particles initially at that point in phase space are still in the satellite and 0 meaning that all particles are already stripped. Each panel shows the fraction at a given time compared with the initial satellite. The energy and the angular momentum of particles shown in the figures are the initial energy and the initial angular momentum. These panels show that satellite stripping is an outside-in process in the energy space.

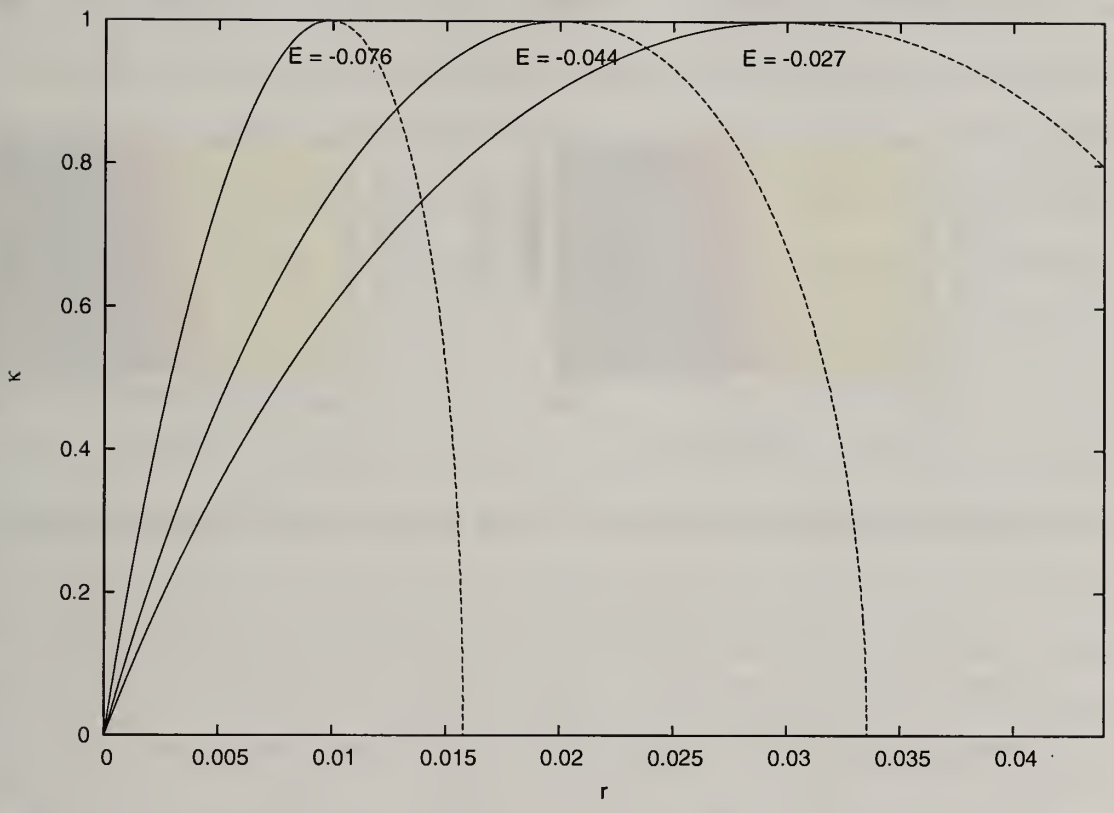

Figure 2.17 The apocenter and pericenter of orbits in the initial satellite model. Dashed lines represent the apocenter and solid lines the pericenter at a given energy. Here we show lines from E=-0.076, -0.044, and -0.027 orbits whose circular radii are 0.01, 0.02, and 0.03, respectively. The x-axis is the distance from the halo center and the y-axis the normalized angular momentum. The area between the pericenter and apocenter lines is the range in radii in which particles with given E and κ orbit.

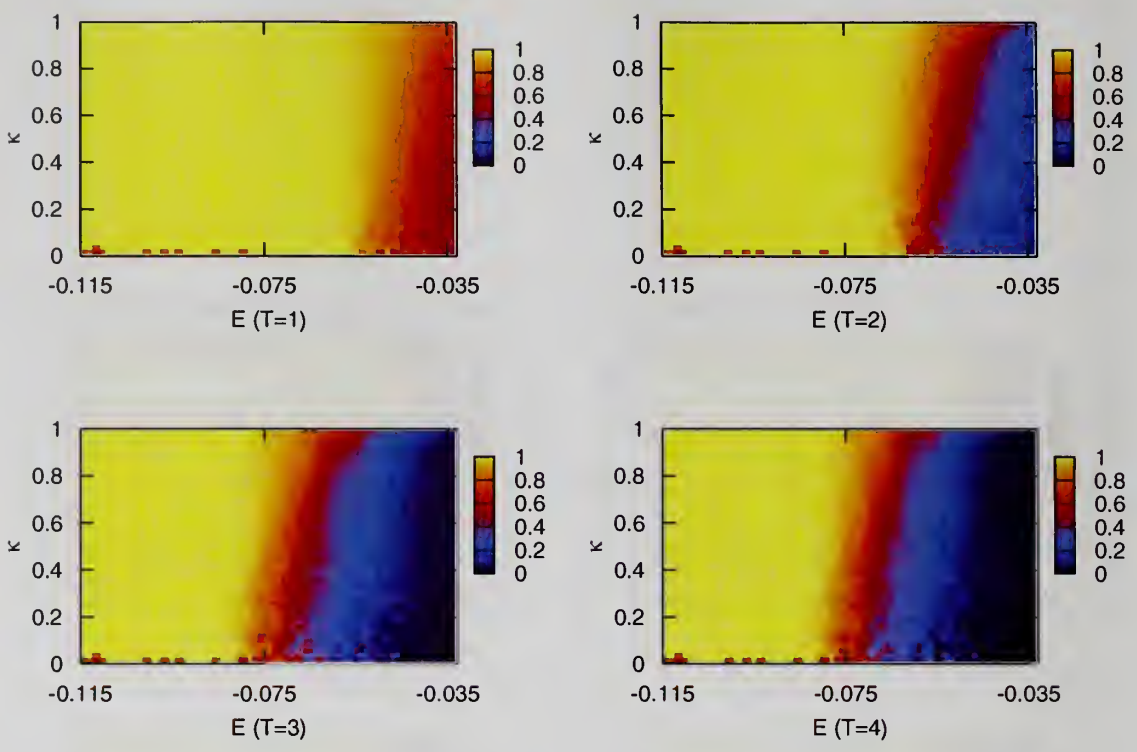

Figure 2.18 The same as Figure 2.16 but for the eccentric orbit simulation.

Figure 2.16 plots the fraction particles, remaining in the phase space, for the circular orbit satellite evolution. It shows that low binding energy particles are stripped earlier and high binding energy particles are stripped later. In other words, the satellite stripping process is an outside-in process in energy space. Since the stripping sequence does not depend on satellite radius, particles in at many radii can be removed simultaneously. The stripping is not sensitive to angular momentum because the fraction of bound particles is an average of an ensemble of particles with a given energy and angular momentum. Figure 2.17 supports this argument. It shows that there is an allowed range in radius for a particle that has a certain energy and angular momentum, and that the allowed radii of particles with different energies and angular momenta can overlap. As a result, although a particle is inside the halo, if its binding energy and angular momentum is low, it can be easily removed.

Figure 2.18 plots the fraction of particles remaining during the eccentric orbit satellite evolution in phase space. The eccentric orbit satellite stripping pattern is similar to the circular orbit satellite stripping pattern; an outside-in process in the energy space. However, the eccentric orbit satellite stripping pattern shows a mild dependence on angular momentum. The stripped fraction for radial orbits is larger than that for circular orbits at a given energy and given time. This angular momentum dependence results from the rapidly changing tidal radius shown in Figure 2.13. Owing to the rapidly changing tidal radius, some satellite particles are temporally located outside of the tidal radius. At this time, particles with a radial orbit tend to escape from the satellite, which causes the angular momentum dependence. However, even for an eccentric orbit, the general pattern of satellite stripping is an outside in process in energy space.

The outside-in stripping in an energy space has significant consequences for satellite galaxy stripping. Since most of the stars and gas of satellite galaxies reside within the central regions of their own dark matter halo, they are protected by their own halo. How much the stars and gas are protected depends on the binding energy of stars and gas and not their location in radius. The stripping probabilities of the disk component and the spheroid component are different. Imagine that there are two satellite galaxies; one is a disk galaxy and another is an elliptical galaxy and that the maximum radius and that they have the same orbit in the host halo and the same physical extend [6]. According to our findings, stars in the elliptical galaxy are stripped earlier than stars in the disk galaxy although two galaxies have the same physical extend, the same host halo, and the same trajectory. At the same radius, a circular orbit has the highest binding energy. The disk galaxy is mostly made from circularly orbiting stars, while the elliptical galaxy is made from a wide range of stellar orbits.

[6]In fact elliptical galaxies are generally more concentrated than disk galaxies.

This difference should be taken into account when modeling satellite galaxy stripping and in estimating the stellar halo distribution.

2.5.1 Finding the LMC stellar tail

Using our understanding of the pattern of satellite stripping, we can estimate the probability of stellar ejecta for a particular object. In this Section, we discuss why there are no stellar ejecta of the LMC in our galaxy.

The LMC is the closest large satellite galaxy of the Milky Way. It has been the subject of numerous observational studies and characteristics of its structure and kinematics have been well established. However, the origin of the Magellanic Stream, a thin neutral hydrogen tail stretching over 100^o along a Galactic polar circle, has remained mysterious. Observations suggest that the Magellanic Stream may be a relic of a past interaction with the Milky Way (Mathewson et al., 1977; Putman et al., 1998). If this is the case, tidally stripped stellar ejecta should be observed as predicted by tidal interaction theory. However, none of the many searches for stellar ejecta has successfully detected a population of stars that are connected with the Magellanic Stream. The missing LMC stellar ejecta have been a major problem in explaining the origin of the Magellanic Stream, and to resolve this conflict alternative scenarios have been suggested. First, that the gas in the LMC is removed by ram-pressure forces caused by an interaction with the hot gas in the Galactic halo instead of a tidal interaction (Moore & Davis, 1994; Mastropietro et al., 2005b). Second, that the origin of the Magellanic Stream is a remnant from the tidal disruption of the Small Magellanic Cloud (SMC) owing to its gravitational interaction with the LMC and the Milky Way (Murai & Fujimoto, 1980; Connors et al., 2006). Both scenarios have not been very successful in explaining the origin of the Magellanic Stream and in answering the missing LMC stellar ejecta problem. In this study, we suggest another scenario for the missing LMC ejecta: LMC stars are protected by the LMC dark

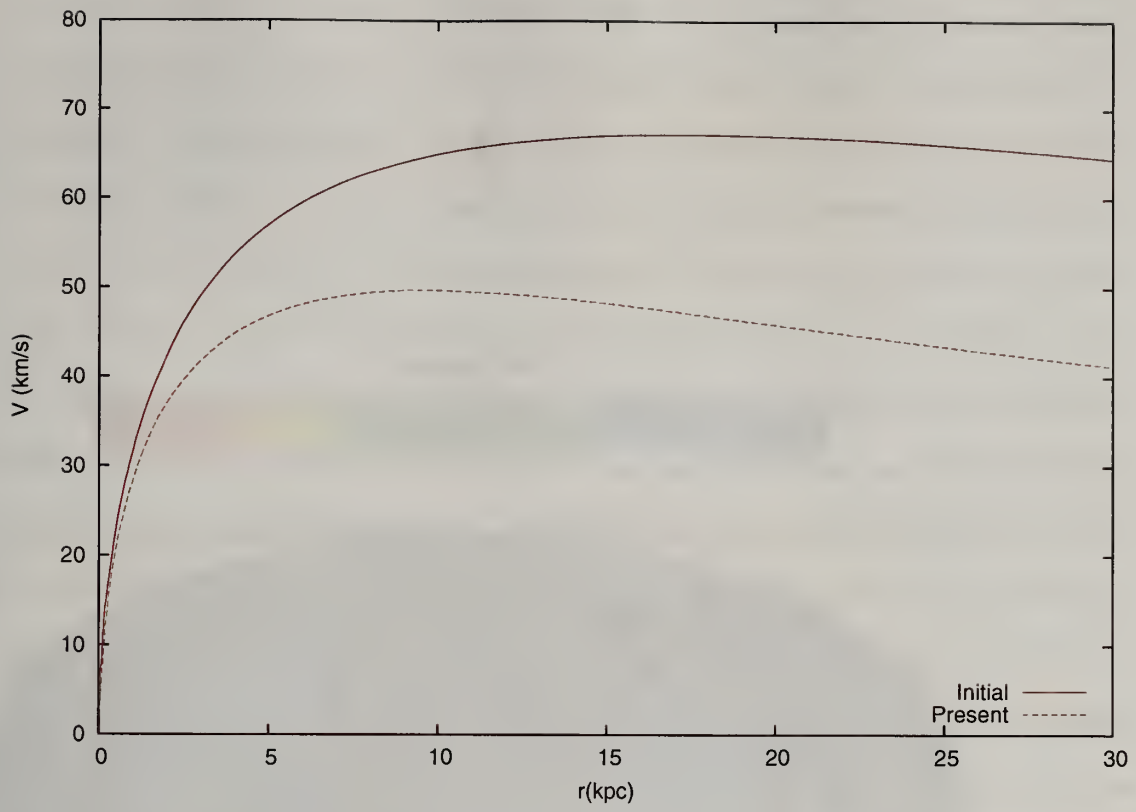

Figure 2.19 The circular velocity curve of LMC dark matter halo at the initial and present time.

matter halo. According to the CDM galaxy formation model, a galaxy is located at the center of the dark matter halo. If this were the case for the LMC, the LMC stars may still be protected by the LMC dark matter halo. The existence of the LMC gas tail is also in this content. The pattern of satellite halo stripping suggests that the low binding energy particles are stripped earlier than the high binding energy particles. If there were gas whose binding energy were low enough to be stripped while most of stars remained bound, the observation would be straightforwardly explained in tidal interaction theory. We implement a simplified N-body simulation for the disruption of the LMC halo and analyze the simulation as above to verify our hypothesis.

We implement an idealized simulation for LMC evolution in the Milky Way dark matter halo. The static Milky Way dark matter halo potential is based on the A1 model of Klypin et al. (2002), $c = 12$ NFW halo with $R_{vir} = 258kpc$, $M_{vir} = 1.0 \times$

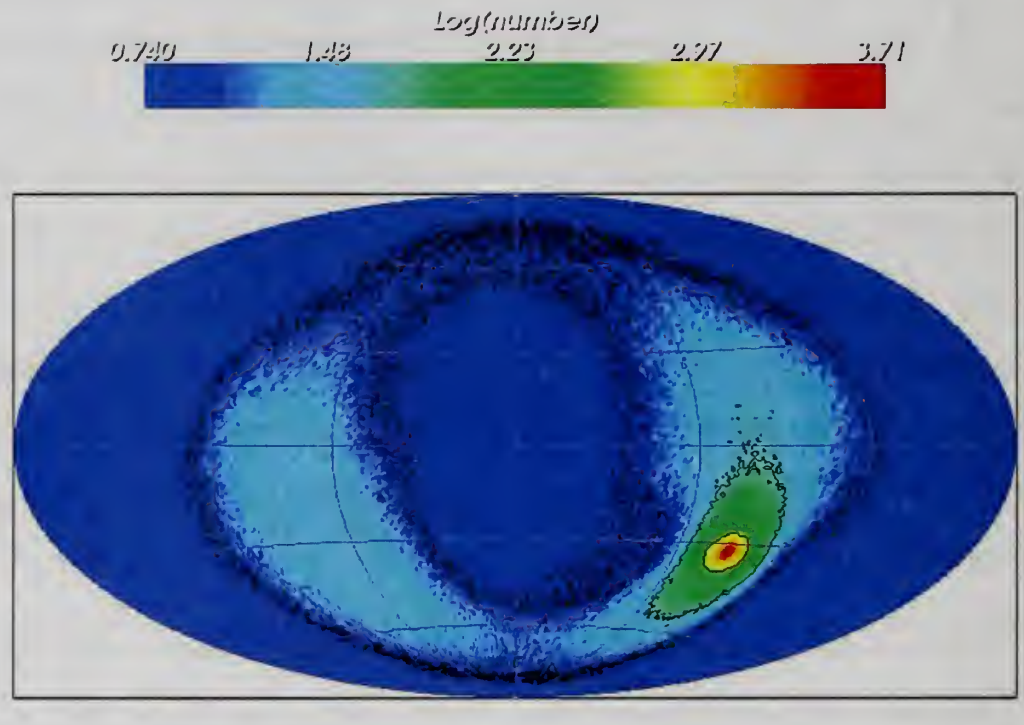

Figure 2.20 An Aitoff Projection of the number density of LMC dark matter halo particles at the present time. The projection shows the well developed LMC tidal tail which stretches over 360° along a Galactic polar circle.

$10^{12} M_{\odot}$, and $V_{max} = 163 km/s$. The live LMC halo is generated in the same way as other satellites in our study. The LMC halo model, which is based on the c=12 NFW halo model, is truncated at its x_e radius assuming that the LMC is located at $0.6 R_{vir}$. To make a stable halo model we performed an Eddington inversion to the truncated LMC halo model as before. In our simulation, the LMC halo is made up 10^6 equal-mass particles. The initial LMC halo circular velocity, $V_{max,LMC} = 0.42 V_{max,host}$, is empirically determined to make the present LMC circular velocity from our simulation match the observed LMC circular velocity, $V_{max,LMC} = 0.3 V_{max,host}$ (Kim et al., 1998; van der Marel et al., 2002). Figure 2.19 shows the initial and present LMC rotation velocity. Since the LMC evolutionary history is not clearly understood, we assume a simple LMC orbit: an e=0.5 orbit with a pericenter at $0.2 R_{vir}$ and an apocenter at $0.6 R_{vir}$. The current LMC is assumed to be located just after its pericenter (Gardiner et al., 1994; Gardiner & Noguchi, 1996). The simulation starts at $0.6 R_{vir}$ and runs a little more than two radial periods so that the last simulation output represents the present LMC. The duration of the simulation corresponds to about 2.5 time unit periods, which is about 5 Gyr. The Aitoff projection of the simulated present LMC is shown in Figure 2.20.

Figure 2.21 shows the fraction of the particles remaining in the LMC phase space and their average distance from the center, with the phase space location in Figure 2.21 based on the initial location. The stripping shown in Figure 2.21 corresponds to an outside-in stripping process in satellite energy space as before. According to Figure 2.21, we can see in which part of the LMC halo has remained intact after tidal stripping. Although our simulation does not include an LMC disk, we can infer the phase space location of such a disk. Since the LMC disk is rotationally supported, it is expected to be located at the high angular momentum area in phase space ($\kappa \geq 0.9$). Therefore, LMC stars should also be located in the high angular momentum region, i.e. particles with large κ.

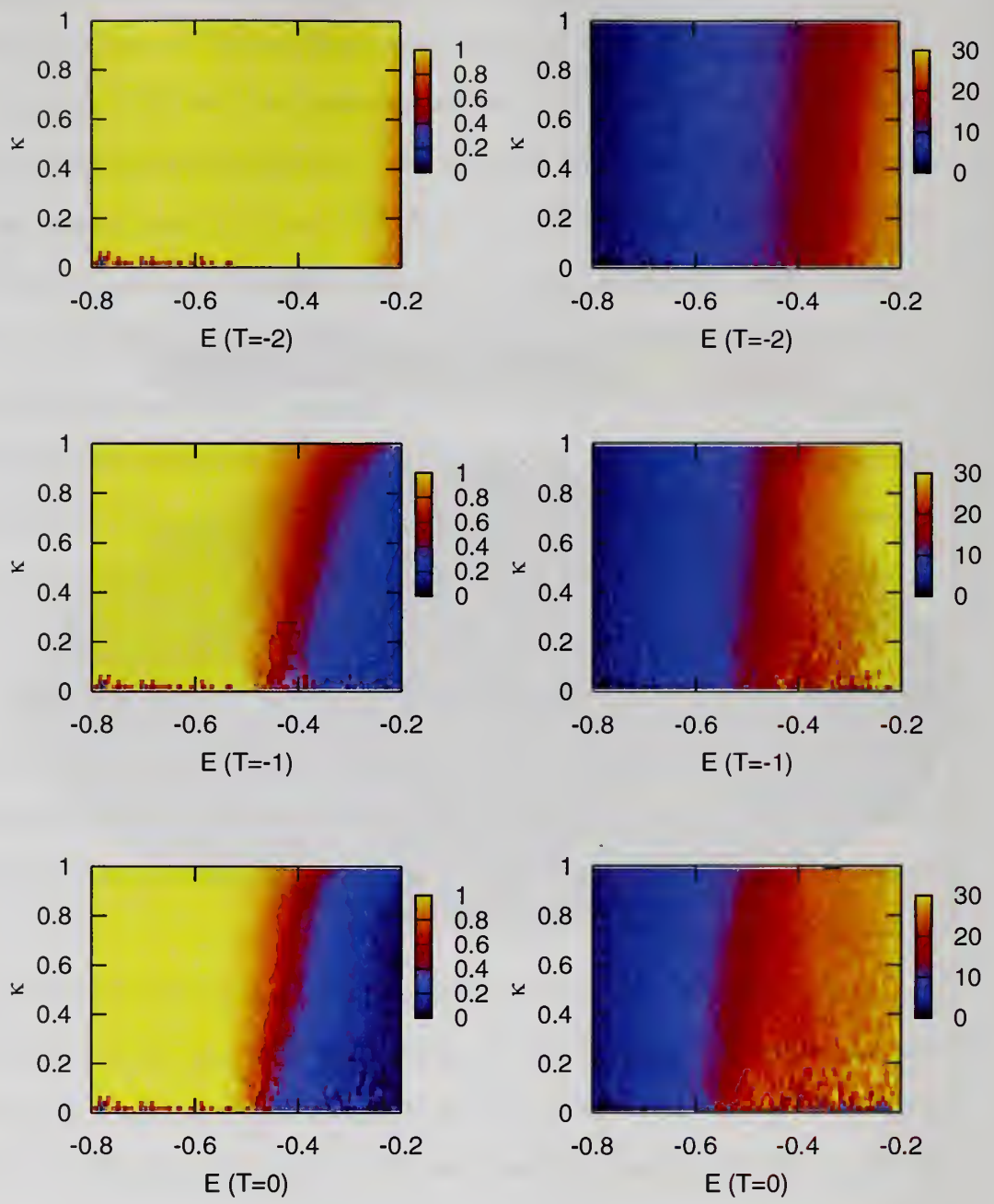

Figure 2.21 The distribution of particles remaining in the LMC halo. *Left panels:* The fraction of particles remaining in the LMC halo based on their initial location in phase space. The color code is linear in the fraction of particles remaining with 1 meaning that all the particles initially at that phase space location are still in the satellite and 0 meaning that all the particles are already stripped. *Right panels:* The average radius of the particles remaining at a given radius.

Figure 2.21 shows that particles whose energy is higher than -0.5 have been seriously stripped. The current mean radius of the particles for $E = -0.5$ and $\kappa = 0.9$ is about 15 kpc. Although 15 kpc is the mean radius, the high κ particles hardly vary in radius because their orbit is close to a circular orbit. 15 kpc is larger than the usually assumed LMC stellar disk radius, which is about 10 kpc or less (Kunkel et al., 1997). This implies that tidal stripping has not damaged the LMC stellar disk and provides an interesting argument as to why we have never detected LMC stellar ejecta. The 15 kpc tidal radius corresponds to the radius for high angular momentum stars. It is possible that some LMC stars have a lower angular momentum. In particular, stars which have been heated by gravitational interaction with the Milky Way (Weinberg, 2000) can be pumped out of the LMC disk and have a low angular momentum. However, the number of these stars is very small compared to the high angular momentum disk stars. Moreover, the phase space location is the initial location when the LMC stars had not been seriously heated. This suggests that the detectable signature of the LMC stellar ejecta is very small. This argument also provides a reason why the Magellanic Stream consists only of gas. There should be a considerable fraction of gas which still exists in the outskirts of a dark matter halo at lower binding energies, while almost all the stars reside in the center of higher binding energies. This low binding energy gas can be stripped along with dark matter and forms the Magellanic Stream. Our phase space argument about satellite stripping naturally explains the existence of the gaseous Magellanic Stream and the absence of the LMC stellar ejecta.

2.6 Estimating satellite mass loss

We have investigated the detailed physical processes of satellite evolution in a host halo and it would be useful if we could establish a simple analytic estimate to predict satellite mass loss based on these processes. In this section, we provide an improved analytic estimation for satellite mass loss based on the findings in this study.

To estimate satellite mass loss, researchers often use a simple formula based on the impulse approximation. The impulse approximation assumes a constant potential energy of stars during the heating (Spitzer, 1987). In Section 2.3 and Section 2.4, we investigated the detailed physical processes of satellite halo disruption and found that satellite halo disruption involves complicated physical processes such as resonant effects, internal structure evolution, and tidal truncation. Therefore, we must to examine how accurately the approximation can estimate satellite mass loss. In particular, Section 2.3 suggested that two distinct resonant effects affect satellite evolution. The contribution of these two resonance effects need to be included in our improved analytic estimation.

In this estimation, we use a mass shell scheme to estimate the satellite mass loss owing to tidal truncation, gravitational shocking, and resonant torquing. A brief sketch of the analytic mass loss estimation scheme is as follows:

1. The satellite model is the same as that of the simulations.

2. The satellite orbits in the scheme follow the same trajectory as those in the simulations.

3. At each time step, x_e is computed according to the satellite location and velocity in the host halo.

4. The satellite mass outside of the tidal radius is stripped. The fraction of stripped mass for each time step is $\Delta t/t_{orb}$ where t_{orb} is the orbital period at the half mass radius of the satellite.

5. The injected energy and angular momentum for given mass shell from the time-dependent external potential is computed.

    - The injected angular momentum owing to the resonant torque is computed at every step.

- The injected energy owing to the gravitational shock is only computed at every pericenter.

6. The injected energy and angular momentum reduce the density of a given mass shell.

7. The reduced density results in mass loss and decreases x_e. Owing to this decrease, mass loss is enhanced.

This analytic mass loss estimation is similar to the scheme used in Taylor & Babul (2001, 2004, 2005a,b). It provides the satellite mass loss history, which can be used in the comparison with the simulation results.

For the gravitational shock heating, we compute the injected energy using the impulse approximation with an adiabatic correction. Gnedin et al. (1999) derive the expression for the mean injected energy by the tidal field from a spherical galaxy. Assuming an isothermal host halo, the injected energy is computed by the simple formula:

$$\Delta E = \frac{1}{6}(\frac{\pi r}{R_p^2 V_p})^2 \frac{M_{halo}}{R_p} A(x) \tag{2.5}$$

where r is the satellite radius, R_p is the pericenter distance, and V_p is the satellite velocity at the pericenter. M_{halo} is the mass of the perturber, which is the enclosed halo mass at the pericenter here. $A(x)$ is an adiabatic correction, which reduces the amount of heating if the dynamical time of satellite orbits is significantly shorter than the impulsive time scale. We adopt both the Spitzer correction and the Weinberg correction (Gnedin & Ostriker, 1999; Weinberg, 1994a,b):

$$A(x) = exp(-2x^2) \qquad (Spitzer) \tag{2.6}$$

$$A(x) = (1+x)^{-1.5} \qquad (Weinberg) \qquad (2.7)$$

where $x = \omega(\frac{\pi R_p}{V_p})$ and ω is the angular velocity of an orbit at a given satellite radius. Equations 2.5 – 2.7 provide the amount of injected energy to a given satellite mass shell for each shock event. The injected energy expands the satellite. Using the virial theorem, the expansion rate can be estimated as $\Delta r = \Delta E r^2$ (Taylor & Babul, 2001). This satellite expansion reduces the density as $\Delta\rho = -\frac{9}{2\pi}\frac{\Delta E}{r^2}$. The reduced density is applied to step (6) in the analytic mass loss estimation.

Section 2.3 confirmed that heating by the resonant torque plays an important role in satellite mass loss. This resonant effect is different from the resonant effect during the gravitational shock (Weinberg, 1994b), and has not been seriously taken into account in a satellite evolution study. To accurately estimate the resonant torque effect we need to use high quality N-body simulations (Weinberg & Katz, 2007a) or complicated perturbation theory calculations (Weinberg, 1986, 1989). However, we can crudely estimate the torque using a toy model. Our crude approximation is based on two steps:

First, we compute the torque on the satellite mass shell using a ring approximation. The torque on the ring is computed using the simple spin-orbit coupling calculation in the planet-satellite interaction. The torque on mass shell is computed as follows:

$$\tau_{ring}(R) = 6GM\frac{R}{R_{sat}} \qquad (2.8)$$

where R_{sat} is the distance from the host halo center to the satellite, R is the distance from the satellite center to a given mass shell, and M is the enclosed host halo mass (Murray & Dermott, 1999, Chapter 5.3 see their Figure 5.7). Equation 2.8 provides the specific torque on the satellite mass shell.

Second, we compute the fraction of resonant orbits per each mass shell. Equation 2.8 computes the torque on the ridge mass shell, not the torque on the mass shell

owing to the resonant interaction. Each mass shell is made up of many different orbits, and those that are nearly commensurate with the perturber's frequency get torque. To estimate the resonant torque on the mass shell, we need to estimate the mass fraction of coupled orbits in the mass shell and multiply the torque on the ridge mass shell by this fraction. As shown in Equation 2.2, determining resonant orbits requires complicated calculations. Since our purpose is to approximate the resonant torque effect, the fraction of resonant particles at a given satellite mass shell is simply estimated as the ratio of the azimuthal angular frequency of the orbiting satellite to the angular frequency of satellite mass shell [7]. Consequently, the torque on the satellite mass shell becomes:

$$\tau_{sat}(R) = \tau_{ring}(R) \times \frac{\Omega_s}{\omega(R)} \qquad (\Omega_s \geq \omega(R)) \qquad (2.9)$$

$$= \tau_{ring}(R) \times \frac{\omega(R)}{\Omega_s} \qquad (\Omega_s < \omega(R)) \qquad (2.10)$$

Torquing the satellite is equivalent to adding kinetic energy to the satellite and this leads to the satellite expansion. The satellite expansion rate can be estimated as $\Delta r = \sqrt{\frac{4r}{M_{sat}(r)}}\tau_{sat}\Delta t$. This satellite expansion reduces the satellite density as $\Delta\rho \propto -\frac{\Delta r}{r^4}$. We also apply this relationship to step (6) in the analytic mass loss estimation routine.

The mass loss histories for the circular orbit simulation, the eccentric orbit simulation, and the inner orbit simulation are shown in Figures 2.22 – 2.24 respectively. Each figure shows several analytic estimations for the mass loss depending on the included physical processes.

For the circular orbit case, there is no gravitational shock effect. Figure 2.22 shows two analytic estimations: "No Shock" and "Torque". "No Shock" only includes the

[7]The angular frequency $\omega = \frac{V_c}{R}$ where V_c is the circular velocity and R is the radius of a given mass shell.

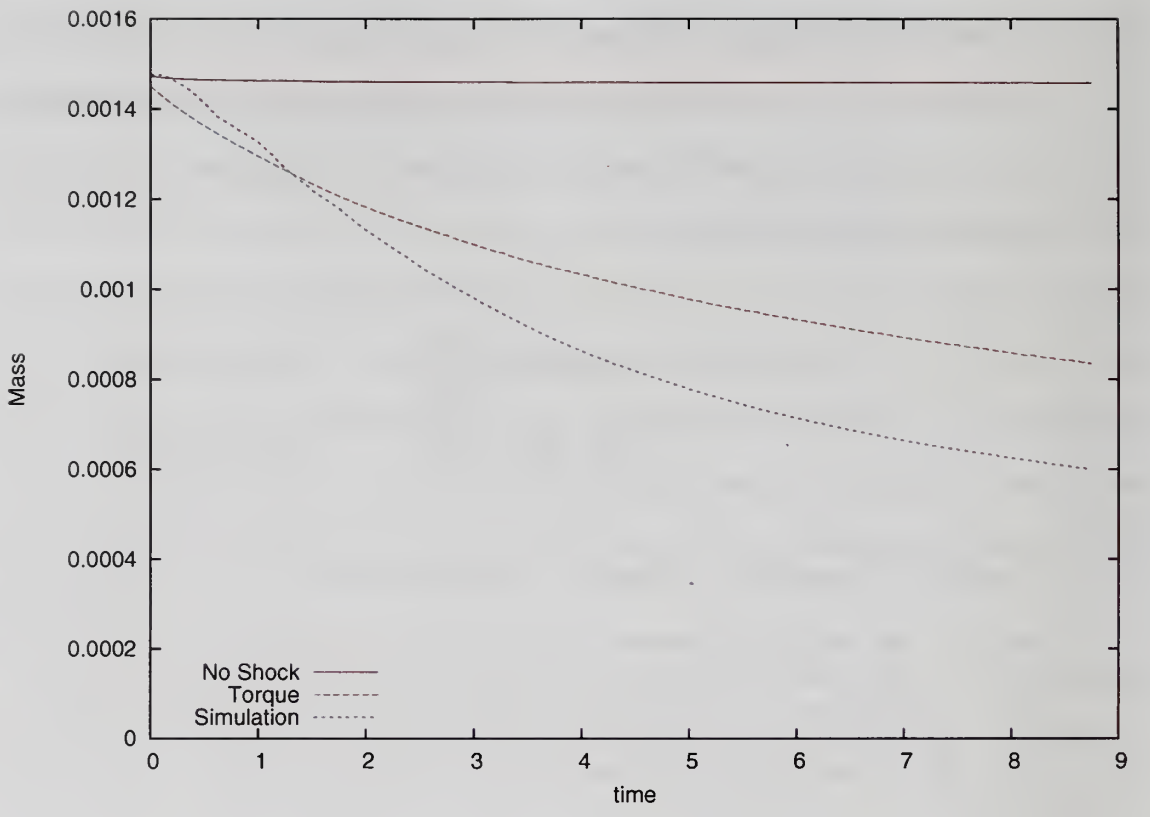

Figure 2.22 The mass loss history of the circular orbit simulation. The analytic estimations of the mass loss history are compared with the simulation. "No Shock" is an analytic estimation only including the effect of tidal truncation. "Torque" is an analytic estimation including the effects of tidal truncation and the resonant torque.

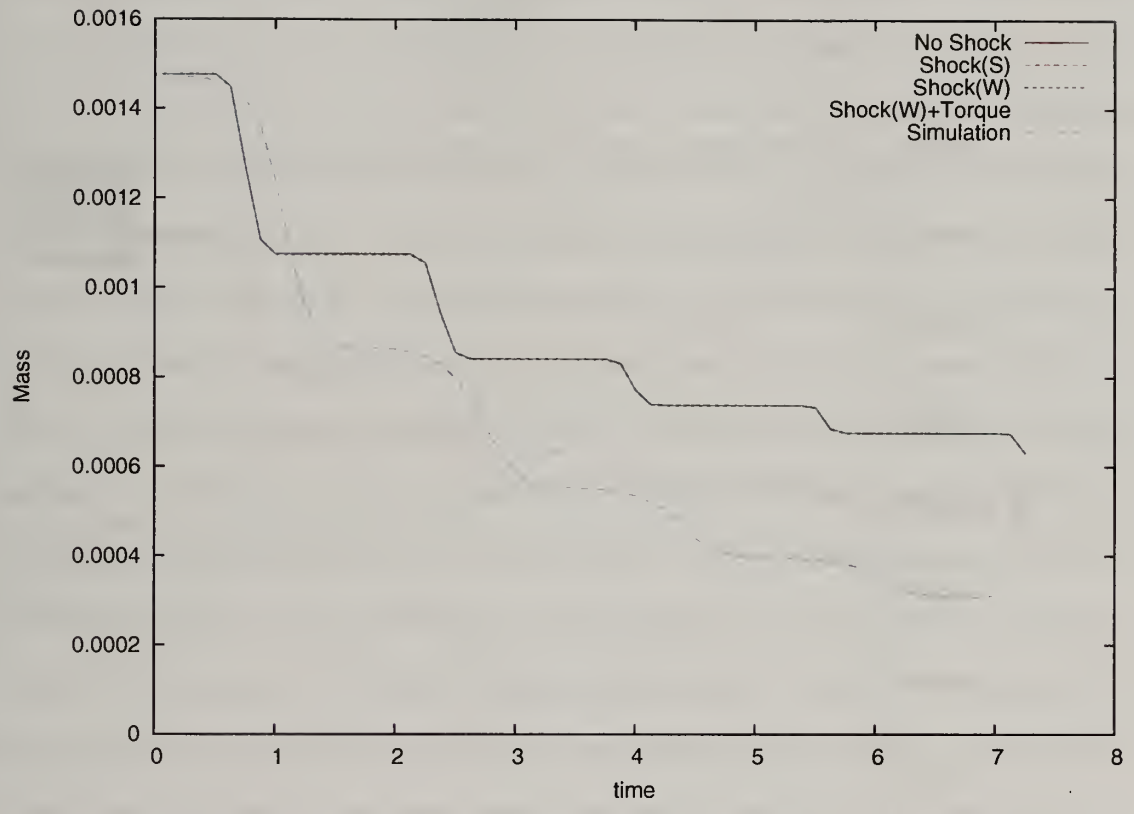

Figure 2.23 Mass loss history for the eccentric orbit simulation. The analytic estimations of mass loss history are compared with the simulation results. "No Shock" is an analytic estimation only including the effect of tidal truncation. Shock(S) is an analytic estimation including the effects of tidal truncation and impulse shock heating with the Spitzer correction. Shock(W) is an analytic estimation including the effects of tidal truncation and impulse shock heating with the Weinberg correction. Shock(W) + Torque is the same as Shock(W) but with the addition of the resonant torque.

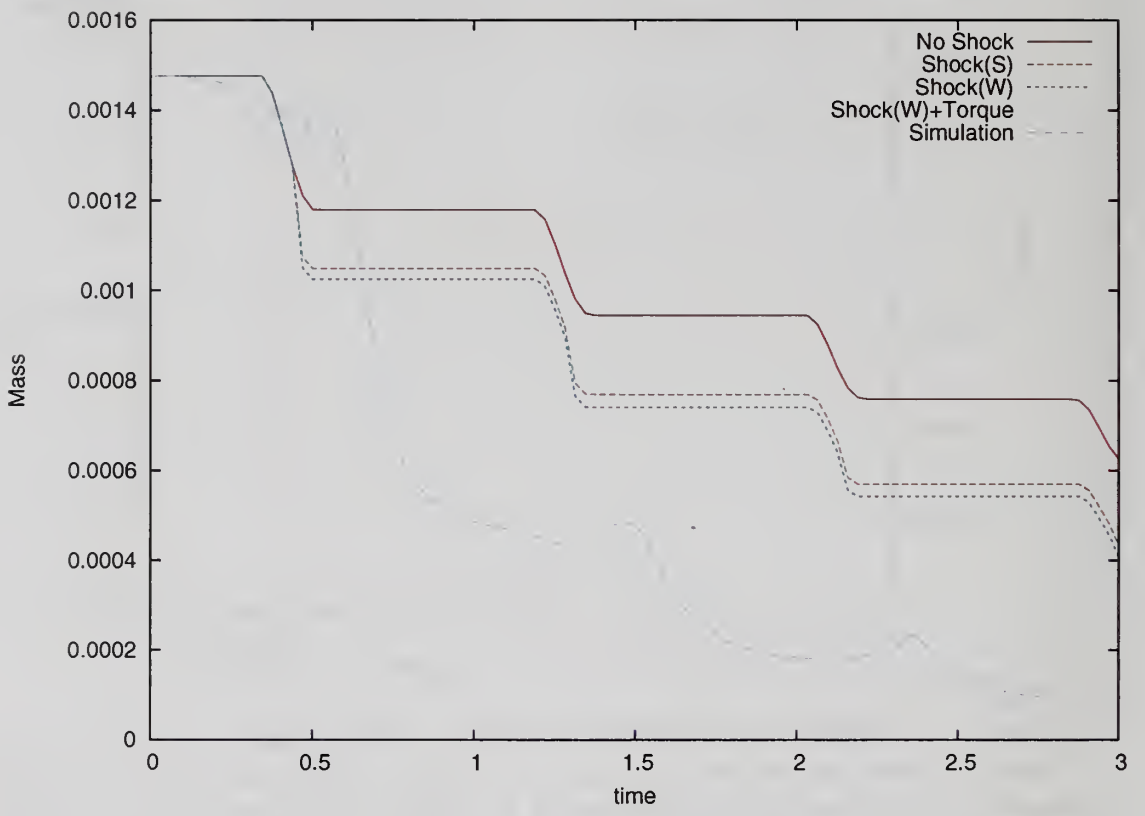

Figure 2.24 The same as Figure 2.23 but for the inner orbit simulation.

tidal truncation effect. "No Shock" predicts almost no mass loss while the satellite loses more than 50% of its original mass in the simulation. "Torque" also includes the resonant torque effect as well as the tidal truncation effect. "Torque" shows a mass loss history that is similar to the simulation. This suggests that the circular orbit satellite mass loss mainly results from the resonant torque effect and our analytic estimation for resonant torque provides a dramatically improved mass loss estimate. In the eccentric orbit and inner orbit simulation cases, the gravitational shock plays an important role in the mass loss history. Figures 2.23 and 2.24 show several analytic mass loss histories: "No Shock", impulse approximation with Spitzer correction, impulse approximation with Weinberg correction, and the resonant torque effect as well as an impulse approximation with Weinberg correction. All the estimations include the tidal truncation effect. Comparing to the simulation results, the analytic estimation that includes the resonant torque effect and impulse approximation with Weinberg correction shows the best agreement. If the resonant torque effect were excluded, all the analytic estimation results predict less mass loss than the simulations. To discriminate the best impulse approximation scheme, we compare three analytic estimations that do not include the resonant torque effect. In the eccentric orbit case, the difference between these three analytic estimations is insignificant. In the inner orbit case, this difference becomes clear: Compared to the simulation, the estimate assuming the impulse approximation with the Weinberg correction agrees best and the estimate assuming only the tidal truncation effect ("No Shock") shows the worst agreement. In conclusion, to approximately estimate satellite mass loss one shall adopt our new, improved analytic estimation which includes torque effect as well as the impulsive shock heating with the Weinberg adiabatic correction.

Although our new analytic estimation provides a dramatically improved satellite mass loss history, some discrepancies still exist, which result from the many complicated physical processes involved in satellite disruption. First, during a compressive

gravitational shock, the satellite's internal structure changes, that is, not only the kinetic energy but also the potential energy change. This fact literally violates the impulse assumption and makes satellite evolution a non-linear process. Second, satellite heating by resonant interactions is too complicated to be accurately represented by a simple parameterization. Although our new analytic estimation includes an adiabatic correction to the impulsive approximation and the torque effect, the resonant dynamics is far too complicated a process to be reproduced with a simple formula. For example, the adiabatic correction simply reduces the amount of heating from the impulsive approximation. However, what really happens in the adiabatic regime is that most orbits conserve their energy and angular momentum while some orbits near resonance gain energy through resonant couplings. This process is hard to accurately reproduce by simply reducing the amount of heating. Third, the mass loss scheme used in the analytic estimation is crude. A real satellite halo has a wide range of orbits, from circular orbit to a radial. The mass shell scheme cannot accurately capture the dynamics of these different orbits. Moreover, the entire satellite structure readjusts its evolution in the course of satellite disruption. This readjustment process is not considered in the mass shell scheme. These arguments suggest that although our new analytic estimations provide improved satellite mass loss histories, high quality simulations are still necessary to estimating satellite mass loss accurately.

2.7 Summary and Conclusions

Using high resolution idealized simulations with cosmologically motivated initial conditions; we investigated the detailed physical processes responsible for the evolution of satellite galaxies in their host halo. We find and explore several important physical mechanisms that result in satellite galaxy disruption:

- According to our study, resonant effects play a key role in satellite disruption. These effects can be characterized by two distinct types: the resonant shock and the resonant torque.

- Our calculations show that some important resonances require a much larger number of particles for dark matter subhalos than the usual particle numbers of dark matter subhalos in current cosmological simulations.

- We study a circular orbit satellite simulation to isolate the resonant torque effect. In the circular orbit satellite, the most dominant resonance is the -1:2:2 resonance because all l=1 resonances and the 0:2:2 and -1:2:2 resonances are located outside the satellite tidal radius. We also find that to accurately reproduce the -1:2:2 resonance heating effect, a satellite needs to be made up more than 10^5 particles within virial radius for our expansion code and an order of magnitude larger number of particles is required for codes affected by small-scale noise, e.g. tree code.

- The most dominant heating mechanism is a compressive gravitational shock that occurs pericenter for eccentric orbit satellite evolution. This heating mechanism has several distinction from the impulsive approximation. First, the satellite structure evolves during the interaction so that not only the kinetic energy but also the potential energy changes. Second, since a satellite galaxy always resides in its host halo, the host halo tidal filed always constrains the satellite size. This constraint enhances mass loss and makes the satellite halos remain out of equilibrium. These two features lead to satellite evolution being a non-linear process.

- With a satellite orbiting closer to the halo center, the number of resonances in the satellite increases as the satellite orbital frequency increases, and the strength of each resonance interaction also increases.

- The general pattern of satellite stripping is an outside-in process in energy space. This provides practical limits of how stars and gas in the satellite galaxies would be stripped by the host halo.

Using our improved understanding of the physical processes involved in satellite evolution, we suggest an improved scheme for analytic satellite mass loss estimation. This scheme, which includes the resonant torque effect as well as the impulse approximation with Weinberg correction, provides a similar mass loss history as the simulations. One should use our new analytic estimation scheme to predict the satellite disruption time scale to understand dark matter halo growth and estimate the satellite mass loss rate more accurately.

Although we improved our understanding of the detailed physical processes responsible for the satellite disruption, there are still outstanding issues. By separating it into two distinct types, we achieved an improved understanding of resonant dynamics for an eccentric orbit. However, a comprehensive perturbation theory calculation, which could provide a full accounting of this process, is not yet achieved. The resonant dynamics of the eccentric orbit is also related to satellite heating by other subhalos. This interaction is an important source of satellite evolution other than the interaction with the smooth host halo. The initially spherical satellite is deformed during disruption owing to the host halo tidal field and this deformation has not been accounted for yet. However, a comprehensive treatment of the deformation might be necessary to understand satellite disruption in detail. Lastly, we also need a better understanding of the non-linear processes that occur during satellite evolution.

In this study, we characterized the linear processes, understanding the detailed consequences of the non-linear process are a future task. We should then finally be also to accurately constrain the satellite disruption mechanism, which is an essential ingredient of galaxy formation and evolution.

CHAPTER 3

THE DYNAMICS OF SATELLITE EVOLUTION BY SUBSTRUCTURES

3.1 Introduction

Galaxy harassment is one of the major processes that transforms galaxy morphology in clusters (Moore et al., 1996b, 1998b). In a cluster environment, a disk galaxy is damaged by high speed close encounters with other galaxies and the accumulated damage leads to morphological transformation. Originally, Moore et al. (1996b) proposed this mechanism to explain the origin of the Butcher-Oemler effect in clusters (Butcher & Oemler, 1978, 1984). They showed that the consequences of galaxy harassment are different from those of galaxy mergers and it agrees with observed distribution of galaxy morphology in clusters (Dressler et al., 1994; Oemler et al., 1997). The success of galaxy harassment suggests that cumulative close encounters with other galaxies is a common phenomenon in galaxy evolution.

One example of these phenomena is the destruction of dark matter subhalos (Moore et al., 1996a). Under the cold dark matter (CDM) model, all galaxies reside in their host halo, and the evolution driven by the host halo has a great influence on galaxy formation and evolution. Recent CDM cosmological simulations predict the existence of a large number of subhalos (Ghigna et al., 1998; Klypin et al., 1999). Both an external potential field of the smooth host halo and interactions with other subhalos will cause the evolution of subhalos. Since the CDM model predicts a large population of subhalos, the interactions with other subhalos may be central mechanism in the subhalo evolution. Unless a subhalo collides with other subhalos, the

interaction are high speed close encounters, similar to galaxy harassment. If the interaction results from cumulative high speed close encounters, the physical processes responsible for this interaction are complex. Simple estimations for the consequences of the interaction using the impulse approximation may lead to incorrect results. Therefore, it is necessary to study detailed physical processes in this interaction using N-body simulations in order to understand the evolution of subhalos.

Unfortunately, the resolution of current cosmological simulations is not sufficient to test the physical mechanism in detail. Moreover, it is hard to investigate the processes of a single mechanism using cosmological simulations because many complicated processes simultaneously happen in cosmological simulations. In order to study the interaction with other subhalos, we perform high resolution idealized simulations of satellite evolution with cosmologically motivated initial conditions. Using these simulations, we investigate the evolution of a single high resolution satellite dark matter halo by the interaction with subhalos. This idealized approach can provide a clear insight into the detailed physical process in this interaction and the satellite evolution.

Most previous studies of the subhalo evolution only focused on either the satellite mass loss (e.g. Moore et al., 1996a) or statistical properties of subhalo population (Ghigna et al., 1998, 2000; Tormen et al., 1998; De Lucia et al., 2004; Diemand et al., 2004; Gao et al., 2004; Oguri & Lee, 2004). However, as the results of previous chapter, it is important to study satellite dark matter halo responses due to the interaction with the host halo and other subhalos. In fact, the satellite mass loss is an outcome of the satellite dark matter halo response. In addition, the satellite dark matter halo response affects the evolution of satellite galaxy. Therefore, investigating both satellite dark matter halo responses and satellite mass loss is an important issue in studying satellite evolution. Since our simulation has sufficient resolution and

is able to follow the satellite evolution in detail, we can therefore investigate both consequences simultaneously.

In this study, we use high resolution idealized simulations of satellite evolution with cosmologically motivated initial conditions to study the satellite evolution due to the interaction with subhalos. In Section 3.2, we present the initial conditions and numerical simulations used in this study. In particular, we demonstrate in detail how to generate realistic subhalo populations based on the CDM model. In Section 3.3, we present mass loss histories of our satellites. In Section 3.4, we investigate satellite dark matter halo responses due to the interactions with subhalos. In Sections 3.3 and 3.4, we compare the simulation results with and without subhalos to distinguish the effects of the interaction with subhalos on satellite evolution. We present conclusion in Section 3.5.

3.2 Review of experimental schemes

All halo models of our simulations are based on the universal CDM halo (Navarro et al., 1997, hereafter NFW) [1]. The host halo potential is represented by a concentration c=15 static NFW halo. As a result, our simulations ignore the effects of dynamical friction and the subsequent reaction of the host halo but since the satellite masses of interest are often much smaller than the host halo mass, the consequences of the dynamical friction are minor. Since the objective of this study is an understanding of the interaction with subhalos, our simulations use a host halo including substructures which we call a lumpy halo hereafter. This lumpy halo is made of both smooth host halo potential and subhalos. Later in this section, we will present subhalo generation procedure. We need to modify the host halo potential by subtracting subhalo distribution. We estimate mass profile of the distribution of subhalos from

[1] $\rho(r) \propto r^{-1}(r + r_s)^{-2}$, where r_s is a scale length characterized by the concentration parameter $c = R_{vir}/r_s$ and R_{vir} is a virial radius of the halo.

initial subhalo distribution, which will be specified below, and subtract this profile from the host halo mass profile. After subtracting the subhalo mass, we smooth new host halo profile using Chebyshev polynomial fit to avoid discontinuity in the profile. The new host halo model is used to compute the fixed part of gravitational potential. The combined total external potential for the satellite for is an good approximation to the initial host halo profile.

Our simulations include a population of subhalo in the lumpy halo based on recent cosmological simulations (De Lucia et al., 2004; Diemand et al., 2004; Gao et al., 2004). Most cosmological simulations predict that total subhalo mass is about 10% of a total halo mass and we adopt this value. We compute the number distribution of subhalos based on subhalo's circular velocity distribution. Since subhalos suffer a tidal stripping, the circular velocity is appropriate choice to characterize the subhalo size (see Choi et al., 2007). We adopt the following relation for the number distribution of the subhalo circular velocity.

$$N(< v_c) \propto v_c^{-3} \tag{3.1}$$

where v_c is subhalo's circular velocity. Using the virial theorem, we can prove that this relation is equivalent to $N \propto m^{-1}$, which is natural outcome if hierarchical merging produces subhalo mass functions that do not depend on the mass of parent halo (Moore et al., 1999; Diemand et al., 2004). The v_c range in our subhalos is $0.03 < v_c < 0.3$. In order to locate the generated subhalos in the host halo, we adopt the radial number distribution suggested by Gao et al. (2004);

$$N(< r)/N_{total} = (1 + ac)r^{\beta}/(1 + acr^{\alpha}) \tag{3.2}$$

where c is the halo concentration, a=0.244, $\alpha = 2.0$, and $\beta = 2.75$ Many different cosmological simulations suggest a similar radial number distribution (De Lucia et al.,

2004; Diemand et al., 2004; Oguri & Lee, 2004) We assume that the subhalo distribution is isotropic from host halo center. In order to compute subhalo's velocity, we construct a distribution function using Osipkov-Merritt model (Osipkov, 1979; Merritt, 1985). In this distribution, an anisotropic radius is chosen $r_a = 0.25$ and the density profile is assumed to be the same as the density profile of the smooth host halo. Subhalo's location in the smooth halo constraints the range of the subhalo's energy and its velocity is computed using accepting and rejection method based on this distribution function. This anisotropic velocity distribution represents the suggested subhalo velocity distribution: isotropic in the inner halo and more radial in the outer halo (Eke et al., 1998; Colín et al., 2000; Diemand et al., 2004). Although the subhalo's size is characterized the circular velocity, the mass and radius of subhalos are necessary to implement N-body simulations. We assume that a subhalo is an isothermal sphere and the radius of subhalo is determined by a tidal radius of satellite at a given location in the host halo. The mass of subhalo is computed by its radius and circular velocity with the isothermal sphere assumption. To perform N-body simulation, the softening length of the subhalo is set to be half of subhalos radius. Modified host halo potential and generated subhalos makes the lumpy halo.

The satellite halo initial condition is the same as described in Chapter 2. Initially, a satellite halo is represented by a c=15 live NFW halo. Its rotation velocity $V_{sat} = \frac{1}{12}V_{host}$. We determine the truncation radius at a given satellite location in the host halo. Here, we use x_e for the truncation radius. The tidal distance in our satellite is $R = 0.4R_{host,vir}$. After truncation, we perform the Eddington inversion in order to make an equilibrium halo model (Binney & Tremaine, 1987, Chapter 4). The output of the Eddington inversion is the final satellite halo model. The satellite halo realization is generated using the acceptance-rejection method with 10^6 equal mass particles. The velocity distribution of satellite particles is isotropic.

In our study, we compare the evolutions for three different satellite orbits: a circular orbit, an eccentric orbit, and an inner orbit. In the circular orbit simulation, the satellite is on a circular orbit at the tidal distance. In the eccentric orbit simulation, the satellite is on an $e = 0.5$ orbit whose apocenter $r_{apo} = 0.6$ and pericenter $r_{peri} = 0.2$ [2]. The circular orbit and the eccentric orbit have same orbital energy. In the inner orbit simulation, the satellite is an $e = 0.72$ orbit whose apocenter $r_{apo} = 0.4$ and pericenter $r_{peri} = 0.064$. The normalized angular momentum (κ) of the inner orbit is 0.55 which is about median κ of subhalos in a sample taken from recent cosmological simulations (Ghigna et al., 1998; Zentner et al., 2005).

We use the 3-dimensional self-consistent field code (SCF, also known as expansion code; Clutton-Brock, 1972, 1973; Hernquist & Ostriker, 1992; Weinberg, 1999). The expansion code determines bi-orthogonal basis sets of density-potential pair and computes the gravitational potential of the system from the basis sets (see Chapter 1. The expansion code is an attractive gravitational potential solver for two reasons. First, the expansion basis may be chosen to follow structure over an interesting range of scales and simultaneously suppresses small-scale noise. In contrast, the noise from two-body scattering can arise at all scales in direct-summation, tree, and mesh based codes. Small-scale noise can give rise to diffusion in conserved quantities, which can lead to unphysical outcomes particularly for studies of long-term galaxy evolution (Weinberg & Katz, 2007a,b). Second, the expansion code is computationally efficient; the computational time only increases linearly with particle number. Hence, the expansion code permits the use of a much larger number of particles than most other codes for the same computational cost.

Our expansion code has been improved to alleviate several intrinsic shortcomings (Weinberg, 1999; Choi et al., 2007). First, employing numerical solution of the Sturm-

[2]The eccentricity of an orbit is defined as $e \equiv (r_{apo} - r_{peri})/(r_{apo} + r_{peri})$

Liouville equation, an initial galaxy model can be used as zero-order basis function for the expansion code. Using this scheme the expansion code requires only a few basis functions to accurately compute the potential. Second, the center of expansion at which the energy minimum is assumed can be traced during the course of a simulation. This centering scheme provides an accurate center for the expansion that is a critical issue in the potential calculation of the expansion code. Third, to reduce truncation error a simulation separately tracks the motion relative to the satellite's center and the motion of the satellite center. With these improvement schemes, the expansion simulations are now able to achieve a high enough resolution and a low enough noise to investigate the detailed physical processes in the satellite disruption properly.

In our simulations, satellite particles feel the satellite's self-gravity, the host halo potential, and the gravity from the population of subhalos. The subhalos behave as a point mass particle with a given softening length. They feel the host halo potential and the satellite potential.

3.3 Mass loss due to harassment

3.3.1 Mass loss

The satellite mass loss influences the distribution and the lifetime of the satellite. Figures 3.1, 3.2, and 3.3 show the mass loss histories for the circular orbit satellite, the eccentric orbit satellite, and the inner orbit satellite respectively. In order to clarify the effect of subhalos, we compare the satellite mass loss in both the smooth halo and the lumpy halo. These figures show that a satellite in the lumpy halo loses more mass than a satellite in the smooth halo. In addition, the amount of mass loss depends on the satellite orbit.

In the circular orbit satellite simulations, satellites in the lumpy halo lose more mass than the satellite in the smooth simulation. In order to confirm this trend, we implement several circular orbit simulations with different orbital paths. Since the

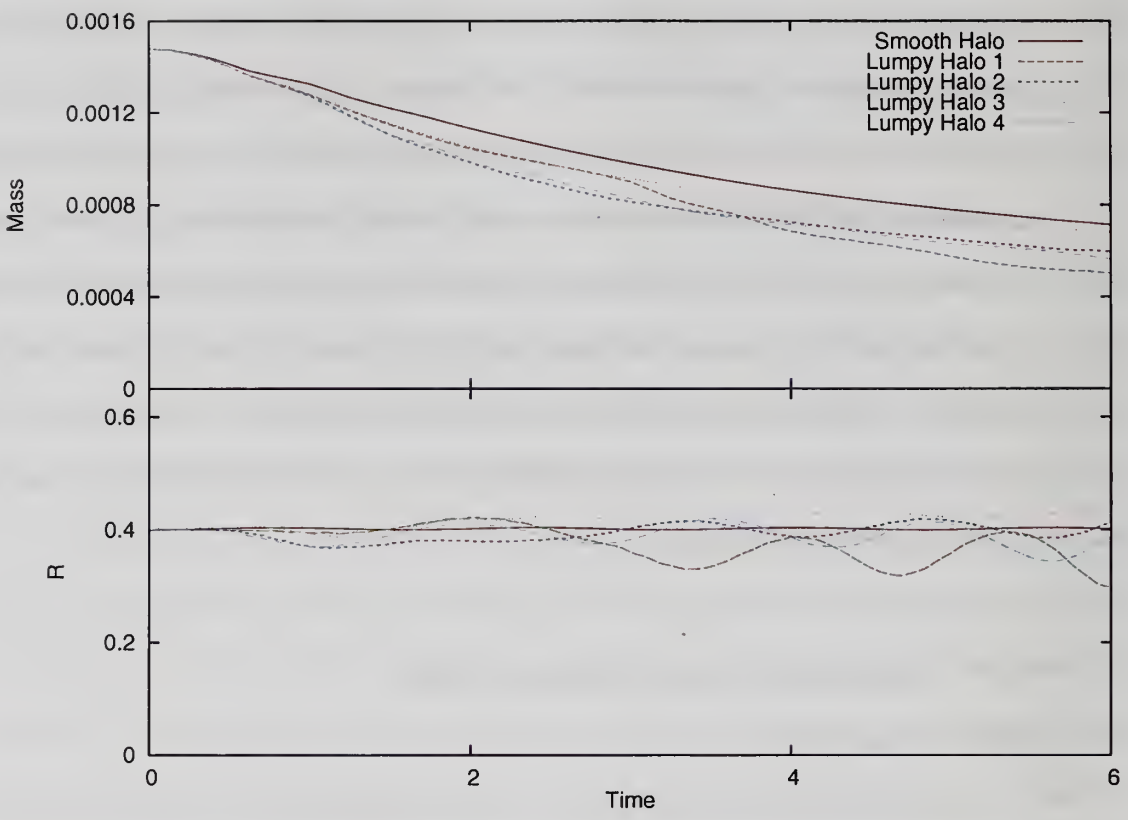

Figure 3.1 The mass loss history of the circular orbit satellites. The top panel shows the mass loss history. The smooth halo represents the satellite evolution in the smooth halo, and the lumpy halo represents the satellite evolution in the lumpy halo. The bottom panel shows the time evolution of the distance of the host halo center to the satellite. The lumpy halo simulations show more mass loss than the smooth simulation.

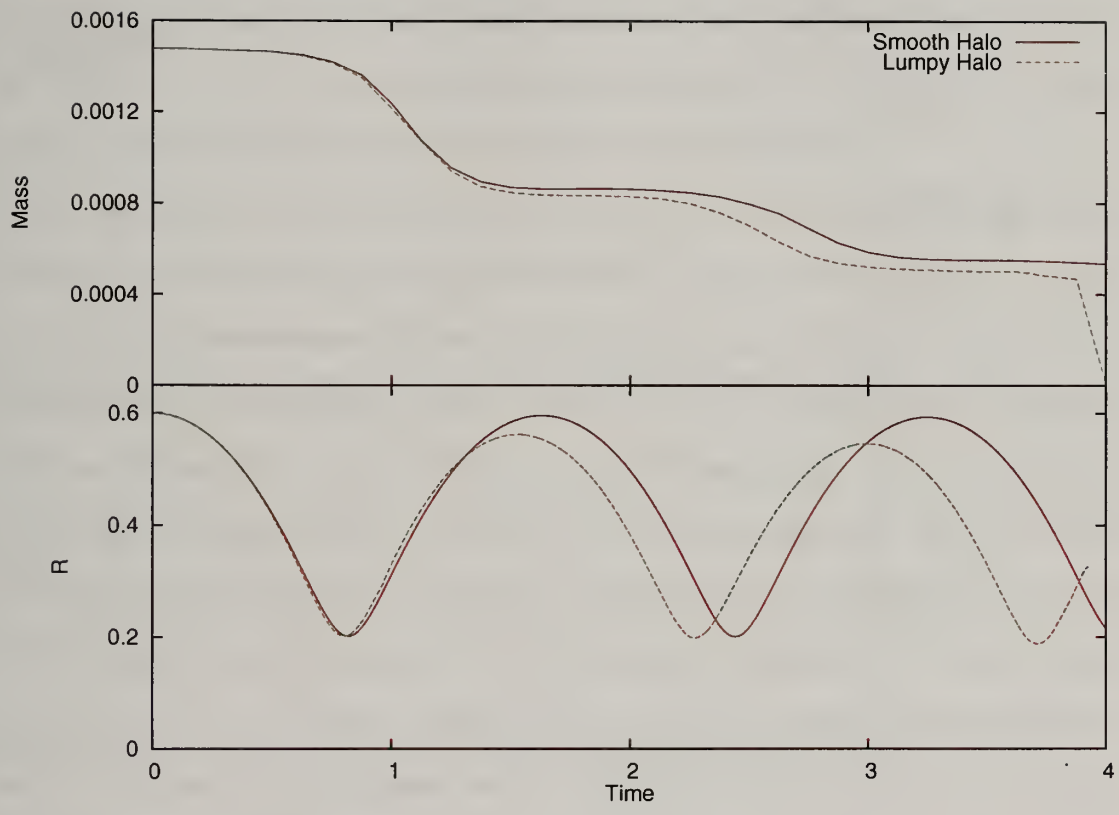

Figure 3.2 The mass loss history of the eccentric orbit satellites. The top panel shows the mass loss history. The smooth halo represents the satellite evolution in the smooth halo, and the lumpy halo represents the satellite evolution in the lumpy halo. The bottom panel shows the time evolution of the distance of the host halo center to the satellite. The lumpy halo simulation shows more mass loss than the smooth simulation.

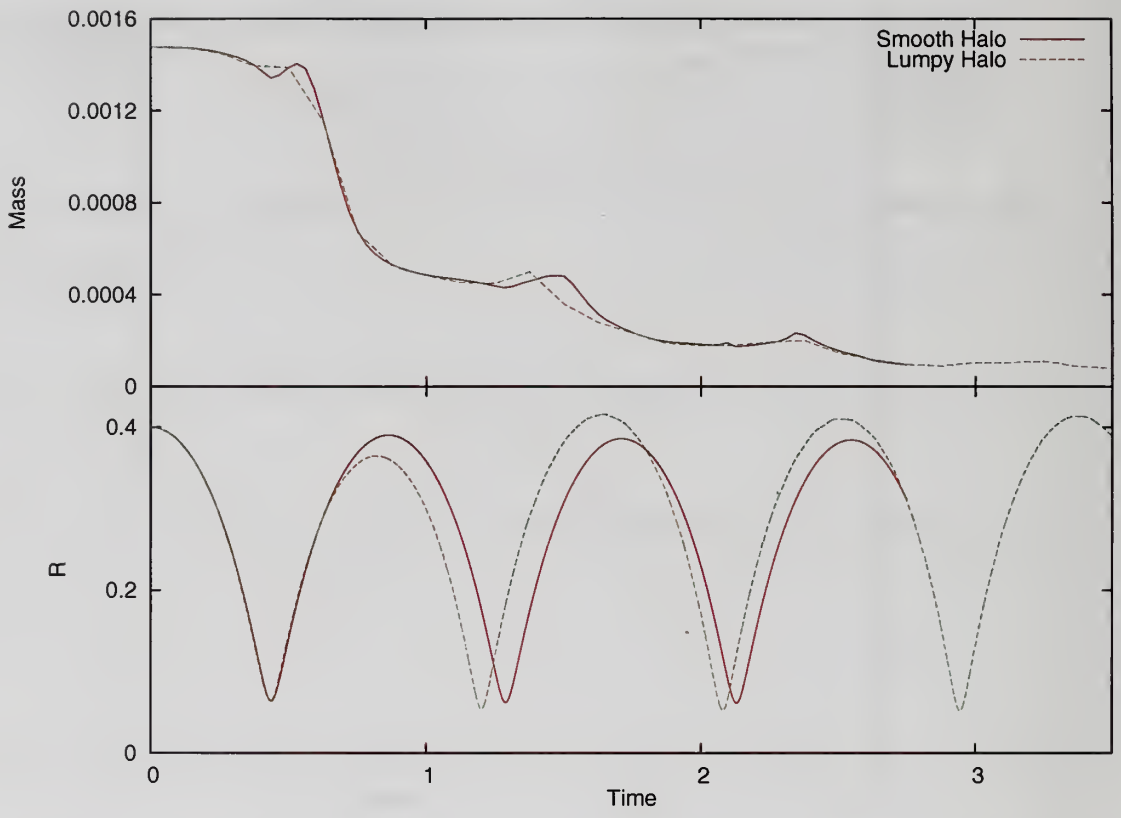

Figure 3.3 The mass loss history of the inner orbit satellites. The top panel shows the mass loss history. The smooth halo represents the satellite evolution in the smooth halo, and the lumpy halo represents the satellite evolution in the lumpy halo. The bottom panel shows the time evolution of the distance of the host halo center to the satellite. The mass loss in the lumpy halo simulation is almost the same as the smooth halo simulation.

distribution of subhalos is not completely homogeneous, satellites on different orbital paths have different interactions with subhalos. We changed both the orbital plane and the direction of the orbit. In Figure 3.1, four circular orbit satellite simulation results show that all satellite in the lumpy halo lose more mass than the satellite in the smooth halo. However, the amounts of the enhanced mass loss for four simulations are different. According to these four simulations, the satellites in the lumpy halo lose about 5% to 25% more mass than the satellite in the smooth halo. Different histories of close encounters are responsible for this difference.

For the eccentric orbit, the satellite in the lumpy halo loses more mass than the satellite in the smooth halo. However, the enhancement of mass loss due to subhalo is smaller than the average difference in the circular orbit simulations. Interestingly, the satellite in the lumpy halo is destroyed at $T \sim 3.8$. In contrast with the circular orbit and the eccentric orbit, satellites in both the lumpy halo and the smooth halo lose almost the same mass in the inner orbit. Both satellites are destroyed during the course of simulations, but the times of the destruction are different. The satellite in the smooth halo is destroyed at $T \sim 2.8$ while the satellite in the lumpy halo is destroyed at $T \sim 3.7$. Later in this section, we will find that the satellite destruction results from loss of equilibrium driven by a strong interaction with the host halo or the subhalos rather than mass loss.

Figures 3.1, 3.2, and 3.3 also describe the time evolution of the distance from the host halo center and the satellite. The figures show that the interactions with the subhalos not only heat the satellite but also distort the satellite orbit. Comparisons of the satellite mass loss histories and the time evolution of the distance suggest that both enhance the satellite mass loss. In Figure 3.1, the distance between the host halo center and the satellite in the lumpy halo deviates from the constant value, which suggests that the orbit deviates from the exact circular orbit. This distorted satellite orbit provides additional gravitational shock heating by host halo potential on the

satellite. However, this effect clearly appears only if the orbit is initially circular. Therefore, we can conclude that although it is not significant, the interaction with subhalos provides additional gravitational shock heat by the host halo potential as well as provide heat by high speed close encounter.

3.3.2 The relative importance of the host halo effect and the subhalo effect

In order to understand the effects of the interactions with the subhalos, we need to distinguish the relative importance of the host halo effects and the subhalos effects. Since our purpose is distinguishing the importance of two effects rather than detailed prediction, we use following simple but crude estimations rather than perturbation theory for computing the force acting on the satellite by the host halo and the subhalos.

$$\begin{aligned} F_{host} &= G m_{sat} \frac{M_{host}(< r_{sat})}{|\vec{r_{sat}}|^2} && (Host\ Halo) \\ F_{sub} &= G m_{sat} \sum_{sub} \frac{m_{sub}}{|\vec{r_{sub}} - \vec{r_{sat}}|^2} && (Subhalos) \end{aligned} \quad (3.3)$$

where the subscript *sub* represents the subhalos, the *host* represents the host halo, and the *sat* represents the satellite, with m being mass and $\vec{r}$ the location in the host halo for each components. The two formulas in Equation 3.3 describe the instantaneous force, acting on the satellite. Hence it can not be an exact measure for the satellite mass loss, However, since our purpose is a rough estimation of the relative importance, we can use this estimate to approximately demonstrate relative importance of two effects later in this section.

Figure 3.4 shows the force acting on satellites on circular orbits. This figure suggests that the force of the subhalos is about seven to eight times smaller than the force of the host halo. The total force of the lumpy halos is usually larger than the force of the smooth halo and leads to the enhanced mass loss for the satellite.

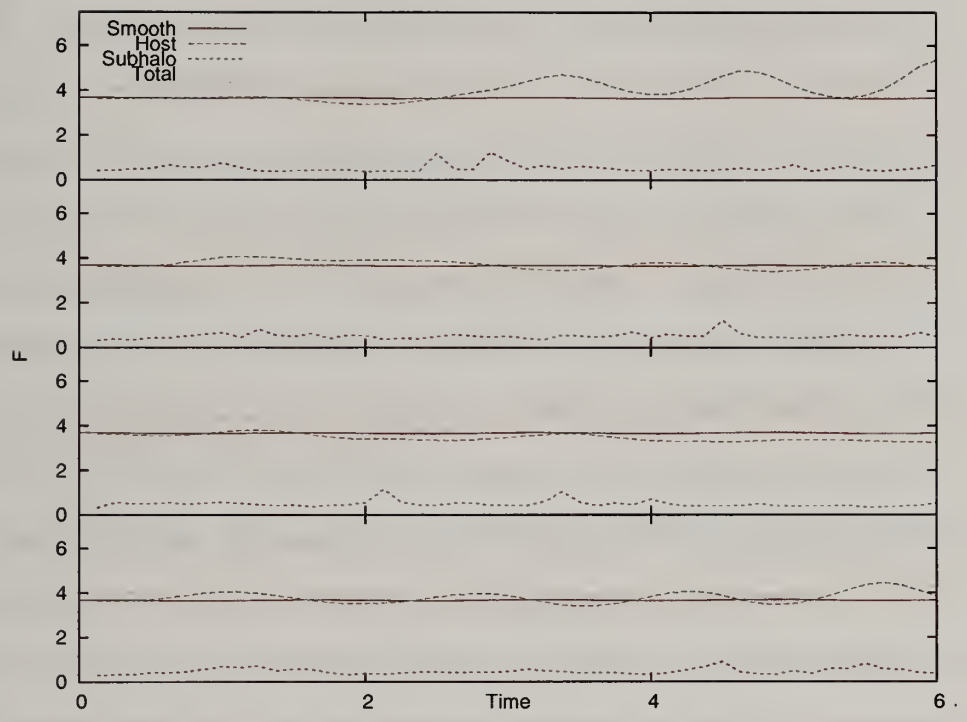

Figure 3.4 Time evolution of force act on the circular orbit satellite. The four panels show four different circular orbit simulations, which are runs 1, 2, 3, and 4 from top to bottom panels. "Host" represents the force of the host halo and "Subhalo" represents the force of the subhalos. "Total" shows the total force by both the host halo and the subhalo. For comparison, we plot the force of the host halo for the satellite in smooth halo.

In Figure 3.1, we find that a few strong close encounters play an important role in satellite mass loss. For example, the circular orbit satellite simulation Run 1 shows a sudden increase in mass loss at $T \sim 3.0$. The time evolution of the force of the subhalo show that there are two strong encounters around $T \sim 2.75$. As we have found earlier in this section, the close encounters not only heat the satellite but also change the satellite orbit. After these two encounters, the satellite orbit is no longer circular and the distance from the host halo center to the satellite decreases. This decrease also causes the force from the host halo to increase. Both strong close encounters and the increase of the host halo force enhances the mass loss. The importance of the two effects is difficult to clearly distinguish because close encounters almost always result in orbit evolution. Fortunately, the circular orbit simulation Runs 2 and 4 provide an indirect comparison of the relative importance of the two effects. The force of the subhalos shows that there is a strong interaction at $T \sim 4.5$. This interaction results in increase in the distance from the host halo center to the satellite which cause decrease in the host halo force. The mass loss histories of these two simulations do not show sudden change of the mass loss rate after this encounter. This suggests that the mass loss driven by the close encounter and the decrease in the host halo force are comparable. However, the perturbation of the orbit permanently affects the rate of satellite mass loss while a close encounter temporally affects on satellite mass loss. Therefore, we can conclude that the interaction with the subhalos enhances the satellite mass loss by the orbit distortion primarily.

Figure 3.5 shows the time evolution of the force acting on the eccentric orbit and the inner orbit satellites. As pointed out above, the mass loss enhanced by subhalos is smaller here than for the circular orbit. For eccentric orbits, the most dominant mechanism for the satellite mass loss is gravitational shock at the pericenter. The effect of the interaction with subhalos is secondary. However, interactions with subhalos are important in satellite destruction: Figures 3.2 and 3.3 show that the

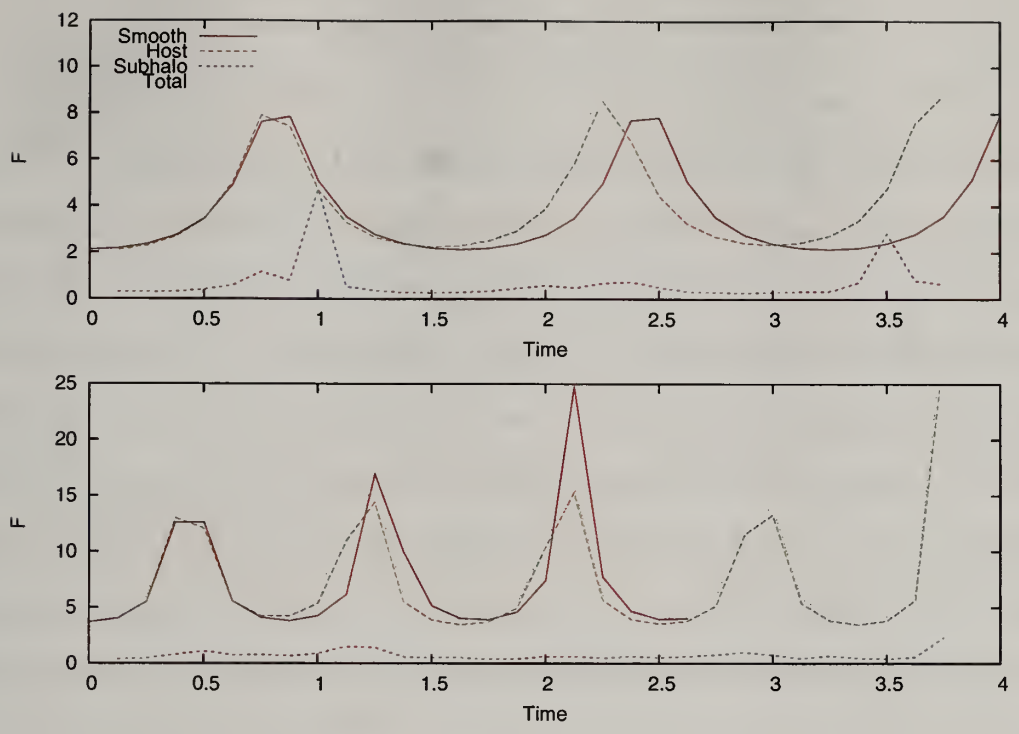

Figure 3.5 The same as Figure 3.4 but for the eccentric orbit satellite (top panel) and the inner orbit satellite (bottom panel).

satellites are destroyed. The eccentric orbit satellite in the lumpy halo is destroyed at $T = 3.75$, the inner orbit satellite in the lumpy halo is destroyed at $T = 3.5$, and the inner orbit satellite in the smooth halo is destroyed at $T = 2.7$. In Figure 3.5, we observe a strong encounter just before satellite destruction for all three simulations. Both the eccentric orbit and inner orbit satellites in the lumpy halo show a sudden increase in the force of subhalos just before satellite destruction. Therefore, a major effect of interactions with subhalos is satellite destruction rather than satellite mass loss.

Interestingly, this encounter, which causes satellite destruction, does not have to be an encounter with subhalos. Strong gravitational shock at the pericenter can also play the same role. The inner orbit satellite in the smooth halo experiences a strong pericenter shock at $T = 2.25$. After this shock, the satellite is destroyed. In contrast with this stronger gravitational shock, the inner orbit satellite in the lumpy

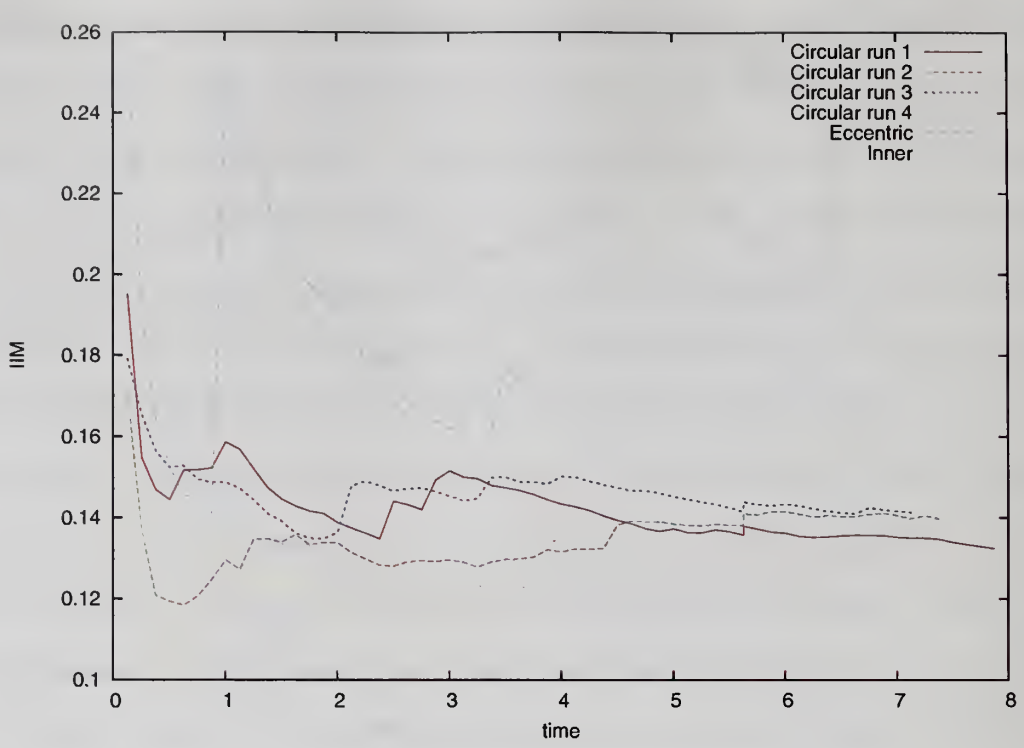

Figure 3.6 The time evolution of IIM for all lumpy halo simulations.

halo experiences weaker pericenter shock and it survives longer than the satellite in the smooth halo. The interaction with subhalos alters the satellite orbit and the satellite can avoid this strong shock. All these results support the argument that any strong external forces, which include both gravitational shock and close encounter, are responsible for the satellite destruction.

We use average properties of the subhalo population from cosmological simulation in generating our subhalo population. However, subhalo population varies depending on the properties of the dark matter halos, such as age and environment. Hence, it is worth characterizing the figure out what kind of dark matter halo subhalo population in our simulation. Knebe et al. (2006) studied the importance of the interaction with subhalos using cosmological simulations. In order to roughly quantify this relative importance, authors defined the dimensionless measure called integral interaction measure (IIM) based on the force act on the satellite.

$$IIM = \frac{1}{T}\int_0^T \frac{F_{sat}(t)}{F_{host}(t)}dt \tag{3.4}$$

where T is time interval of the satellite evolution and F_{sat} and F_{host} are the same as Equation 3.3. Knebe et al. (2006) found that an IIM decreases with time. Since larger IIM value indicates more and stronger interaction, the interaction of subhalos is more important in a younger halo. Figure 3.6 demonstrates the time evolution of IIM for our lumpy halo simulations and the average IIM for our simulations is ~ 0.14. Compared with Knebe et al. (2006), this IIM values indicates our lumpy halo is a rather old system. According to the IIM-age relation from cosmological simulation results in Knebe et al. (2006), our halo is approximately 7 Gyr old halo. This old halo is an expected outcome since our subhalo initial condition is based on $z = 0$ cosmological simulations. In addition, we are interested in the Milky Way type system, so that the old lumpy halo is preferred. However, the effects of subhalo interactions averaged in our simulations are lower than expected over their history. Therefore, the enhanced mass loss due to the interaction with subhalos will be larger than our results in realistic satellite galaxy evolution.

3.4 Satellite dark matter halo response due to harassment

In Section 3.3, we have found that the interaction with subhalos can enhance the satellite mass loss. However, the enhanced mass loss is an indirect consequence of the interaction with subhalos. This suggests that the violent satellite evolution such as mass loss is governed by the effect of the host halo because the effect of the host halo is stronger than the effect of subhalos. Therefore, investigating the satellite mass loss can not demonstrate the actual effects of this interaction with subhalos. The effect of subhalos may play a role in the quiescent satellite evolution such as the distortion of galaxy morphology. In order to study the quiescent satellite evolution, we need to investigate the satellite dark matter halo response. Remember that the effect

of original galaxy harassment is the transformation of galaxy morphology. In this section, we investigate the satellite dark matter halo response due to the interaction with the subhalos.

Figure 3.7 shows the evolution of density profiles for three different orbit simulations. For the circular orbit satellite in the lumpy halo simulation, we show the results of Run 1. The density profile evolutions of the satellite dark matter halo are very similar to both the smooth halo and lumpy halo simulations. Density profiles in the lumpy halo simulation are lower than those in the smooth halo simulation but the difference is small. Even with this difference, the overall shapes of the density profiles in both simulations are very similar. This difference in the density almost disappears in the eccentric and inner orbit simulations because the enhanced mass loss of the satellite in the lumpy halo is decreased. The profile evolution at $T = 4.0$ in the eccentric orbit lumpy halo simulation is considered the destruction of the satellite. In conclusion, the density profile evolutions show almost no difference in the satellite dark matter halo response in the smooth halo and the lumpy halo simulations

One interesting feature in the density profile evolution is that the decrease in density occurs at all radial ranges of the halo for both the smooth halo and the lumpy halo simulations. It is particularly remarkable in the inner orbit simulation. Even at $r \leq 0.001$ the density decreases with the satellite evolution. The gravitational shock near pericenter produces this evolution. Although the density decreases, the steepness of the density profile does not decrease.

Figures 3.8 – 3.10 show the distribution of relative ΔL_z in the phase space for three different orbit simulations, where L_z is the angular momentum for perpendicular orbital plane axis. In these figures, we compare the results from both the smooth halo simulation and the lumpy halo simulation. The distribution of relative ΔL_z for both the smooth halo simulation and the lumpy halo simulation shows similar results. In particular, the circular orbit satellites and the eccentric orbit satellites results show

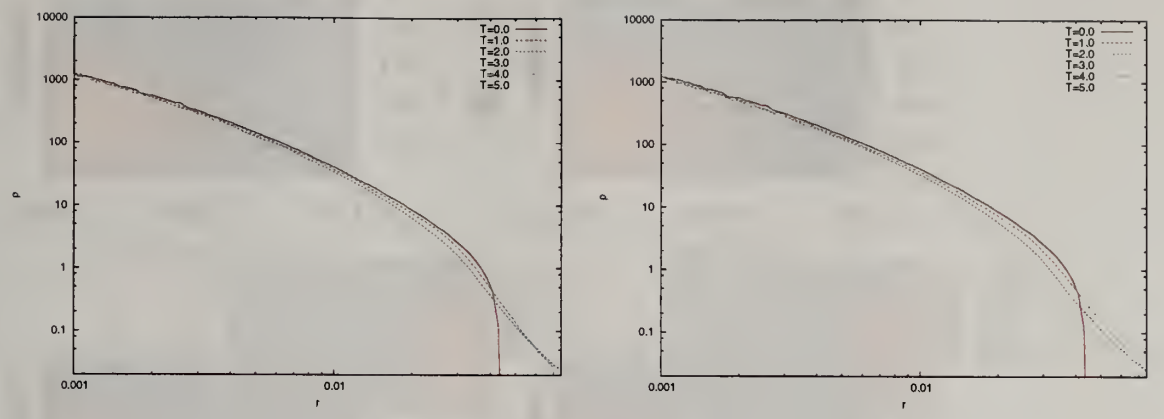

(a) The circular orbit

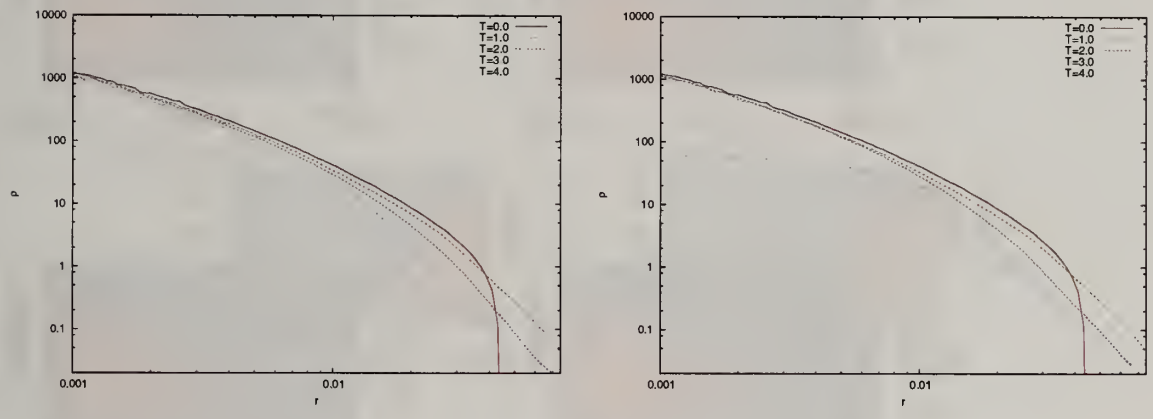

(b) The eccentric orbit

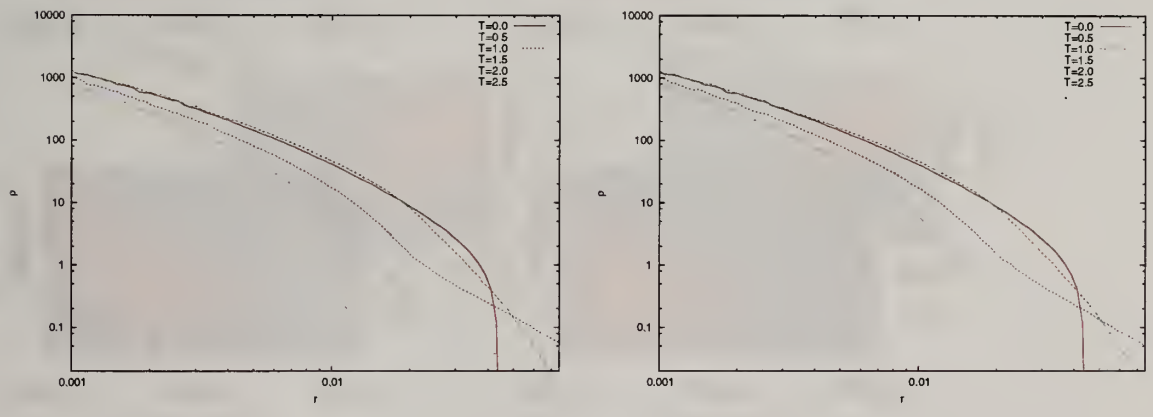

(c) The inner orbit

Figure 3.7 The density profiles of the satellite dark matter halos for three satellite orbit simulations. The left panels show the density profile evolution of the smooth halo simulations. The right panels show the density profile evolution of the lumpy halo simulations. Both smooth halo simulations and lumpy halo simulations results show similar density profile evolutions.

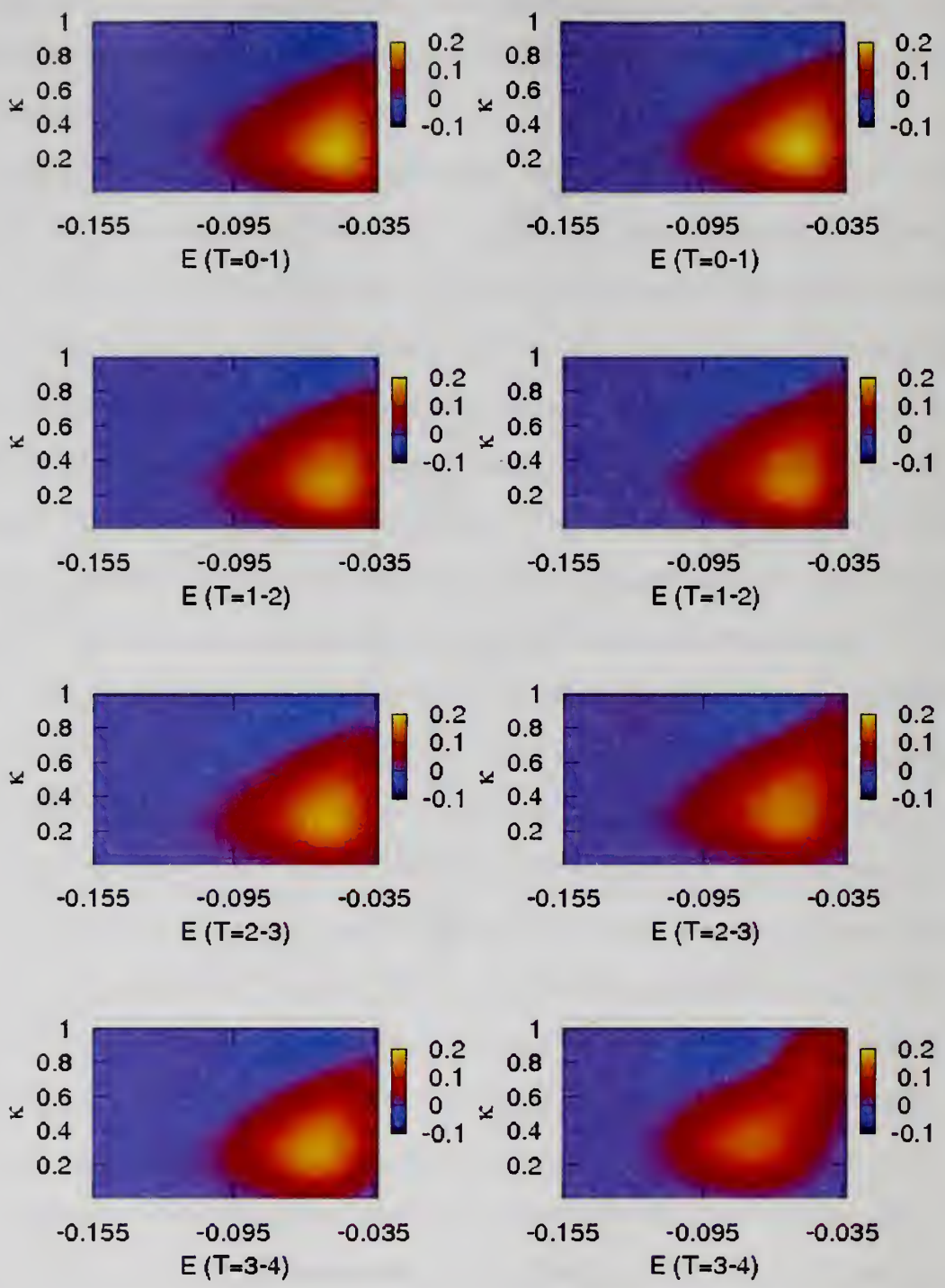

Figure 3.8 Distribution of relative ΔL_z in the phase space for the circular orbit satellite in the smooth halo and the lumpy halo. The color code represents the amount of the angular momentum transfer. The left panels are the smooth halo simulation results and the right panels are the lumpy halo simulation results. The position and the velocity of the halo center are the EJ centers of the satellite dark matter halo.

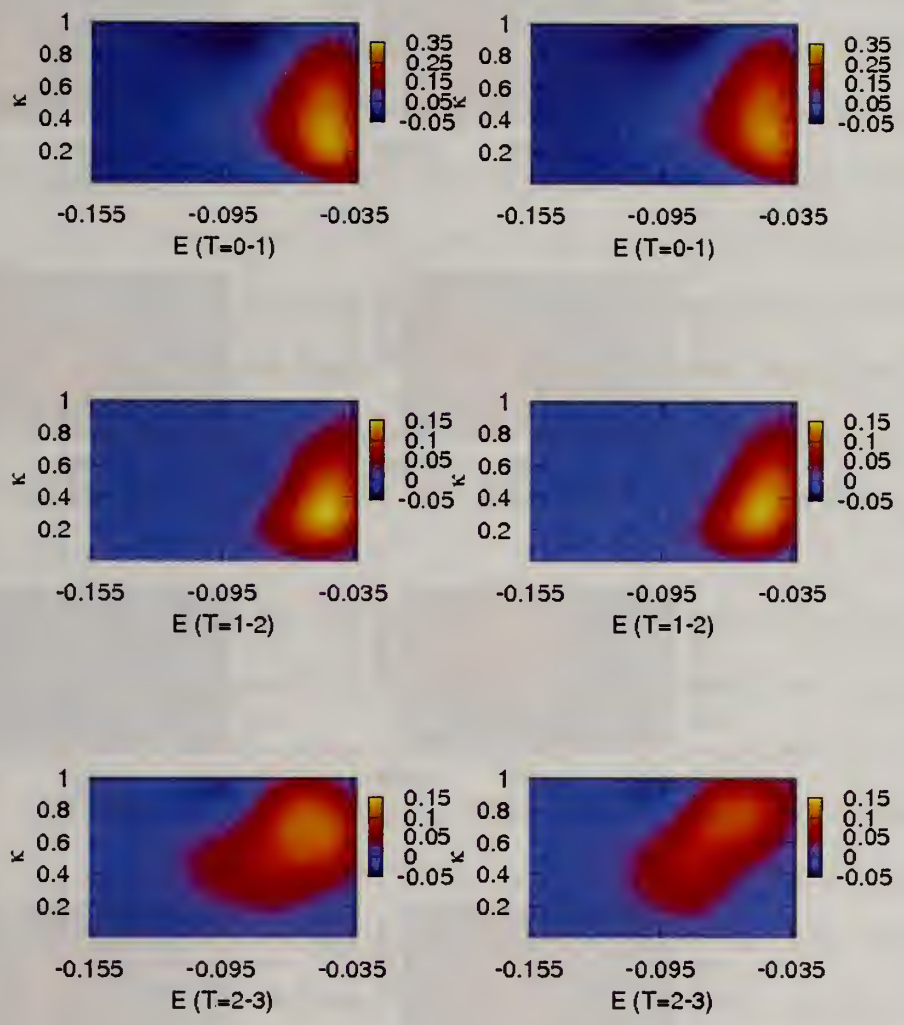

Figure 3.9 The same as Figure 3.8, but for the eccentric orbit satellite simulation.

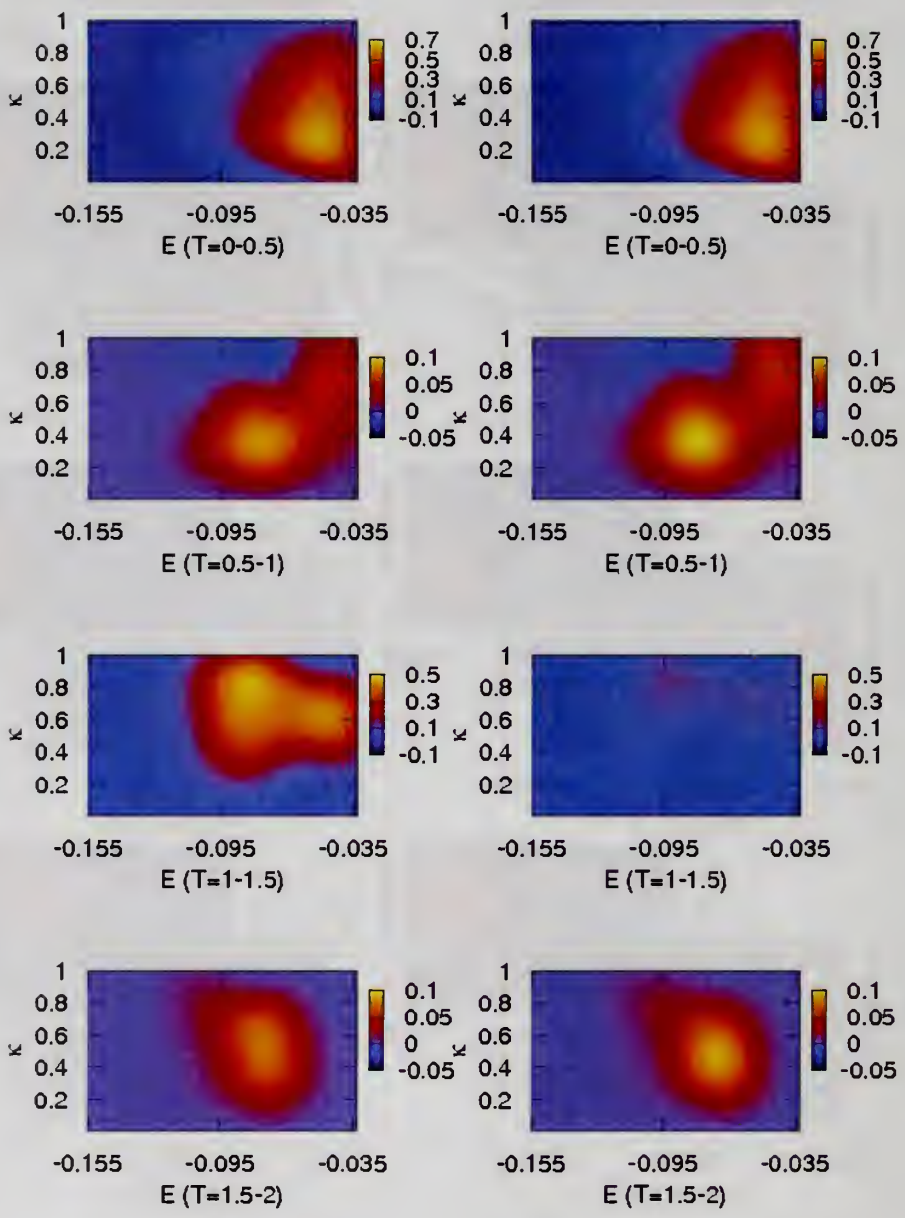

Figure 3.10 The same as Figure 3.8, but for the inner orbit satellite simulation.

almost identical relative ΔL_z distributions for two different halo simulations except for the ΔL_z distributions in the last time frames of these figures. Due to the different mass loss histories, the ΔL_z distribution for $T = 1 - 1.5$ for the inner orbit in the smooth halo simulation shows a remarkable angular momentum transfer while the ΔL_z distribution in the lumpy halo simulation shows a significantly similar total angular momentum transfer. This difference results from the different magnitude of the angular momentum transfer. After decreasing the range of the color code of the relative ΔL_z distribution for the lumpy halo result, we find that the phase space distribution of two results are similar. The different angular momentum transfer results from the different strength of the gravitational shock at the pericenter. This is also seen in Figure 3.5; the satellite in the smooth halo experiences stronger gravitational shock at the pericenter than the satellite in the lumpy halo. Therefore, we can conclude that the satellites in both the smooth halo and the lumpy halo show a similar ΔL_z distribution.

Figures 3.11 – 3.13 show the equidensity contour plots of the satellite dark matter halos for the three different orbit simulations. In these figures, we compare the satellite dark matter halo responses for the satellites in the smooth halo and the lumpy halo. The overall dark matter halo responses for these two different halo simulations are similar. In these figures, the most noticeable response is the outer elongated distortion. This response results from the satellite mass loss. During the satellite mass loss, the satellite material is stripped through satellite tidal tails. During the stripping, the satellite particles are aligned in the direction of tidal tails before escaping the satellite, and this alignment produces the outer elongated distortion. In addition to the outer response, the figures also show an inner elongated distortion. This region is located well inside the satellite tidal radius. It represents true dark matter halo density wakes which cause a transformation of a galaxy morphology due to the interaction with both the host halo potential and subhalos. Previous galaxy

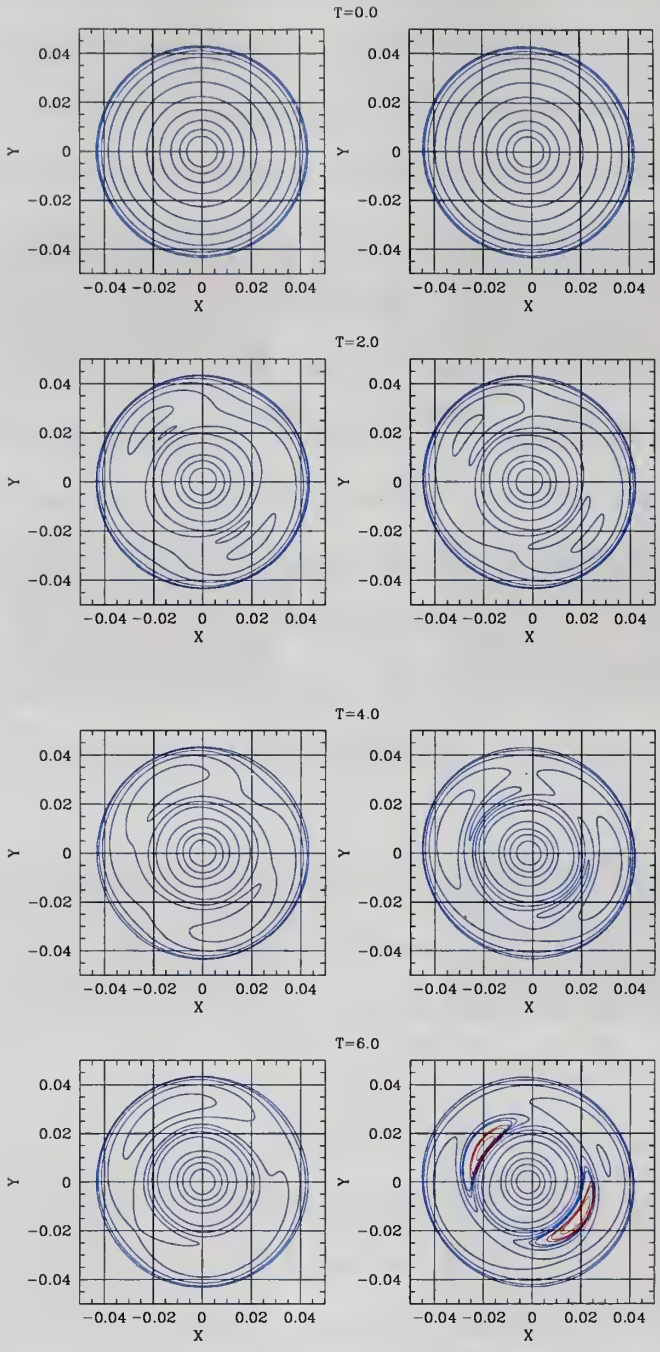

Figure 3.11 The equidensity contour plot of the dark matter halo from the circular orbit satellite simulation. The left panels are the smooth halo simulation results and the right panels are the lumpy halo simulation results. The center of the plot is the EJ center of the satellite dark matter halo. The x-y plane coincides with the satellite orbital plane. The blue lines represent positive density contours and the red lines represent negative density contours. The negative density results from significant decrease of the density from the initial density profile.

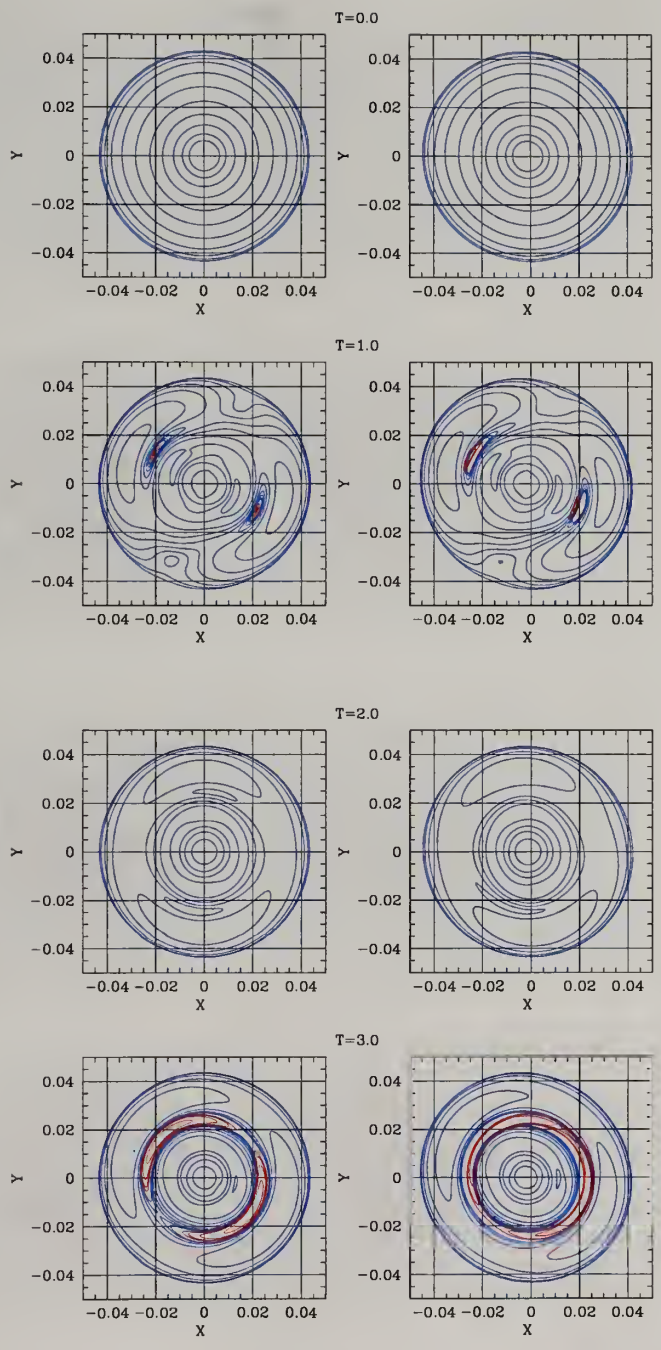

Figure 3.12 The same as Figure 3.11, but from the eccentric orbit satellite simulation.

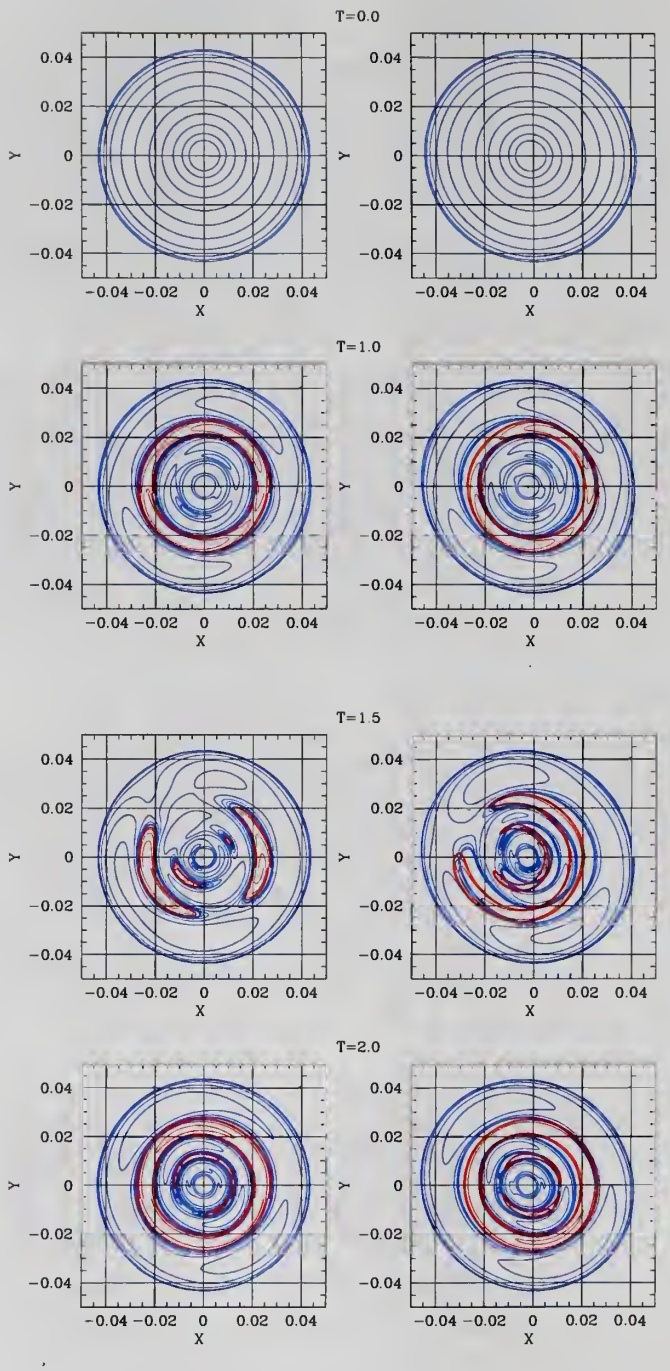

Figure 3.13 The same as Figure 3.11, but from the inner orbit satellite simulation.

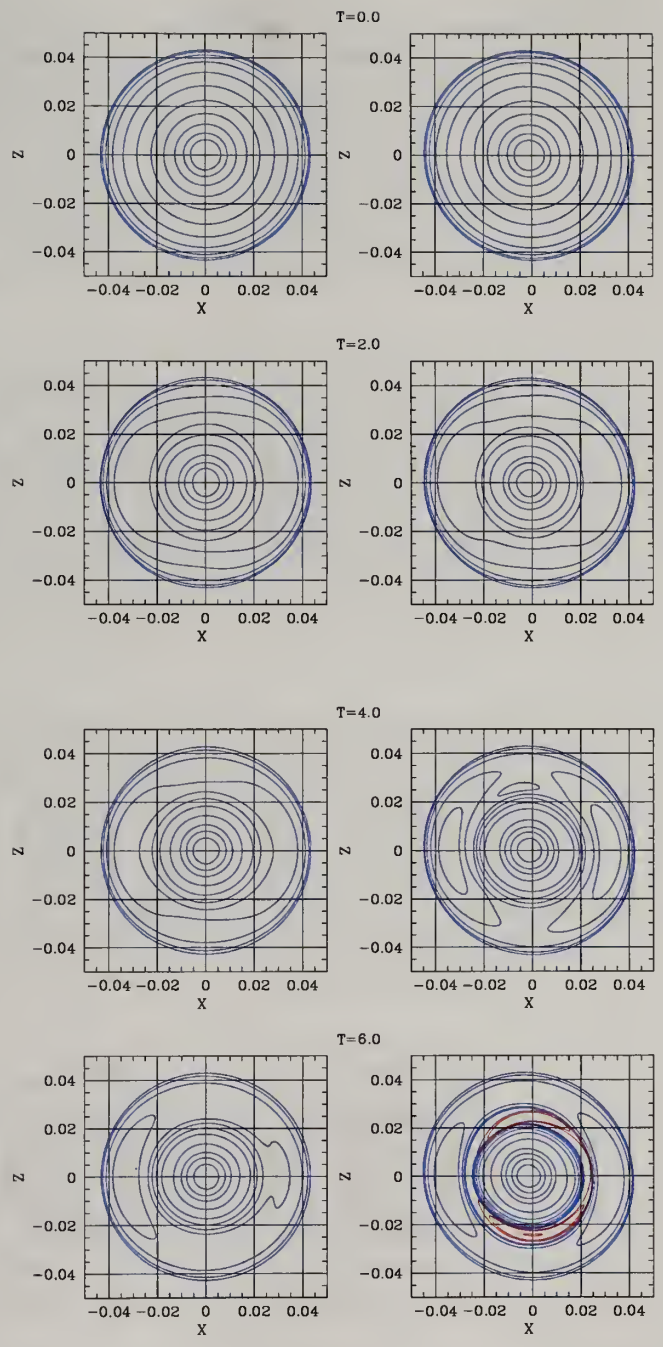

Figure 3.14 The same as Figure 3.11, but the projection plane is perpendicular to the satellite orbital plane (the x-z plane).

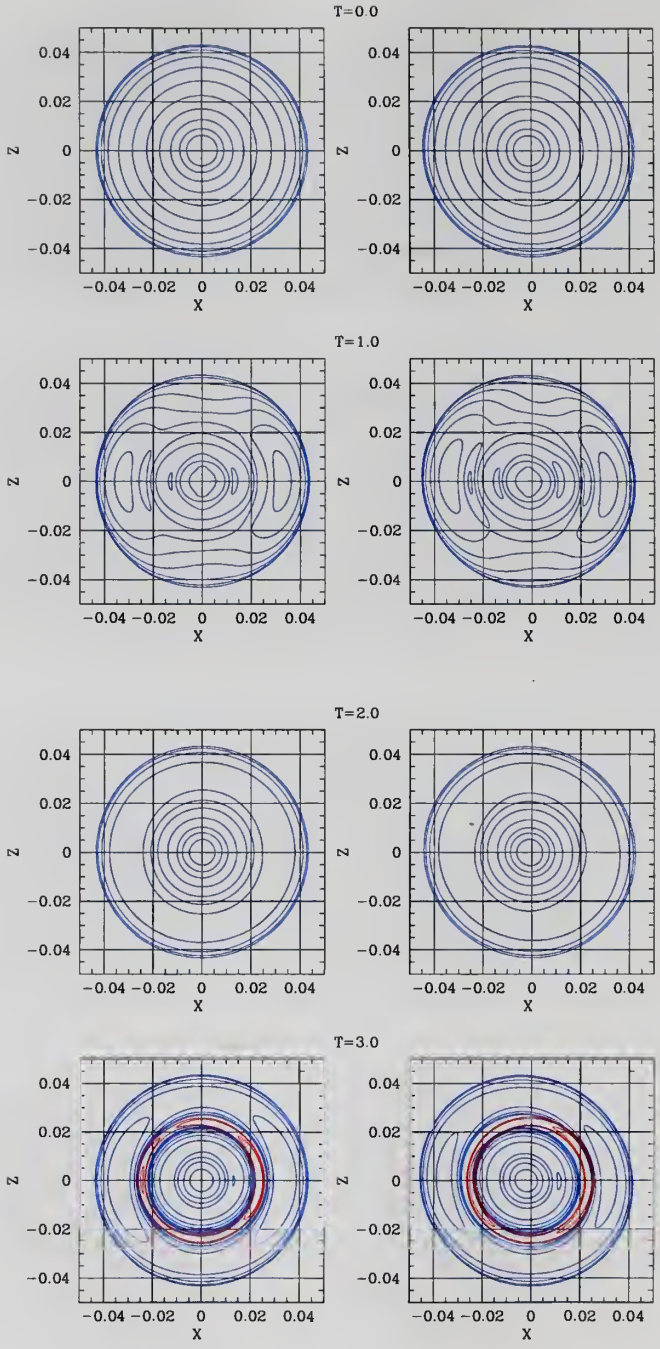

Figure 3.15 The same as Figure 3.12, but the projection plane is perpendicular to the satellite orbital plane (the x-z plane).

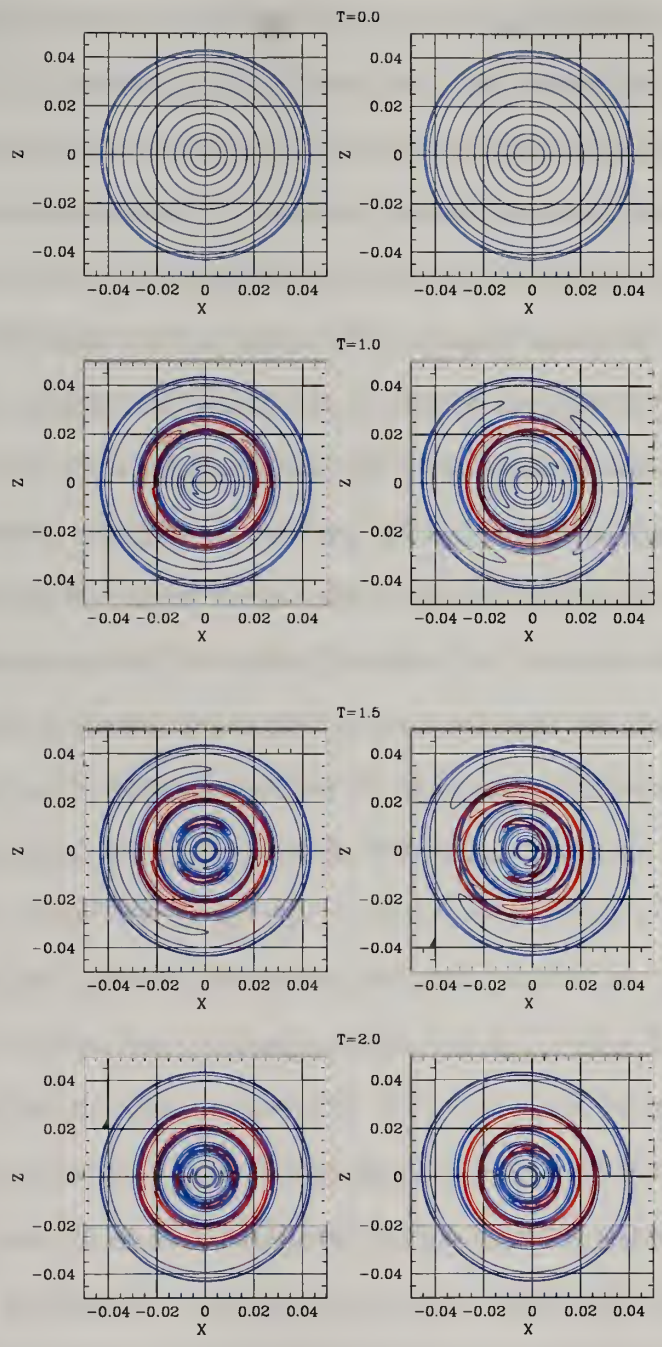

Figure 3.16 The same as Figure 3.13, but the projection plane is perpendicular to the satellite orbital plane (the x-z plane).

harassment studies (Moore et al., 1996b; Gnedin, 2003; Mastropietro et al., 2005a) show that galaxy harassment leads to disk thickening or bar formation. Since the morphology of this inner elongated distortion resembles a bar-like structure, this halo response is responsible for a morphological transformation of a galaxy.

Strangely, some equidensity contour plots show a negative density. This negative density results from a significant decrease in the density from the initial density profile. Since the equidensity contour is computed by an expansion method whose basis function is the initial density profile, a considerable difference of the density profiles can result in a negative density. Interestingly, the negative density region coincides with the border of the outer elongated distortion and inner elongated distortion regions. It agrees with the explanation that the negative density implies the boundary between the severely stripped region and the protected region of a satellite. In fact, the negative density is an numerical artifact. If we decrease the number of the radial basis function, the negative density disappears. However, too few radial basis funcation can erase important response features, so that we use the same number of the radial basis functions as our N-body simulations for computing equidensity contour plots.

Although the overall dark matter halo responses of satellites in both the smooth halo and the lumpy halo are similar, these two dark matter responses become moderately different later on. This difference mainly results from different mass loss histories. However, there is a clear pattern in the different responses. The dark matter halo response of the satellite in the lumpy halo shows a more complicated response than that of the satellite in the smooth halo. This feature is demonstrated clearly in Figures 3.14 – 3.16. These figures are the same equidensity contour plots as those in Figures 3.11 – 3.13, but the projection plane is now perpendicular to the satellite orbital plane. Because the projection plane is perpendicular to the host halo center, the effect from the host halo potential to satellite dark matter halo responses becomes

weaker than the previous projection. As a result, these figures can emphasize the effects from the interaction with subhalos. In Figure 3.14, the distortion of the satellite in the lumpy halo shows little more complex response features than the distortion of the satellite in the smooth halo. While the satellite response in the smooth halo shows clear elongated distortion aligned to the satellite orbital plane, the satellite response in the lumpy halo shows some additional distortions besides this elongated distortion. The additional complex responses shown in the lumpy halo simulation is indeed a combination of many wakes, which produce elongated distortion from all directions in the satellite. This suggests that both the host halo potential and the subhalos excite the dark matter halo response in similar ways. Both interactions produce asymmetric elongated distortion. These asymmetric distortion agree with previous galaxy harassment studies on dark matter halo responses (e.g. Vesperini & Weinberg, 2000). However, the strength of the host halo potential is so dominant that the effects from the subhalos become of secondary importance (see Figures 3.4 and 3.5). However, we can not ignore the role of the interaction with subhalos in dark matter halo response. In particular, this interaction plays an important role when the effect of the subhalo is comparable with the effect of the host halo such as the evolution of satellite galaxies in the outer halo.

3.5 Conclusion

We have studied the evolution of satellite dark matter halos in a lumpy host halo. Our lumpy host halo is based on summary properties from recent cosmological simulations. By comparing the simulation results of the satellites in the smooth halo and the lumpy halo, we have investigated the effects of the interaction with subhalos.

According to our comparison study of the satellites in the smooth halo and the lumpy halo, the satellite in the lumpy halo loses a little more mass than the satellite in the smooth halo. The amount of enhanced mass loss for the circular orbit satellite is

less than 20% of the amount of mass loss in the smooth halo simulation. However, the amount of enhanced mass loss decreases for an eccentric orbit satellites. Interestingly, the enhanced mass loss for the circular orbit satellite mostly results from distortion of the satellite orbits due to subhalo interactions. Heating from the interaction with subhalos does not play a major role in the enhanced mass loss partially because our lumpy halo represents a quiescent old halo. In the real universe, a satellite in a young dark matter halo will experience stronger subhalo interactions and will result in more enhanced mass loss. Previous studies have already demonstrated the lack of the importance of the heating from interactions with subhalos. For example, Boily et al. (2004) carried out a simple tidal heating calculation using a predicted subhalo population and concluded that, in general, the tidal interaction with subhalos alone is not enough to destroy a satellite. Even in this circumstance, the effects of the heat from the subhalo interaction is still surprisingly weak. Investigating the physical process which connects the satellite mass loss and the subhalo interaction using perturbation theory will be interesting future work.

The major effect of the interaction with subhalos is satellite destruction. It is generally expected that a satellite dark matter halo loses mass by external tidal force during its evolution, and is finally destroyed due to significant mass loss. In contrast, our simulations demonstrate that most of satellite destruction results from strong encounters. Due to these strong encounters, a satellite galaxy loses equilibrium and falls apart. The interaction with subhalos plays a major role in this destruction process. Although the average effect of the subhalo on the satellite mass loss is not remarkable, there are typically a few strong and close encounters which greatly influence a satellite. Therefore, the satellite can be destroyed by the interaction with subhalo.

All of our simulation results suggest that the host halo effect on the satellite evolution is stronger than the subhalo effect. We roughly quantify the relative importance

of these two effects and find that the host halo effect is about 7 to 8 times larger than the subhalo effects. Some cosmological simulations (e.g. Knebe et al., 2006) suggested that unless the age of a halo is very young, the host halo effect is generally more important than the subhalo effect. In future study, we plan to investigate the satellite evolution in a more realistic lumpy halo which includes an age dependent effect of subhalo interactions.

Due to the interaction with both the host halo and the subhalos, asymmetric elongated distortion develop in satellite dark matter halos. The host halo effect is more important than the subhalo effect in stimulating the dark matter halo response. However, the halo response due to the interaction transforms satellite's morphology at the outskirt of the host halo where the host halo forcing is comparably small. In addition, the asymmetric distortion by the subhalo interaction can be generated in any direction because of the isotropy of the subhalo distribution. These orientation-free, asymmetric distortions explain some extraordinary kinematic signatures of satellite galaxies. For example, some dwarf galaxies show the kinematically decoupled core (van Zee et al., 2004; De Rijcke et al., 2004). Some researchers suggest that this phenomenon can be explained as consequence of galaxy harassment (González-García et al., 2005). The dominated characteristics of the satellite dark matter halo responses suggest that the interaction with subhalos can excite many different asymmetric distortions in the satellite galaxy.

Although we use high resolution simulations, it has not been confirmed if our simulation can properly reproduce the resonant dynamics effects of the subhalo interaction. Since subhalos are usually on eccentric orbit, perturbation calculations for this interaction are very complicated. Vesperini & Weinberg (2000) investigated the effect of single fly-by interactions. We find that our simulation results are similar and suggests that our simulations can most likely reproduce the resonant effects of the subhalo interaction. However, the required particle number for these resonant effects

increases as the amplitude of perturbation decreases (Weinberg & Katz, 2007a). In addition, we find that at least 10^5 particles are required for a satellite dark matter halo to properly reproduce important resonant effects of the interaction with a host halo (see Chapter 2). Since the amplitude of individual subhalo perturbations is a few orders of magnitude smaller than the amplitude of the host halo perturbation, it is expected that extravagantly high resolution simulations would be required to correctly reproduce the resonant dynamics for interactions with subhalos. This requirement surpasses the current capacity of computational power. If we can correctly reproduce the resonant dynamics effects for interactions with subhalos, we can expect additional features in the satellite evolution such as significantly enhanced mass loss. One of our future tasks will be to implement this simulation and fully understand the resonant effects.

CHAPTER 4

THE DYNAMICS OF TIDAL TAILS FROM MASSIVE SATELLITES

4.1 Introduction

According to the currently favored galaxy formation scenario, the cold dark matter (CDM) cosmogony, galaxies are built up from the assembly of small structures. In this paradigm the assembly mechanism plays a key role in understanding the formation history of galaxies. Recent cold dark matter cosmological numerical simulations predict the existence of a large population of *subhalos*. Comparisons with the observed population of dwarf galaxies and detailed predictions of the present-day subhalo population, dark or luminous, have become important tests of the CDM galaxy formation paradigm (Ghigna et al., 1998, 2000; De Lucia et al., 2004; Diemand et al., 2004; Gao et al., 2004; Oguri & Lee, 2004). Most studies to date use large cosmological simulations and classify their properties statistically. However, to properly investigate these processes, one needs to perform high resolution idealized simulations of subhalo evolution within the CDM paradigm (Hayashi et al., 2003). Alternatively, in this study, we investigate one important consequence of subhalo disruption: the formation and evolution of tidal tails. By adopting initial conditions motivated by the CDM simulations, we can focus our computational resources on understanding the dynamical mechanism.

Satellite galaxy tidal tails are an important observable fossil signature to help understand the formation history of the Milky Way and to test CDM theory as a consequence. Tails and streams provide information about the Galactic halo mass

model as well as the evolutionary history of the observed satellite galaxy. In the CDM model, galaxies are embedded in massive dark matter halos. Estimating dark matter halo structure is essential to understand galaxy formation and tidal tail morphology probes halo structure (Johnston et al., 1999; Helmi & de Zeeuw, 2000; Ibata et al., 2001a,b). Several space missions, for example the ESA astrometric satellite GAIA (Lindegren & Perryman, 1996; Perryman et al., 2001), are planned to measure the position and motion of stars in the Milky Way with very high accuracy, in the near future. Together with ground-based radial velocity experiments, e.g. RAVE [1](Steinmetz et al., 2006), these surveys will provide full phase space information. Accurate six dimensional phase space information of Milky Way stars will provide observational information of the tidal tail and hence the formation history of the Milky Way. The time is ripe to carry out a detailed theoretical study of satellite galaxy disruption and the induced tidal tail morphology.

In this study we perform numerical simulations of satellite galaxy disruption and its induced tidal tail morphology within the CDM cosmogony. The objective of this study is to understand the physical processes responsible for satellite galaxy disruption rather than reproducing the evolutionary history of any individual Milky Way satellite galaxy. In particular, satellite disruption in N-body simulations is produced by escaping satellite particles. In addition, the gravitational shock, which is caused by the slowly varying host halo potential as the satellite goes through its orbit, changes the satellite's internal structure. An initially stable satellite galaxy and accurate numerical integration of a satellite particle's orbit are necessary to represent these physical processes correctly. We investigate satellite galaxy evolution by performing high resolution and low noise N-body simulations with such stable initial conditions.

[1]See http://www.rave-survey.org

Table 4.1 Initial properties of the three satellite models

Satellite	$M/M_{vir,host}$	$R/R_{vir,host}$	$V_{max}/V_{max,host}$
Massive	1.9×10^{-2}	9.02×10^{-2}	0.45
Low-Mass	9.0×10^{-4}	3.38×10^{-2}	0.16
Tiny-Mass	9.9×10^{-5}	1.66×10^{-2}	0.08

In addition, we can estimate any trends of satellite tidal tail morphology with satellite properties from our simulations, even though we do not reproduce the evolutionary history of any specific Milky Way satellite. Our simulation results show that the gravity of the satellite alters the location of the tidal tails relative to the satellite orbit. The satellite decelerates (accelerates) the leading (trailing) tail beyond the tidal radius, which is proportional to the satellite mass. For more massive satellites, this results in the leading tail being located well inside and the trailing tail being located well outside of the satellites orbit, rather than tracking the original satellite orbit (Johnston et al., 1996, 2001; Moore & Davis, 1994). Since the satellite torques the tidal tail, the distribution of the tidal tail in the observational plane is rather different from predictions that exclude such satellite torquing. In addition, the simulations provide six-dimensional phase-space information of the tidal tail to compare with upcoming astrometric measurements.

In Section, 4.2 we describe how we make stable satellite initial conditions and provide a brief overview of the simulation algorithm. In Section, 4.3 we investigate satellite disruption and the formation of the tidal tail, including the effects of the satellite potential on the tidal tail, and in Section 4.4, we investigate the observational consequences. In Section 4.5, we summarize our results and discuss their importance.

4.2 Initial conditions and N-body methodology

The initial conditions of our simulations are motivated by the CDM cosmology. CDM cosmological simulations suggest that dark matter halos have a universal density profile (Navarro et al., 1997, hereafter NFW), $\rho(r) \propto r^{-1}(r+r_s)^{-2}$, where r_s is a scale

length characterized by the concentration parameter $c = R_{vir}/r_s$ and R_{vir} is the virial radius of the halo. Although there are some disagreements regarding the accuracy of this simple formula in describing halos in numerical simulations and in comparisons with observed galaxies, it remains the accepted CDM halo density profile and we adopt it for our study.

We represent the host halo by a static NFW halo potential. Hence our simulations ignore the effects of dynamical friction and the subsequent reaction of the host halo. Obviously this is not realistic but since the satellite masses of interest are often much smaller than the host halo mass, the consequences are minor. Moreover, the prime motivation of this study is to understand the physical processes responsible for satellite disruption and tidal tail formation and not the evolutionary history of the satellite. Dynamical friction is not vital to understand these processes.

Before tidal truncation, the satellites have an NFW density profile. However, the NFW profile extends to infinity and real astronomical systems have a finite size. The conventional solution limits the size of an isolated dark matter halo to its virial radius (Gunn & Gott, 1972; Bryan & Norman, 1998). The host halo's tidal field then determines the size of satellite halo. The host halo's tidal field affects a satellite halo even before the satellite halo passes within the host halo's virial radius. As a result, it is computationally expensive to simulate the entire evolution of a satellite. Remember, the objective of our study is to understand the physical processes responsible for tidal tail formation not the reproduction of a particular tail feature. Therefore, we place the satellite in the host halo on the desired orbit to start and include the host halo's tidal field when we generate a satellite's initial phase-space distribution. It is natural to characterize the tidal length scale in the satellite by the radius of the X-point that this satellite would have at some fiducial galactocenteric radius in its orbit. We call this fiducial radius the *tidal distance*. In other words, the satellite on a circular orbit at the tidal distance would have the X-point $r_\times$. At this point, the gravitational

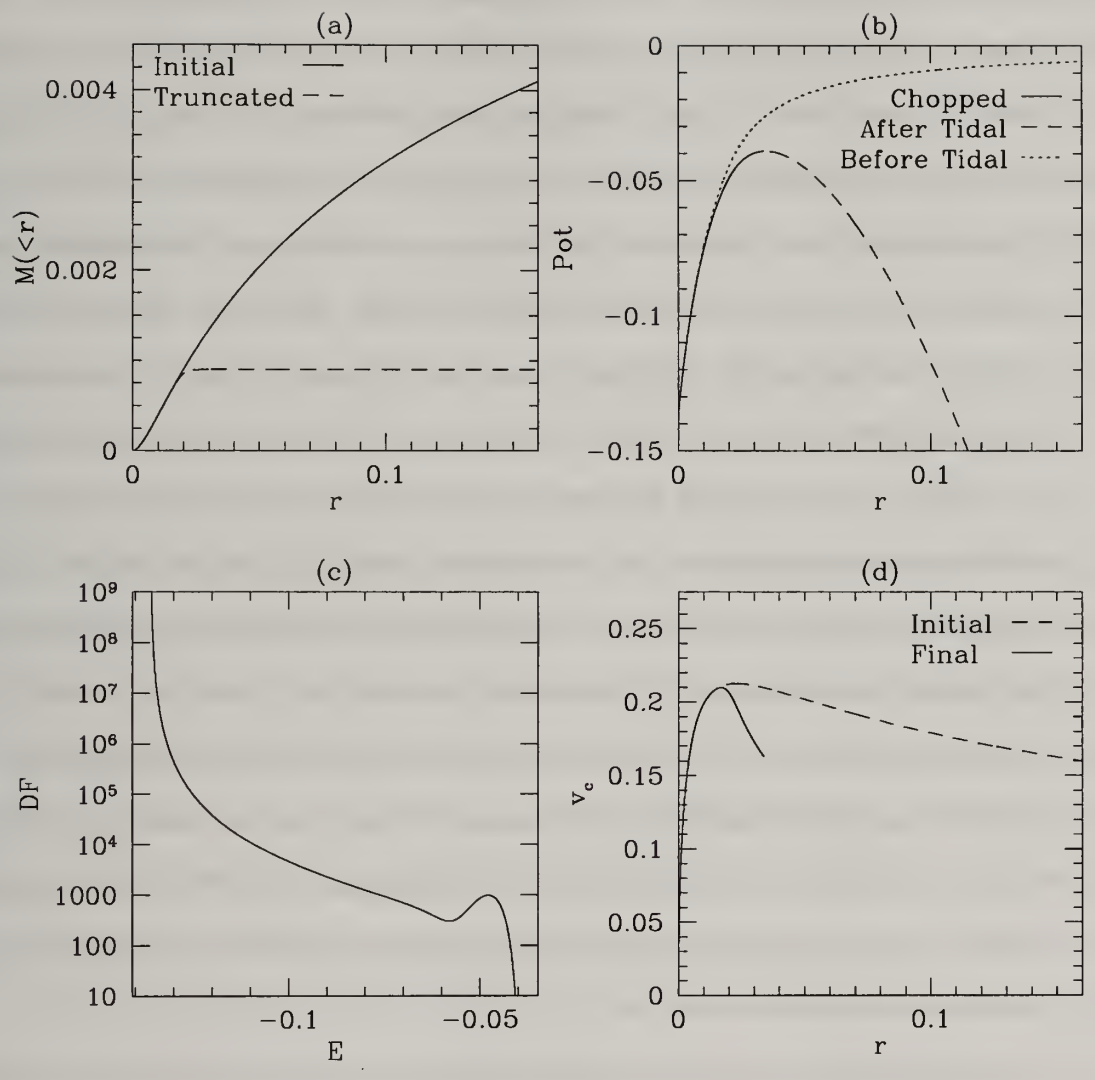

Figure 4.1 The effect of our truncation procedure (see text) on a satellite's initial NFW profile. (a) The enclosed mass profile. (b) The effective potential profile. (c) The Distribution function versus energy. (d) The circular velocity profile. We use *system* units unless otherwise specified: $G = 1$, $M_{vir,host} = 1$, and $R_{vir,host} = 1$.

force from the satellite exactly balances the gravitational force from the host halo and non-inertial centrifugal force.

The details of the iterative procedure that we use to generate the satellite's initial condition is as follows. First, we truncate the virial radius limited NFW satellite halo at the X-point radius, $r_\times$, using the error function, $\{1 - \mathrm{erf}[(r - r_\times)/s]\}$. We then compute the distribution function using Eddington inversion and calculate a new satellite density profile by integrating the distribution function over velocity. The parameter s in the error function truncation formula is increased from zero until a smooth phase-distribution function results. We iterate these steps until the density–distribution-function pair is converged. Figure 4.1 shows an example of how this procedure modifies an initial satellite halo. At the conclusion of the procedure, the effective tidal radius is approximately 75% of the initial X-point radius radius. We characterize a satellite halo by its *initial* maximum circular velocity; Figure 4.1 demonstrates that this velocity is only weakly affected by the truncation procedure. We denote the outer radius of the satellite after the truncation procedure as the *effective tidal radius.* It is smaller than $r_\times$ owing to the truncation with the error function and the Eddington inversion process. Finally, we use an acceptance-rejection algorithm to generate each particle halo realization. Since the initial satellites are already truncated, satellite particles are ejected only through interactions with the host halo during the simulation.

We simulate a set of satellite realizations with the same tidal distance but different initial maximum rotation velocities. We investigate the effects of a satellite's size and orbit on its tidal tail morphology by varying them separately but keeping the other parameters fixed. In detail, we choose a $c = 15$ NFW model for both the host halo potential and for the satellites. We generate three different size satellites, which we refer to as the massive satellite, the low-mass satellite, and the tiny-mass satellite. We use the maximum rotation velocity, $V_{max,sat}$, as a measure of satellite size since the

continuous mass loss makes mass an inexact measure. We use a $V_{max,sat}$ of 0.45, 0.16, and 0.08 times $V_{max,host}$ for the massive, low-mass, and tiny satellite, respectively. The tidal distance for all three satellites is $0.4R_{vir}$. We also set the galactocenteric orbital radius to $0.4R_{vir}$ for our circular orbit simulations. After our truncation procedure is complete, the initial mass of the massive satellite is 0.018 M_{host}, the low-mass satellite 0.001 M_{host}, and the tiny-mass satellite 0.0001 M_{host}. Converting our simulation units to a Milky Way size galaxy system and evolving for a few satellite orbits, the low-mass satellite roughly corresponds in mass to the Sagittarius dwarf galaxy halo (Majewski et al., 2004; Law et al., 2005). The massive and tiny-mass satellites are an order of magnitude more and less massive, respectively. The properties of these satellite halos is summarized in Table 4.1 in units of the virial quantities of the host halo. All satellite initial conditions in this study have 10^6 particles.

We evolve each of the three satellites on three different orbits with the same energy but with different eccentricities. We define the eccentricity of the orbits as $e \equiv (r_a - r_p)/(r_a + r_p)$ where r_a and r_p are the apocenter and the pericenter of a satellite. The first orbit is circular ($e = 0$) at $0.4R_{vir}$. The second orbit has an $e = 0.5$ with a pericenter of $0.2R_{vir}$ and an apocenter of $0.6R_{vir}$, and the third orbit has $e = 0.74$ with a pericenter of $0.1R_{vir}$ and an apocenter of $0.67R_{vir}$. The third orbit is particularly relevant cosmologically since its *circularity* (κ) [2] is 0.5, which is the median κ of subhalos in a sample taken from recent cosmological simulations (Ghigna et al., 1998; Zentner et al., 2005). We quote results using the following *system* units unless otherwise specified: $G = 1$, $M_{vir,host} = 1$, and $R_{vir,host} = 1$. The timestep for our N-body simulations is 2.5×10^{-4} system time units. Therefore, one circular orbit is made of about 8000 timesteps because one circular orbit period is $T_{period} \sim 2.0$

[2] $\kappa \equiv J/J_c$,where J is the angular momentum and J_c is the angular momentum of a circular orbit with the same energy.

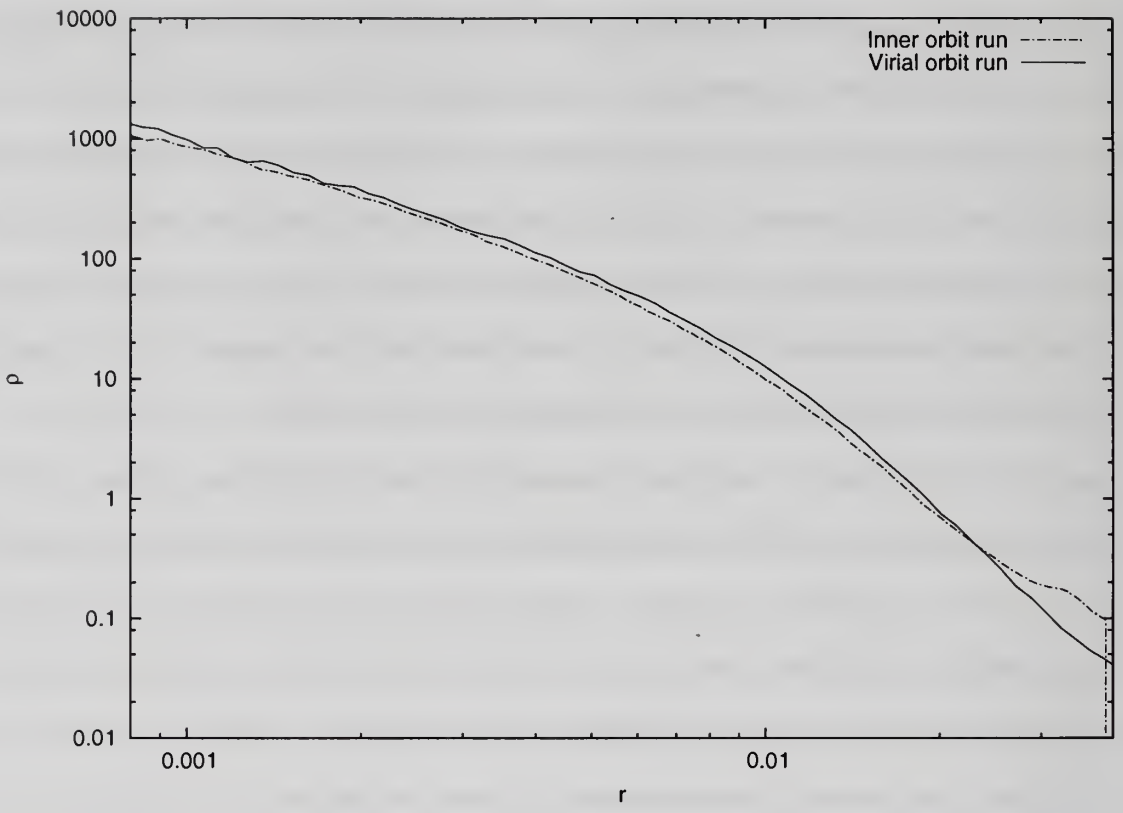

Figure 4.2 Comparison of the evolved density profiles of two identical, low mass satellite halos evolved with different starting radii. The inner orbit begins with $r = 0.67R_{vir}$ and a tidal distance corresponding to $0.4R_{vir}$ with an eccentricity $e = 0.73$. The virial radius orbit begins with $r = 1.0R_{vir}$ and a tidal distance corresponding to $1.0R_{vir}$ with $e = 0.5$. Owing to gravitational heating, the evolution of the two satellites is different but the profiles approximately agree when the total mass lose is the same.

Our satellite subhalo is initially truncated without considering its evolutionary history and without including any gravitational heating. This is crudely consistent with our initial condition generation procedure that assumes an equilibrium configuration at some radius inside the host halo to start. Fortunately, this idealized setup does not produce an unrealistic satellite mass loss history. Stoehr et al. (2002) and Hayashi et al. (2003) performed a quantitative study of NFW subhalo evolution in a host halo using idealized N-body simulations and claim that satellites on two different orbits have similar mass and velocity profiles after losing the same amount of mass. To check this, we compared the evolved density profiles of two low-mass satellites on orbits with $e = 0.74$ but at two different tidal distances: 1) the radius of a circular orbit with the same energy; and 2) the host halo virial radius, R_{vir}. The first test describes the satellite evolution scenario adopted for this study. The second test describes the cosmologically-motivated scenario of a satellite entering the host halo for the first time. Certainly, these two satellites have quite different evolutionary histories. However, when the bound mass of the two satellites is scaled to the same value, their evolved density profiles are similar, as shown in Figure 4.2. This test, together with the results of Stoehr et al. (2002) and Hayashi et al. (2003), suggests that our tidally truncated satellite models are a fair representation of CDM subhalos (see Figure 10 in Hayashi et al., 2003). In addition, although tidal heating, which is sensitive to a satellite's structure, plays an important role in the satellite disruption process, we will show that the tidal tail morphology does not depend on a satellite's inner structure but only on a satellite's mass and orbit.

For the gravitational potential solver, we use a three-dimensional self-consistent field algorithm (SCF, also known as an *expansion* algorithm, e.g., Clutton-Brock, 1972, 1973; Hernquist & Ostriker, 1992; Weinberg, 1999). This algorithm produces a bi-orthogonal basis set of density-potential pairs from which it computes the gravitational potential of a N-body system, given the mass and positions of the particles.

For an arbitrary basis, e.g. spherical Bessel functions, the expansion generally requires a large number of terms to achieve convergence, which introduces small-scale noise as well as requiring greater computational expense. The situation was dramatically improved by Weinberg (1999) using a numerical solution of the Sturm-Liouville equation to match the lowest-order pair to the equilibrium profile, and therefore, the expansion series converges rapidly. Here, we use the current density profile as the zero-order basis function.

For our purposes, this expansion algorithm is attractive for two reasons. First, the expansions can be chosen to follow structure over an interesting range of scales and simultaneously suppresses small-scale noise. In contrast, noise from two-body scattering can arise at all scales in direct-summation, tree algorithm, and mesh based codes. Small-scale scattering can give rise to a diffusion in conserved quantities, which can lead to unphysical outcomes particularly for studies of long-term galaxy evolution (see Weinberg & Katz, 2007a,b). Second, the expansion algorithm is computationally efficient; the computational time only increases linearly with particle number. Hence, the expansion algorithm permits the use of a much larger number of particles than most other algorithms for the same computational cost.

An accurate potential solver for a cuspy halo demands a precise determination of the expansion center, $\mathbf{C}$. This is the major disadvantage of the expansion algorithm relative to a Lagrangian potential solver such as a tree code. We developed and tested the following algorithm for evolving cuspy dark matter halos with an expansion code:

1. At time step n, we compute $\mathbf{C}_n$ from the center of mass of the N_{min} most bound particles;

2. To evaluate the expansion center at time step $n+1$, a predicted center $\mathbf{C}_{pred,n+1}$ is estimated from a linear least squares solution using the previous N_{keep} centers: $\{\mathbf{C}_j | n - N_{keep} < j \leq n\}$;

3. For $n < 2$, we set $\mathbf{C}_{pred,n+1} = \mathbf{C}_n$.

4. To reduce truncation error, we separately track the motion relative to the satellite's center and the motion of the center itself.

The linear least squares estimator for the expansion center $\mathbf{C}_{pred}$ reduces the Poisson noise from the N_{min} particles used to determine each of the $\mathbf{C}_n$. For our simulations we have adopted $N_{min} = 512$ and $N_{keep} = 10$ and have verified that this centering scheme maintains the cusp while the satellite orbits in a host halo for situations where the tidal field is insignificant.

4.3 The morphology of satellite tidal tails

Time-dependent forcing by the host halo's tidal field adds energy to the satellite, driving mass loss and, ultimately, disruption. These forces are a combination of the differential force from the host halo and the non-inertial forces from the satellite orbit. The work done against the satellite's gravitational potential results in mass loss. In addition, these forces *deform* the outer density contours of the satellite. To understand the evolution of the ejecta, one must also consider the gravitational field of the satellite. The gravitational force from the satellite decelerates (accelerates) the leading (trailing) tail, modifying the energy and angular momentum of the ejecta well past the point of escape. The conserved quantities of the ejecta, then, may be dramatically different than that of the satellite center of mass. The strength of the satellite gravity increases with satellite mass, of course. These effects combine to make the morphology of tidal tails more complicated than previously suggested (Moore & Davis, 1994; Ibata & Lewis, 1998; Johnston et al., 2001; Helmi & White, 1999; Mayer et al., 2002), especially for a massive satellite. We investigate the causes of these effects and their consequences in detail below.

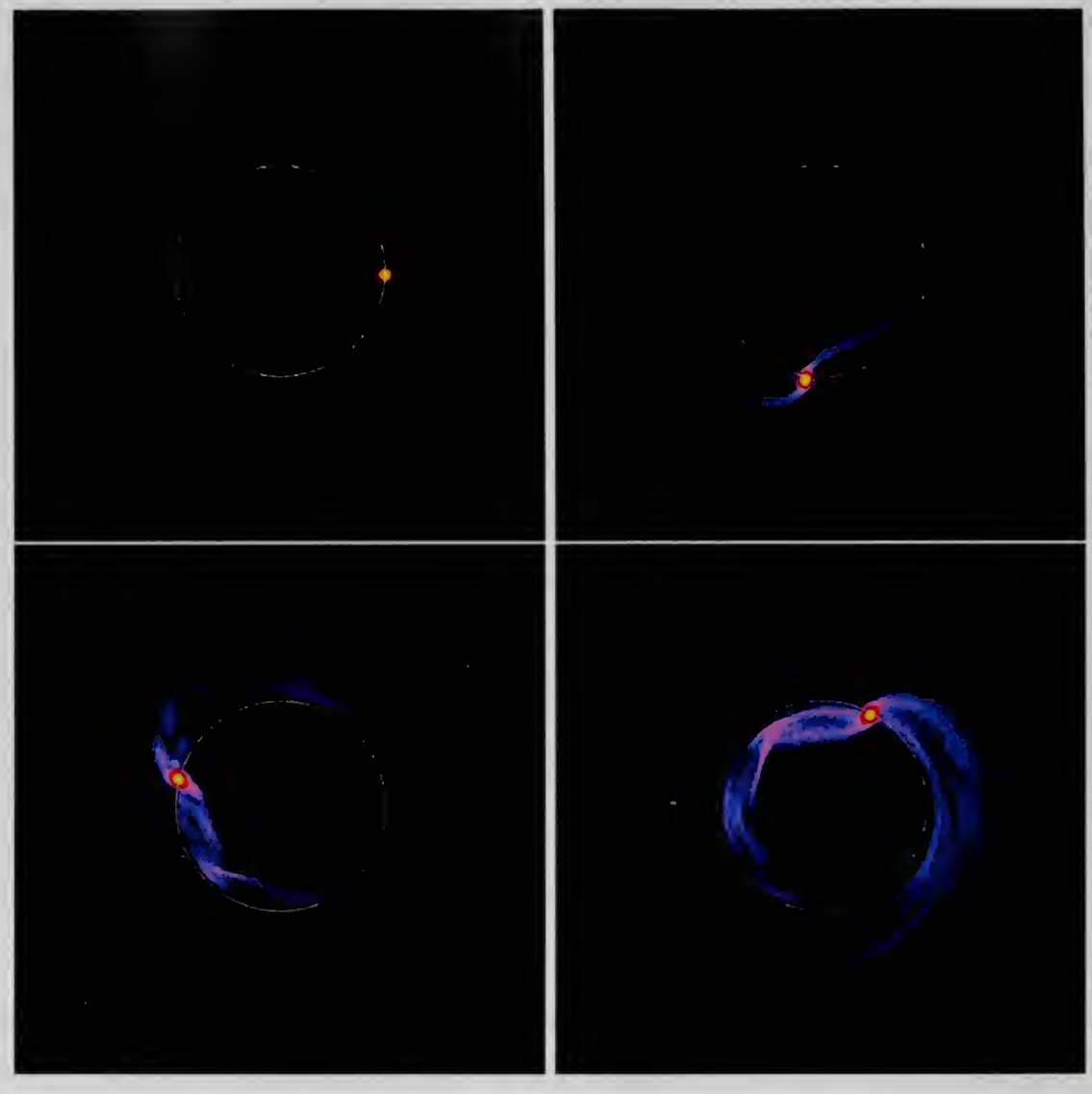

Figure 4.3 The mass density of the low-mass satellite on a circular orbit with $r = 0.4R_{vir}$ at $T = 0.0$ (top-left), 1.5 (top-right), 3.0 (bottom-left), and 4.5 (bottom-right). Recall that the orbital period for the circular orbit in this simulation is $T_{period} \approx 2.0$. The color scale is logarithmic in the dark matter mass density, increasing from blue to red, and is fixed for all times T. Each panel has a linear size of 2 host-halo virial radii. For this simulation, the tail particles do not feel the gravitational force of the satellite after escape. The circles show the satellite orbit. The multiple streams in the tail owe to phase crowding near apocenter for initially prograde and retrograde orbits.

4.3.1 Satellite disruption

We begin by describing the dynamics and morphology of the tidal tails in a simulation that *ignores* the gravitational field of the satellite past the tidal radius. Figure 4.3 shows a sequence of snapshots of the low-mass satellite ($0.001M_{host}$) on a circular orbit at $0.4R_{vir}$. We use units where $M_{vir} = 1$, $R_{vir} = 1$, and Newton's gravitational constant $G = 1$, together which defines a natural time unit. Scaled to the Milky Way, 0.5 natural time units is approximately 1 Gyr. Appealing to the standard zero-velocity Roche potential, which balances the effective gravitational potential in the rotating frame with the halo potential, we expect the mass to become unbound in the vicinity of the Lagrange or X-points. Indeed, we observe the double cometary appearance of tails leading and trailing the satellite, enforced by the conservation of angular momentum. For this halo model, the leading ejecta orbits faster than the satellite and has a position angle of 300° measured from the positive vertical axis, the direction of satellite's instantaneous motion. The trailing tail moves slower than the satellite and has a position angle of 120°. Since the simulation in Figure 4.3 ignores the satellite's gravity beyond the tidal radius, the orbit of the tidal tail merely represents the kinematic condition of the tail material just when it escapes from the satellite.

An example of a randomly chosen orbit in the leading tail is shown in Figure 4.4. As expected, the orbit describes a rosette with its apocenter at the radius of the satellite orbit. The energy and angular momentum lost during the escape changes the conserved quantities of the ejecta orbits from that of the satellite orbit; the leading (trailing) ejecta lose (gain) energy during deformation. Moreover, the distribution of the tails fills a wide region about the satellite orbit. This reflects the broad distribution of phases for orbits at escape. Hence, the width of the tail is nearly the same as the distance between the apocenter and the pericenter of a typical rosette orbit. Each tail has several distinct *streamers* filling a common envelope. The two

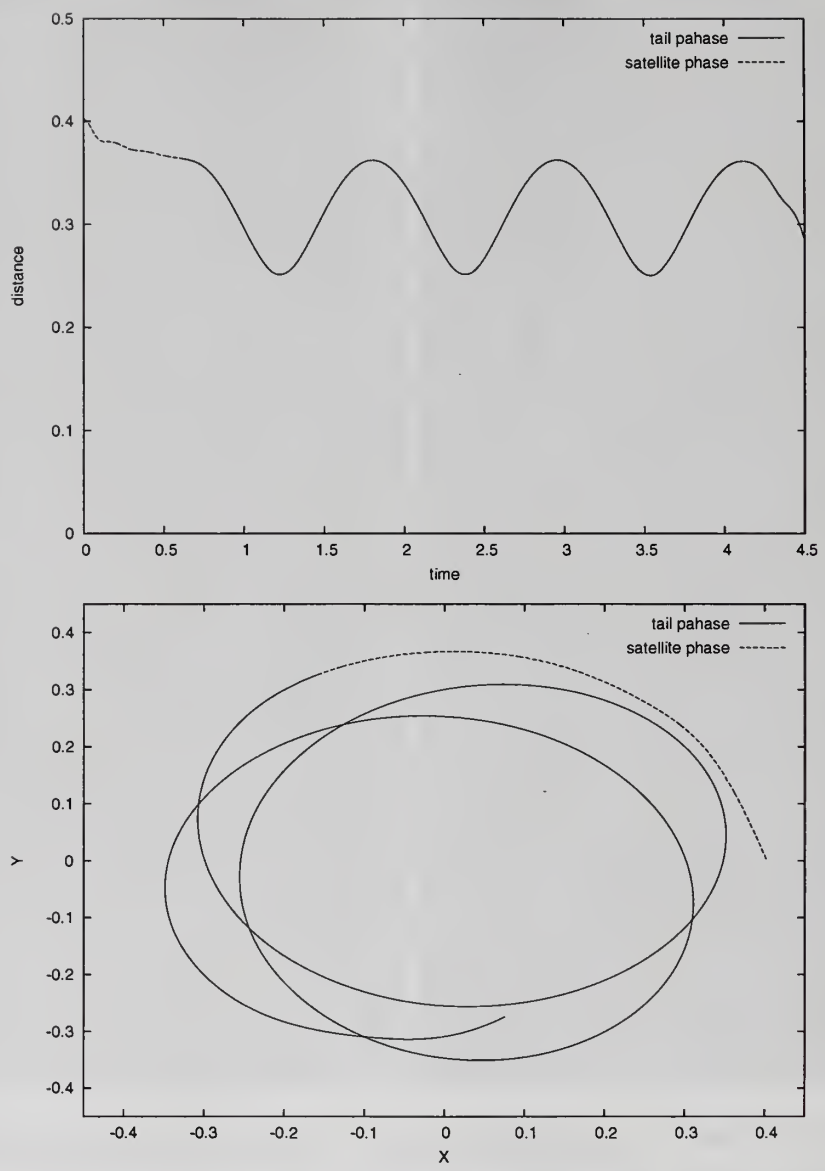

Figure 4.4 The orbit of a random particle in the leading tail for the simulation presented in Figure 4.3. The top panel plots galactocenteric radius versus time and the bottom panel shows the trajectory in the orbital plane. In both panels, the trajectory is plotted as a dashed line when it is still bound to the satellite and as a solid line after escape. The particle describes a rosette with its apocenter near the satellite orbital radius after escape.

primary streams in each tail demarcate the escape of the most extreme prograde and retrograde orbits. The originally prograde orbits have lower specific angular momentum and, therefore, smaller pericenters and larger epicyclic amplitudes. In contrast, originally retrograde orbits have larger pericenters and smaller epicyclic amplitudes. Distinct streamers result from the phase caustics near apocenter, similar to shells in elliptical galaxies caused by merger ejecta with a velocity dispersion much smaller than its new orbital velocity. This mechanism, illustrated in Figure 4.3, is the *massless* description of tail formation. This massless description assumes that the orbital energy and angular momentum of a tail is the same as those of a satellite; this yields a simple easy-to-compute prescription for the tails' location.

In contrast, Figure 4.5 repeats the simulation including the gravity of both the halo and the satellite at all times. At early times (upper-right panel), the evolution is similar. However, at later times (lower panels), the effects of the satellite gravity are marked. The continued acceleration of the tail by the satellite after escape decreases the internal velocity dispersion and narrows or focuses the tail as a consequence. The streamers in Figure 4.3 become less distinct when accelerated by the gravity of the satellite and the host halo together for the same reason (see Figure 4.6). Similarly, the acceleration of the ejecta by the satellite also decreases the angular separation between the streamers. Although the multi-streamer feature is diminished as the satellite gravitational field accelerates the ejecta, the feature can still be seen very close to the tidal radius.

4.3.2 Tail evolution

4.3.2.1 Circular orbits

The importance of a satellite's gravity increases with mass and, therefore, we begin with a study of the tail produced by a massive satellite. Figure 4.7 shows snapshots of a massive satellite ($0.018M_{host}$) on an circular orbit at $0.4R_{vir}$, where

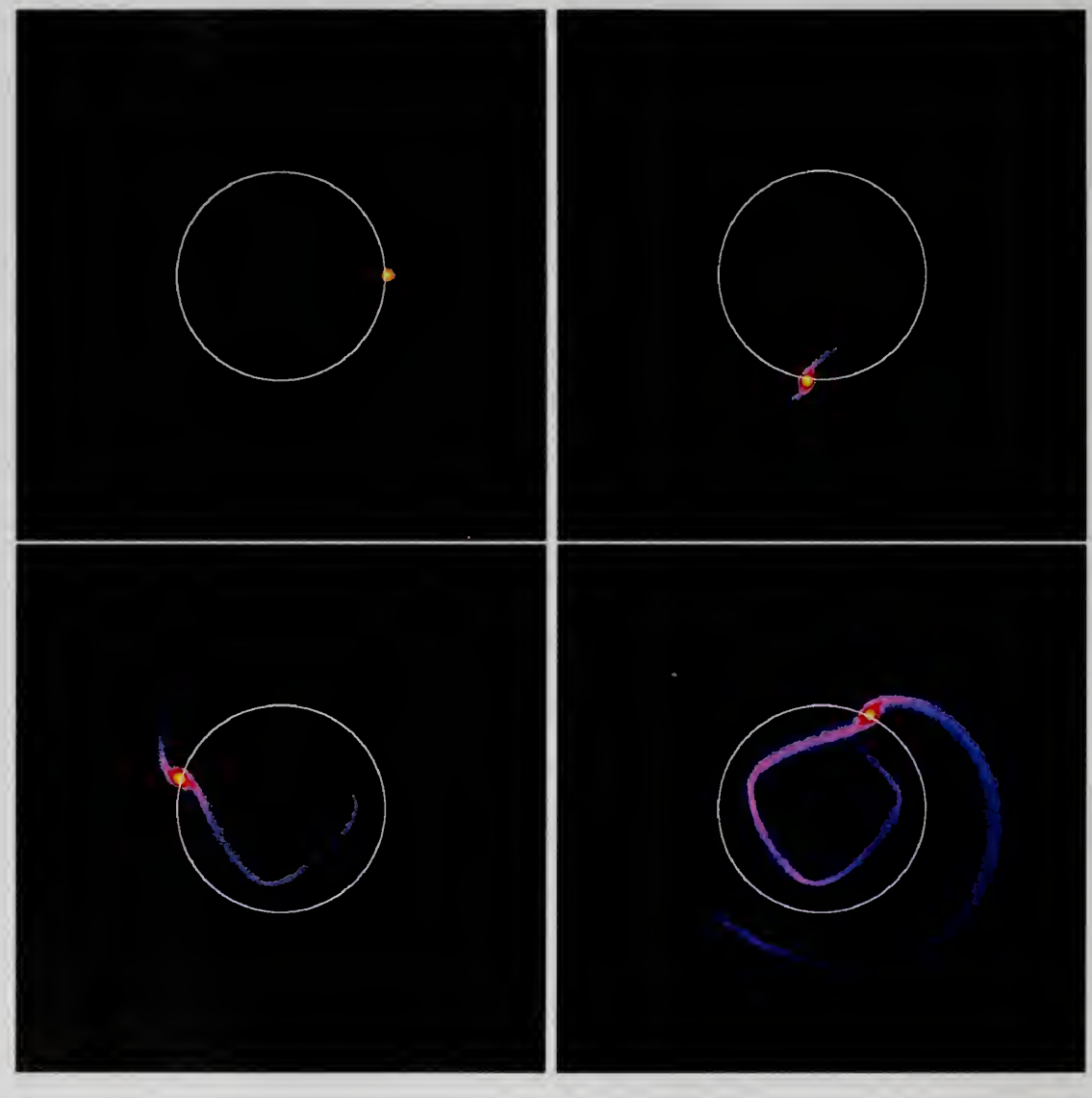

Figure 4.5 As in Figure 4.3 but including the gravitational attraction of the satellite on the ejecta at all times.

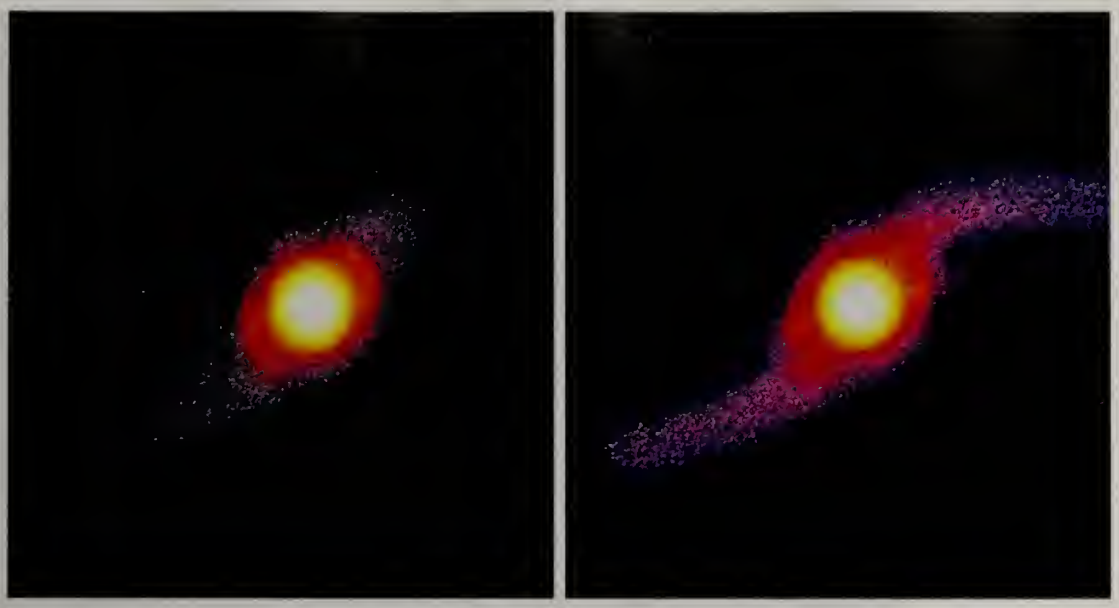

Figure 4.6 A high-resolution view of the tail streamers in the low-mass satellite simulation without (left) and with (right) the gravitational acceleration by the satellite at $T = 4.5$ (compare with Figure 4.3 left panel, and Figure 4.5 middle panel, respectively). The two steamers are clear in left panel but very weak in the right panel. Although very weak, the second streamers can be identified near the tidal radius.

once again the tail particles always feel the gravitational force from the satellite. The overall evolution of the satellite and its disruption time is similar to the less massive satellite shown in Figure 4.5. However, the long-term acceleration of the ejected material by the remaining satellite significantly alters these orbits. As the tail continues to lose mass, the leading and trailing tails evolve to positions that are well inside and well outside the satellite's orbit and hence does not trace the satellite orbit at all (Johnston et al., 2001; Moore & Davis, 1994). The leading tail significantly tilts toward the center of the halo and almost points directly there at late times. The trailing tail is distributed throughout a wide annulus in the outer halo. This difference results from the torque applied by the satellite *well* after escape. Orbits in the leading tail that lose energy and angular momentum fall toward the center of halo, while orbits in the trailing tail gain energy and angular momentum and spread over a wide range of radii in the outer halo.

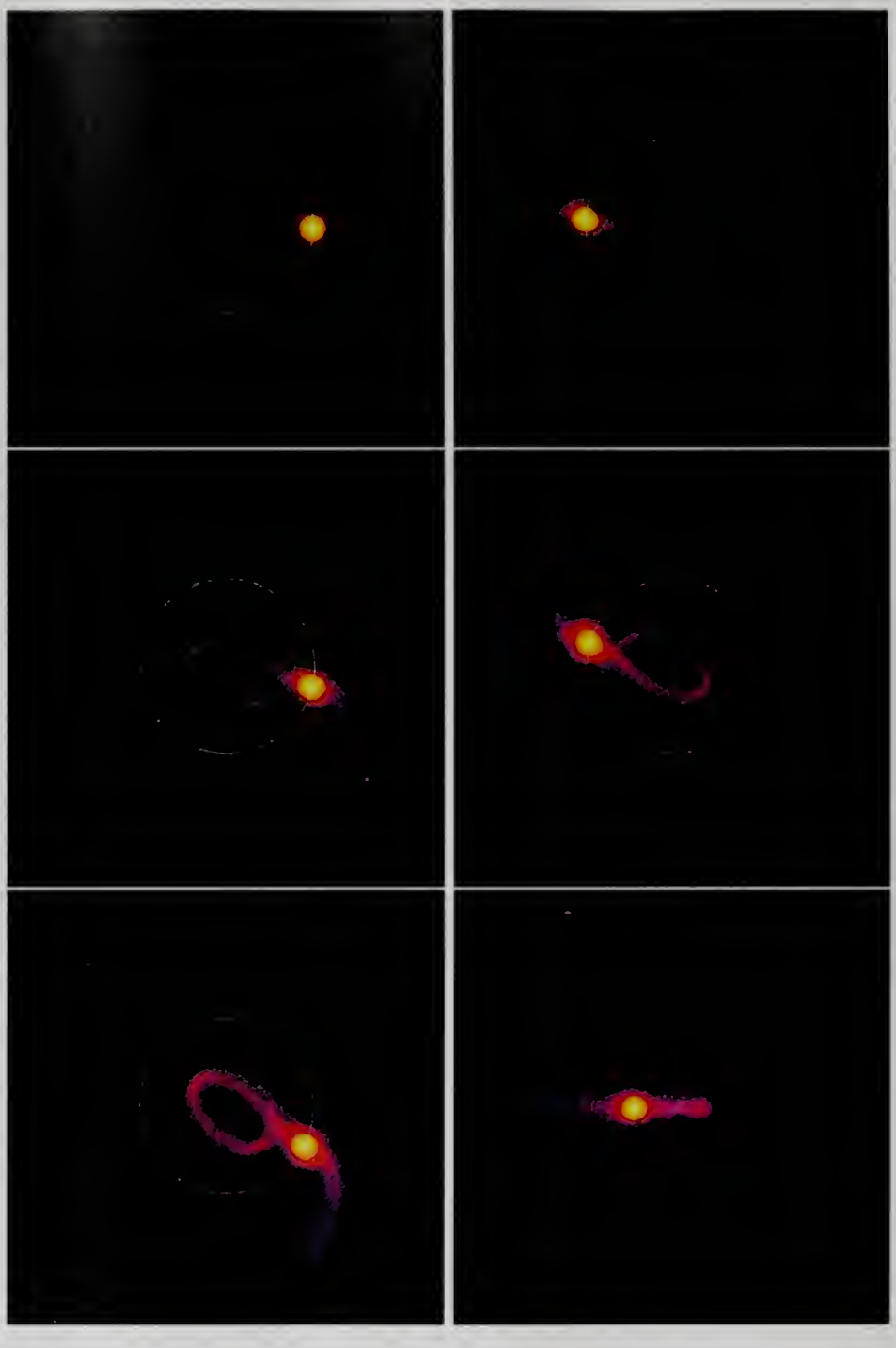

Figure 4.7 The mass density in the orbital plane for a massive satellite halo on a circular orbit with $r = 0.4R_{vir}$ at $T = 0.0$, 1.0, 2.0, 3.0, and 4.0 in the top-left, top-right, middle-left, middle-right, and bottom-left panels, respectively. Recall that the orbital period of the circular orbit is $T_{period} \sim 2.0$. The bottom-right panel shows the edge on view at $T = 4.0$. The color scale is logarithmic in the dark matter mass density from blue to red. The color scale is fixed for all snapshots (as described in Figure 4.3). The circles show the satellite orbit. The tail remains confined to the orbital plane as expected (lower-right panel).

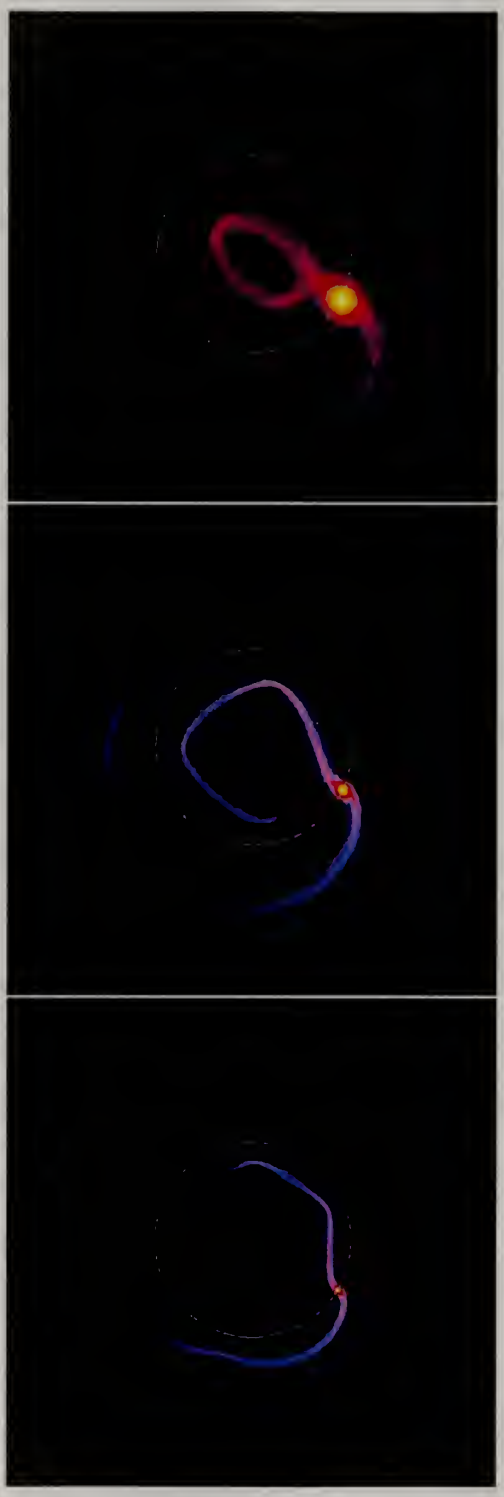

Figure 4.8 As in Figure 4.7 but comparing the ejecta at $T = 4.0$ for the massive, low-mass, and tiny-mass satellites from top to bottom, respectively.

We show the tail morphology for our satellites with three different masses (see Table 4.1) on circular orbits at $T = 4$ in Figure 4.8. The tidal tails in the low-mass and tiny-mass satellites (0.001 and $0.0001 M_{host}$, respectively) very roughly follow the satellite orbit, with the leading and trailing tail located inside and outside of the satellite orbit. Compared to Figure 4.3, it is clear that the differences decrease with the satellite mass. As we described in Section 4.2, the low-mass satellite corresponds to the Sagittarius dwarf spheroidal galaxy halo and the tiny-mass satellite corresponds to the Draco dwarf spheroidal galaxy halo.

Figure 4.9 shows the evolution of the distance from the host halo center and the satellite's gravitational potential for an ensemble average of 10 randomly sampled particles near the tip of the leading tail in the three satellites. The tail from a massive satellite receives a larger torque and a larger shift to smaller energies and angular momentum than the tail from a lower-mass satellite. The bottom panel in Figure 4.9 shows that the decay results from interactions with the satellite potential. Figure 4.9 also shows that the satellite potential remains important in the low-mass and tiny-mass satellites when the tail is close to the satellite but it is unimportant when the tail is far from satellite. The satellite potential always remains significant for the massive satellite tail. The long-term influence of the satellite on the tail morphology makes any inference of the satellite orbit from the tidal tail impractical, especially for satellites on non-circular orbits (see Section 4.3.2.2).

The leading tail from the low-mass and the tiny-mass satellites in Figure 4.8 exhibits kinks. The kinks are a consequence of the epicyclic motion of the tail orbits and of acceleration by the satellite at subsequent apocenters. Figure 4.10 shows the ensemble averaged distance and positions for a sample of leading tail particles orbits taken from the low-mass satellite simulation shown in Figure 4.5. The kink occurs at the first apocenter of the ejecta, after it is decelerated by the satellite during and subsequent to its escape. The deceleration during escape tends to correlate the phases

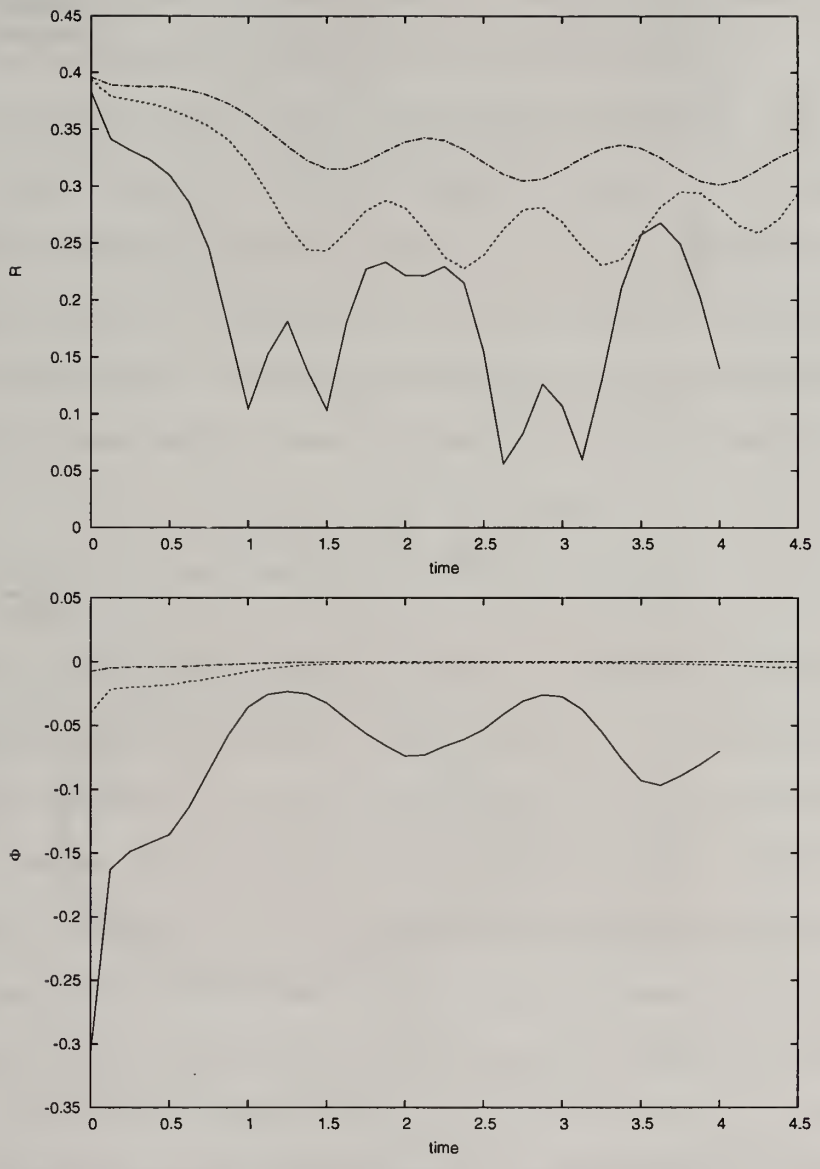

Figure 4.9 The evolution of the mean radius (top panel) and satellite potential (lower panel) for an ensemble of particles randomly selected from the leading tails in Figure 4.8 for the massive (solid), low-mass (dotted), and tiny-mass (dash-dot) satellites.

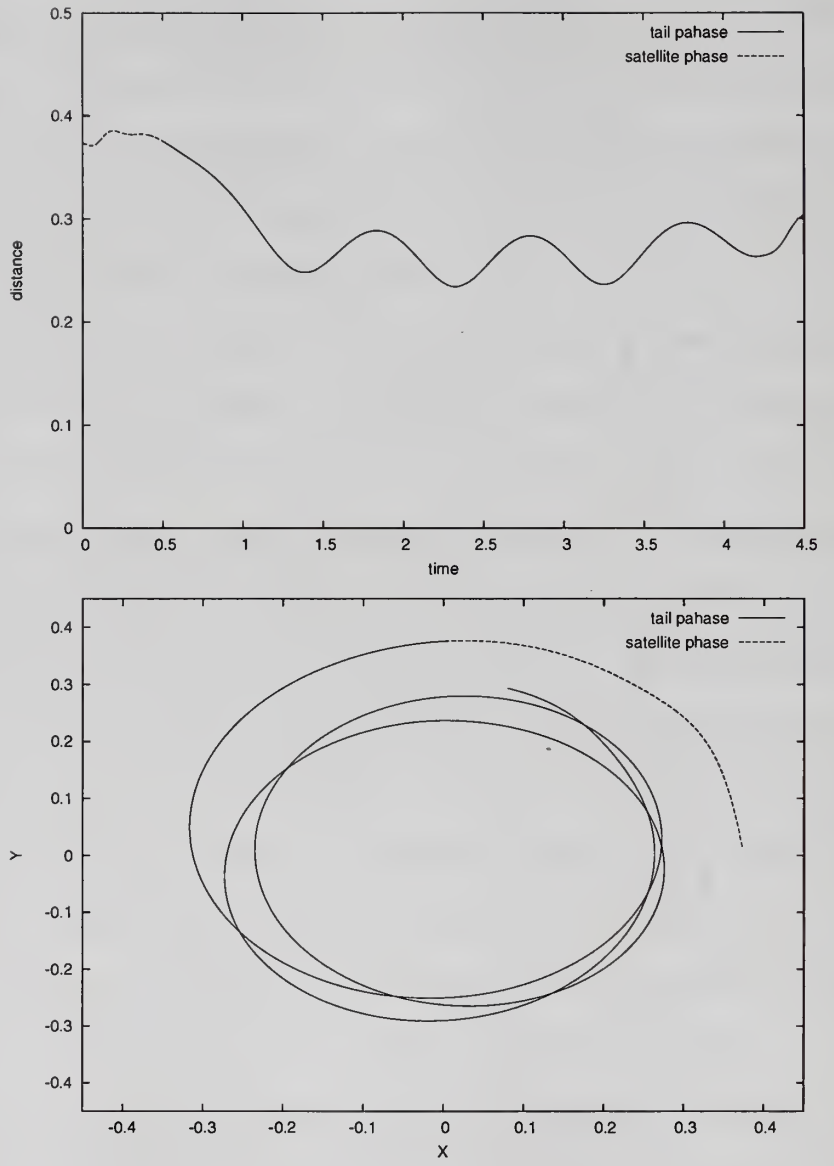

Figure 4.10 As in Figure 4.4 but now *including* the gravitational force of the satellite at all times. This force significantly lowers the energy and angular momentum of the leading orbit, decreasing its mean and apocenteric radius. This initial period of deceleration ($T < 1$) is responsible for the observed 'kink' in the tail (see Figure 4.8).

of the ejected orbits and results in a narrowing of the tidal tail's width. In contrast, the satellite potential accelerates the trailing tail particles, which increases the peri- and apocenters of the trailing tail. The analogous kink in the trailing tail is not so obvious because of its lower orbital frequencies. However, a plot analogous to Figure 4.10 does show a similar oscillation with lower angular frequency.

The large changes in the orbits of escaping particles orbits are easily understood using a restricted three-body approach. Consider a satellite of mass M_s in circular orbit at galactocenteric radius r_s in a halo of mass M_h. In the frame of reference moving with a satellite of vanishingly small mass, the effective potential is symmetric about the satellite center. Although orbital energy and angular momentum are not conserved, this system admits a conserved quantity, the Jacobi constant:

$$E_J = E - \vec{\Omega}_s \cdot \vec{L} \tag{4.1}$$

where E and $\vec{L}$ are the orbital energy and angular momentum and $\vec{\Omega}_s$ is the satellite's angular frequency about the host halo. This expression is easily derived by identifying a perfect time derivative in the inner product of the velocity vector and Newton's equations of motion in the rotating frame of reference (Binney & Tremaine, 1987, Section 3.3.2). An isocontour of the Jacobi constant passes through the X-points, $r_\times$, and demarcates the bound and unbound trajectories as shown in Figure 4.11a. As the satellite mass increases, the inversion symmetry about the satellite center is broken and the unstable points separate as shown in Figure 4.11b. For small-mass satellites, therefore, the tidal force is symmetric about the satellite center leading to symmetric tidal tails as seen in globular clusters. However, for large-mass satellites, the asymmetry in the tidal force leads to asymmetric mass loss.

Now consider the mass lost through the inner (outer) critical point, $r_\times$. Such orbits will have an inward (outward) velocity and unbound values of the Jacobi constant. The force from the satellite continues to affect the orbit beyond the tidal radius in

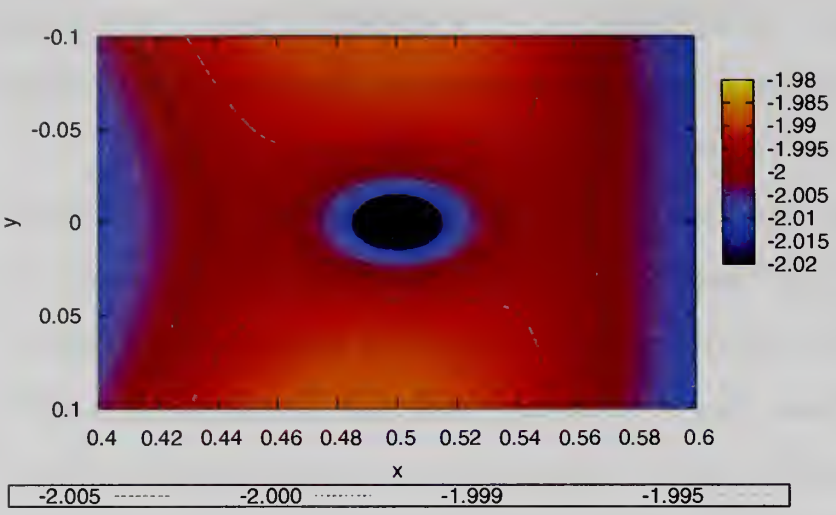

(a) 5×10^{-4}

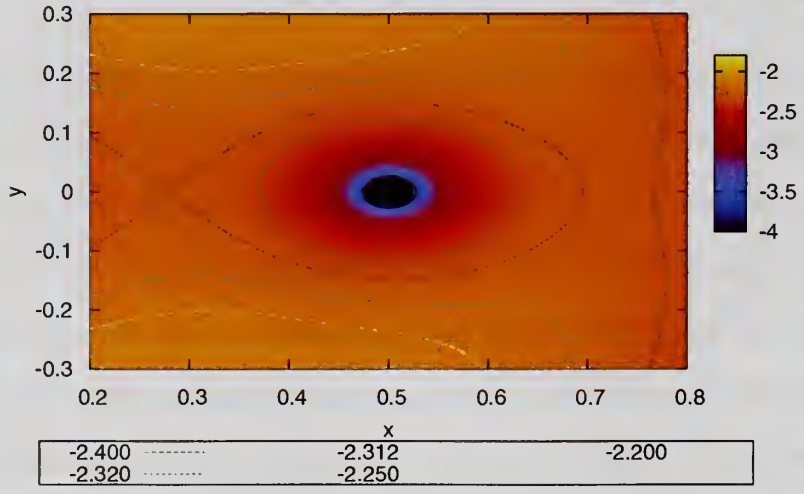

(b) 5×10^{-2}

Figure 4.11 Contours of the Jacobi constant for two satellites with different masses as labelled. They follow a circular orbit with a radius of $q_s = 0.4$ in a $c = 15$ NFW halo of $M_h = 1$ and a virial radius $R_h = 1$. The x-axis describes the distance between the host halo center and the satellite center and the y-axis describes the location in the direction of orbital motion. Note the strong asymmetry in x about the center for the higher mass satellite in Panel (b).

this restricted problem as in the N-body simulations. Moreover, the smaller the mass of the satellite, the closer the radius is to that of the satellite, and the ejected orbit *lingers* near the original satellite orbit, partly offsetting the smaller gravitational force. For this reason, the orbit does not take on the orbital actions of the satellite but continues to be torqued by the satellite. One may estimate the scaling of this energy change by computing the work done in the satellite frame on the escaping tail particle; this naturally takes into account the lingering. Begin with the standard restricted three-body problem with generalized forces. Assuming that the satellite orbits in the x-y plane and using Hamilton's Equations, one may compute the z-component torque on an escaping particle and the change in angular momentum of the escaping particle after an interval T becomes

$$\Delta L_z = \int_0^T dt \left(-\frac{\partial H}{\partial \phi}\right) = \int_0^T dt \left(-\frac{\partial V_s}{\partial \phi}\right) \tag{4.2}$$

where H is the Hamiltonian, ϕ is the azimuthal coordinate conjugate to L_z and

$$V_s = -\frac{GM_s}{|\mathbf{r} - \mathbf{r}_s(t)|}$$

is the gravitational potential of the satellite. The second equality in Equation (4.2) owes to the ϕ independence of all the other terms in H. We may consider an escaping orbit in the limit that the mass of the satellite M_s is much smaller than the mass of halo M_h and use perturbation theory to evaluate Equation (4.2). To do this, let the unperturbed orbit be the circular orbit that passes through the X-point, $r_\times$ at $t = 0$. Expanding to lowest contributing order in M_s/M_h, after some straightforward algebra and taking the limit $T \to \infty$, one may show that

$$\Delta L_z = \frac{GM_s}{r_\times^2} \left(\left.\frac{\partial \Omega_\phi}{\partial r}\right|_{r_s}\right)^{-1}$$

where Ω_ϕ is the azimuthal orbital frequency. Finally, it follows that $\Delta E = \Omega_s \Delta L_z$ from the conservation of the Jacobi constant (Equation 4.1) which yields:

$$\Delta E = -2\Omega_s^2 r_s^2 \left(- \left. \frac{\partial \ln \Omega_\phi^2}{\partial \ln r} \right|_{r_s} \right)^{-1/3} \left(\frac{M_s}{M_h} \right)^{1/3}. \tag{4.3}$$

Since G, r_s, and Ω_s are constant, Equation (4.3) implies that the work done is proportional to $(M_s/M_h)^{1/3}$. In other words, the change in the orbital energy of the escaping particle decreases as the satellite mass decreases but only weakly!

Although the derivation of the scaling assumes $M_s/M_h \to 0$, we demonstrate numerically that it applies over all values of interest by integrating the equations of motion in the rotating potential. We adopt $r_s = 0.4$ and choose values of the Jacobi constant that are 1% larger than the critical value passing through $r_\times$ with zero velocity. The initial motion, in the rotating frame, is along (or against) the direction of rotation for inner (outer) escapees. Figures 4.12–4.14 show the resulting trajectories and conserved quantities for $M_s/M_h = 10^{-4}, 10^{-3}, 10^{-2}$. For inner (outer) escapees, the energy and angular momentum decrease (increase) after the initial transient for $t < 0.5$. Figure 4.15 shows that the energy change for ensembles of orbits in the leading tail chosen as follows. The initial position is chosen to be 2% of $r_\times$ outside of the X-point and the velocities are chosen to have a normal distribution in the satellite frame with a dispersion that is 2% of the satellite's circular velocity at $r_\times$. The orbits in Figures 4.12–4.14 are representative members of these ensembles. The magnitude of the energy change ΔE is defined as the ensemble average of $|E_{min} - E_{init}|$ where E_{init} is the initial energy and E_{min} is the minimum energy along the orbit. These numerical values are consistent with the predicted scaling $(M_s/M_h)^{1/3}$. Circumstance may eventually bring the ejected particle close to the satellite once again, as seen in Figure 4.14. The radial extent of the annulus covered by the orbit increases only gradually with increasing satellite mass, reflecting the same weak dependence on M_s/M_h. In the simulations, the mass loss and subsequent reequilibration of the

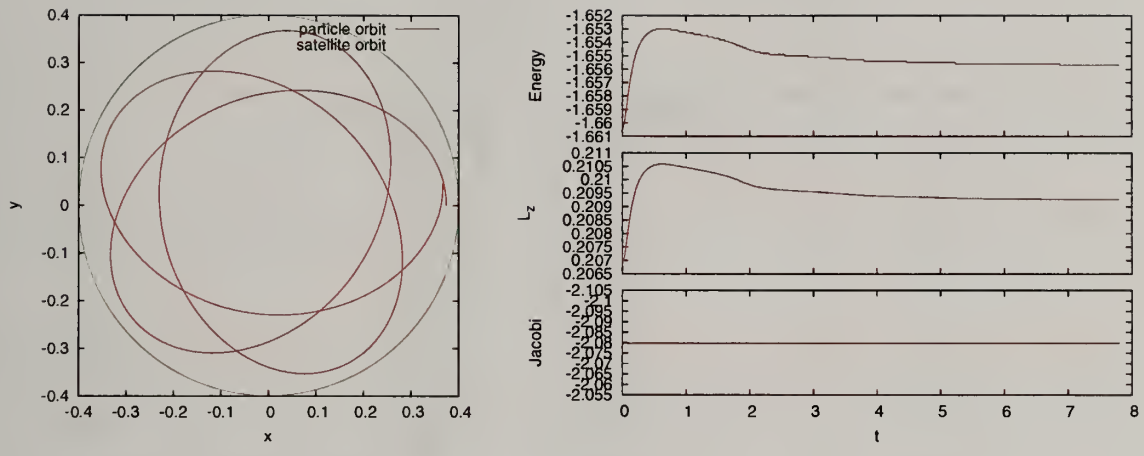

(a) inner

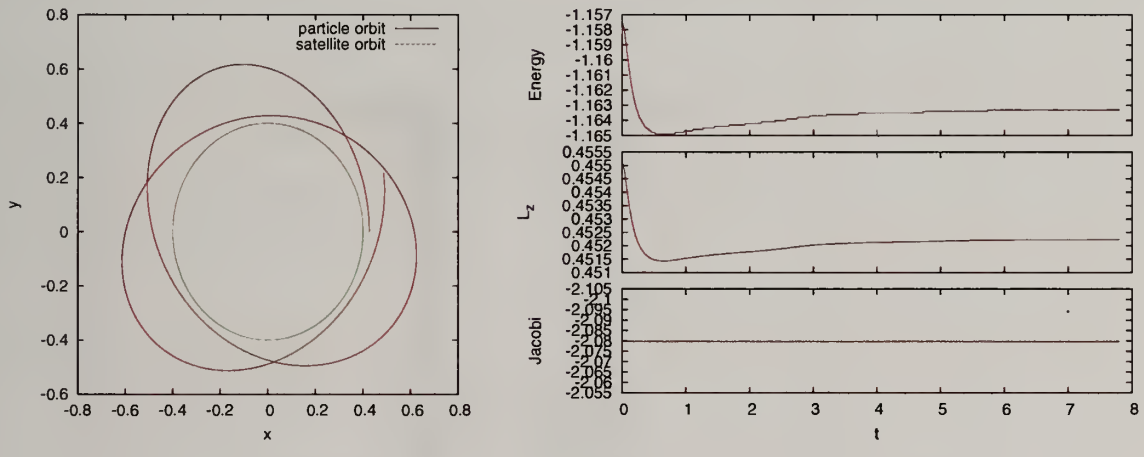

(b) outer

Figure 4.12 The evolution of two orbits escaping from the inner (upper panels) and the outer (lower panels) tidal radii for $M_s/M_h = 10^{-4}$ where M_s is the satellite mass and M_h is the host halo mass. The left panels show the orbital plane and the right panels show the evolution of energy, angular momentum, and the Jacobi constant. The value of the Jacobi constant is conserved as expected.

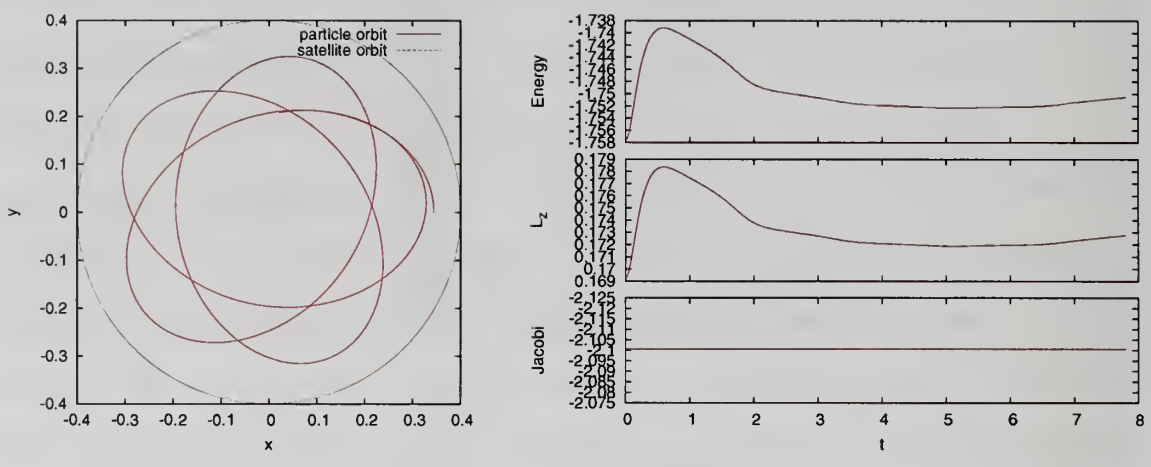

(a) inner

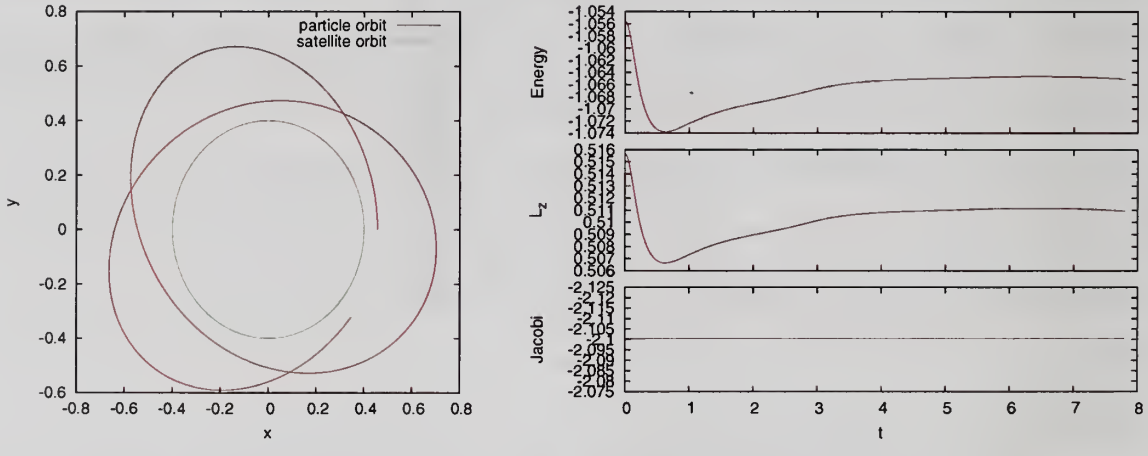

(b) outer

Figure 4.13 As in Figure 4.12 but for $M_s/M_h = 10^{-3}$.

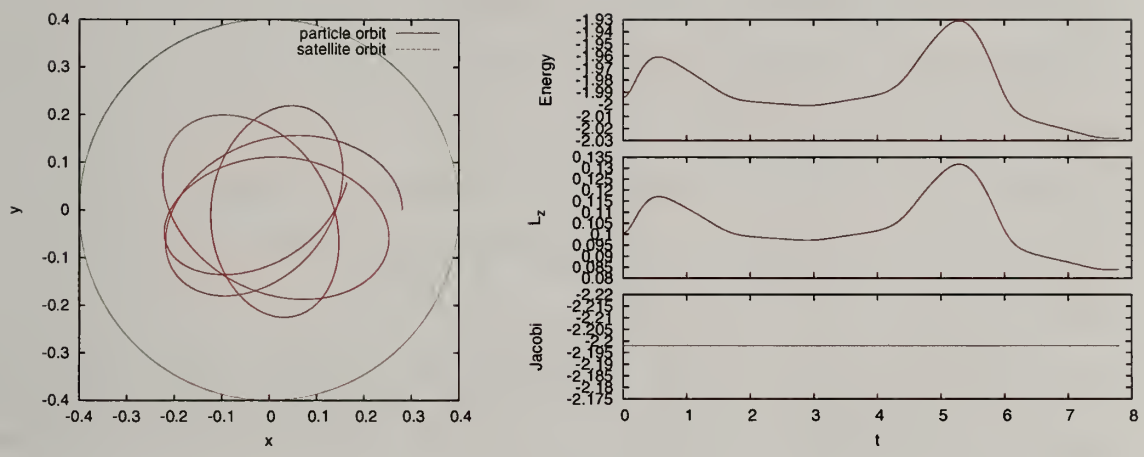

(a) inner

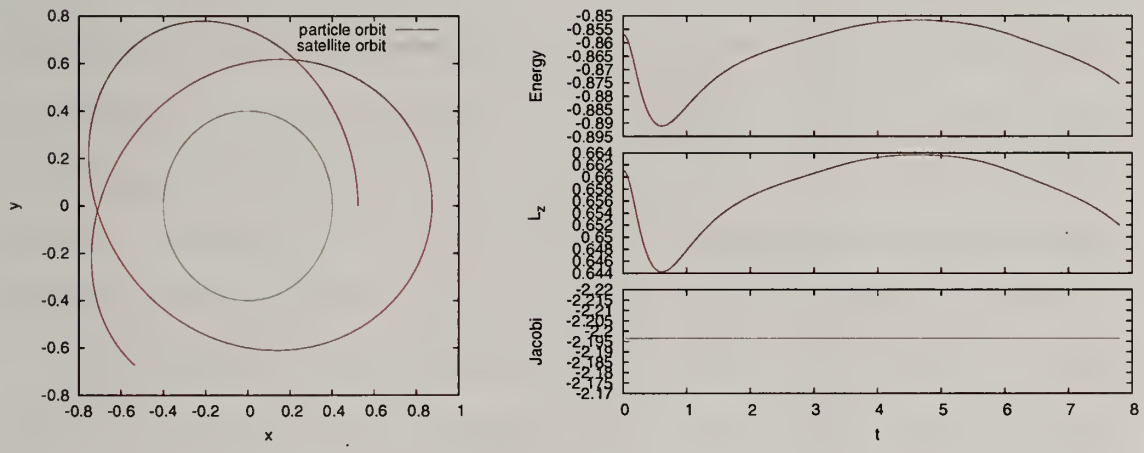

(b) outer

Figure 4.14 As in Figure 4.12 but for $M_s/M_h = 10^{-2}$.

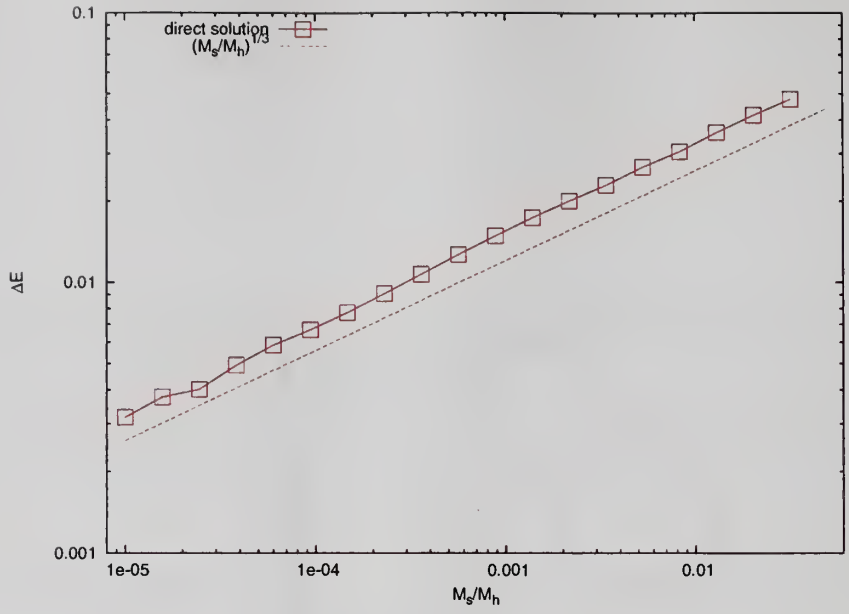

Figure 4.15 A numerical test of the predicted scaling of the energy change of escaping particles (Equation 4.3) with satellite mass. The x-axis is the ratio of satellite mass M_s to total halo mass M_h and the y-axis is the magnitude of the energy change, ΔE. The straight line is the relation $(M_s/M_h)^{1/3}$.

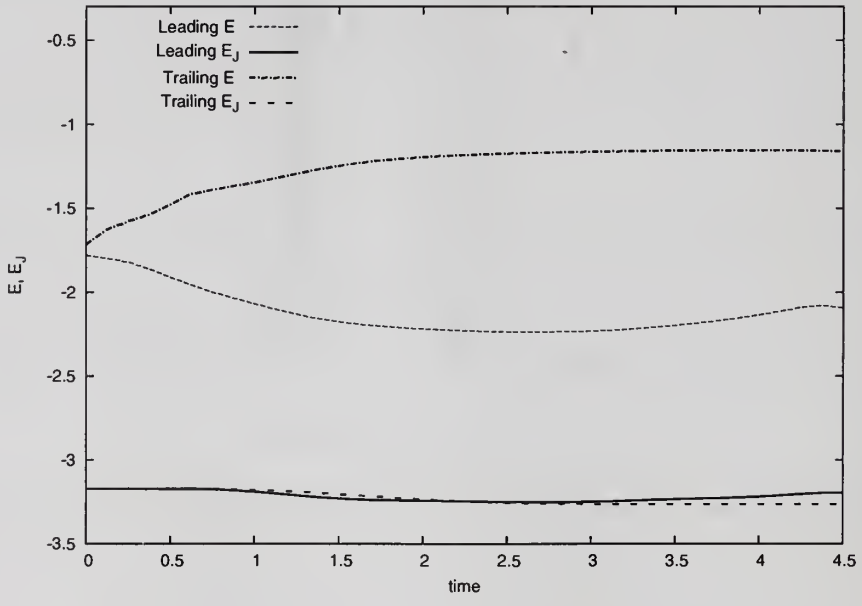

Figure 4.16 The time evolution of the energy, E, and the Jacobi constant, E_J, for two ensembles of particles ejected from the low-mass satellite selected from the leading and trailing tail, respectively. The value E_J is nearly conserved while the energy changes owing to work done during escape. Changes in E_J are caused by mass loss and the resulting evolution of the satellite's gravitational potential.

satellite potential causes small deviations in the Jacobi constant even though the satellite orbit remains circular as shown in Figure 4.16. Nonetheless, the restricted three-body dynamics explains most of the features seen in the orbit evolution.

4.3.2.2 Non-circular orbits

Although we still expect some of the insight gained from the restricted three-body problem to carry over to the evolution of a satellite on an *eccentric* orbit, this more complex situation requires direct simulation. Figure 4.17 shows the tidal tails of a massive and low-mass satellite on an eccentric, $e = 0.5$, orbit. The tidal tail morphology for eccentric satellite orbits is significantly more complex than for circular satellite orbits and varies more strongly with satellite mass. In the left panel of Figure 4.17, the massive satellite has dramatically decelerated the leading tail, which now reaches the host halo center and forms an inner "reservoir" of ejecta. The deceleration by the satellite causes the leading tail to appear close to radial. In the right panel of Figure 4.17, the multiply segmented tail from the low-mass satellite is caused by two mechanisms. First, during each satellite orbit, the leading tail forms during the approach to pericenter. After pericenter, the tidal strain and the mass-loss rate diminishes resulting in a gap in the tail. Second, deceleration by the satellite changes the orbits of the newly disconnected leading tail, producing a distinct segment.

Figure 4.18 shows the evolution of a massive satellite on an e=0.74 orbit. Initially, the leading tail points directly toward the halo center but the strong deceleration by the satellite eventually fills the inner halo with ejecta. Figure 4.19 provides a finer time sampling of the evolution between pericenter and apocenter for the same simulation. Instantaneously, the morphology can be very complex and the position angle of the leading tail can vary significantly from its nearly radial average. There is little correlation between the tail location and the satellite orbit. The location of the inner ejecta, e.g. its outer turning points, is determined by the host halo

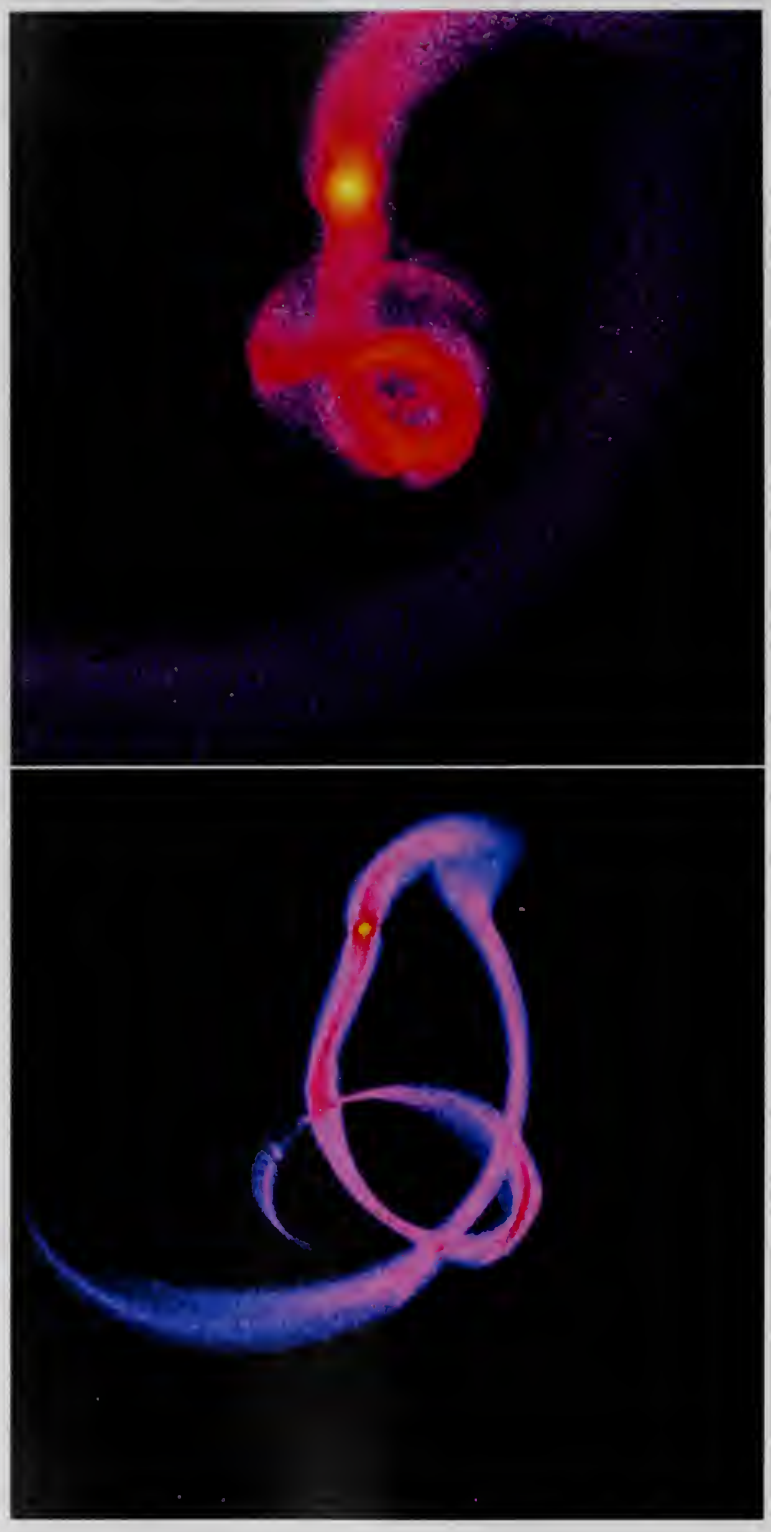

Figure 4.17 Tails at time $T = 5.0$ for the massive (left) and the low-mass (right) satellite on an eccentric, $e = 0.5$, orbit.

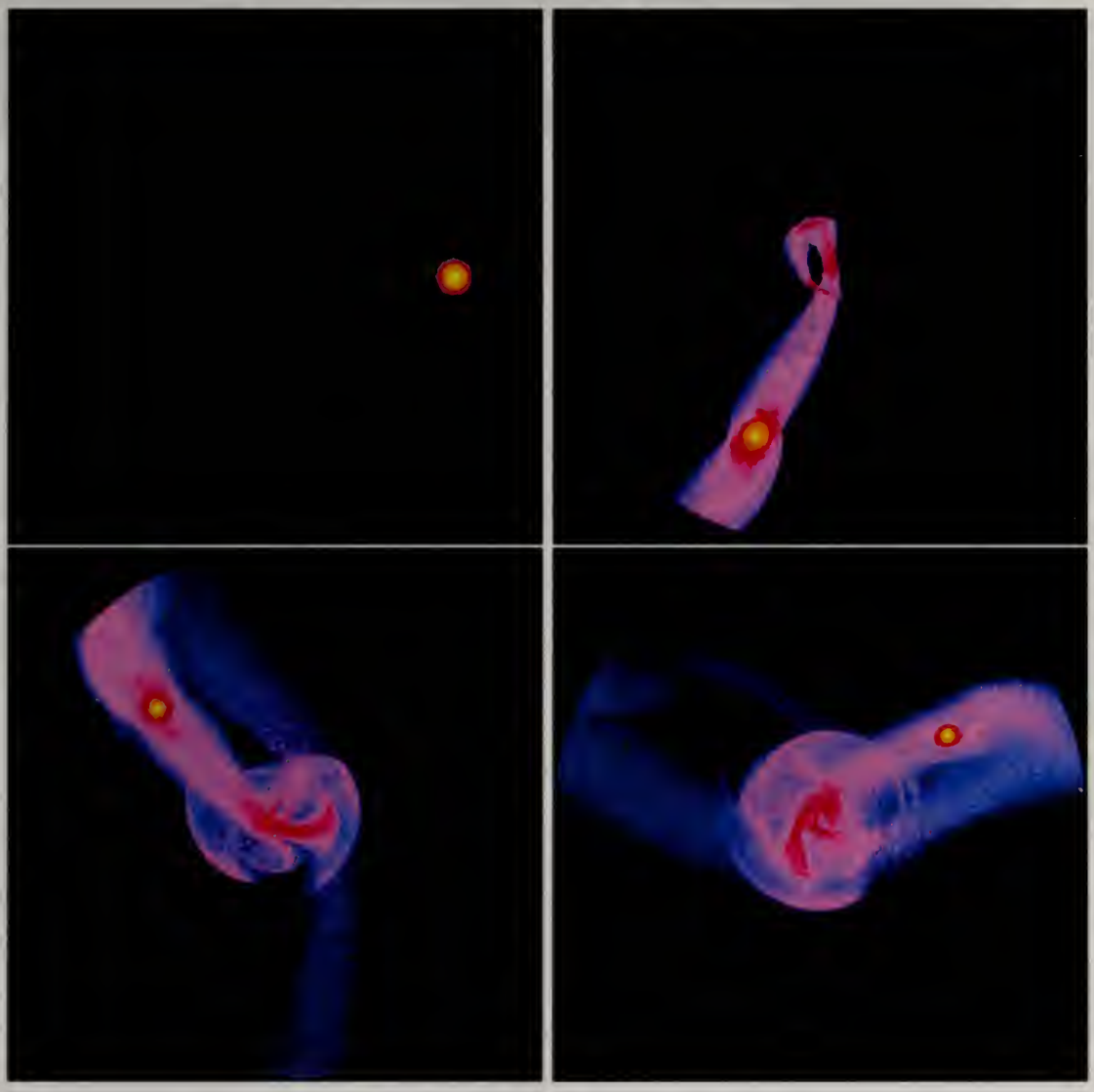

Figure 4.18 As in Figure 4.7 but for the massive satellite on an $e = 0.74$ orbit at $T = 0.0$, 1.5, 3.0, and 4.5 in the top-left, top-right, bottom-left panels, and bottom-right panels, respectively.

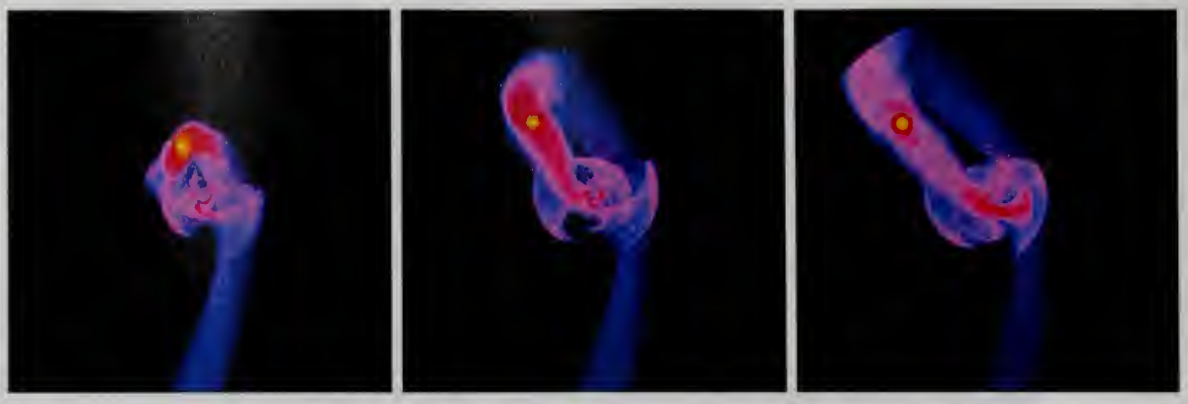

Figure 4.19 The same as Figure 4.18 but for times T = 2.5, 2.75, and T=3.0 from left to right, respectively, as the the satellite moves from pericenter to apocenter. Owing to the deceleration by the satellite potential, the leading tail falls toward the center of the host halo.

potential, the time-varying satellite potential, and the satellite orbit in combination. Therefore, unlike streams from very low-mass satellites, the tail orientation is not directly informative. However, through dynamical modelling, the location of the inner ejecta may provide constraints on combinations of satellite properties and its history, and the galaxy potential.

4.4 Observational applications

We have demonstrated that tail morphology depends sensitively on the satellite mass and orbit. For modest to high-mass satellites, the ejected tails have orbits that differ significantly from that of the progenitor satellite. In this section, we illustrate the observational implications of these results.

4.4.1 Projected satellite tail morphology

The observational implications for Milky Way streams can be summarized by projecting the tail star counts and radial velocity signatures against the sky with the observer at the center[3] of host halo. Figure 4.20 shows Aitoff projections of number

[3]A specific Milky Way model would take into account the solar position and an orbital estimate for a particular progenitor satellite. However, in this study, the satellites are chosen to be only

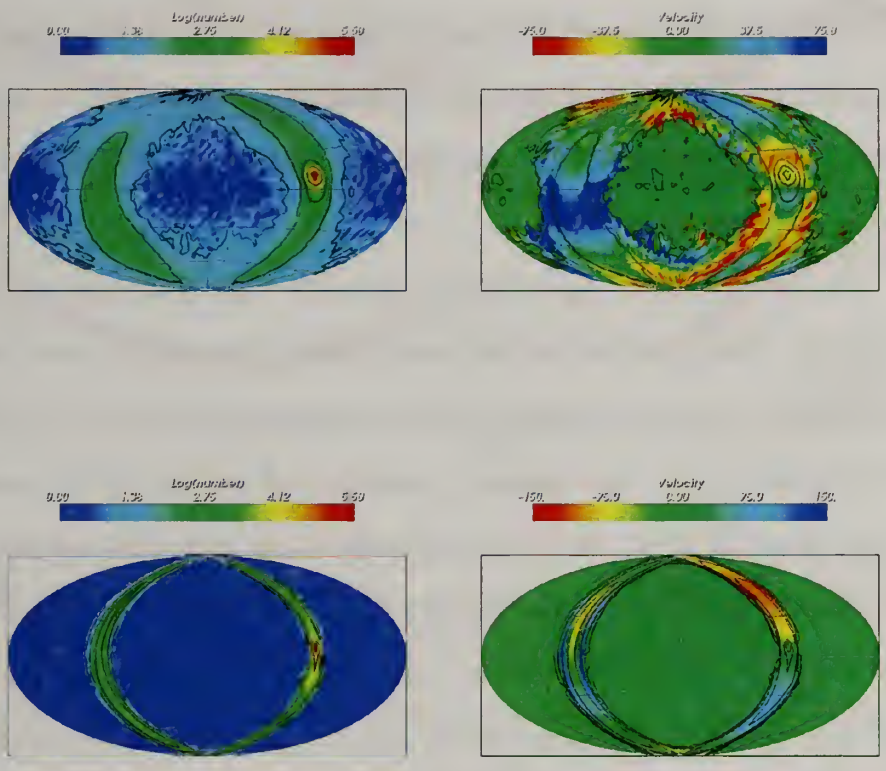

Figure 4.20 Aitoff projections of the massive satellite (top panels) and the low mass satellite (bottom panels) on an $e = 0.5$ orbit. The snapshots for these projections are shown in Figure 4.17. The observer is located at the center of the host halo. The left panels show the number density of particles and the right panels show the mean radial velocity. The black isocontours in all four panels represent the particle number density. Color bars show the number density (left) and radial velocity (right) scales.

density and mean radial velocity for the massive satellite (top panels) and the low-mass satellite (bottom panels) with an $e = 0.5$ orbit (the same simulations described in Figure 4.17 at the same time, $T = 5.0$). The Aitoff projection covers the entire sky, $0° \leq l \leq 360°$ and $-90° \leq b \leq 90°$, and the pixel size is $4^o \times 4^o$. The number density of the particles (left panels) and the mean radial velocity (right panels) are coded by color. The contours in all the panels represent the particle number density. Velocity outliers at low number density are trimmed by setting to $\bar{v}_r = 0$ all the pixels with fewer than 10 particles. The satellites are located at $l \approx 270^o$ and $b \approx 0^o$ and move in the positive b direction.

The radial velocity signatures of the massive and low-mass satellites are distinctly different. These qualitative differences are a direct consequence of the large energy and angular momentum changes of the ejecta orbits leading to the phase wrapping of the leading tail and the dramatic broadening of the trailing tail (see Section 4.3.2.2). This causes the lower overall mean velocity values with a more rapid angular variation around the sky. In contrast, the mean velocity of the leading and trailing tails for the low-mass satellite are smooth and slowly vary around the sky. Quite clearly, the debris from the massive satellite will not show the distinct kinematic and spatial signatures that have been exploited in recent observational campaigns.

Near $b = 0°$ and $l = 90°$, one observes a region of receding orbits surrounded in longitude by regions of approaching orbits. Figure 4.17 (right snapshot) shows that line-of-sight projections will encounter strong leading and trailing tails from same satellite at different radii. The closer the tail to the observer, the larger the angular extent perpendicular to the motion of the stream. Their velocity signature in the Aitoff projection occurs as a single line of sight cuts through these tails at different radii.

---

representative of CDM predictions and, in the same vein, the galaxy center is an intuitively simple inner-galaxy view point.

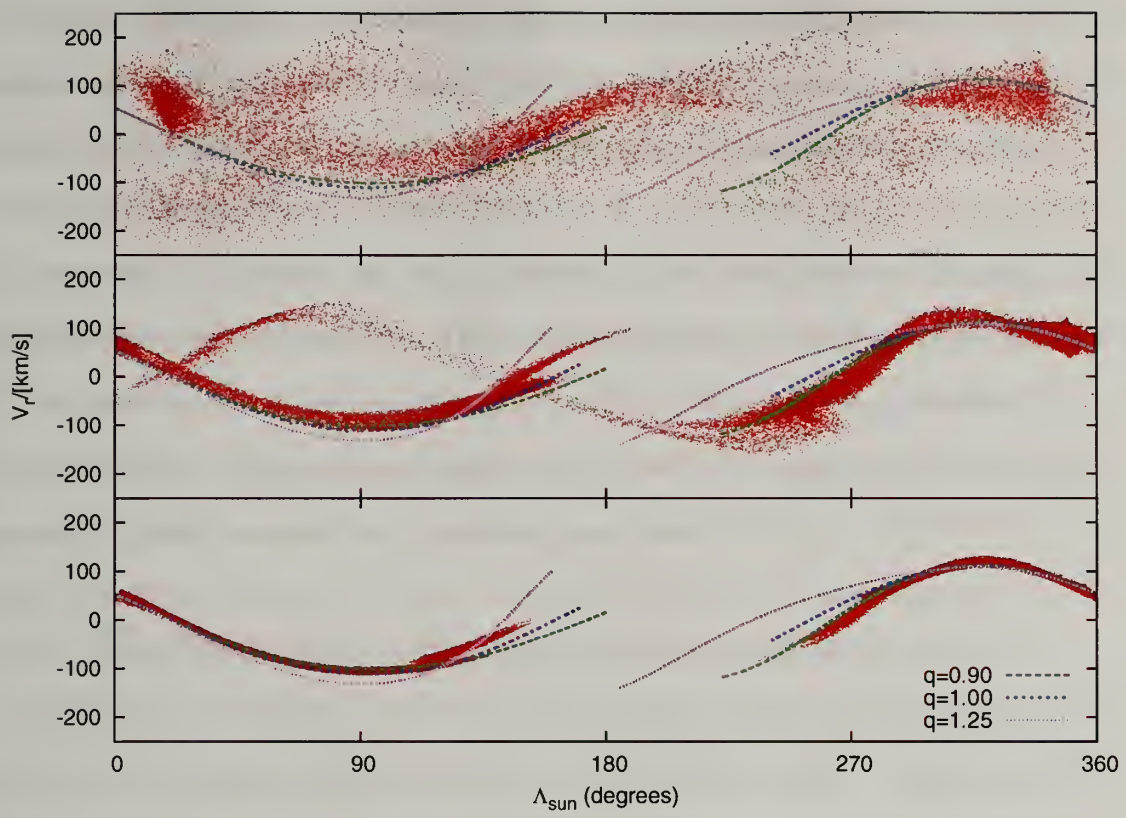

Figure 4.21 The radial velocity of tail particles as a function of orbital longitude for the massive satellite, low-mass satellite, and tiny mass satellite, from top to bottom, shown in Milky Way units. All three satellites have orbits with $e = 0.5$ and are centered at a longitude of 0^o. The width of the distribution in $|v_r|$ increases with satellite mass. For comparison, the satellite trajectories for halos with flattenings of $q = 0.9$, 1.0, 1.25 are also shown. Although all three simulations are performed in a spherical host halo potential, the tail locus is better matched for a satellite trajectory with $q = 0.9$.

The Aitoff projections contain most of the information that one might obtain from combined kinematic–photometric surveys such as RAVE (Steinmetz et al., 2006). In particular, these results show that tail morphology depends on satellite mass. Therefore, a wide range of kinematic "template" models may be required to best exploit the information implicit in observed halo stars.

4.4.2 The effects on tidal tail radial velocity

Radial velocity–orbital longitude diagrams are frequently used to characterize large-scale kinetic features in the Milky Way. Figure 4.21 shows radial velocity–

orbital longitude diagrams for the ejecta of satellites with orbits having $e = 0.5$ for each of our three masses. We convert simulation units to Milky Way units by assuming a virial radius of 250 kpc and a total mass of $1.0 \times 10^{12} M_{\odot}$ (Klypin et al., 2002). In Figure 4.21, the Sun has $\mathbf{R} = (-8.0, 0.0, 0.0)$ kpc and the Galactic plane and the satellite's orbital plane are coincident. Here we adopt the Sagittarius longitudinal coordinate system described in Majewski et al. (2003) for the orbital longitude. All satellites have $\mathbf{R} = (50.0, -7.5, 0.0)$ kpc and move in the y direction. Therefore, the satellite has $l \approx 0°$ and longitude increases along the trailing tail (in the $-y$ direction). The radial velocity is measured from the halo center. The spread in $|v_r|$ is proportional to the satellite mass, as expected from the previous discussion and hence the mean velocity will be an unbiased diagnostic of the satellite orbit only for very low mass satellites. Although we have only modelled the dark matter, it is likely that the $v_r - l$ space distribution for stellar and dark matter ejecta will be similar in most cases since the internal satellite velocity dispersion plays only a minor role in shaping the ejecta distribution.

Law et al. (2005) use M giants from the Two Micron All-Sky Survey (2MASS, Skrutskie et al., 2006) to map the position and velocity distributions of tidal debris from the Sagittarius dwarf spheroidal galaxy. Assuming that tidal tails approximately align with the satellite trajectory, the authors note that the radial velocity distribution of tidal debris suggests an prolate Milky Way halo with an axis ratio of $q = c/a = 1.25$. However, our results demonstrate that the tails do *not* follow the satellite orbit. In Figure 4.21, we also plot satellite trajectories for three different halo flattenings to compare with the particle distributions of our simulations evolved in a spherical host halo. Following Law et al. (2005), we flatten our host halo parallel to the satellite's motion and compute point-mass satellite trajectories to compare with our simulated $v_r - l$ diagrams. Surprisingly, the distributions of the low-mass satellite and the tiny-mass satellite tidal tails most closely matches a $q = 0.9$ halo. The gravitational

acceleration by the satellite shifts the tail location in the radial velocity distribution and this trend is degenerate with the effects of halo flattening. For instance, the location of the leading tails decelerated by a massive satellite is degenerate with the trajectories of tails in an oblate halo with no satellite deceleration. We have not attempted to model the Milky Way in sufficient detail to estimate the halo flattening including satellite deceleration. However, the degeneracy between halo flattening and the shift caused by the satellite gravitational acceleration suggests that the Law et al. (2005) conclusions may be biased and a more careful analysis including the full dynamics of the halo-satellite interaction is necessary.

4.4.3 The effects on the tidal tail phase space distribution

Several groups have proposed phase-space-based detection diagnostics for moving groups associated with disrupted dwarf galaxy and star cluster streams. Lynden-Bell & Lynden-Bell (1995) proposed using the intrinsic correlation of moving groups' radial energy and galactocenteric radius to identify disrupted systems. The procedure is as follows. Assuming a spherical gravitational potential for the outer galaxy, one estimates the radial energy $E_r = v_r^2/2 + \Phi(r)$ and the galactocenteric radius r of the putative ejecta stars from observations. Then, assuming that all of the debris from a single satellite has the same orbital energy, E, and angular momentum, L, conservation of energy implies a simple linear relationship in r^{-2}: $E = E_r - L^2/2r^2$. Hence, linear features in the observed E_r–r^{-2} diagram indicate the detection of a tidal stream. Recently Belokurov et al. (2007) used this method to support the detection of stellar streams in the Sloan Digital Sky Survey.

However, as we have now seen, a massive satellite will modify the conserved quantities of the ejecta orbits and change their location in $E_r - r^{-2}$ space. Figures 4.22 and 4.23 show the $E_r - r^{-2}$ diagrams for the low-mass and tiny-mass satellite simulations on an $e = 0.5$ orbit. For clarity, we have reduced the point density by randomly sam-

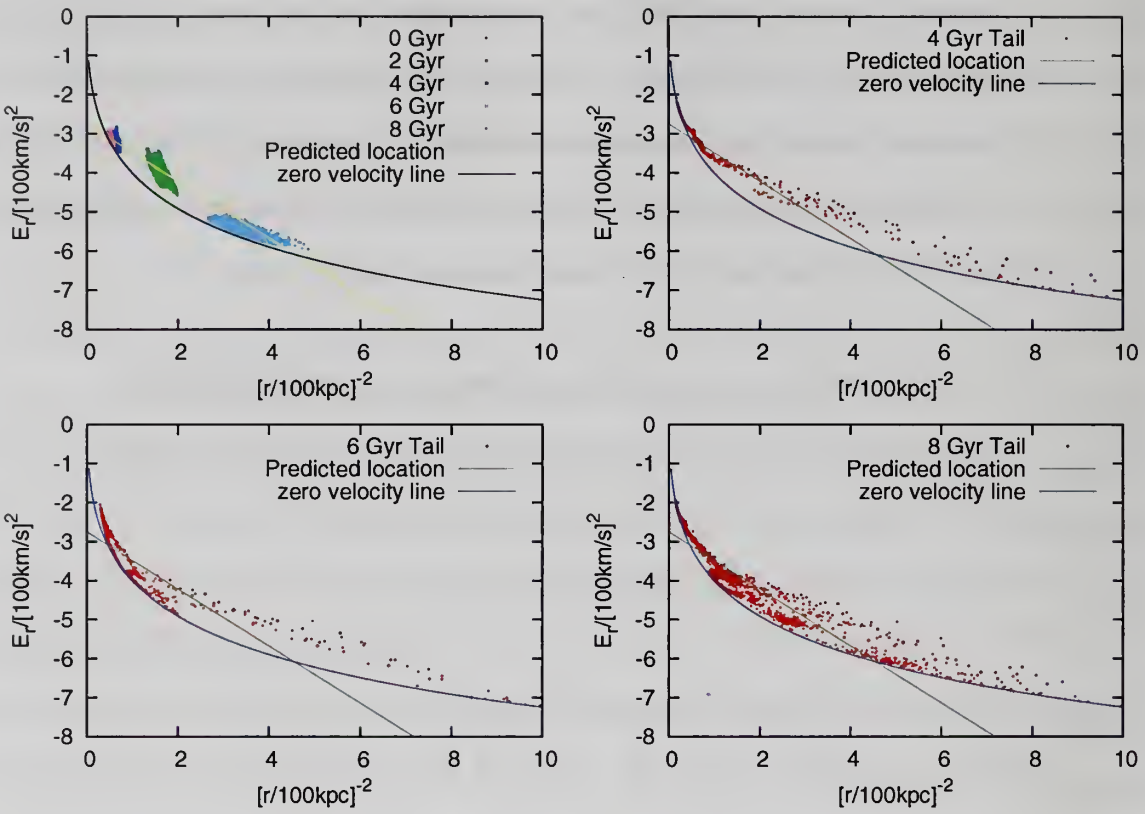

Figure 4.22 Radial energy, $E_r = v_r^2/2 + \Phi(r)$, plotted against inverse galactocenteric radius, r^{-2}, for the low-mass satellite with an $e = 0.5$ orbit. Particles with the same energy and angular momentum as the satellite will lie on a particular straight line. The zero velocity curve describes the lowest possible energy at a given radius for this host halo. The material bound to the satellite follows the straight locus at all times (top left). The escaped particles are shown at $T = 2.0$ (top right), $T = 3.0$ (bottom left) and $T = 4.0$ (bottom right), respectively. Only one particle out of 250 are plotted for visibility. Because the leading (trailing) tail loses (gains) energy, the ejecta deviates from the predicted straight line with significant scatter. Times in Gyrs are scaled to the Milky Way.

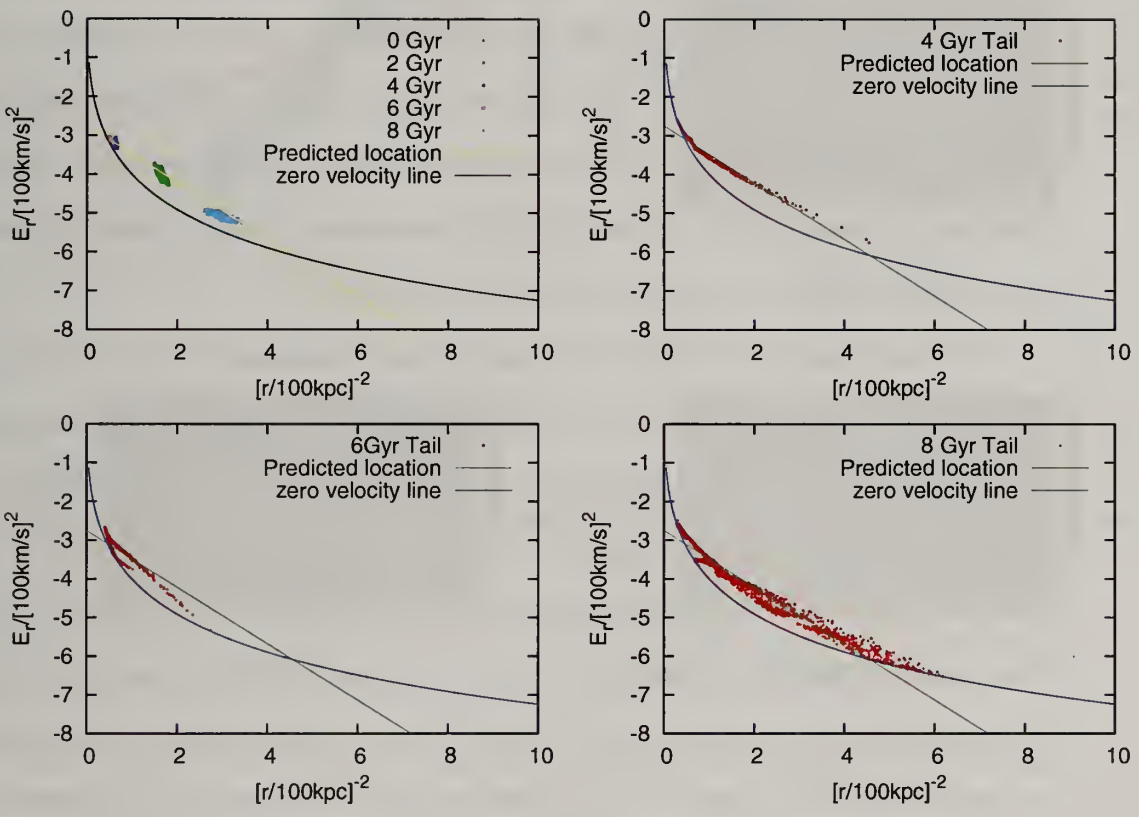

Figure 4.23 The same as Figure 4.22 but for the tiny-mass satellite.

pling the simulation phase space and plot the bound particles at five different times in the upper-left panels. We calculate the expected linear relation from the satellite's initial position and velocity. The bound material in low-mass and tiny-mass satellites lies along the predicted linear relation at all times. We plot the tail particles at three different times in the other three panels. As one can see in Figure 4.22, the deviation of the tail particles from the predicted locus and the scatter in E at fixed r^{-2} for the low-mass satellite is large. Especially at late times, e.g. the bottom right panel in Figure 4.22, the tail nearly fills the region between the zero velocity curve and the predicted locus. However, one can see from Figure 4.23 that tail particles from the tiny-mass satellite do follow the predicted linear relation. Therefore, we conclude that the Lynden-Bell & Lynden-Bell (1995) diagnostic can only detect streams from very low-mass satellites such as globular clusters.

Motivated by the prospect of six-dimensional phase-space data from future astrometric missions, Helmi & de Zeeuw (2000) proposed to identify phase-mixed satellite debris by a cluster analysis in (E, L, L_z) space. We explore the consequences of tail evolution on this approach using the same two simulations in Figure 4.24 for the low-mass satellite and in Figure 4.25 for the tiny-mass satellite. For simplicity, we assume that we know the orbital orientation and consider only the E–L_z projection. The top-left panels show the distribution at 0 Gyr ($T = 0$) and at 8 Gyr ($T = 4$) when scaled to the Milky Way halo in E–L_z space. Once again, we randomly sampled the material to improve clarity. The top-right and bottom-left panels show density estimates in E–L_z space for the satellite at 0 Gyr and at 8 Gyr, respectively. In the bottom-right panels we show the density of only the tail particles at 8 Gyr. The overall position of the satellite and its tail changes little from 0 Gyr to 8 Gyr, although the shape of the distribution shifts. In both figures, there are two or more peaks at high and low energy with respect to the satellite owing to decelerations and accelerations of tail particles by the satellite potential. Moreover, the tidal field is nonaxisymmetric and

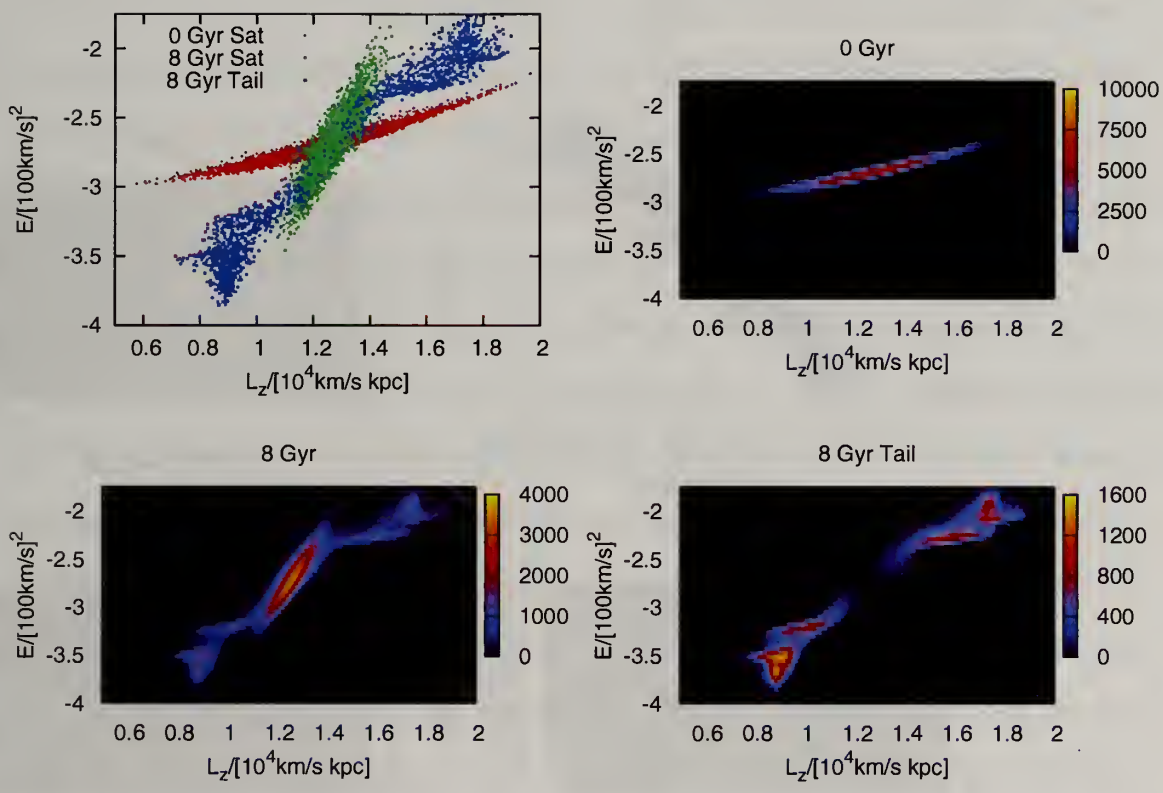

Figure 4.24 The distribution of particles bound to the low-mass satellite on an $e = 0.5$ orbit and its ejected tail particles plotted in E–L_z space. *Top left:* The phase-space distribution at $T = 0.0$ and $T = 4.0$ for the bound satellite and its tail (subsampled as in Figure 4.22). Density plots of the phase-space distribution are shown at $T = 0.0$ (top right), at $T = 4.0$ (bottom left) and at $T = 4.0$ for the ejected tail particles alone (bottom right).

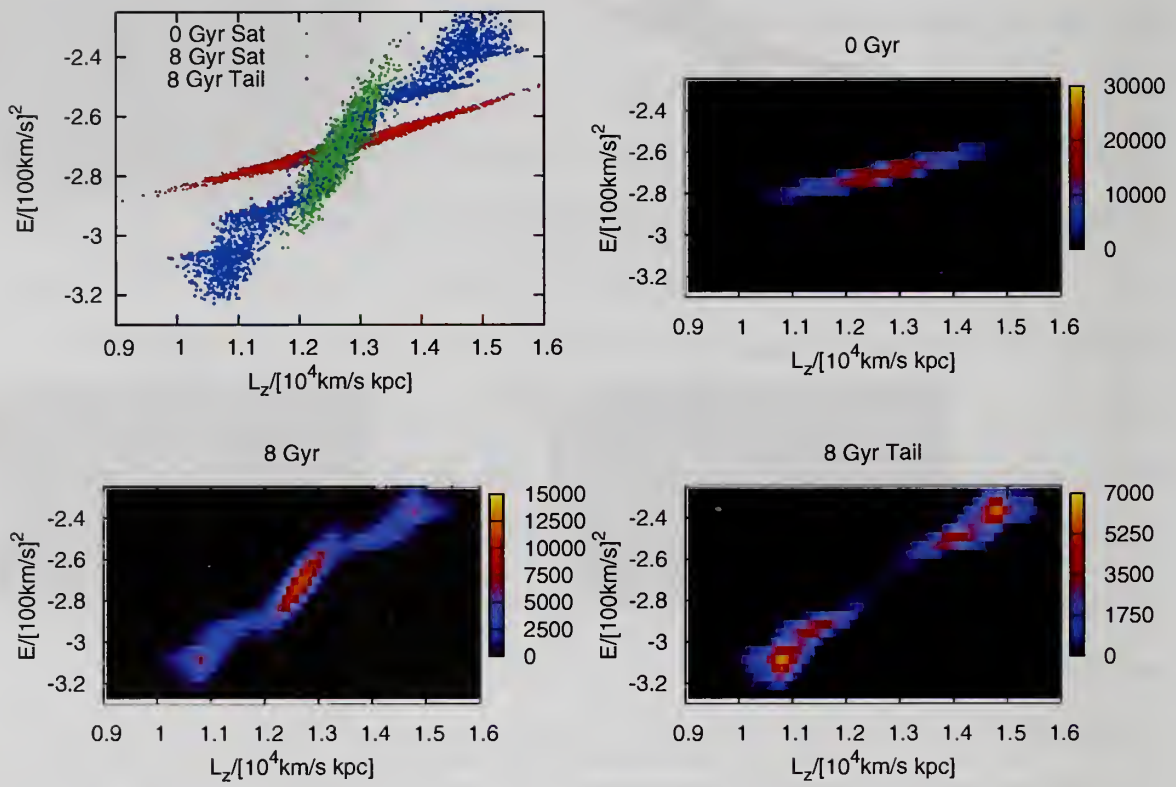

Figure 4.25 The same as Figure 4.24 but for the tiny-mass satellite

this leads to spatial correlations in the energy and angular momentum of the least bound satellite particles, which in turn leads to the production of several apparently disassociated phase-space clumps before disruption.

4.5 Discussion and summary

The observational detection of "S"- or "Z"-shaped tidal tails in globular clusters (e.g. Leon et al., 2000; Odenkirchen et al., 2003; Grillmair & Dionatos, 2006) promises sensitive statistical tests of the Galaxy's gravitational potential and has renewed the quest for streams from larger satellites. For globular clusters, i.e. very low mass satellites, the tidal tail morphology is easily interpreted. (Capuzzo Dolcetta et al., 2005; Montuori et al., 2007) However, for massive satellites, the bisymmetry that leads to this simple morphology is broken by the interaction of the host halo's gravitational field and the self-gravity of the satellite itself. We present new dynamical aspects and morphologies of tidal tails produced in satellites of significant mass, $M_s/M_h \geq 0.0001$. There are two dynamical principles that affect the tail production for massive satellites. First, the leading and trailing X-points, points where the attractive force of the host halo and satellite are balanced at zero velocity, do not occur at equal distances from the center nor do they have the same equipotential value for large-mass satellites (see Figure 4.11). Second, the escaped ejecta in the leading (trailing) tail continues to be decelerated (accelerated) by the satellite's gravity leading to large offsets of the ejecta orbits from the satellite's original orbit (see Figure 4.17). We show that this is consistent with Hill-Jacobi theory (generalized to dark-matter halos) for satellites on circular orbits. In particular, the effect of the satellite's self gravity on the tail decreases only weakly with decreasing satellite mass, proportional to $(M_s/M_h)^{1/3}$ (see Section 4.3.2.1) and, therefore, the acceleration by the satellite after escape is important for dwarfs and dark halos of modest mass.

These findings have several important and useful theoretical and observational consequences. First, for a finite mass satellite, the morphology of the leading and trailing tails will be different owing to the gradient in the underlying halo potential across the satellite. In addition, the tail ejection occurs over a range of azimuth relative to the X-point owing to the dynamical response of the originally prograde and retrograde orbits to the tidal and non-inertial acceleration. These effects should be observable in high resolution imaging for both dwarf spheroidal and globular clusters (see Figs. 4.17–4.19).

Second, the radial velocity of tail particles will be displaced from that of the satellite orbit. The magnitude of the displacement is proportional to the satellite mass. These trends distort the ejecta from the gravitationally bound satellite trajectory in the $v_r - l$ plane in much the same sense as a satellite trajectory in a flattened halo (see Figure 4.21). In other words, in fitting the $v_r - l$ diagram for tidal tails to satellite orbits of different flattenings, the satellite mass is covariant with halo flattening, i.e. the *shape* parameter $q = c/a$. Therefore, a constraint on the Milky Way halo shape using tidal streams requires mass-dependent modelling. Finally, the acceleration of ejecta by a massive satellite during escape spreads the velocity distribution and obscures the signature of a well-defined "moving group" in phase space (see Figs. 4.22–4.25).

Although we believe that the physical effects described in this study are robust, our intentionally idealized simulations ignore several possibly relevant processes. First, the dynamical friction and the self-gravitation of the tail are ignored, although in all but the most extreme mass satellites their effects on the tail morphology will be negligible, since the mass in the tail is very small. Second, we assume a smooth and static spherical host halo potential. In reality, over time, as the host halo mass grows its shape may change, and the ejecta will be perturbed by substructure. These time dependent effects will not affect the applicability of the dynamics described here but will complicate the prediction of observational signatures. Finally, we have not

included the physics of a dissipational baryonic component that may have slightly different kinematics than that of a dark collisionless component. In spite of these shortcomings, our study elaborates the details of satellite tidal tail production and the dynamics that bear on the interpretation of observed streams.

As an example, Moore & Davis (1994) and Johnston et al. (1996) find that satellite tails follow the satellite orbit for dwarf galaxies whose mass is negligible compared to the galaxy mass. The mass of these satellites is usually similar to or less than our tiny-mass satellite. Using these simulation results, Johnston et al. (2001) developed an efficient numerical method to investigate the detectability and interpretation of tidal debris tails. However, we have demonstrated here that the gravity of the satellite for $M_s/M_h \geq 0.0001$ will change the actions of the tidal ejecta to mimic halo flattening (see Section 4.4.2, Figure 4.21). In addition to the spatial distribution, the velocity distribution of the tail is affected by the satellite potential (see Section 4.4.3). We would like to note that (Fujii et al., 2006) have also noticed a systematic distance offset for leading (trailing) tails inside (outside) the orbit of a satellite owing to the satellite potential. However, they did not focus on the tail morphology.

In summary, we have shown that the interplay between the satellite and the host halo results in a complex tail morphology whose amplitude scales weakly with mass. Although these findings complicate the interpretation of stellar streams and moving groups, the intrinsic mass dependence provides additional leverage on both the halo and on the progenitor satellite properties. A statistical study of these trends will further constrain the dark halo potential and the mass accretion history of the Milky Way.

BIBLIOGRAPHY

Arnol'd, V. I. 1995, Mathematical methods of classical mechanics (Encyclopaedia of mathematical sciences, Berlin, New York: Springer, —c1995, 2nd ed. 1989, corr. 3rd printing 1995)

Baldwin, J. E., Lynden-Bell, D., & Sancisi, R. 1980, MNRAS, 193, 313

Belokurov, V. et al. 2007, ApJ, 658, 337

Benson, A. J., Frenk, C. S., Lacey, C. G., Baugh, C. M., & Cole, S. 2002, MNRAS, 333, 177

Binney, J. 1992, ARA&A, 30, 51

Binney, J. & Tremaine, S. 1987, Galactic dynamics (Princeton, NJ, Princeton University Press, 1987)

Boily, C. M., Nakasato, N., Spurzem, R., & Tsuchiya, T. 2004, ApJ, 614, 26

Briggs, F. H. 1990, ApJ, 352, 15

Bryan, G. L. & Norman, M. L. 1998, ApJ, 495, 80

Bullock, J. S., Kravtsov, A. V., & Weinberg, D. H. 2000, ApJ, 539, 517

—. 2001, ApJ, 548, 33

Butcher, H. & Oemler, Jr., A. 1978, ApJ, 226, 559

—. 1984, ApJ, 285, 426

Capuzzo Dolcetta, R., Di Matteo, P., & Miocchi, P. 2005, AJ, 129, 1906

Chandrasekhar, S. 1943, ApJ, 97, 255

Chernoff, D. F. & Weinberg, M. D. 1990, ApJ, 351, 121

Choi, J.-H., Weinberg, M. D., & Katz, N. 2007, astro-ph/0702353

Clutton-Brock, M. 1972, Ap&SS, 16, 101

—. 1973, Ap&SS, 23, 55

Coleman, M. G., Da Costa, G. S., Bland-Hawthorn, J., & Freeman, K. C. 2005, AJ, 129, 1443

Colín, P., Klypin, A. A., & Kravtsov, A. V. 2000, ApJ, 539, 561

Colpi, M., Mayer, L., & Governato, F. 1999, ApJ, 525, 720

Connors, T. W., Kawata, D., & Gibson, B. K. 2006, MNRAS, 371, 108

Davis, M., Efstathiou, G., Frenk, C. S., & White, S. D. M. 1985, ApJ, 292, 371

De Lucia, G., Kauffmann, G., Springel, V., White, S. D. M., Lanzoni, B., Stoehr, F., Tormen, G., & Yoshida, N. 2004, MNRAS, 348, 333

De Rijcke, S., Dejonghe, H., Zeilinger, W. W., & Hau, G. K. T. 2004, A&A, 426, 53

Diemand, J., Kuhlen, M., & Madau, P. 2007, ApJ, 657, 262

Diemand, J., Moore, B., & Stadel, J. 2004, MNRAS, 352, 535

Dressler, A., Oemler, A. J., Butcher, H. R., & Gunn, J. E. 1994, ApJ, 430, 107

Eke, V. R., Navarro, J. F., & Frenk, C. S. 1998, ApJ, 503, 569

Fujii, M., Funato, Y., & Makino, J. 2006, PASJ, 58, 743

Gao, L., White, S. D. M., Jenkins, A., Stoehr, F., & Springel, V. 2004, MNRAS, 355, 819

Gardiner, L. T. & Noguchi, M. 1996, MNRAS, 278, 191

Gardiner, L. T., Sawa, T., & Fujimoto, M. 1994, MNRAS, 266, 567

Ghigna, S., Moore, B., Governato, F., Lake, G., Quinn, T., & Stadel, J. 1998, MNRAS, 300, 146

—. 2000, ApJ, 544, 616

Gnedin, O. Y. 2003, ApJ, 589, 752

Gnedin, O. Y., Hernquist, L., & Ostriker, J. P. 1999, ApJ, 514, 109

Gnedin, O. Y. & Ostriker, J. P. 1999, ApJ, 513, 626

Goerdt, T., Moore, B., Read, J. I., Stadel, J., & Zemp, M. 2006, MNRAS, 368, 1073

Goldstein, H. 1950, Classical mechanics (Addison-Wesley World Student Series, Reading, Mass.: Addison-Wesley, 1950)

González-García, A. C., Aguerri, J. A. L., & Balcells, M. 2005, A&A, 444, 803

Governato, F., Colpi, M., & Maraschi, L. 1994, MNRAS, 271, 317

Grillmair, C. J. & Dionatos, O. 2006, ApJL, 641, L37

Gunn, J. E. & Gott, J. R. I. 1972, ApJ, 176, 1

Hayashi, E., Navarro, J. F., Taylor, J. E., Stadel, J., & Quinn, T. 2003, ApJ, 584, 541

Haynes, M. P., van Zee, L., Hogg, D. E., Roberts, M. S., & Maddalena, R. J. 1998, AJ, 115, 62

Helmi, A. & de Zeeuw, P. T. 2000, MNRAS, 319, 657

Helmi, A. & White, S. D. M. 1999, MNRAS, 307, 495

Hernquist, L. & Ostriker, J. P. 1992, ApJ, 386, 375

Holley-Bockelmann, K., Weinberg, M., & Katz, N. 2005, MNRAS, 363, 991

Ibata, R., Irwin, M., Lewis, G., Ferguson, A. M. N., & Tanvir, N. 2001a, Nature, 412, 49

Ibata, R., Lewis, G. F., Irwin, M., Totten, E., & Quinn, T. 2001b, ApJ, 551, 294

Ibata, R. A. & Lewis, G. F. 1998, ApJ, 500, 575

Jing, Y. P. & Suto, Y. 2000, ApJL, 529, L69

Johnston, K. V., Hernquist, L., & Bolte, M. 1996, ApJ, 465, 278

Johnston, K. V., Sackett, P. D., & Bullock, J. S. 2001, ApJ, 557, 137

Johnston, K. V., Zhao, H., Spergel, D. N., & Hernquist, L. 1999, ApJL, 512, L109

Kim, S., Staveley-Smith, L., Dopita, M. A., Freeman, K. C., Sault, R. J., Kesteven, M. J., & McConnell, D. 1998, ApJ, 503, 674

Klypin, A., Gottlöber, S., Kravtsov, A. V., & Khokhlov, A. M. 1999, ApJ, 516, 530

Klypin, A., Zhao, H., & Somerville, R. S. 2002, ApJ, 573, 597

Knebe, A., Power, C., Gill, S. P. D., & Gibson, B. K. 2006, MNRAS, 368, 741

Kormendy, J. & Kennicutt, Jr., R. C. 2004, ARA&A, 42, 603

Kunkel, W. E., Demers, S., Irwin, M. J., & Albert, L. 1997, ApJL, 488, L129+

Law, D. R., Johnston, K. V., & Majewski, S. R. 2005, ApJ, 619, 807

Leon, S., Meylan, G., & Combes, F. 2000, A&A, 359, 907

Lichtenberg, A. J. & Lieberman, M. A. 1983, Regular and stochastic motion (Applied Mathematical Sciences, New York: Springer, 1983)

Lindegren, L. & Perryman, M. A. C. 1996, A&AS, 116, 579

Lynden-Bell, D. & Kalnajs, A. J. 1972, MNRAS, 157, 1

Lynden-Bell, D. & Lynden-Bell, R. M. 1995, MNRAS, 275, 429

Mackey, A. D. & Gilmore, G. F. 2003, MNRAS, 340, 175

Majewski, S. R., Skrutskie, M. F., Weinberg, M. D., & Ostheimer, J. C. 2003, ApJ, 599, 1082

Majewski, S. R. et al. 2004, AJ, 128, 245

Mastropietro, C., Moore, B., Mayer, L., Debattista, V. P., Piffaretti, R., & Stadel, J. 2005a, MNRAS, 364, 607

Mastropietro, C., Moore, B., Mayer, L., Wadsley, J., & Stadel, J. 2005b, MNRAS, 363, 509

Mathewson, D. S., Schwarz, M. P., & Murray, J. D. 1977, ApJL, 217, L5

Mayer, L., Moore, B., Quinn, T., Governato, F., & Stadel, J. 2002, MNRAS, 336, 119

Merritt, D. 1985, AJ, 90, 1027

Montuori, M., Capuzzo-Dolcetta, R., Di Matteo, P., Lepinette, A., & Miocchi, P. 2007, ApJ, 659, 1212

Moore, B. & Davis, M. 1994, MNRAS, 270, 209

Moore, B., Ghigna, S., Governato, F., Lake, G., Quinn, T., Stadel, J., & Tozzi, P. 1999, ApJL, 524, L19

Moore, B., Governato, F., Quinn, T., Stadel, J., & Lake, G. 1998a, ApJL, 499, L5+

Moore, B., Katz, N., & Lake, G. 1996a, ApJ, 457, 455

Moore, B., Katz, N., Lake, G., Dressler, A., & Oemler, A. 1996b, Nature, 379, 613

Moore, B., Lake, G., & Katz, N. 1998b, ApJ, 495, 139

Murai, T. & Fujimoto, M. 1980, PASJ, 32, 581

Murali, C., Katz, N., Hernquist, L., Weinberg, D. H., & Davé, R. 2002, ApJ, 571, 1

Murray, C. D. & Dermott, S. F. 1999, Solar system dynamics (Solar system dynamics by Murray, C. D., 1999)

Navarro, J. F., Frenk, C. S., & White, S. D. M. 1996, ApJ, 462, 563

—. 1997, ApJ, 490, 493

Odenkirchen, M., Grebel, E. K., Dehnen, W., Rix, H.-W., Yanny, B., Newberg, H. J., Rockosi, C. M., Martínez-Delgado, D., Brinkmann, J., & Pier, J. R. 2003, AJ, 126, 2385

Oemler, A. J., Dressler, A., & Butcher, H. R. 1997, ApJ, 474, 561

Oguri, M. & Lee, J. 2004, MNRAS, 355, 120

Osipkov, L. P. 1979, Pis ma Astronomicheskii Zhurnal, 5, 77

Perryman, M. A. C., de Boer, K. S., Gilmore, G., Høg, E., Lattanzi, M. G., Lindegren, L., Luri, X., Mignard, F., Pace, O., & de Zeeuw, P. T. 2001, A&A, 369, 339

Pruess, S. & Fulton, C. T. 1993, ACM Trans. Math. Software, 19, 360

Putman, M. E. et al. 1998, Nature, 394, 752

Quilis, V., Moore, B., & Bower, R. 2000, Science, 288, 1617

Quinn, P. J. & Goodman, J. 1986, ApJ, 309, 472

Read, J. I., Goerdt, T., Moore, B., Pontzen, A. P., Stadel, J., & Lake, G. 2006, MNRAS, 373, 1451

Sellwood, J. A. 2006, ApJ, 637, 567

Sellwood, J. A. & Debattista, V. P. 2006, ApJ, 639, 868

Skrutskie, M. F. et al. 2006, AJ, 131, 1163

Somerville, R. S. 2002, ApJL, 572, L23

Spitzer, L. 1987, Dynamical evolution of globular clusters (Princeton, NJ, Princeton University Press, 1987)

Steinmetz, M. et al. 2006, AJ, 132, 1645

Stoehr, F., White, S. D. M., Tormen, G., & Springel, V. 2002, MNRAS, 335, L84

Taylor, J. E. & Babul, A. 2001, ApJ, 559, 716

—. 2004, MNRAS, 348, 811

—. 2005a, MNRAS, 364, 515

—. 2005b, MNRAS, 364, 535

Tormen, G., Diaferio, A., & Syer, D. 1998, MNRAS, 299, 728

Tremaine, S. 1981, in Structure and Evolution of Normal Galaxies, ed. S. M. Fall & D. Lynden-Bell, 67–84

Tremaine, S. & Weinberg, M. D. 1984, MNRAS, 209, 729

Valenzuela, O. & Klypin, A. 2003, MNRAS, 345, 406

van den Bosch, F. C., Weinmann, S. M., Yang, X., Mo, H. J., Li, C., & Jing, Y. P. 2005, MNRAS, 361, 1203

van der Marel, R. P., Alves, D. R., Hardy, E., & Suntzeff, N. B. 2002, AJ, 124, 2639

van Zee, L., Skillman, E. D., & Haynes, M. P. 2004, AJ, 128, 121

Vesperini, E. & Weinberg, M. D. 2000, ApJ, 534, 598

Weinberg, M. D. 1985, MNRAS, 213, 451

—. 1986, ApJ, 300, 93

—. 1989, MNRAS, 239, 549

—. 1994a, AJ, 108, 1398

—. 1994b, AJ, 108, 1403

—. 1999, AJ, 117, 629

—. 2000, ApJ, 532, 922

—. 2004, astro-ph/0404169

Weinberg, M. D. & Katz, N. 2002, ApJ, 580, 627

—. 2007a, MNRAS, 375, 425

—. 2007b, MNRAS, 375, 460

White, S. D. M. & Rees, M. J. 1978, MNRAS, 183, 341

Zentner, A. R., Berlind, A. A., Bullock, J. S., Kravtsov, A. V., & Wechsler, R. H. 2005, ApJ, 624, 505